UNIVERSITY OF SOUTHAMPTON

SCHOOL OF ENGINEERING SCIENCES

MATERIALS RESEARCH GROUP

Thesis Submitted for the Degree of Doctor of Philosophy

FATIGUE OF ALUMINIUM LININGS IN PLAIN AUTOMOTIVE BEARINGS

by Mark Richard Joyce

December 2000

UNIVERSITY OF SOUTHAMPTON

ABSTRACT

SCHOOL OF ENGINEERING SCIENCES
MATERIALS RESEARCH GROUP

Doctor of Philosophy

FATIGUE OF ALUMINIUM LININGS IN PLAIN AUTOMOTIVE BEARINGS

by Mark Richard Joyce

Modern plain bearing designs as used in small automotive engines typically comprise a number of layers of different material. The development of these material systems has been carried out in a semi-empirical manner over many years to maintain pace with new engine designs. The service loading for plain bearings is becoming increasingly severe and it is important that new bearing material systems are designed to provide the longest possible operating life at these higher loads. To date very little work has been carried out to characterise the fundamental fatigue behaviour of such material systems. This thesis presents the results of a three year research program concentrating on one modern bearing design. This is a typical shell bearing, constructed in two parts or half shells, which are clamped together within a housing to support the journal. Each half shell comprises a thin layer of a complex Al, Sn, Si, Cu lining material, bonded to a steel backing layer via a thin layer of aluminium foil.

A series of standard experimental material characterisation techniques are applied to investigate the material system's macroscopic geometry and properties, as well as more advanced statistical tessellation-based approaches, used to characterise the lining material microstructure. In addition, the results of a detailed experimental program of fatigue testing are presented, characterising the initiation and short fatigue crack growth behaviour in this material system. These are used to establish the key parameters controlling early crack propagation, hence providing material optimisation data. Further insight into the preferential location of fatigue crack initiation events is obtained through the application of tessellation approaches, which provide statistical identification of microstructural features associated with fatigue crack initiation. Subsequently, this information is combined with microstructural scale finite element modelling to investigate the correlation between crack nucleation sites and the highly local stress and strain fields produced on a microstructural level under applied loading. Finite element modelling was also applied to gain additional understanding of the complex propagation behaviour of fatigue cracks as they interact with each other and the multi-layer material system. The modelling program was extended parametrically to examine the influence of several material system parameters on predicted component fatigue life, as well as predicting the behaviour of potential future bearing designs.

CONTENTS

ACKNOWLEDGEMENTS

I am grateful to EPSRC and Dana Glacier Vandervell for financial and material support during this project. In particular Dr. Carl Perrin and Dr. Paul Shenton of Dana Glacier Vandervell for their help and advice.

I would like to acknowledge the support and encouragement of my supervisors Dr Philippa Reed and Dr Stavros Syngellakis without whose guidance this work would not have been possible.

I would also like to thank the technical staff for their assistance during the experimental phase of this project, in particular Eric Bonner, for manufacture of various rigs, specimens and other assorted "can you justs". Finally I am indebted to my office mates for providing enthusiasm, realism and cynicism in roughly equal quantities.

NOMENCLATURE

α	-	Ramberg Osgood power law coefficient
β	-	Wetting angle
δ_{ij}	-	Krondecker delta
ε	-	Strain
$\varepsilon_{0.2}$	-	0.2% strain
ε_2	-	2% strain
ε_{app}	-	Applied strain
ε_c	-	Constrained strain
ε_{max}	-	Maximum strain
ε_p	-	Plastic strain
ε_t	-	Free strain
ε'_f	-	Fatigue ductility coefficient
ε_y	-	Yield strain
ϕ	-	Angle of crack deflection
γ_s	-	Surface energy
γ	-	Surface tension
Γ	-	Contour surrounding crack tip
η	-	Kinematic viscosity
κ	-	Elastic constant dependent on Poison's ratio
μ	-	Shear modulus
ν	-	Poisson's ratio
θ	-	Angle ahead of crack tip
θ_0	-	Preferential direction of crack propagation
ρ	-	Density
σ	-	Stress
σ_a	-	Stress Amplitude
σ_C	-	Critical stress for fracture initiation
σ_{cl}	-	Closing stress
σ_{eff}	-	Effective stress
σ_e	-	Endurance limit
σ_f	-	Critical stress for fracture initiation
σ_m	-	Mean stress
σ_{max}	-	Maximum stress
σ_{min}	-	Minimum stress
σ_{op}	-	Opening stress
σ'_f	-	Fatigue strength coefficient
σ_{TS}	-	Tensile strength
σ_{UTS}	-	Ultimate tensile stress
σ_y	-	Yield stress
τ	-	Shear stress
a	-	crack length
A	-	Crack area
b	-	Fatigue strength or Basquin exponent

B	-	Thickness
c	-	Crack depth
C	-	Empirical factor (Paris law)
D	-	Deflected ligament length
d	-	Depth of oil penetration
E	-	Young's modulus
E_l	-	Lining Young's modulus
E_b	-	Backing Young's modulus
E'	-	Effective Young's modulus
e	-	Fatigue ductility exponent
f	-	Frequency
G	-	Strain energy release rate
h	-	Crack opening displacement
$<h>$	-	Average crack opening displacement
H_v	-	Vickers hardness
I	-	Second moment of Area
I_n	-	Empirical factor (dependent on n)
J	-	J-integral
J_{app}	-	Applied J-integral
J^C	-	Cyclic J-Integral
$J_{closing}$	-	J-integral evaluated at closing crack tip
J_{free}	-	J-integral evaluated at free crack tip
J_{tip}	-	Near tip J-integral
J_ϕ	-	J-integral for given crack deflected ligament angle
k	-	Local stress intensity factor
K	-	Stress intensity factor
K_{cl}	-	Closing stress intensity factor
K_{eff}	-	Effective stress intensity factor
K_{IC}	-	Mode I fracture toughness
K_{max}	-	Maximum stress intensity factor
K_{min}	-	Minimum stress intensity factor
K_{op}	-	Opening stress intensity factor
$K^*_{\max}$	-	Maximum stress intensity factor caused by internal oil pressure
l	-	Distance behind crack tip
L	-	Length
L_l	-	Lining thickness
L_b	-	Backing thickness
L_c	-	Core region size
L_e	-	Embedding region size
M	-	Bending moment
m	-	Empirical factor (Paris law)
N	-	Cycles
n	-	Strain hardening exponent
$\boldsymbol{n}$	-	Unit outer normal vector to path Γ
N_f	-	Number of cycles to failure
o	-	Oxide layer thickness
p	-	Hydrodynamic pressure
P	-	Load
P_{max}	-	Maximum load

P_{min}	-	Minimum load
Q	-	Undeflected ligament length
q	-	Solution step number
R	-	Load ratio
r	-	Distance ahead of crack tip
r_0	-	Contour radius used for strain energy density calculation
$r_{c,0}$	-	Cyclic plastic zone radius ahead of crack tip
$r_{p,0}$	-	Monotonic plastic zone radius ahead of crack tip
$r_{p,max}$	-	Maximum monotonic plastic zone radius
s	-	Arc length along contour Γ
S	-	Loading span
S_e	-	Eshelby tensor
t	-	Time
T	-	"T term"
T_D	-	Distortional strain energy density
$\boldsymbol{T}$	-	Traction vector
T_{ij}	-	Components of Traction vector $\boldsymbol{T}$
T_v	-	Dilational strain energy density
$\boldsymbol{u}$	-	Displacement vector
U	-	Total energy (of a plate)
w	-	Strain energy density
w_c	-	Critical value of strain energy density for crack propagation
w_e	-	Elastic component of strain energy density
w_p	-	Plastic component of strain energy density
W	-	Width
W_p	-	Potential energy
W_s	-	Surface energy
x	-	Distance into crack
y	-	Distance from neutral axis
Y	-	Shape factor

1.0 INTRODUCTION AND LITERATURE REVIEW

Due to advances in material selection, plain bearing fatigue failures in small automotive engines are not currently observed in service. However car manufacturers are constantly striving to both increase the power output as well as reduce the weight of next generation engines. It is recognised that these measures will lead to increases in the service loading for crankshaft and big-end plain bearings, leading to the possibility of fatigue failure in current bearing designs. To address this, new bearing designs are required, typically these are developed using artificial accelerated test rigs, which aim to simulate the service loading, but allow its magnitude to be increased to a level causing rapid bearing failure. Modern plain bearings such as those considered by this study comprise; an aluminium alloy lining bonded to a steel backing layer by a thin aluminium foil interlayer. In a typical fatigue failure it is observed that multiple cracks initiate on the surface of the lining and propagate towards the backing layer, eventually causing a piece of lining to become detached, precipitating rapid bearing failure.

The process of bearing development via accelerated test rigs has been used to considerably improve bearing performance in a semi-empirical manner for many years, however this approach does not allow investigation of the fundamental fatigue behaviour of these components. To address this a single advanced bearing design is considered in this project and subjected to a series of tests under well defined stress states.

Chapter 2 reports the results of a detailed program of material characterisation including optical and electron microscopy. Chapter 3 contains the methodology and results of the experimental program of fatigue testing employed to characterise the fundamental fatigue performance of the studied bearing material system. Subsequent chapters are concerned with a number of analysis techniques employed to gain further understanding of the fatigue behaviour observed. These methods include statistical tessellation methods, and multi-scale finite element modelling.

Before considering new work it is appropriate to present a review of several sections of the literature, which are directly relevant to the work presented in this thesis.

1.1 Literature Review Topics

Sections 1.2 to 1.7 of this literature review are concerned with relevant sections of the classical fatigue literature, including;

- Fatigue crack initiation and growth mechanisms in ductile materials.
- Total life approaches to fatigue life characterisation.
- Damage tolerant approaches using linear elastic fracture mechanics (LEFM).
- Parameters for characterising fatigue crack growth rates including stress intensity factor, K, and the J integral.
- Closure effects, and the impact of variable amplitude loading.
- Special considerations for short fatigue cracks.
- The effect of environment on fatigue crack propagation.

Section 1.8 reviews research concerning the fatigue optimisation of plain bearings. In addition to the prior work discussed in this chapter, it should be noted that further references to relevant sections of the literature are made in Chapters 4, 5 and 6.

1.2 Fatigue Crack Growth in Ductile Materials

Fatigue is a form of failure found to occur in components subjected to cyclic loading. It is generally considered to consist of the initiation and growth of one or more cracks until final failure. Typically this final failure is preceded by a considerable amount of stable crack growth. The cyclic loading, which gives rise to fatigue can be quantified in a number of ways, typically in terms of mean stress, σ_m and stress amplitude, σ_a or load ratio, R. Expressions for mean stress, stress amplitude and load ratio are given in Eqns 1.1, 1.2 and 1.3 respectively

$$\sigma_m = \frac{(\sigma_{max} + \sigma_{min})}{2} \tag{1.1}$$

$$\sigma_a = \frac{\Delta\sigma}{2} = \frac{(\sigma_{max} - \sigma_{min})}{2} \tag{1.2}$$

$$R = \frac{\sigma_{\min}}{\sigma_{\max}} \tag{1.3}$$

where σ_{max} and σ_{min} are the maximum and minimum stresses respectively in the loading cycle.

The mechanisms by which fatigue cracks initiate and grow have been investigated extensively. Considering first crack initiation behaviour, it was shown by Forsyth[1] that in the absence of pre-existing defects, fatigue cracks initiate along slip planes with the highest shear stress (those at 45° to the applied stress). The rapid and repeated movement of dislocations along the slip band eventually causes a small crack to form, which can then propagate to adjacent grains.

It is generally accepted that fatigue crack growth is split into three regimes. The first of these, termed stage I, concerns the crack's growth immediately after initiation. A micrograph of typical initiation and stage I growth behaviour in a Ni-base alloy is shown in Figure 1.1. In this regime crack growth is seen to be highly microstructurally dependent, the crack growing along pre-existing slip planes in the crystal lattice. Stage I growth is relatively slow and causes a rough facetted fracture surface, usually extending over only a few grains, although its exact extent is dependent on loading and material properties.

Forsyth[1] also demonstrated that eventually a faster crack growth regime takes over from stage I propagation. In this second regime, termed stage II growth, it was observed that fatigue cracks grew perpendicular to the remote tensile axis. A typical section of fracture surface produced during this second regime of crack growth in an Al alloy is shown in Figure 1.2. Striations are clearly evident on the surface, these together with beach marks have been observed in many materials by several researchers including Zapphe and Worden[2]. A micro-mechanism for stage II crack advance accounting for these striations was proposed by Laird and Smith[3], this is shown in schematic form in Figure 1.3. It was proposed that the incremental crack extension during each loading cycle is caused by the plastic blunting and re-sharpening of the crack tip, and that each successive blunting forms a striation in the crack wake. Since a striation is formed during each loading cycle, Forsyth and Ryder[4] showed that it is possible to relate crack growth rate to striation spacing.

The third regime of crack growth is the final accelerated growth to failure, the crack growing by fatigue and additional static tearing modes. This regime is generally short lived in most engineering components, and can usually be ignored in lifing calculations, although several researchers including Ritchie[5] have shown that in some components, such as reactor pressure vessels, stage III growth is important.

1.3 Total Life Approaches to Fatigue

In the majority of cases, catastrophic failure by fatigue is preceded by a considerable amount of stable crack growth. This behaviour may be characterised in several ways, one of these is the so called total life approach; this was proposed in 1860 by Wöhler[6] and seeks to express the total fatigue life of a given component or sample as a function of the applied loading.

1.3.1 Stress-life approaches

The earliest total life approaches are the so called "stress-life" approaches, these attempt to relate sample lifetime to the maximum applied stress. Typically tests are performed using rotating bend samples and a diagram of stress amplitude against cycles to failure plotted; an example of such an *S-N* curve is given in Figure 1.4. Under constant amplitude loading conditions, many materials exhibit a plateau in the *S-N* curve beyond 10^6 cycles. At stress amplitudes below this level, the sample may be cycled indefinitely without failure through fatigue. This critical stress amplitude is known as the fatigue limit or endurance limit, σ_e. Aluminium alloys and some other materials typically do not exhibit a fatigue limit, for these materials the endurance limit is defined as the stress amplitude which they can support for 10^7 cycles.

It was noted by Basquin[7] that if the *S-N* curve was redrawn on a log-log scale, a linear relation is typically observed. The expression for relating stress amplitude to the number of cycles to failure, N_f is given by Eqn 1.4; the Basquin equation.

$$\sigma_a = \sigma'_f \left(2N_f\right)^b \tag{1.4}$$

where σ'_f is the fatigue strength coefficient and b is the fatigue strength exponent or Basquin exponent. The Basquin relation in this form applies to samples

tested under reversed bend conditions ($R = -1$, $\sigma_m = 0$). However fully reversed cycles with zero mean stress are unrepresentative of many fatigue situations, and hence modifications for other conditions have been proposed. Most common are those of Gerber[8], Goodman[9] and Soderberg[10], whose expressions are given in Eqns 1.5, 1.6 and 1.7 respectively.

$$\sigma_a = \sigma_a\big|_{\sigma_m=0}\left\{1-\frac{\sigma_m}{\sigma_y}\right\} \tag{1.5}$$

$$\sigma_a = \sigma_a\big|_{\sigma_m=0}\left\{1-\frac{\sigma_m}{\sigma_{TS}}\right\} \tag{1.6}$$

$$\sigma_a = \sigma_a\big|_{\sigma_m=0}\left\{1-\left(\frac{\sigma_m}{\sigma_{TS}}\right)^2\right\} \tag{1.7}$$

where σ_a is the stress amplitude for a non zero mean stress and $\sigma_a\big|_{\sigma_m=0}$ is the stress amplitude for fully reversed loading ($R = -1$ and $\sigma_m = 0$). σ_y and σ_{TS} are the yield and tensile strengths of the material respectively.

1.3.2 Strain-life approaches

Stress-life approaches as discussed in the previous section are generally only applicable to elastic situations. In cases where plastic deformation is expected, an approach based on the component strain-life is typically found to perform better. It was noted independently by Coffin[11] and Manson[12] that when plastic strain amplitude $\Delta\varepsilon_p$ was plotted against cycles to failure on a log-log scale a linear relation resulted. This relation is given in Eqn 1.8.

$$\frac{\Delta\varepsilon_p}{2} = \varepsilon_f'\left(2N_f\right)^e \tag{1.8}$$

where ε_f' is the fatigue ductility coefficient and e is the fatigue ductility exponent.

1.4 Damage Tolerant Approach to Fatigue

Rather than characterising the fatigue life of a given component as a single parameter, the damage tolerant approach seeks to characterise the growth of individual cracks. This is achieved through either energy methods or more advanced fracture mechanics based techniques.

1.4.1 Energy approach (Griffith fracture theory)

Modern fracture mechanics is based upon the work of Griffith[13], who formulated criteria for crack advance in brittle materials using an energy balance method considering a elliptical crack in an infinite flat plate, as shown in Figure 1.5. It was formulated that the total energy of the plate, U could be expressed as Eqn 1.9.

$$U = W_P + W_S = -\frac{\pi a^2 \sigma^2 B}{E'} + 4aB\gamma_s \tag{1.9}$$

where $E' = \frac{E}{(1-\nu^2)}$ in plane strain or $E' = E$ in plane stress, W_P and W_S are the potential and surface energies respectively, and γ_s is the surface energy per unit surface area. Griffith noted that the critical condition for the onset of cracking is given by Eqn 1.10.

$$\frac{dU}{d\mathrm{A}} = \frac{dW_P}{d\mathrm{A}} + \frac{dW_S}{d\mathrm{A}} = -\frac{\pi a \sigma^2}{E'} + 2\gamma_s = 0 \tag{1.10}$$

where A is the crack area ($2aB$) and dA denotes an incremental change in crack area. Solving Eqn 1.10 and rearranging gives Eqn 1.11, the critical stress, σ_f for fracture initiation

$$\sigma_f = \sqrt{\frac{2E'\gamma_s}{\pi a}} \tag{1.11}$$

An approach for characterising the crack tip driving force in a cracked body using an equivalent approach to that of Griffith was proposed by Irwin[14], who introduced, G, the strain energy release rate. This parameter is defined, and the Griffith criteria for crack extension rewritten in terms of G in Eqn 1.12.

$$G = -\frac{dW_P}{dA} = \frac{\pi\sigma^2 a}{E'} = 2\gamma_s$$

(1.12)

1.4.2 Fracture mechanics applied to the plane problem

Fracture mechanics can be used to evaluate the stress and strain fields ahead of a crack under purely elastic or elasto-plastic conditions. In order to further quantify the stress and strain fields ahead of a crack it is important to characterise the basic modes of crack opening. Cracks are typically categorised into three orientations, which are shown in Figure 1.6. Figure 1.7 shows the stresses ahead of an infinite plate containing a semi-infinite crack, since this problem is 2D, only mode I and II opening are possible. Irwin[15] derived the purely elastic near tip fields ahead of such a crack in terms of a stress intensity factor, K. The equilibrium equations are given in polar co-ordinates by Eqn 1.13.

$$\frac{\partial\sigma_{rr}}{\partial r} + \frac{1}{r}\frac{\partial\sigma_{r\theta}}{\partial\theta} + \frac{\sigma_{rr} - \sigma_{\theta\theta}}{r} = 0$$

$$\frac{\partial\sigma_{r\theta}}{\partial r} + \frac{1}{r}\frac{\partial\sigma_{\theta\theta}}{\partial\theta} + \frac{2\sigma_{r\theta}}{r} = 0$$

(1.13)

It can be shown that for the plane problem the crack tip stresses are described by Eqn 1.14.

$$\sigma_{ij} = \frac{K_I}{\sqrt{2\pi r}}\tilde{\sigma}_{ij}^{I}(\theta) + T\delta_{ix}\delta_{jx}$$

(1.14)

where K_I is the mode I stress intensity factor, δ_{ij} is the Krondecker delta and $\tilde{\sigma}_{ij}^{I}$ describes the far field mode I stress. The first term of Eqn 1.14 is the leading singular term for mode I linear elastic cracks, the second term or "T term" contains the non singular stress. Generally the "T term" is omitted when characterising linear elastic problems, however it may be important in problems involving small cracks, high levels of mode mixity or cracks not propagating parallel to the far field tensile axis. The mode I crack tip stresses in Cartesian co-ordinates omitting the "T term" are given by Eqn 1.15.

$$\begin{Bmatrix}\sigma_{xx}\\ \sigma_{yy}\\ \sigma_{xy}\end{Bmatrix} = \frac{K_I}{\sqrt{2\pi r}}\cos\frac{\theta}{2}\begin{Bmatrix}1-\sin\frac{\theta}{2}\sin\frac{3\theta}{2}\\ 1+\sin\frac{\theta}{2}\sin\frac{3\theta}{2}\\ \sin\frac{\theta}{2}\cos\frac{3\theta}{2}\end{Bmatrix} \quad (1.15)$$

Similar expressions may be derived for the crack tip stresses in modes II and III.

The stress intensity factors in Eqn 1.15 are a measure of the intensity of the near tip fields under purely linear elastic conditions. They are only valid in an annular region ahead of the crack, known as the region of K dominance, within which K provides a unique measure of the stress and strain intensity. The size of this region is given by the area over which the stress fields as described by the singular "K term" are within ~10% of the true value incorporating the "T term" and other vanishing terms. This is typically ~10% of crack length, but ahead of the crack tip.

Since K is a measure of the stress intensity ahead of a crack it seems reasonable that that it may be used to characterise fatigue crack initiation and growth. The formulation of the analysis for K is based on purely linear elastic assumptions, fatigue however is a locally plastic phenomenon. Thus K cannot be used to explicitly characterise the elasto-plastic behaviour occurring in the process zone at the crack tip, however K is valid in the area surrounding this zone, but within the annular region of K dominance. Thus in order to use K to characterise fatigue crack growth rate the crack tip plastic zone must be confined within the annular region of K-dominance. This condition is known as the "small scale yielding condition", and requires that $a, W-a, B \le \left(\frac{K}{\sigma_y}\right)^2$ are all satisfied[16], where a is crack length, and B and W are specimen thickness and width respectively. Under such conditions K may be simply described by Eqn 1.16

$$K_I = Y\sigma\sqrt{\pi a} \quad (1.16)$$

where Y is a factor dependent on specimen and loading geometry.

1.4.3 Fracture toughness

Under linear elastic conditions, the initiation of a crack under monotonic quasi static loading conditions may be characterised by a critical value of the stress intensity factor K_C. The value of this parameter is dependent on several factors including, the loading mode, environmental conditions and strain rate. The critical value of the mode I stress intensity factor under plane strain conditions is commonly referred to as the fracture toughness, K_{IC}, of the material and is given by Eqn 1.17 Similarly the critical values in the sliding and tearing modes are designated K_{IIC} and K_{IIIC} respectively.

$$K_{IC} = Y\sigma\sqrt{\pi a} \tag{1.17}$$

K_{IC} is the stress intensity factor at which a crack will propagate under monotonic loading, under cyclic loading a flaw may initiate and grow at K levels well below this.

1.4.4 Characterising fatigue crack growth rate by K

The stress intensity factor has been used successfully to characterise the initiation and growth behaviour of fatigue cracks. Although fatigue is at least a locally plastic process and K is entirely based on LEFM assumptions, providing the small scale yielding conditions are not violated, the use of K to characterise fatigue crack growth rates is valid. Figure 1.8 shows a diagram of crack growth rate (da/dN) against stress intensity factor range (ΔK) plotted on a log-log scale for a typical fatigue crack growing under small scale yielding conditions. The three regimes of crack growth may be clearly distinguished. Paris[17] noted the linear region in the stage II crack growth regime and proposed the relation given as Eqn 1.18.

$$\frac{da}{dN} = C\Delta K^m \tag{1.18}$$

where C and m are empirical factors dependent on material parameters and loading conditions. This relation has been used successfully to characterise the stage II growth of fatigue cracks in many materials.

1.4.5 Equivalence of *G* and *K*

It can be shown that the strain energy release rate G is equivalent to the stress intensity factor K under purely elastic conditions by comparison of Eqn 1.12 and 1.16, hence for a semi infinite crack in an infinite plate K_I is related to G by Eqn 1.19

$$G = \frac{K_I^{\,2}}{E'} \tag{1.19}$$

1.4.6 Plastic zones ahead of fatigue cracks

Fatigue crack propagation is always at least a locally plastic process, and therefore there exists a region of material ahead of the crack tip which undergoes irreversible deformation during fatigue crack growth. Several authors have investigated the plastic zone produced at a crack tip under monotonic loading. However fatigue occurs under cyclic loading, and hence the presence of a zone of reversed plastic flow is also considered.

1.4.6.1 Monotonic plastic zone size. Various estimates exist of the size of the monotonically loaded "plastic zone". Irwin[18] proposed a zone in which the von Mises equivalent stress calculated from the crack tip stress fields given by Eqn 1.15, exceeds the yield stress σ_y. He found that the extent of this zone $r_{p,0}$ ahead of the crack tip (θ=0) was proportional to the square of the stress intensity factor K. Therefore, by this method, the plastic zone sizes ahead of a crack under monotonic mode I loading in plane stress and strain are given by Eqn 1.20.

$$r_{p,0} = \frac{1}{3\pi}\left(\frac{K_I}{\sigma_y}\right)^2, \qquad \text{for plane strain}$$

$$r_{p,0} = \frac{1}{\pi}\left(\frac{K_I}{\sigma_y}\right)^2, \qquad \text{for plane stress} \tag{1.20}$$

Another model for plastic zone size was proposed by Dugdale[19], who considered a mode I crack in a thin elastic-perfectly plastic plate subject to plane stress loading. In the Dugdale model, the plastic zone is thought of as a narrow strip of near zero height extending to a distance r_p ahead of the crack tip, which is loaded by the traction $\sigma_{yy}=\sigma_y$ over the length r_p. Using superposition it was shown that in plane stress, $r_{p,0}$ was given by Eqn 1.21

$$\frac{r_{p,0}}{a} = \sec\left(\frac{\pi\sigma^{\infty}}{2\sigma_y}\right) - 1$$

(1.21)

Where σ^{∞} is the far field tensile stress. By imposing the conditions such that $\sigma^{\infty} << \sigma_y$ and $r_p << a$, this gives the plastic zone size as Eqn 1.22,

$$r_{p,0} = \frac{\pi}{8}\left(\frac{K_I}{\sigma_y}\right)^2$$

(1.22)

In addition to the classical analytical models, several authors including Levy[20] have used finite element modelling to provide estimates of the maximum plastic zone radius, $r_{p,max}$, and the radius directly ahead of the crack tip, $r_{p,o}$ in plain strain conditions, these are given in Eqns 1.23 and 1.24 respectively.

$$r_{p,\max} = 0.471\left(\frac{K}{\sigma_y}\right)^2$$

(1.23)

$$r_{p,o} = 0.108\left(\frac{K}{\sigma_y}\right)^2$$

(1.24)

1.4.6.2 Cyclic plastic zone size. It was proposed by Paris[21] and Rice[22] that during cyclic loading, in addition to the monotonic plastic zone, there exists a zone of reversed plastic flow ahead of the crack tip at the end of the unloading step. The size of this region was estimated by Rice[22], who considered a cracked plate of elastic-perfectly plastic material, subjected to a far field load P as shown in Figure 1.9. The monotonic loading creates a plastic zone of size r_p ahead of the crack tip. If the load P is then reduced by an amount ΔP (as in cyclic loading), reversed plastic flow is instigated. If the crack tip is assumed to be sharp then the infinite crack tip stress concentration leads to the formation of a zone of reversed plastic flow embedded within the monotonic plastic zone. It was proposed that the size of this cyclic plastic zone r_c can be estimated by replacing K_I with ΔK_I and σ_y with $-2\sigma_y$ in Eqn 1.20, to account for the reversed plastic flow in the previously yielded material and then the

yielding in compression, thus an estimate for the cyclic plastic zone size r_c is given by Eqn 1.25.

$$r_{c,0} \approx \frac{1}{\pi}\left(\frac{\Delta K_I}{2\sigma_y}\right)^2 \tag{1.25}$$

1.4.7 Elasto-plastic fracture mechanics and the J-integral

The stress intensity factor K provides a unique characterisation of crack tip stress fields under small scale yielding conditions. The corresponding parameter for characterising monotonic fracture in a material having a non-linear stress/strain response (i.e. an elasto-plastic material) is the J-integral as proposed by Rice[23].

The J-integral is defined by considering a cracked body subjected to a monotonic load P, as shown in Figure 1.10. Assuming that the crack faces are traction free and the tractions T_r surrounding the crack tip are independent of crack size, then the line integral J along any contour Γ which encircles the crack tip is given by Eqn 1.26.

$$J = \int_{\Gamma}\left(wdy - T_r\frac{\partial u}{\partial x}ds\right) \tag{1.26}$$

where $\boldsymbol{u}$ is the displacement vector, y is the distance along the direction normal to the plane of the crack, s is the arc length along the contour, $\boldsymbol{T_r}$ is the traction vector and w is the strain energy density of the material. It is found that the value of J is independent of the contour Γ used to compute the integral. Under small scale yielding conditions in plane strain, it can be shown that J is related to K by Eqn 1.27.

$$J = \left(\frac{1-\nu^2}{E}\right)K_I^2 \tag{1.27}$$

Since the J-integral is based on non-linear elastic assumptions, the major restriction on its use to describe elasto-plastic materials is that no unloading should occur. Then the irreversible plastic deformation evident on unloading cannot be accounted for and the integral becomes invalid.

Similar to the stress intensity factor, J has a region of validity or dominance. This is described by the Hutchinson-Rice-Rosengren (HRR) stress and deformation

fields. Given a material whose response is governed by the Ramberg Osgood relationship, since near the crack tip the elastic terms are negligible compared to the power law terms, the material response may be approximated by Eqn 1.28.

$$\frac{\varepsilon}{\varepsilon_y} \approx \alpha \left(\frac{\sigma}{\sigma_y} \right)^n \tag{1.28}$$

where ε_y is the yield strain, n is the strain hardening exponent and α is a material dependent parameter. It was shown by Hutchinson[24] and Rice-Rosengren[25] that, for non linear elastic materials undergoing small strain deformation, the strength of the near tip fields is the J integral and the stress, strain and displacements exhibit $r^{-1/(n+1)}$, $r^{-n/(n+1)}$ and $r^{1/(n+1)}$ singularities respectively. The HRR singular fields for stress, strain and displacement are given in Eqn 1.29.

$$\sigma_{ij} = \sigma_y \left(\frac{J}{\alpha \sigma_y \varepsilon_y I_n r} \right)^{\frac{1}{(n+1)}} \tilde{\sigma}_{ij}(\theta, n)$$

$$\varepsilon_{ij} = \alpha \varepsilon_y \left(\frac{J}{\alpha \sigma_y \varepsilon_y I_n r} \right)^{\frac{n}{(n+1)}} \tilde{\varepsilon}_{ij}(\theta, n)$$

$$u_i = \alpha \varepsilon_y \left(\frac{J}{\alpha \sigma_y \varepsilon_y I_n} \right)^{\frac{n}{(n+1)}} r^{\frac{1}{(n+1)}} \tilde{u}_i(\theta, n) \tag{1.29}$$

where I_n is a factor mildly dependent on the strain hardening exponent, n. In order for the J-integral to uniquely characterise the singular near tip fields in non-linear fracture, the deformation theory of plasticity employed must be an adequate model of the small strain behaviour of the real elastic-plastic material under monotonic loading. Also the region in which finite strain effects dominate and the region where the microscopic failure processes occur must be well within the region described by the singular HRR fields.

1.4.8 Equivalence of *J* and *G*. In a similar manner to the equivalence between G and K, it may shown that J is also related to the strain energy release rate. Rice showed that J is the rate of change of potential energy (with respect to crack advance) in a

material of non linear elastic properties by combining Eqns 1.12 and 1.27 to give Eqn 1.30.

$$J = G = -\frac{\partial W_p}{\partial a} \tag{1.30}$$

where W_p is potential energy and a is crack length.

1.5 Fatigue Crack Closure

Typically fracture mechanics approaches characterise fatigue crack growth rates with reference to the conditions ahead of the crack tip. However Elber[26,27] showed that crack growth rates were also dependent on conditions behind the crack tip, i.e. as a function of the loading history, due to the build up of residual plasticity behind the crack tip, as shown in Figure 1.11. It was shown that this so called plastic wake could severely retard the growth of fatigue cracks, by causing their flanks to come into contact prematurely. Elber[26] hypothesised that in order to propagate, a fatigue crack must be able to open and close under the applied cyclic loading. "Closure" is the term he gave to describe the condition when something prevents the crack from fully closing at minimum load. He proposed that the degree of closure can be described by the parameters K_{cl}, and K_{op}. These define the crack tip stress intensity factors, when the crack faces first touch during unloading and when the crack becomes fully open during loading respectively. Elber argued that fatigue cracks can only propagate during the portion of the loading cycle when the crack faces are separated, hence with closure present, the crack grows under an effective stress range $\Delta\sigma_{eff}$ and the corresponding stress intensity factor range ΔK_{eff}. Expressions for $\Delta\sigma_{eff}$ and ΔK_{eff} are given in Eqns 1.31 and 1.32 respectively.

$$\Delta\sigma_{eff} = \sigma_{\max} - \sigma_{op} \text{ if } \sigma_{op} > \sigma_{\min} \tag{1.31}$$

$$\Delta K_{eff} = K_{\max} - K_{op} \text{ if } K_{op} > K_{\min} \tag{1.32}$$

Hence at higher R-ratios, where K_{min} is greater than K_{op}, closure-free behaviour will be observed. Thus based on LEFM, stage II crack growth rate may be described by Eqn 1.33.

$$\frac{da}{dN} = C\left(\Delta K_{eff}\right)^m \tag{1.33}$$

Several analytical models justifying the use of ΔK_{eff} to characterise fatigue crack growth rates have been developed, including that by Budiansky and Hutchinson[28].

1.5.1 Additional causes of closure

In addition to the plasticity induced closure described by Elber, several other causes of closure have been documented through the research of Ritchie *et al*[29], Suresh *et al*[30] and Suresh & Ritchie[31,32]. Other mechanisms by which a fatigue crack may become prematurely closed are shown in Figure 1.12, and include;

- Oxide induced closure, where the crack flanks become prematurely closed due to the formation of an oxide layer on the newly exposed material. (Paris *et al*[33], Ritchie *et al*[29]),
- Roughness induced closure, in which asperities in the crack path cause the crack to become prematurely closed (Nowack *et al*[34], Halliday and Beevers[35])
- Viscous fluid induced, where crack is prevented from closing by the penetration of a fluid (typically oil) into the crack (Endo *et al*[66], Ryder *et al*[36])
- Phase transformation induced closure, in which closure is brought about by material phase transformation at the crack tip, e.g. strain-induced martensitic transformation in metastable austenitic steels (Pineau and Pelloux[37], Horbogen[38])

Both oxide and viscous fluid induced closure mechanisms are important when considering bearing fatigue, hence these concepts are presented in more detail in Sections 1.7.2 and 1.7.3, respectively.

1.5.2 Variable amplitude loading

One of the consequences of the work on closure was a method of explaining material responses to variable amplitude loading. Considering a propagating fatigue crack, Corlby and Pickman[39] report that a tensile overload will typically cause a small period of accelerated growth, followed by a prolonged period of retarded crack

growth rate. These effects were explained by Elber[27] and Riemelmoser and Pippan[40] using arguments based on plasticity induced crack closure. It was proposed that the initial acceleration in growth following the overload may be attributed to increased crack flank spacing (crack blunting) due to the large plastic deformation at the crack tip. Then as the crack advances through this stretched zone of material, it forms a wedge of plastic material in the crack wake. It is this wedge of plastically deformed material which causes the crack to become prematurely closed upon unloading and hence the reduced crack growth rate observed. It should be noted that this hypothesis is strongly disputed by Vasudevan *et al*[41], who in fact dispute the existence of plasticity induced closure entirely.

A similar argument may be applied to explain underload effects, which are observed when the load level is increased following a period of cyclic loading at a reduced level. These effects are characterised by a transient period of accelerated crack growth, which then decays to a constant value. This behaviour may be explained by a hypothesis based on plasticity induced crack closure, since at the point of ΔK increase, K_{max} rises immediately, but K_{cl} remains unchanged. Therefore ΔK_{eff} is also abruptly increased, giving an enhanced crack growth rate. This effect is however transitory, since plastic crack wake is built up at the new ΔK level, thereby increasing K_{cl} until a new equilibrium is reached giving a stable crack growth rate.

1.6 Short Cracks

In lifing calculations the growth of fatigue cracks is typically characterised using fracture mechanics in terms of da/dN and ΔK. Generally such fracture mechanics data will have been collected using specimens containing long cracks, typically tens of millimetres in length. It has been shown by several researchers, that the behaviour of small flaws is considerably different from such long cracks, and hence the use of such data may lead to dangerous overestimations of fatigue life in some applications. Suresh & Ritchie[42] proposed several definitions of what constitute a short crack.

• Microstructurally short – cracks whose length is comparable to grain size in monolithic materials, or interparticle size in composites.

• Mechanically short – cracks in smooth specimens whose length is comparable with their own near tip plasticity, or those engulfed by the plastic strain field of a notch.
• Physically short – cracks whose length is significantly larger than the characteristic microstructural dimension and local plasticity, but whose length is merely a millimetre or two and where closure may not have fully developed.
• Chemically short – cracks that normally behave as predicted by LEFM, but below a certain crack length, exhibit anomalies in growth rate caused by dependence on local crack tip environmental stress corrosion fatigue effects, which vary with crack length.

It was noted by Pearson[43] that the fatigue behaviour of "small cracks" is markedly different from that of the so called long cracks. He found that short cracks in a precipitation hardened aluminium alloy grew up to 100 times faster than long flaws at the same nominal ΔK. The increased growth rate of short cracks has been noted by many authors as has its unstable nature characterised by rapid acceleration and retardation and indeed periods of crack arrest. It was shown by Morris[44] that these effects were often microstructurally dependent when he noted that periods of growth rate retardation occurred whenever the crack tip approached a grain boundary. Figure 1.13 shows typical short crack behaviour plotted with typical long crack behaviour for the same material. The scatter band is caused by the constant changes in short crack growth rate, but this band eventually converges onto the long crack data. It can also be seen that short flaws may propagate at nominal ΔK levels lower than the long crack threshold.

1.6.1 Characterising the growth rate of short cracks.

In Section 1.4.2 it was mentioned that K will not be valid for "small cracks", since the assumption that the crack dimensions are large compared to its plastic zone size is false. Hence attempting to characterise the fatigue growth of "small cracks" using linear elastic fracture mechanics can lead to large errors in growth rate. However many studies in the literature continue to use stress intensity factor as a means to compare long and short crack growth behaviour. Therefore various methods for calculating short crack ΔK levels have been proposed, the most common being those of Scott & Thorpe[45] and Newmann & Raju[46].

To overcome the limitations of LEFM, Dowling[47] suggested that the cyclic J integral, J^C, could be used to characterise the driving force for elasto-plastic small

flaws. He proposed Eqn 1.34 to characterise the growth of a small half penny shaped flaw growing in an initially smooth low cycle fatigue specimen.

$$J^C \approx 3.2(\Delta w_e)a + 5.0(\Delta w_p)a = \frac{1.6(\Delta\sigma)^2 a}{E} + \frac{5.0(\Delta\sigma)(\Delta\varepsilon_p)a}{\left(\frac{n+1}{n}\right)} \tag{1.34}$$

where Δw_e and Δw_p are the elastic and plastic components of the nominal strain energy density range, a, is the depth of the surface flaw (of length $2a$) and n is the strain hardening exponent. The Dowling method provides an improvement over other characterisation methods and gives good correlation with experimental data, however the use of J^C remains questionable since fatigue is by definition a plastic process and therefore involves irreversible deformation which appears to violate the fundamental basis of the J-integral.

1.7 Effect of Environment

Several authors report that environmental conditions have a strong influence on fatigue crack initiation and growth behaviour. It is generally agreed that fatigue crack growth rates in aluminium alloys may be as much as an order of magnitude lower under vacuum conditions than in moist air due to suppression of oxide build up, and hence more reversible slip at the crack tip. However the fatigue behaviour of materials in oil environments has been the subject of greater debate, since many factors are important. Endo *et al*[66] found lower crack growth rates in bearing materials (white metal lining – steel backing) when tested in an oil environment. it was hypothesised that oil penetration reduced crack growth rate by a closure mechanism. In their model, Endo *et al* assumed complete oil penetration of the crack irrespective of crack size and loading conditions, thus implying that the internal oil pressure and hence the level of closure produced in a closing fatigue crack is directly proportional to oil viscosity. Tzou *et al*[67] proposed that the extent of oil penetration into a fatigue crack could be found by considering capillary flow. They tested 2.25Cr-1Mo steel samples in both paraffin and silicone oil environments, using silicone oils of viscosity 5, 1000, 15000 and 60000 mm^2/s, and paraffin oils of viscosity of 25 and 75 mm^2/s. They found that generally growth in oil was slower than in air; however this was not

the case at near-threshold conditions (~10^{-6}mm/cycle), where growth rate was slightly higher. Tzou *et al* also found that at low load ratios and growth rates above ~10^{-6}mm/cycle growth in high viscosity oils is faster than in low viscosity oils.

Tzou *et al*[67] proposed that the growth rate of fatigue cracks in an oil environment is dependent on two competing factors, corrosion fatigue mechanisms such as hydrogen embrittlement and active path corrosion, which increase crack growth rate, as well as closure mechanisms, which will slow fatigue crack growth. It appears that the corrosion mechanisms dominate at higher load ratios and high growth rates, whereas the effect of closure mechanisms becomes increasingly important at near threshold conditions.

1.7.1 Hydrogen embrittlement.

This effect most often caused by water vapour is generally thought to cause environmentally enhanced crack growth rates. It is known that aluminium alloys are susceptible to hydrogen embrittlement, particularly those containing Cu, Mg, Si, Zn or Li[48], which includes AS1241. Hydrogen embrittlement is thought to consist of two phases[49], a series of transport steps to cause atomic hydrogen to be absorbed into the material surrounding the crack tip, and a second stage where this absorbed hydrogen acts to embrittle the material. The rate dependency of the absorption phase is thought to account for hydrogen embrittlement being found to have a greater effect at low fatigue crack growth rates (time dependent i.e. near threshold or low frequency[50]). The embrittlement mechanism is highly dependent on alloy composition, and is thought to generally consist of hydrogen diffusing along and causing the segregation of grain boundaries, and hence the promotion of intergranular fracture[51].

Since water at the crack tip is known to be one of the primary causes of growth rate enhancement by hydrogen embrittlement, it would be expected that this effect would be minimised *in vacuo*. However in the absence of any attempts to dehumidify an oil environment, the possibility of hydrogen embrittlement mechanisms must be considered.

1.7.2 Oxide induced closure.

Reduced fatigue crack growth rates observed in aluminium alloys tested *in vacuo*. have been linked to the reduction in striation formation observed in such samples. Noting that the inert atmosphere should prevent oxide formation,

Pelloux[52,53] hypothesised that the slip process by which striations form may be reversible in the absence of such an oxide layer. Reversed slip leads to lower damage accumulation, and hence a reduced fatigue crack growth rate. A second hypothesis was suggested by Neumann[54], who proposed that enhanced rubbing of the crack flanks, in the absence of a protective oxide film, may cause both striations to be obliterated by increased fretting and reduced crack growth rate *in vacuo*.

Evidence that oil provides an inert crack tip environment in steel samples was provided by Vasudevan *et al*[55] who reported that corrosion debris are 20-40 times thicker in fatigue cracks grown in moist air than those grown in oil environments. Therefore closure via oxide induced mechanisms should be severely reduced by the oil environment. Suresh *et al*[56] showed that in a moist air environment, oxide induced closure is usually most pronounced at near-threshold conditions, since the oxide layer thickness becomes comparable to the crack tip opening displacement.

The relative effect of oxide induced crack closure was examined by Suresh *et al*[56] using a simple model of a rigid wedge within a linear elastic crack. The closure stress intensity factor, K_{cl}, was estimated in terms of the maximum oxide wedge thickness, o, located at distance, $2l$, behind the crack tip, and is given by Eqn 1.35.

$$K_{cl} \approx \frac{oE'}{4\sqrt{\pi l}} \tag{1.35}$$

Eqn 1.35 under plane strain conditions was applied to a steel sample containing a single crack, where it was estimated that in ambient conditions $K_{cl} \approx 4.5$ MPa$\sqrt{m}$, whereas in an oil environment $K_{cl} \approx 0.1$ MPa$\sqrt{m}$. Suresh *et al* performed their tests at a nominal ΔK of 8 MPa$\sqrt{m}$ with a load ratio of 0.1, thus in air ~56% of the applied stress intensity range is lost to closure, compared to only ~1% in oil. This clearly demonstrates that, in an inert oil environment, fatigue crack driving force appears to be far less restricted by oxide induced closure mechanisms. However, at high load ratios the effect of differing environments on fatigue crack growth rate is minimal since $K_{min} > K_{cl}$. Fatigue tests carried out at a load ratio of 0.75 showed negligible difference between oil and air environments. Hence whilst an oil environment will reduce oxide formation and hence inhibit oxide induced closure mechanisms, it was shown that an increase in crack growth rate compared to ambient conditions will only be seen at low load ratios.

Hence the formation of an oxide layer may cause enhanced crack growth rates by promoting irreversible slip at the crack tip. However if the oxide layer becomes thicker (and testing is carried out at low load ratios) an oxide induced closure mechanism may become active causing reduced crack growth rate.

1.7.3 Viscous fluid induced closure.

If oil penetrates into a fatigue crack, considerable internal oil pressure will be generated during the unloading phase. Tzou *et al*[67] showed that this pressure will act as a closure mechanism the magnitude of which is dependent on oil viscosity. The kinetics of oil penetration into a fatigue crack was assessed by Tzou *et al* using capillary flow equations, rather than just assuming full penetration, as in Endo's[66] model of viscous fluid closure. Eqn 1.36, Newman's[57] equation for capillary flow, gives the depth of oil penetration , d, into a crack of length, a, after time, t, as,

$$d^2(t) = \left(\frac{\gamma \cos\beta}{3\eta\rho}\right)\int_0^t \langle h\rangle dt \qquad (1.36)$$

where, $\langle h\rangle$ is the average crack opening displacement,

γ = surface tension of the oil,

β = wetting angle between fluid and crack flank,

η = kinematic viscosity,

ρ = density.

The resulting hydrodynamic pressure distribution $p(x)$, where x is defined as the distance into the crack, was then estimated from the analysis of Endo *et al* for the fully penetrated crack (d/a=1); Eqn 1.37, or from Fuller's[58] analysis of fluids between parallel plates for the partially penetrated crack (d/a<1); Eqn 1.38.

$$p(x) \approx 6\eta\rho\left(\frac{1}{h^3}\frac{dh}{dt}\right)a^2 \log\left(1-\frac{x}{a}\right), \quad d/a = 1,\ x/a \le 1 \qquad (1.37)$$

or

$$p(x) \approx 6\eta\rho\left(\frac{1}{\langle h\rangle^3}\frac{d\langle h\rangle}{dt}\right)x(d-x), \quad d/a < 1, \quad x/d \le 1 \qquad (1.38)$$

where h is the crack mouth opening displacement, and $\frac{d\langle h \rangle}{dt}$ is the closing velocity of the crack flanks. Superposition was then used to find the maximum resultant stress intensity factor K^*_{max} caused by this oil pressure. The effective stress intensity range, including viscous fluid induced closure is given by Eqn 1.39.

$$\Delta K_{eff} = K_{max} - \left(K_{min} + K^*_{max}\right) \tag{1.39}$$

Tzou *et al* showed by this analysis that closure by this mechanism will increase with viscosity, until at very high viscosity, K^*_{max} will be limited by the oil's inability to penetrate into the crack. Generally it was found that oils with kinematic viscosity lower than 12500 mm^2/s, penetrated fatigue cracks.

Such observations should be equally true of aluminium alloy bearing lining material as the steel samples tested by Tzou *et al*, since they are not dependent on material chemistry, but merely on oil viscosity.

1.8 Classical Bearing Fatigue Literature

Plain bearings have been the subject of semi-empirical research for many years. In that time many aspects of their design have been investigated, and the influence of these on overall fatigue performance assessed, including;

- Relative bearing lining thickness and properties.
- Housing compliance.
- The effect of oil cooling holes or grooves.
- Bearing clearance and hence fluid film thickness.
- Overall bearing and journal shape.
- Oil film behaviour and the effects of oil temperature and pressure.

Many authors have investigated the relationship between relative lining thickness and overall bearing fatigue resistance. Love *et al*[59] suggested that since backing materials have a higher elastic modulus, the lining should be made thinner in order to transfer more load to the backing. As shown in Figure 1.14, they theorised that if the lining and backing thicknesses were in proportion to their elastic moduli, the bearing's overall fatigue resistance would be increased. From these hypotheses it

would be expected that optimum component fatigue life would be realised with as great a ratio of elastic moduli as possible. This effect was investigated experimentally by Duckworth & Walter[60], but no relation was found between elastic modulus ratio and increased resistance to fatigue as lining thickness was reduced. Their observations suggested that a reduction in lining thickness was causing apparently increased cyclic yield stress, and that it was this effect giving the rise in fatigue resistance.

It was observed by Blount[61] that the fatigue life of a bearing is influenced directly by the compliance of its housing. He found bearings tested in rigid housings had much higher fatigue resistance, than those tested in compliant housings. This was attributed to the housing and the shell flexing, and thus applying bending stresses to the bearing in addition to the compressive stresses from the journal. Blount[61] also showed that if the bearing shell thickness was increased without significantly increasing its rigidity, then its fatigue resistance is reduced, possibly because the thicker bearing is harder to fit tightly within its housing. He therefore concluded that optimum fatigue resistance could be achieved with a very thin and compliant bearing mounted within as rigid a housing as possible.

Despite apparently increasing lubrication and cooling, the addition of a circumferential oil groove, as shown in Figure 1.15, has been found to consistently reduce fatigue resistance. Blount[61] linked this to the reduction in bearing land area causing narrower oil films and, hence, higher oil pressures. It was also found that bearings with an oil groove tend to run hotter than their un-grooved counterparts. Chen[62] found that, although the higher oil flow rate seen in grooved bearings should increase cooling, the consequent reduction in oil film thickness and increase in heat generation more than offset the benefit from increased oil flow.

The effect of bearing clearance and hence oil film thickness on fatigue strength was investigated by several authors including Blount[61] and Gyde[63]. Both concluded that increasing the clearance between journal and bearing leads to a lower resistance to fatigue. This can be explained by the consequent increase in journal orbit eccentricity giving a more "peaky" pressure distribution within the oil film. Gyde[63] also suggested that in bearings with higher clearances, the oil film becomes more disrupted, hence increasing the bearing temperature. It should be noted however that Blount[61] found no evidence of elevated temperatures.

The effect on bearing fatigue life of varying the journal shape from a simple cylinder to something more exotic has been investigated as shown in Figure 1.16.

Sasaki *et al*[64] examined the fatigue resistance of barrel and other shaped bearings in their study, before concluding that plain cylindrical journals gave optimum bearing fatigue performance.

It has been shown that the wetting of bearing alloys during testing has a strong influence on fatigue resistance. Peeken[65] found that samples tested in air had a much higher resistance to fatigue than those tested in oil, a contrary result compared with the work of Endo *et al*[66] and Tzou *et al*[67] [68]. On closer examination it is seen that Peeken performed his air tests at 26 °C and his tests in oil at 80 °C, it seems therefore likely that this temperature discrepancy will make the direct comparison of his results invalid.

In a separate series of experiments reported by Peeken[65], samples were tested in air and in oil at varying pressure. This time lower fatigue resistance was reported for samples tested in air. This can be explained by a combination of enhanced crack tip corrosion in moist air and by lack of viscous fluid closure mechanisms[67]. An interesting point from these results is that in tests in oil, fatigue resistance was seen to rise with increasing oil pressure. Peeken gives no explanation for this, although this observation does contradict M^{c}Callion & Lotfi[69]. Who postulated that at high oil pressures and at some critical flaw size, oil will penetrate the crack, exert a wedging force and give increased crack growth rate, in a similar argument to that of Way[70].

Gyde[63] observed that in well aligned bearings, fatigue failure only occurred in the central part of the bearing land, leaving edge areas intact, as shown in Figure 1.17. He linked this to earlier work by researchers at the Glacier Metal Company, who showed that the fluid film within a bearing breaks down under cyclic loading. Gyde noted that the areas near the edge of the bearing did not contain an oil film, hence leaving the central portion to support the entire load. It is generally agreed that the remaining oil film breaks down into a number of discontinuous islands, and that these islands set up tensile stresses in the surface of the lining along their peripheries. Clearly these oil islands must constantly change shape during the loading cycle, and consequently the points of maximum tensile stress are constantly moving. Hence a network of complex cyclic stresses is set up leading to the onset of fatigue in the lining material. As the points of maximum tensile stress are constantly moving, several cracks usually initiate rather than just one. Thus in a typical failure through fatigue as observed by Shenton[71], cracks initiate at multiple points on the surface of the bearing. A typical example of the sub-surface fatigue crack behaviour is shown in

Figure 1.18, in which it can be seen that the crack has propagated downwards to the interlayer, where it has bifurcated and continued to grow along the interlayer. It is thought that several such cracks will coalesce and cause a piece of lining material to detach (spalling); this in turn will cause the bearing to seize.

A two-stage crack growth argument was proposed by M^{c}Callion & Lotfi[69]. They postulated that initially the crack grows in a manner governed by the Paris law. Then at some critical crack size, high pressure oil from the fluid film is able to penetrate the crack, greatly increasing crack growth rate towards final failure. This hypothesis seems unlikely for several reasons. Firstly, it seems improbable that the growth rate of such a small crack (less than 1 mm) could be governed by the Paris law. Secondly, once oil does penetrate the crack, whilst it may exert a wedging effect and increase peak opening stress, it is likely also to cause closure and hence reduce crack growth rate.

1.8.1 Industrial fatigue testing of bearings.

Since no failures through fatigue are seen in normal service in small automotive bearings of this type, almost all of the studies in the literature relate to failed bearings produced via artificial accelerated test techniques. There are several different rigs all of which aim to simulate the loading regime within an engine, and allow this loading to be made severe enough to cause failure through fatigue within a reasonable time. The most common and now widely accepted of these is the Sapphire or BICERA rig described by Wilson[72], and shown in schematic form in Figure 1.19.

In this type of machine the test bearing is mounted between the piston con-rod and an eccentric portion of the main shaft. As this shaft rotates in its slave bearings, it causes the piston to reciprocate within its oil filled cylinder. A hydraulic control unit allows the loading applied via this cylinder to be precisely controlled. The operating temperature of the tested bearing can be controlled via its lubricating oil.

This type of rig is used by Dana Glacier Vandervell for their bearing testing. A typical test would be conducted at an oil temperature of either 80 °C or 140 °C and at a nominal load, the rig would be run for 20 hrs after which time, if no failure had occurred, the load would be increased by increasing the maximum pressure applied to the hydraulic ram by 7MPa, and the machine restarted. This procedure of incremental load increase is continued until a marked rise in coolant temperature indicates bearing failure.

Other types of testing rig exist, although their use has been curtailed since the introduction of the more advanced servohydraulic Sapphire rig. Generally earlier rigs were centripetal machines using rotating offset masses to induce cyclic stresses in their bearings, the most common of these early devices were the Underwood and Soda rigs. Descriptions of these machines and their use may be found in Cuthbertson[73] and Fukuoka *et al*[74].

1.8.2 Modelling of bearings.

The first modelling attempts were made by Lang[75,76] and Harbordt[77], who studied the relationship between journal loading and fatigue resistance; they calculated that surface tensile stresses were likely to occur near the cavitation breakdown boundary of the oil film. They further claimed that fatigue cracks would occur in the region of maximum cyclic circumferential tensile stress. These findings were supported by the observations of many experimenters including Blount[61], who had found that primary fatigue cracks propagate axially (i.e. are caused by tangential stresses), and occur in the area subject to the maximum pressure gradient. It was later shown by Lang[78] that the highest tensile tangential stress is likely to occur where a steep pressure gradient drops to virtually zero.

M^{c}Callion & Lotfi[69], Peeken[65] and Martin *et al*[79] used finite element models to try and relate the bearing stress distribution to the location of fatigue cracking. M^{c}Callion & Lotfi compared the positions of the maximum circumferential tensile stresses to the locations of the fatigue cracks observed by Gyde[63] and Blundell[80,81]. They found an excellent correlation, and hence concluded that surface tensile stresses must be responsible for the fatigue failure of journal bearings.

The results discussed so far were based on the findings of very simple 2D elastic models. The results from such models are inherently inaccurate as under real service conditions the bearing lining layer yields at a very early stage as shown by Shenton[71]. Also the load is applied to the bearing in such a non-uniform way in both the axial and the circumferential directions that a 2D model cannot be representative of actual bearing behaviour. In many previous models, the bearing housing has been treated as rigid. This is probably not a wise assumption since Blount[61] showed that housing compliance has a marked influence on fatigue life, and as Fenner[82] showed, on oil pressure distribution. A far more complex model using an axisymmetric 3D geometry was proposed by Bahai and Xu[83]. This used the elasto-hydrodynamic

pressure distribution calculated by Conway-Jones[84] from the earlier work of McIvor & Fenner[85] to simulate loading from the journal. Bahai and Xu's[83] model was the first to simulate the 3D plastic straining of the aluminium bearing layer, and hence is probably the most accurate representation of bearing stress distribution in service to date. It should be noted that this model is currently being refined and extended by Xu[86].

1.9 Summary

Much of the work concerning the fatigue failure of plain bearings was conducted in the 1960's and 1970's and is based on a total life approach, which whilst valid leads to a semi empirical understanding of the fatigue behaviour of these components. In order to further investigate the problem it is necessary to consider more advanced approaches. The fatigue failure of bearings is a very complex problem and this project cannot hope to fully resolve it. However it should be possible to better quantify fatigue crack initiation and early growth by applying many of the new advanced techniques and understanding of fatigue mechanisms. This literature review notes the characterisation of both crack tip fields and fatigue crack growth by fracture mechanics, as well as, the effects of crack deflection, closure and service environment, all of which may be applied to further the understanding of the fatigue performance of these material systems.

1.10 References

[1] P.J.E.Forsyth, A two stage process of fatigue crack growth, In crack propagation: proc. Cranfield symposium pp76-94 (1962)

[2] C.A.Zappfe & C.O.Worden, Fractographic registrations of fatigue, Trans ASM 43 pp958-69 (1951)

[3] C.Laird and G.C.Smith, Crack propagation in high stress fatigue, Philosophical magazine 8 pp 847-57 (1962)

[4] P.J.E.Forsyth and D.A. Ryder, Fatigue fracture, Aircraft Engng 32 pp96-9 (1960)

[5] R.O.Ritchie, Near-threshold fatigue crack growth in steels, Int Metals Rev. 20 pp205-30 (1979)

[6] A. Wöhler, Versuche uber die festigkeit der eisenbahnwagenachsen. Zeitschrift fur bauwesen V10 (1860); English summary, Engng V4 pp160-1 (1867)

[7] O.H. Basquin, The exponential law of endurance tests, Proc ASTM V10 pp625-30 (1910)

[8] H. Gerber, Bestimmung der zulassigen spannungen in eisen-konstructionen, Zeitschrift des bayerischen architeteckten und ingenieur-vereins, V6 pp 101-10 (1874)

[9] J. Goodman, Mechanics applied to engineering. London: Longmans Green (1899)

[10] C.R. Soderberg, Factor of safety and working stress. Trans ASME V52 pp13-28 (1939)

[11] L.F. Coffin, A study of the effect of cyclic thermal stresses on a ductile metal, Trans. ASME V76 pp15-22 (1954)

[12] S.S. Manson, Behaviour of materials under conditions of theramml stress, National advisory commission on aeronautics: report 1170 (1954)

[13] A.A.Griffth, The phenomenon of rupture and flow in solids, Trans Roy Soc A221 pp 163-97 (1921)

[14] G.R. Irwin, Onset of fatst crack propagationin high strength steel and aluminium alloys. In proc. of the second sagamore conf. vII pp289-305 (1956)

[15] G.R.Irwin, Analysis of stresses and strain at the end of a crack traversing a plate, J. App Mech 24 pp 361-4 (1957)

[16] ASTM. Designation: E647 – 95a. Standard test method for measurement of fatigue crack growth rates.

[17] P.C.Paris, M.P.Gomez and W.P.Anderson, A rational analytic theory of fatigue. The trend in engineering 13 pp-9-14 (1961)

[18] G.R.Irwin, Plastic zone near a crack and fracture toughness, Proc 7th Sagamore ordnance materials conf. 4 pp63-78 (1960)

[19] D.S.Dugdale, Yielding of steel sheet containing slits, J Mech and Phys Solids 8 pp100-8 (1960)

[20] N.Levy, P.V.Marcal, W.O.Ostergren and J.R.Rice, Small scale yielding near a crack in plane strain: A finite element analysis, Int J of Fract V7 pp 143-156 (1971)

[21] P.C.Paris, The growth of cracks due to variations in load, Ph.D. thesis Bethlehem: Lehigh Univ (1960)

[22] J.R.Rice, Mechanics of crack tip deformation and extension by fatigue, In Fatigue crack propagation Special Tech Pub 415 pp247-309 (1967)

[23] J.R.Rice, A path independent integral and the approximate analysis of strain concentration by notches and cracks, Trans ASME J of Applied mechanics V pp379-386 (1968)

[24] J.W.Hutchinson, Singular behaviour at the end of a tensile crack in a hardening material, J mech phys solids 16 pp 13-31 (1968)

[25] J.R.Rice and G.F.Rosengren, Plane strain deformation near a crack tip in a power law hardening material, J mech phys solids 16 1pp1-12 (1968)

[26] W.Elber, Fatigue crack closure under cyclic tension, Eng Fract Mech V2 pp37-45 (1970)

[27] W.Elber, The significance of fatigue crack closure, In damage tolerant aircraft structure, special technical publication 486 pp230-42 (1971)

[28] B. Budiansky and J.W. Hutchinson, Analysis of closure in fatigue crack growth, J. App. Mech. V45 pp267-76 (1978)

[29] R.O.Ritchie, S.Suresh and C.M.Moss, Near threshold fatigue crack growth in 2¼Cr-1Mo pressure vessel steel in air and hydrogen, J Eng Mats & Tech 102 pp937-40 (1980)

[30] S.Suresh, G.F.Zaminski and R.O.Ritchie, Oxide induced crack closure: an explanation for near threshold fatigue crack growth behaviour, Met Trans 12A pp 1435-43 (1981)

[31] S. Suresh and R.O.Ritchie, A geometric model for fatigue crack closure induced by fracture surface morphology, Met Trans 13A pp 1627-31 (1982)

[32] S.Suresh and R.O.Ritchie, Near threshold fatigue crack propagation : a perspective on the role of crack closure. In fatigue crack growth threshold concepts pp 227-261 (1984)

[33] P.C.Paris, R.J. Bucci, E.T. Wessel, W.G. Clark and T.R. Mager, Extensive study of low fatigue crack growth rates in A533 and A508 steels, In stress analysis and growth of cracks, Spec. Tech. Publ. 513 pp 141-76. Philadelphia: ASTM. (1972)

[34] H. Nowack, K.H. Trautmann, K. Schulte and G. Lütjering, Sequence events in fatigue crack propagation; mechanical and microstructural contributions. In fracture mechanics, Spec. Tech. Publ. 677, pp36-53. Philadelphia: ASTM (1979)

[35] M.D. Halliday and C.J. Beevers, Some aspects of crack closure in two contrasting titanium alloys, J. testing and evaluation, V9 pp 915-201, (1981)

[36] D.A. Ryder , M. Martin and M. Abdullah, Some factors influencing stage I fatigue crack growth, J. Met. Sci, V11 pp340-4 (1977)

[37] A.G. Pineau and R.MN. Pelloux , Influecne of strain induced martensitic transformations on fatigue crack growth rates in stainless steels, Met Trans. V5A pp 1103-12 (1974)

[38] E. Horbogen , Martensitic transformation at a propagating crack, Acta Met V26 pp147-52 (1978)

[39] D.M. Corlby and P.F. Packman, On the influence of single and multiple peak overloads on fatigue crack propagation in 7075-T6511 aluminium, Engng. Fract. Mech. V5 pp479-97 (1973)

[40] F.O Riemelmoser and R. Pippan, Crack closure: a concept of fatigue crack growth under examination. Fat. Fract. Engng. Mater. Struct. V20 pp1529-40 (1997)

[41] A.K Vasudevan , K.Sadananda and N. Louat, Reconsideration of fatigue crack closure, Scripta. Met. V27 pp 1673-78 (1992)

[42] S. Suresh and R.O.Ritchie, Propagation of short fatigue cracks, Int. Met. Rev. V29 pp 445-76 (1984)

[43] S.Pearson, Initiation of fatigue crack in commercial aluminium alloy and the subsequent propagation of very small cracks, Eng Fract Mech 7 pp235-47 (1975)

[44] W.L.Morris, Microcrack closure phenomena for AL2219-T851, Met trans V10A pp5-11 (1979)

[45] P.M.Scott and T.W.Thorpe, A critical review of crack tip stress intensity factors for semi-elliptic cracks, Fatigue of Engineering Materials and Structures Vol 4 pp291-309 (1981)

[46] J.C.Newmann Jr and I.S.Raju, An empirical stress-intensity factor equation for the surface crack, Engineering Fracture Mechanics V15 pp185-192 (1981)

[47] N.E.Dowling, W.R.Brose and W.K.Wilson, Notched member fatigue life predictions by local strain approach. In fatigue under complex loading pp55-84 (1977)

[48] I.J.Polmear, Light alloys – Metallurgy of the light metals, Arnold London (1995)

[49] G. Henaff, K. Marchel and J. Petit, On fatigue crack propagation enhancement by a gaseous atmosphere: Experimental and theoretical aspects, Acta. Met. Vol.43 pp.2931-42 (1995)

[50] A.D.B. Gingell and E.E. King, The effect of frequency and microstructure on corrosion fatigue crack propagation in high strength aluminium alloys, Acta Mater. Vol.45 pp.3855-70, (1997)

[51] R.G. Song, M.K. Tseng, B.J. Zhang, J. Liu, Z.H. Jin and K.S. Shin, Grain boundary segregation and hydrogen-induced fracture in 7050 aluminium, Acta Mater. Vol.44 pp.3241-48 (1996)

[52] R.M.N. Pelloux, Mechanisms of formation of ductile fatigue striations, Trans A.S.M.E. V62 pp 281-5 (1969).

[53] R.M.N. Pelloux, Crack extension by alternating shear, Engng. Fract. Mech. V1 pp697-704 (1970).

[54] P. Neumann , Fatigue In *Physical Metallurgy* pp1554-93 Amsterdam, Elsevier Science (1983).

[55] A.K.Vasudevan and S.Suresh, Influence of corrosion deposits on near-threshold fatigue crack growth behaviour in 2XXX and 7XXX series aluminium alloys, Met trans 13a pp 2271-80 (1982)

[56] S.Suresh, D.M.Parks and R.ORitchie, Crack tip oxide formation and its influence on fatigue thresholds, In Fatigue thresholds 1 pp391-08 (1982)

[57] S.Newman, Kinetics of wetting of surfaces by polymers: Capillary flow, J Colloid and Interface Science 26 pp 209-213 (1968)

[58] D.D.Fuller, Theory and Practice of lubrication for engineers: Wiley (1956)

[59] P.P.Love, P.G.Forrester and A.E.Burke, Functions of materials in bearing operation (1953)

[60] W.E. Duckworth and G.H.Walter, Fatigue of plain bearings, Int conf on fatigue and metals pp582-92 (1956)

[61] E.A.Blount, Design factors influencing the fatigue resistance of connecting -rod big-end bearings, Proc inst Mech Engrs V175 No10 pp513-27 (1961)

[62] S.K.Chen and S.Chen, Some resolved and unresolved areas in journal orbit analysis, SAE paper 920486 (1992)

[63] N.Gyde, Fatigue fracture in babbit lined journal bearings, Ph.D. thesis Technical uni of Denmark Copanhagen (1969)

[64] S.Sasaki, H.Kato, K.Yamaguchi, M.Ando and M.Isobe, Effects of geometric defects in journals on bearing performance, SAE paper 870581 (1987)

[65] H.J.Peeken, Fatigue strength of dynamically loaded journal bearings, Proc. Int Trib Conf pp79-84 (1985)

[66] K.Endo, T.Okada and T.Hariya, Fatigue propagation in bearing metals lining on steel plates in lubricating oil, Bulletin of JSME V15 No82 pp 439-445 (1972)

[67] J.L.Tzou, S.Suresh and R.O.Ritchie, Fatigue crack propagation in viscous environments, Mechanical behaviour of materials 4 pp711-17 (1983)

[68] J.L.Tzou, S.Suresh and R.O.Ritchie, Fatigue crack propagation in oil environments-I. Crack growth behaviour in silicone and paraffin oils, Acta Met v33 pp105-116 (1985)

[69] H.McCallion and M.Lotfi, Tensile surface stresses and fatigue in plain journal bearings, Trib International pp247-257 (1992)

[70] S.Way, Pitting due to rolling contact, J App Mech 2 pp 49-58 (1935)

[71] P. Shenton and C. Perrin, Private communication, Dana Glacier Vandervell

[72] W.H. Wilson, A test machine for assessing the fatigue propoerties of impulsively loaded plain bearings, Proc I. Mech E. V182 pp129-131 (1967)

[73] .W.Cuthbertson, The fatigue testing of bearings (1955)

[74] T.Fukuoka, H.Kato, S.Kamiya and N.Soda, Fatigue and life of plain bearings under alternating or rotating loads, Proc JSLE Int Tribology Conference pp 91-96 (1985)

[75] O.R.Lang, Plain bearing fatigue under dynamic loading (1975)

[76] O.R.Lang, Bearing fatigue, presented at the conference limits of lubrication (1975)

[77] J.Harbordt, Stresses and material fatigue in bi-metal shells of journal bearings (1976)

[78] O.R.Lang, Surface fatigue of plain bearings, Wear V43 pp 25-30 (1977)

[79] F.A.Martin, D.R.Garner and D.R.Adams, Hydrodynamic aspects of fatigue in plain bearings, ASME Lub Tech 103 pp 150-56 (1981)

[80] J.K.Blundell, The fatigue of dynamically loaded journal bearings, Ph.D. thesis, University of Nottingham, (1977)

[81] J.K.Blundell, Fatigue initiation in thin walled journal bearings, ASLE trans v33 No2 pp131-140 (1978)

[82] D.N.Fenner, J.D.C. McIvor, J.M.Conway-Jones and H.Xu, The effects of compliance on peak oil film pressure on connecting rod bearings, Proc of the 19th Leeds-Lyon symposium on tribology (1992)

[83] H.Bahai and H. Xu, Three dimensional elasto-plastic finite element and elastohydrodynamic analyses of journal bearings, Proc. ImechE j. Mech Engng. Sci V211 pp143-52 (1997)

[84] J.M. Conway-Jones, Effect of housing flexibility on peak oil film pressure (1992)

[85] J.D.C.McIvor and D.N.Fenner, Finite element analysis of dynamically loaded flexible journal bearings: A fast Newton-Raphson method, ASME Trib 111, pp 597-04 (1989)

[86] Hao Xu , Recent advances in engine bearing design analysis, Proc IMechE. J. Eng V213 pp239-251 (1999)

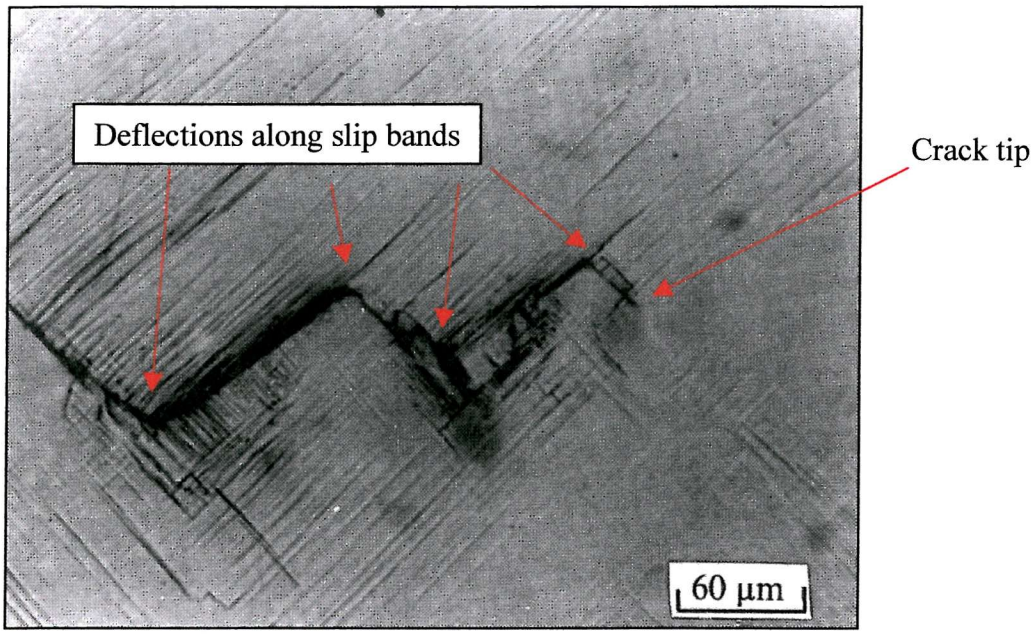

Figure 1.1: Typical stage I crack propagation in Mar-M-200 Ni base superalloy (Aswath and Suresh 1988)

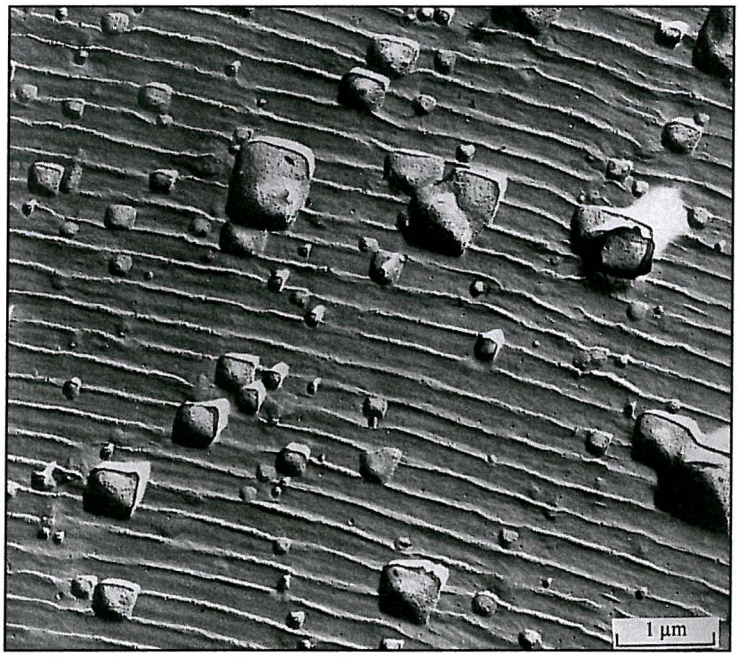

Figure 1.2: Visible striations on fracture surface produced during stage II fatigue crack propagation in Al 2024-T3.(Pelloux 1969)

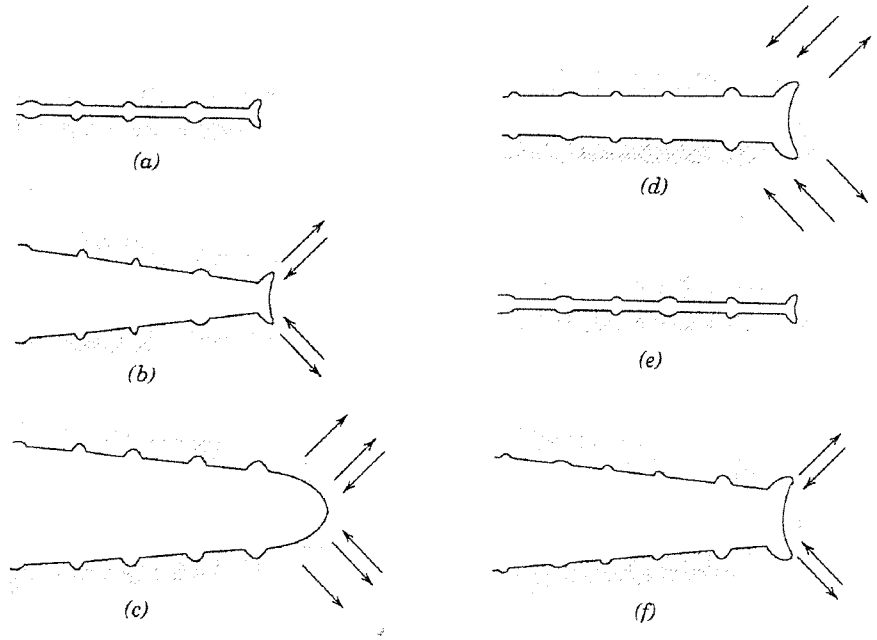

Figure 1.3: Micro mechanism for fatigue crack advance proposed by Laird and Smith. (Laird 1967)

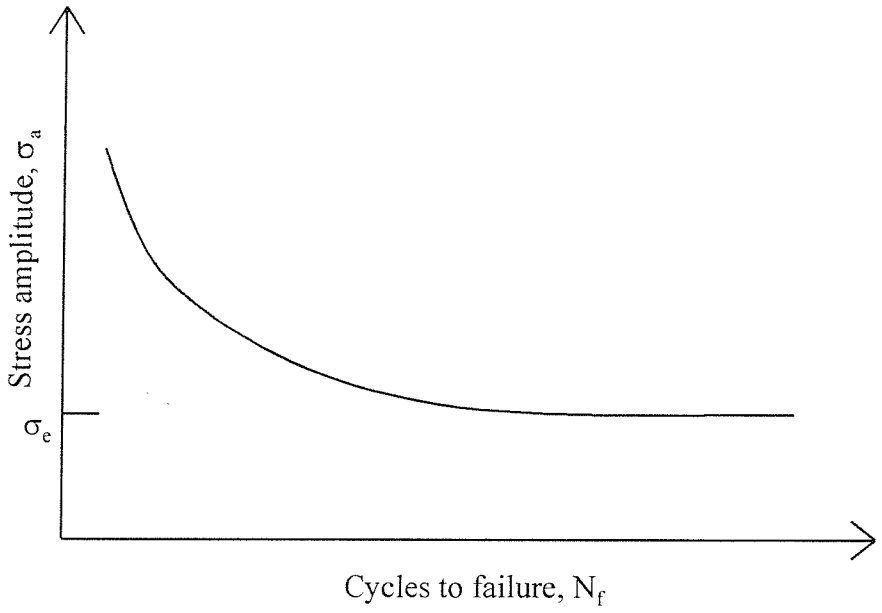

Figure 1.4: Typical stress life (S-N) curve

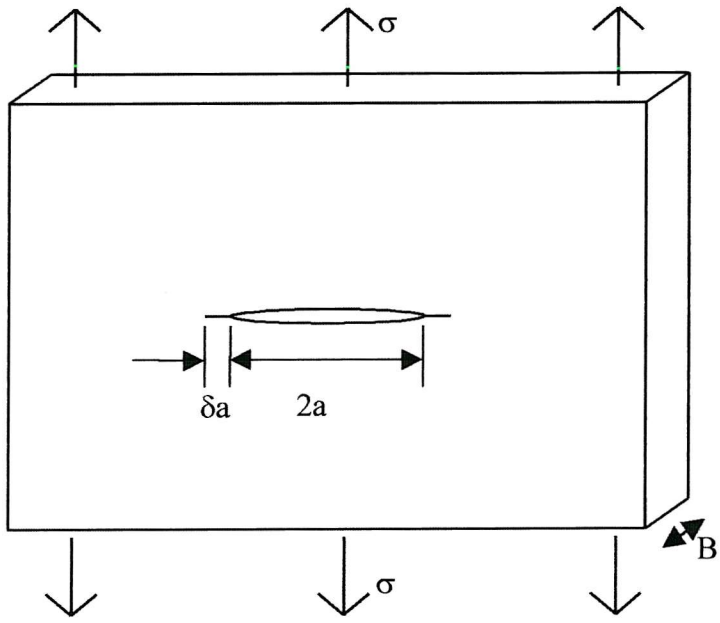

Figure 1.5: Cracked body used for Griffith energy balance approach

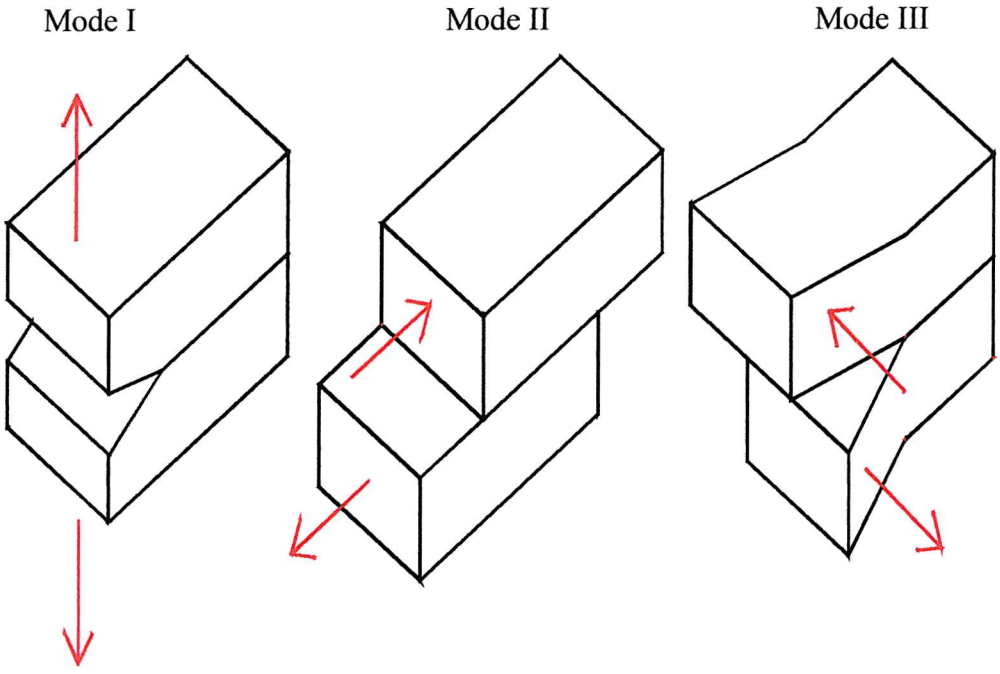

Figure 1.6: 3 Basic crack opening modes

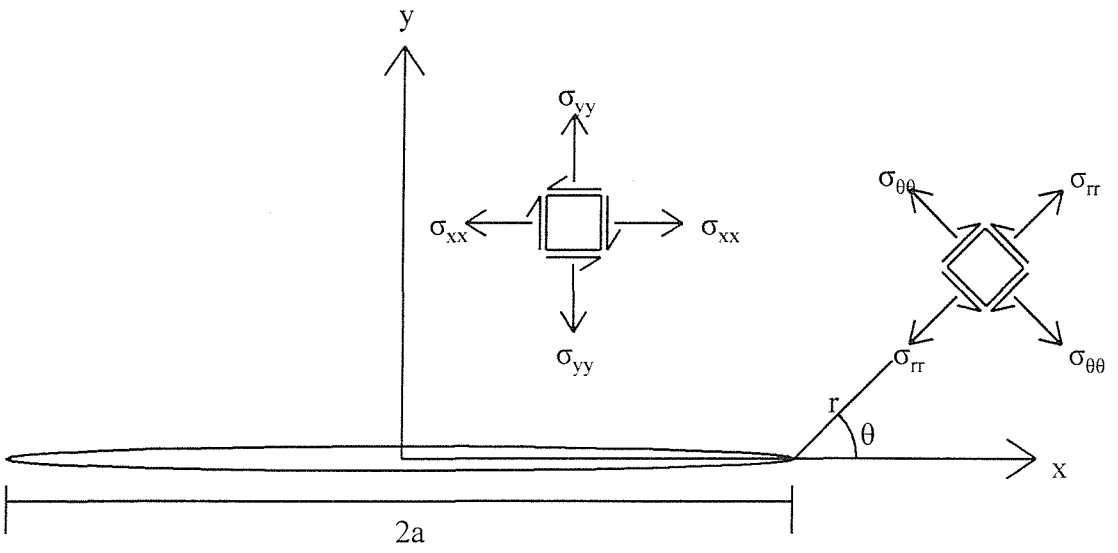

Figure 1.7: Nomenclature used to describe stresses in an infinite plate containing semi-infinite crack

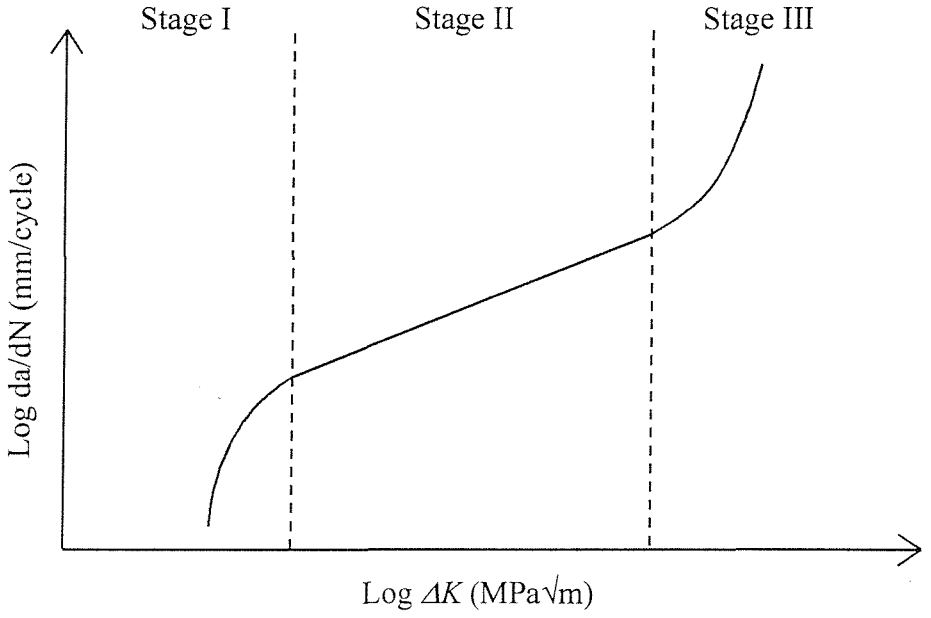

Figure 1.8:Use of stress intensity factor (ΔK) to characterise crack growth rates (da/dN)

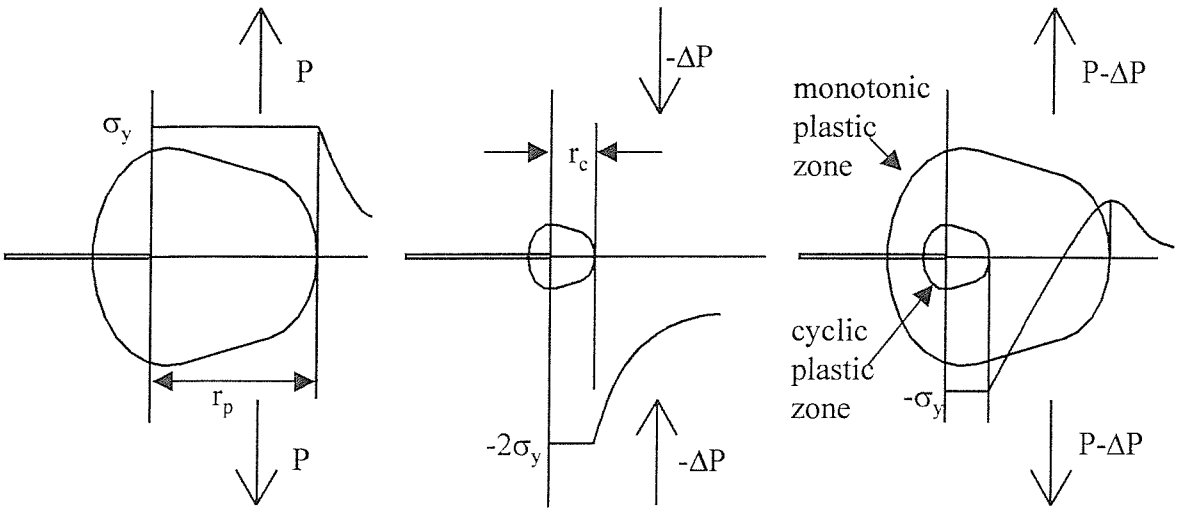

Figure 1.9: Relative monotonic and plastic zones sizes according to Irwin approximation

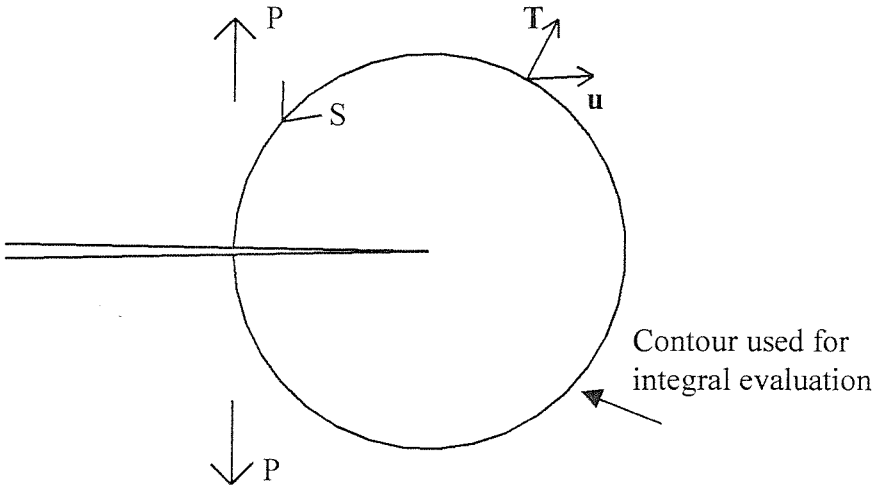

Figure 1.10: Cracked body geometry used for J-integral definition

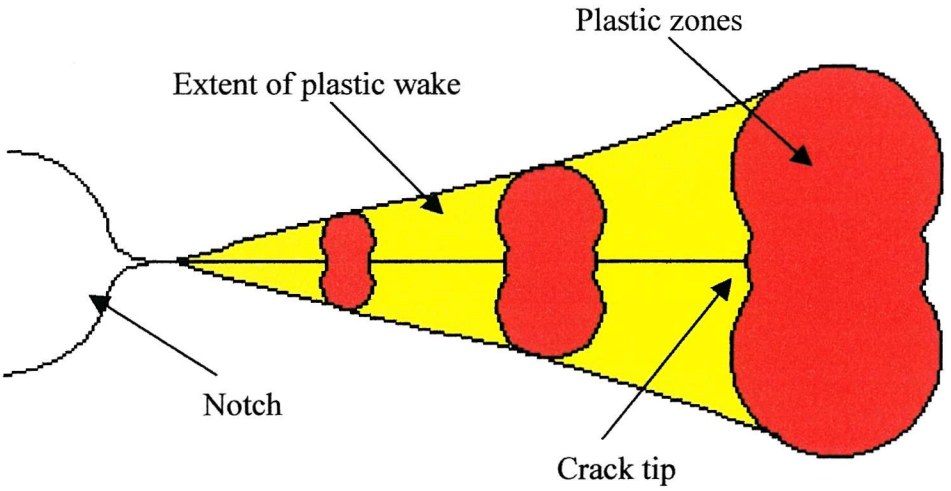

Figure 1.11: Plasticity induced fatigue crack closure as proposed by Elber

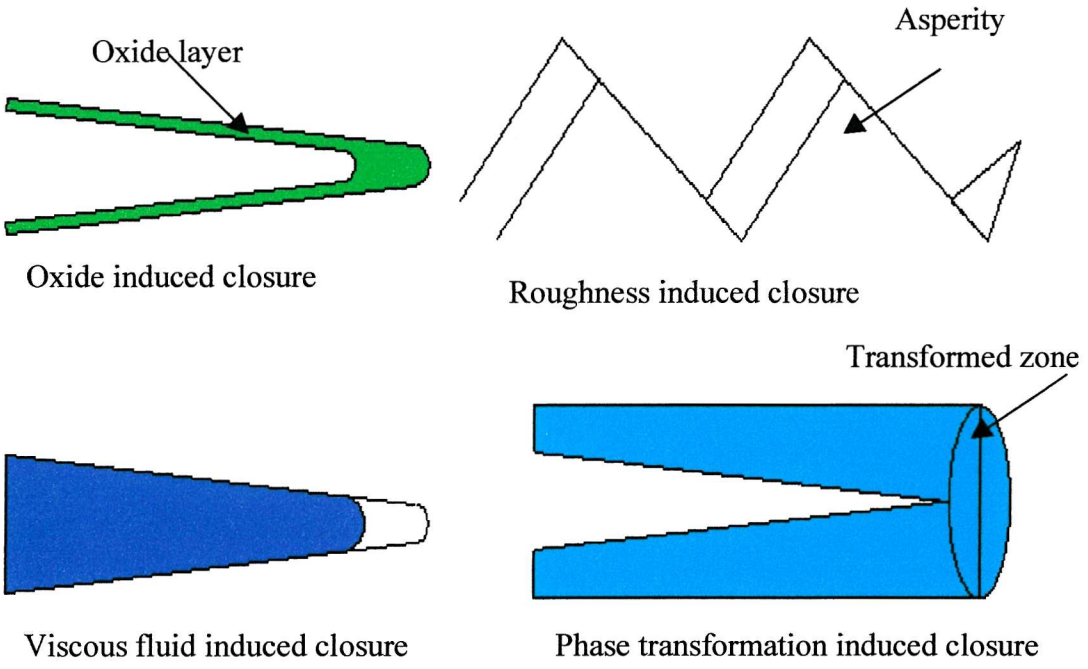

Figure 1.12: Other documented closure mechanisms

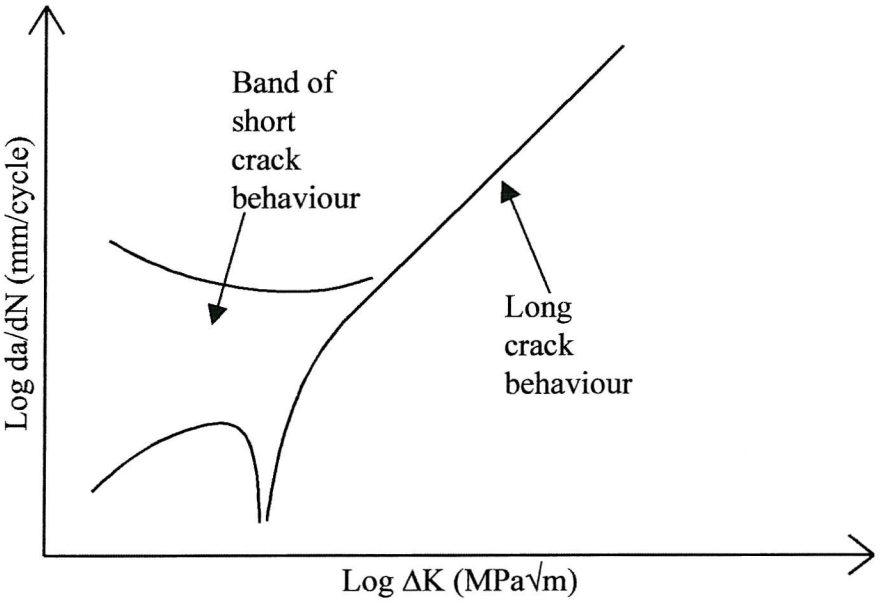

Figure 1.13: Comparison of long and short fatigue crack behaviour in a typical aluminium alloy

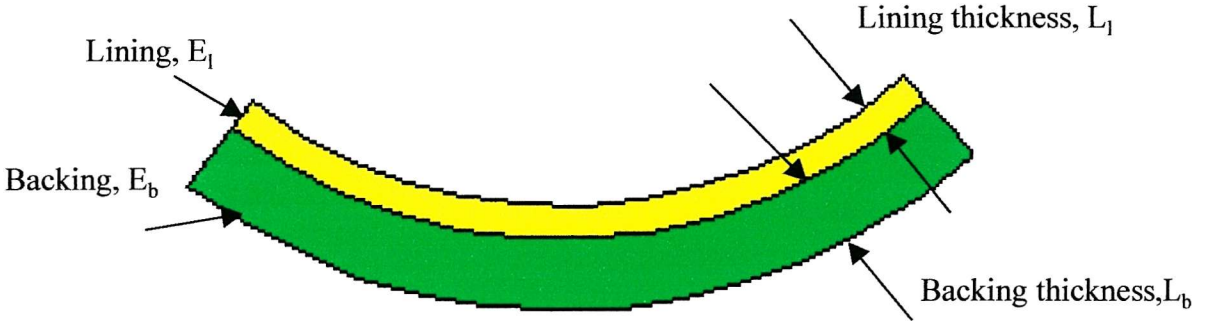

Love et al hypothesise $E_b/E_l=L_b/L_l$ and that the ratio E_b/E_l should be maximised for optimum fatigue performance.

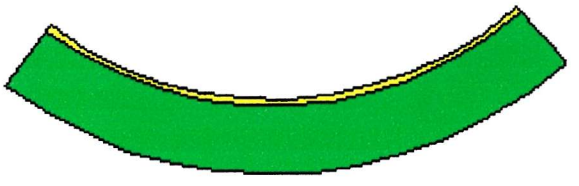

$\therefore$ Optimum bearing design, thin and soft lining, thick and stiff backing

Figure 1.14: Layer properties and thickness' as proposed by Love et al for optimum fatigue properties

Note decrease in bearing land area caused by inclusion of circumferential oil groove

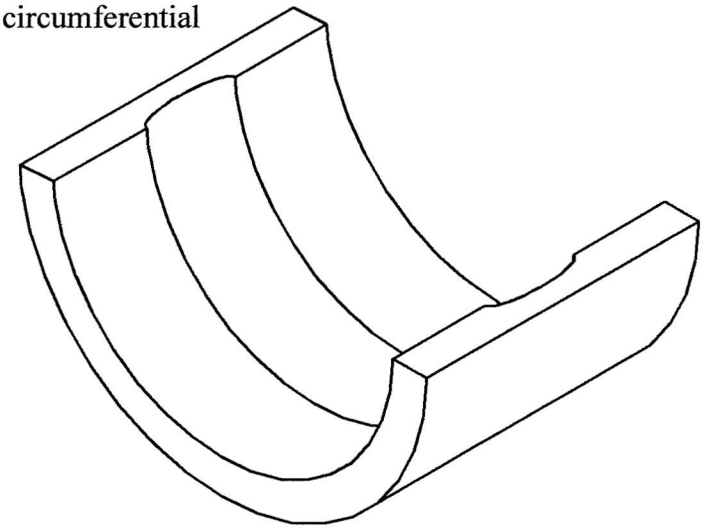

Figure 1.15: Bearing with circumferential oil groove

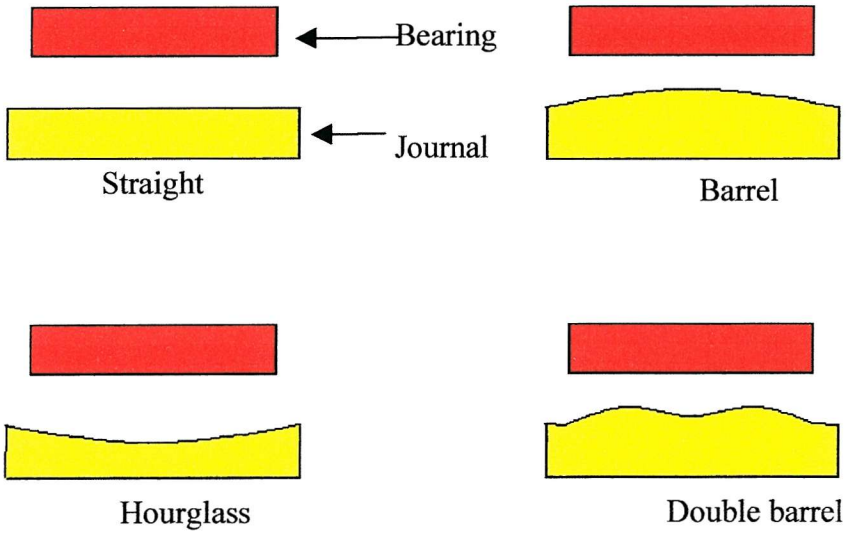

Figure 1.16:Axial profiles of different journal shapes, as tested by Sasaki et al.

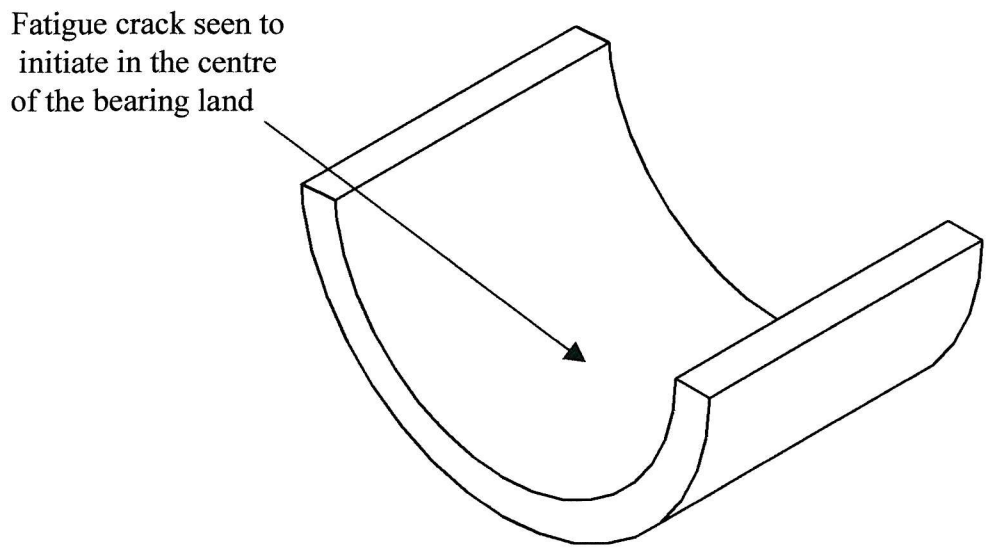

Figure 1.17: Area of crack initiation observed in rig tested bearings.

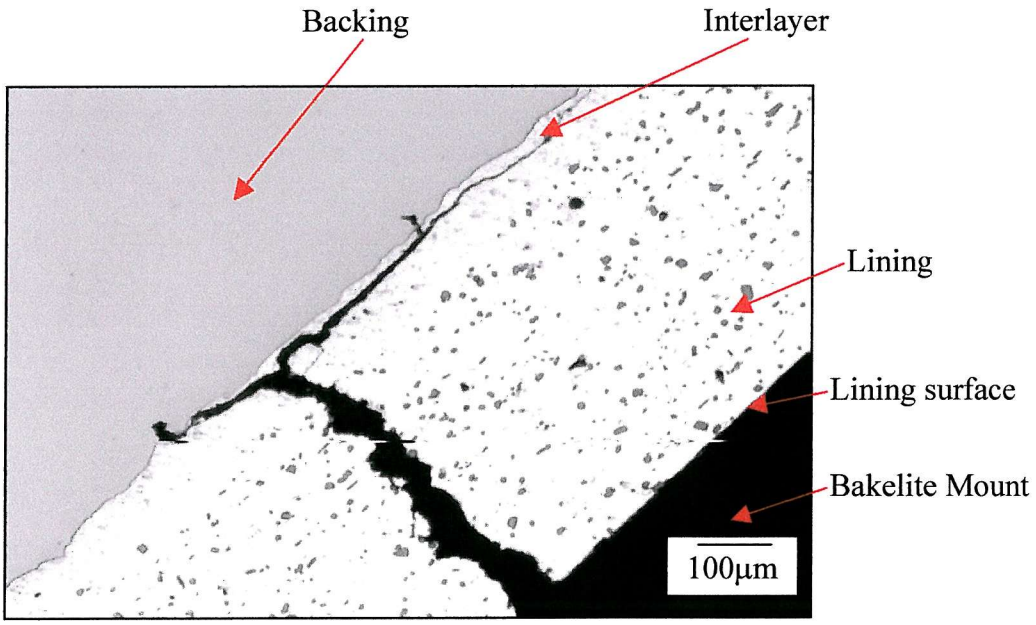

Figure 1.18: Typical sub surface behaviour observed in Sapphire tested plain bearings.

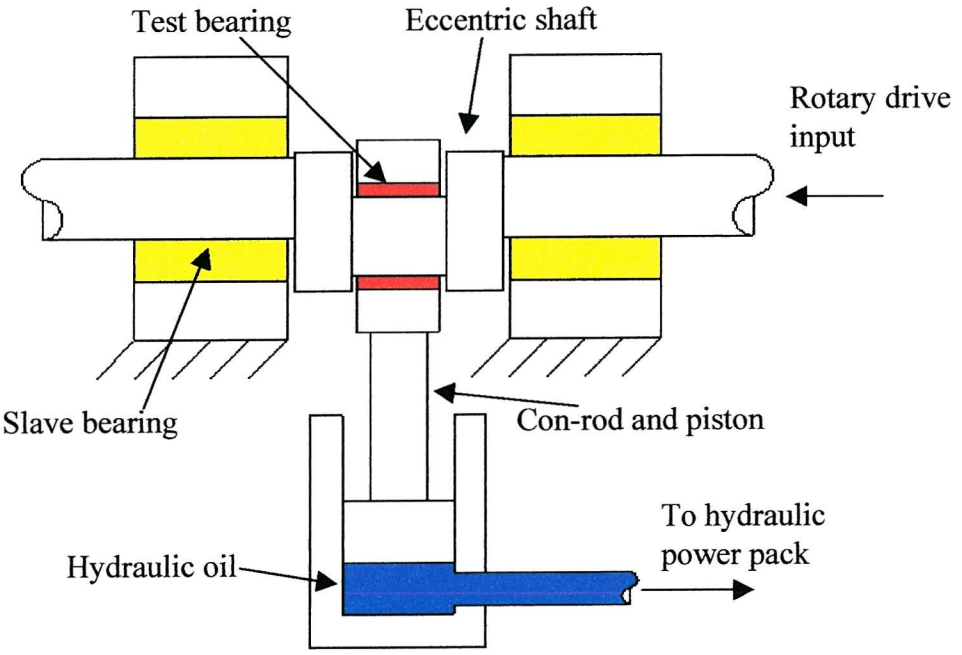

Figure 1.19: Schematic of Sapphire accelerated bearing fatigue test rig

2.0 CHARACTERISATION OF BEARING MATERIAL SYSTEM

Unlike much of the previous work pertaining to plain bearings discussed in Section 1.8, the bearings considered in this thesis are of a modern design, typically employed as main bearings in high output automotive engines. In common with earlier designs they are constructed in two parts, or half shells which are clamped together within the bearing housing to support the journal between them, as shown in Figure 2.1. Each half shell comprises several layers of different material. This chapter gives further details of both the bearing architecture and characterises the material microstructures within the bearing.

2.1 Bearing Description and Processing Route

The bearings considered in this thesis are produced by Dana Glacier Vandervell by a proprietary route, and therefore full processing details cannot be made available. The aluminium alloy lining material is continuously cast as a 25 mm thick slab, before being cut into billets. The billets are then homogenised, however this heat treatment causes tin to bleed onto the billet surface. Hence 3mm of material are machined from the upper and lower billet surfaces reducing its overall thickness to 19mm. At this stage, a layer of pure aluminium is roll bonded to both the upper and lower surfaces of the billet, one of these forms the interlayer, whilst the other is machined away in the bearing finishing operation. This interlayer serves to bond the lining to the backing, as well as preventing Sn from the lining alloy diffusing into the steel backing.

A series of further rolling and annealing operations reduce the overall material thickness to 0.89 mm, after which it is bonded to the steel backing and undergoes a final annealing treatment. The material is then formed into bearings and broached to give the desired lining thickness. The dimensions of the resulting bearings are shown in Figure 2.2 and the typical thickness of individual material layers are given in Table 2.1.

These bearings were supplied to Southampton in an "as finished" condition. In addition, material was made available for testing in two other forms; firstly, bearing

material was also supplied as a flat sheet, in the condition immediately prior to the bearing forming operation, secondly, a small quantity of monolithic lining material was available. This had been produced by a similar series of rolling and heat treatment operations so that the material was in a similar condition to that of the lining of the finished bearing. The layer thickness of the bearings, flat strip and monolithic lining materials are given in Table 2.1.

Table 2.1: Measured layer thickness in as supplied bearing

Material	Thickness (mm)		
	Bearing	Flat strip	Monolithic lining
Al alloy lining	0.244	0.46	0.51
Al interlayer	0.06 ± 10%	0.06 ± 10%	N/A
Steel backing	1.505	1.505	N/A

2.2 Optical Microstructural Characterisation

Of the three material layers the Al alloy lining material is of greatest interest, since this is the layer directly subjected to hydrodynamic pressure and where fatigue cracks are seen to initiate in samples from accelerated bearing test rigs[1]. The lining material used in the bearings studied in this thesis is designated AS1241, its nominal composition is given in Table 2.2.

Table 2.2: Nominal composition of AS1241

Element	Aluminium	Tin	Silicon	Copper
% by mass	Balance	12	4	1

In order to examine the lining material microstructure a section of bearing was taken and mounted in Bakelite to facilitate polishing. The polishing route employed was fairly complex since both hard and soft phases were present in the lining material microstructure. The polishing route used is similar to that suggested for very soft materials by Struers[2] with an additional step at an abrasive size of 1μm to reduce relief polishing; see Table 2.3 for details.

Table 2.3: Polishing route for AS1241 lining material

Stage	Plain grinding	1st Polish	2nd Polish	3rd Polish	4th Polish	5th Polish
Cloth	SiC	DP-Pan	DP-Dur	DP-Mol	DP-Mol	OP-Nap
Abrasive	600 Grit	15μm Diamond	6μm Diamond	3μm Diamond	1μm Diamond	0.25 μm OPS
Lubricant	Water	DP-Blue	DP-Blue	DP-Red	DP-Red	-
Force (N)	340	450	450	340	340	115
Speed (rpm)	300	150	150	150	150	150
Time (min)	Till plane	5	4	3	3	1

After polishing the sample was examined using optical and scanning electron microscopy (SEM); an optical micrograph of the bearing lining material is shown in Figure 2.3. It is clear that AS1241 is a multiphase material, with the Si and the Sn existing as two distinct secondary phases. The silicon phase is a darker grey, spheroidal and apparently uniformly distributed, whilst the lighter grey phase is the Sn. This is often seen to be associated with the Si phases occasionally encapsulating them entirely. Grain boundaries were not visible on the surface of the un-etched sample, and attempts to etch the material using NaOH and Kellers reagent were generally unsuccessful. Figure 2.4 shows the lining material after etching in 15% NaOH, revealing the recticular structure of the Sn phase; it is thought that this structure is aligned along grain boundaries[1].

A polished and unetched section of bearing lining microstructure was examined using a Jeol 6400 SEM at an accelerating voltage of 20kV; Figures 2.5 and 2.6 show backscattered images of the sample surface. The secondary phases may clearly be distinguished by this method, and to confirm their composition. Energy dispersive x-ray (EDX) spectra were obtained for each phase, the locations of these are shown in Figure 2.6. Spectra 1 is shown in Figure 2.7 and clearly shows that the matrix comprises Al as expected, and that Cu is also present. The apparent Ar peak is false, caused by the detector becoming swamped (Ar has almost exactly twice the x-ray energy of Al). Given that no secondary phases were obvious, and in view of the multiple heat treatments, it is likely that the Cu has formed a solid solution with the Al matrix. Figure 2.8 shows the spectra obtained from the Si secondary phase, it appears that this phase is exclusively Si, with no other elements present. Figure 2.9

shows the spectra obtained for the Sn phase, again this appears to be exclusively Sn. Finally Figure 2.10 shows the spectra for an intermetallic particle, which appears to contain predominantly Al, with lesser and approximately equal quantities of Si and Fe.

In order to both compare the three sample types and investigate the layered construction, sections of bearing, flat strip and monolithic lining material were taken in three orientations as shown in Figure 2.11. Figures 2.12 to 2.14 show sections of lining material microstructure from each sample in each orientation. Whilst Figures 2.15 and 2.16 are at a lower magnification to show the layered structure of the bearing and the flat strip material respectively. In both cases individual material layers are easily distinguished, though the interfaces between them are not completely smooth. The interlayer is the secondary phase-free region adjacent to the steel backing as indicated. Comparing the two structures, it may be seen that the lining of the flat strip material is considerably thicker and retains the second pure aluminium layer, whilst this is machined away in the finished bearings.

A section through finished bearing (orientation 2 as shown in Figure 2.11) was etched in 2% Nital to reveal the steel microstructure. Figure 2.17 clearly shows the grain structure present within the steel layer. The grains appear elongated, as they have been deformed during the rolling stages in manufacture. Figure 2.18 shows a higher magnification micrograph of the steel microstructure, which appears to comprise of pearlite and proeutectoid ferrite.

2.3 Statistical characterisation of lining material microstructure

Since much of the fatigue testing was to be carried out on the flat strip and monolithic lining material it was necessary to confirm that the lining microstructure in these samples was similar to that in the finished bearing. To assess any differences the lining microstructures were compared using a tessellation approach.

2.3.1 Development of tessellation approaches

Tessellation approaches provide a method of statistically characterising a multiphase microstructure. The definition of a distribution of tessellated cells surrounding each particle, such that all points within a given cell are closer to the

included particle than any other, has been identified by several authors[3,4] as a powerful analytical tool. The characteristics of this tessellation may be assessed as an overall distribution on a global volume or area averaged basis, the ability to quantify such parameters on a cell by cell basis allows considerable insight into nucleation type processes.

The most established method of generating such a structure is the Dirichlet tessellation approach[5], in which particle centroids are used to construct a network of polygon cells, such that any point within a given cell is closer to that cell centre (and hence the particle centroid) than any other. The construction of such a Dirichlet type tessellation is shown in Figure 2.19. By its definition the Dirichlet tessellation ignores the size and shape of the included particles, and this may result in particle and cell overlaps, particularly where large or elongated particles are involved. To address this problem a finite body tessellation approach was proposed by Boselli *et al*[6]

Figure 2.20a shows a binary image consisting of feature and non feature pixels of the secondary phase distribution to be tessellated. A distance transform is applied to this region converting it to a greyscale image, in which each non feature pixel is assigned a grey value which approximates its distance to the nearest feature pixel[7], the resulting image is shown in Figure 2.20b. This transformed image may be thought of analogous to a topographical map in which grey value is a representative of elevation. The feature regions lie at the bottom of the catchment basins whilst the ridges are the watersheds. A binary image of these dividing lines is generated by a watershed algorithm, which simulates the immersion of the distance transformed image[8], hence producing the tessellation shown in Figure 2.20b.

The finite body tessellation approach is capable of generating representative tessellated structures from phase distributions containing large or elongated particles. Figure 2.21 shows a section of Al-SiC_p composite overlaid with Dirichlet and finite body tessellations. It can be seen that the finite body tessellation has a wider distribution of cell sizes, indicating a greater sensitivity to local microstructural variation. Furthermore, since cell/particle overlaps do not occur using the finite body approach, the cells generated by this method are far more representative of the region with which the included particles may be expected to interact. These features make the finite body approach a far more powerful tool for characterising nucleation type events associated with individual particles.

2.3.2 Application of tessellation methods to bearing materials

Only the Si secondary phase distribution has been considered, as the tendency of the Sn to encapsulate other phases makes it difficult to assess the Sn distribution unambiguously. Tessellation was carried out on sections of microstructure in the plane of the original sample surface (orientation 1), as in other orientations the lining layer is too narrow to contain a statistically relevant number of secondary phases. Four sections of lining microstructure were randomly selected from each material (typically each contained ~600 Si secondary phases). These were converted to binary images by hand, then tessellated using the finite body method described previously. All the cells on the edge of the tessellated region were discarded as they are inadequately defined[6]. Then using the definition of near neighbours shown in Figure 2.22, the 11 measurements described below and shown in Figures 2.23 and 2.24 were made on each of the remaining cells.

- Object area: area of the object, i.e. Si particle
- Object aspect ratio: aspect ratio of the object (maximum chord length divided by maximum width perpendicular to the maximum chord length).
- Object angle: angle of the object's longest chord with respect to the horizontal (between 0 and $\pi/2$ radians).
- Cell area: area of the cell
- Cell aspect ratio: aspect ratio of the cell (maximum chord length divided by the maximum width perpendicular to the maximum chord length)
- Cell angle: angle of the cell's longest chord with respect to the horizontal (between 0 and $\pi/2$ radians).
- Local area fraction: object area/Cell area x 100.
- Number of near-neighbours: number of objects sharing a cell boundary with object of interest.
- Nearest-neighbour distance: shortest interfacial distance with any of the near-neighbours
- Mean near-neighbour distance: average of shortest interfacial distances to all of the near neighbours
- Nearest-neighbour angle: angle of the line joining the centroid of the object to the centroid of the nearest neighbour, measured with respect to the horizontal (between 0 and $\pi/2$ radians).

The mean values and one standard deviation for each measurement are given in Table 2.4, while Figures 2.25 to 2.35 show the results plotted as frequency histograms to allow comparison between the material types.

Table 2.4: Tessellation results from base microstructures

Material	Object area (μm^2)	Object aspect ratio	Object angle (rad)
Bearing	7.75 ± 6.06	1.50 ± 0.34	0.62 ± 0.378
Flat strip	7.20 ± 6.08	1.55 ± 0.46	0.99 ± 0.36
Monolithic lining	7.97 ± 7.47	1.50 ± 0.38	0.967± 0.38

Material	Cell area (μm^2)	Cell aspect ratio	Cell angle (rad)
Bearing	90.54 ± 50.62	1.53 ± 0.59	0.76 ± 0.42
Flat strip	108.54 ± 70.00	1.86 ± 2.92	0.79 ± 0.45
Monolithic lining	103.36 ± 69.83	1.67 ± 1.25	0.78 ± 0.44

Material	Local area fraction	Number of near neighbours	Nearest neighbour distance (μm)
Bearing	9.37 ± 6.10	5.73 ± 1.45	2.04 ± 1.96
Flat strip	7.63 ± 5.69	5.65 ± 1.49	2.23 ± 2.10
Monolithic lining	9.20 ± 7.76	5.66 ± 1.49	1.96 ± 2.07

Material	Mean near neighbour distance (μm)	Nearest neighbour angle (rad)
Bearing	6.97 ± 2.72	0.75 ± 0.47
Flat strip	8.05 ± 3.32	0.94 ± 0.45
Monolithic lining	7.59 ± 3.44	0.90 ± 0.45

The tessellation results indicate that the materials are generally similar though small differences are present. Considering the size distribution of Si secondary phases, it can be seen that in the case of the bearing, the distribution peak is less pronounced, and there is a trend towards slightly larger particles. However this is not reflected in the mean values, although the bearing mean Si particle size is higher than that for the strip material, the figure for the monolithic lining material is higher due to the presence of a small number of very large particles. It was also seen that generally, cell area was lower in the bearing case, this in conjunction with the generally higher object area, causes a shift in the distribution of local area fractions towards higher values in the bearing case. This correlates with the variation observed in the mean near neighbour distance distribution, in which the bearing case shows a shift towards

smaller distances, indicating that generally the particles are closer packed in the bearing material.

In all the materials the object angle histogram shows a binary distribution, the Si phases generally aligned at either 30 or 60 degrees to the rolling direction. It is likely that this is due to the rolling operations in the manufacturing route.

All the observed variations between the sample types were small, and generally their microstructural distributions were found to be similar enough to allow direct comparison.

2.4 Material Characterisation Tests

A series of simple material tests were performed to compare the monotonic material properties of the three sample types. These tests comprised micro hardness indents and tensile tests under monotonic loading.

2.4.1 Micro-hardness indentation tests.

In order to assess any difference in plastic flow behaviour between the three sample types a series of hardness tests were carried out. Vickers micro-hardness was used, since its small indent size is more suitable for thin samples. All indents were carried out using a pyramidal indentor at a load of 200 g and an indention time of 20 seconds.

To compare the three sample types, a section of each was mounted such that indents could be taken along an axis normal to the original sample surface. In addition, sections of the bearing and flat strip sample were mounted such that indents could be made along an axis parallel with the original sample surface. The monolithic material was not mounted in this manner, since its low thickness and thus low constraint, would preclude any valid results being obtained. Sample orientations for all sections are shown in Figure 2.36.

A total of 50 indents were made at random locations across the surface on each of the samples mounted in orientation 1, the mean hardness values and standard deviations from which are shown in Table 2.5.

Table 2.5: Results from indents taken normal to the sample specimen surface

Material	Vickers Hardness (H_v)
Bearing	54.84 ± 2.5
Flat Strip	55.75 ± 1.83
Monolithic lining	52.94 ± 1.426

When testing the samples mounted in orientation 2, the indents were taken along a line as shown in Figure 2.37, to investigate any property variation through the sample thickness. The line is at an angle of ~30° to the original lining surface to ensure sufficient spacing between indents (c.f. indent size ~65 μm, spacing ~250 μm), whilst retaining a high number of indents across the lining thickness. Mean values and standard deviations for these results are given in Table 2.6.

Table 2.6: Average values for through thickness traverses

Material	Vickers Hardness (H_v)
Bearing	47.79 ± 8.067
Flat Strip	57.13 ± 8.067

The micrograph in Figure 2.38 shows the size difference of the indents in steel interlayer and lining. Unfortunately due to its low thickness it was not possible to make valid indents solely within the interlayer. However simply comparing the relative indent sizes between those made in the lining and those in the interlayer, indicates that the interlayer is considerably softer than the lining.

The results from traverses across the bearing and flat strip samples are shown in Figures 2.39 and 2.40 respectively. They show some scatter, but some trends are discernible. It appears that the lining is softer near the original sample surface and near the interlayer. Both of these trends may be explained by a reduction in local constraint, due to, in the first case, the Bakelite mount, and in the second case, the soft interlayer.

2.4.2 Tensile testing.

Tensile tests were carried out to investigate the properties of both the AS1241 lining and the steel backing. Tensile test dog bone specimens as shown in Figure 2.41 were manufactured from the monolithic lining material and from the flat strip material, the lining was then ground away from these second samples leaving only the steel backing. These samples were all tested according to British standard procedures[9]

at room temperature using a screw driven Instron 1196 at a strain rate of 10 mm/min, using a 50 mm gauge length extensometer.

The measured properties and typical stress strain curves for AS1241 and the steel backing are given in Tables 2.7 and 2.8 and in Figures 2.42 and 2.43 respectively. In addition Table 2.7 gives the expected property values for AS1241 provided by the sponsoring company. The only available data for the steel layer is a buying specification (σ_{uts} 280-340 MPa, elongation 25% minimum), which does not account for any property change during the bearing processing route (e.g. work hardening effects).

Table 2.7: Tensile test results for AS1241

Specimen	Yield Stress (MPa)	0.2% Proof Stress (MPa)	Ultimate Tensile Stress (MPa)	Elongation to failure (%)
1	56.4	76.2	211.0	17.5
2	52.5	69.4	186.0	18.8
3	53.1	71.4	190.8	16.3
Average and standard deviation	54.0 ± 2.1	72.3 ± 3.5	196.0 ± 13.2	17.5 ± 1.2
Expected values	56.6 ± 2.5	72.6 ± 1.8	172.9 ± 3.0	19.7 ± 1.7

Table 2.8: Measured tensile properties of steel backing

Specimen	Yield Stress (MPa)	0.2% Proof Stress (MPa)	Ultimate Tensile Stress (MPa)	Elongation to failure (%)
1	416.7	475.9	493.4	17.7
2	425.46	485.07	497.9	20.4
3	416.8	486.26	499.5	21.5
Average and standard deviation	419.65 ± 5.03	482.41 ± 5.67	496.9 ± 3.16	19.9 ± 2.0

The results obtained for AS1241 correlated well with the expected values provided by the sponsoring company, though a slightly higher ultimate tensile stress was recorded. A failed AS1241 tensile test sample was mounted in Bakelite and the fracture surface examined in the SEM, this revealed typical ductile failure behaviour as shown in Figure 2.44. Micro-voids are evident on the surface which have formed around secondary phases, most of which, from their shape, appear to be silicon.

In addition to confirming material properties the tensile test stress-strain curves obtained for both the lining and the steel were used to generate plastic material response curves required for subsequent finite element models.

2.5 Discussion and Summary

The material system examined was known to comprise several layers, and it was possible to distinguish these layers on polished unetched samples. The AS1241 lining material was found to be multiphase with the Si and Sn existing as two distinct secondary phases. EDX analysis showed that these phases are pure Si and Sn respectively, this technique also revealed the presence of occasional intermetallic particles which from their relative compositional peak heights, and with reference to a ternary phase diagram appear to be $FeSiAl_5$.

Similar phase arrangements were observed in the three sample types provided. Statistical comparison of the Si particle population by tessellation methods revealed that these particles appear to be generally larger and more densely packed in the bearing than in the flat strip or monolithic material. It should however be noted that these differences are very small and overall the three lining microstructures were comparable.

The Vickers hardness of the lining was found to be similar for all three sample materials (flat strip, bearing and monolithic lining material) when tested parallel to the sample surface. Due to the small thickness of these samples in the indenting direction (c.f. indent depth ~14 μm, lining thickness ~100-200 μm) these results may be affected by varying sub-surface compliance between sample types. Indeed in samples with a low compliance steel backing (flat strip and bearing) the hardness results are generally higher than for the monolithic lining material.

More reliable results come from the indents taken on sections through the sample thickness, where a marked difference was observed between the average Vickers micro-hardness values for the flat strip and bearing (57.13 and 47.79 respectively). As stated previously, the monolithic material was not tested in this orientation due to it low thickness (c.f indent size ~70 μm, sample thickness ~500 μm). The micro-hardness traverses also showed that lining material flow stress is lower at the sample surface and at the interface, this apparent reduction at the surface

is almost certainly due to lack of constraint from the Bakelite mount. The reduction at the interface is caused by the interlayer, which was expected to have a lower hardness than the lining. This was confirmed as the indents in the interlayer region were considerably larger than those in the lining material. It was not possible to take indents entirely within the interlayer, since the thickness of this layer is smaller than the indentor size (c.f. interlayer thickness ~60 μm, apparent indent size ~100 μm).

The AS1241 tensile test results obtained correlate well with the data provided by the sponsoring company, although a ~10% greater σ_{uts} was recorded, and thus the usual correlation between Vickers hardness and σ_{uts}, given in Eqn 2.1, was not observed in this case.

$$H_v \approx \frac{1}{3}\sigma_{UTS} \tag{2.1}$$

The failure of this correlation may be due to an inaccurate hardness value, the indents in the monolithic material being taken in a possibly non optimum direction (due to the small specimen dimensions), or it could merely be a reflection of batch to batch variation.

The tensile properties recorded for the steel backing indicated that it is considerably harder than the buying specification, having a higher σ_{uts} and a lower elongation to failure. The tensile test results coupled with the obviously deformed grain structure indicates that, these property changes are probably due to work hardening during the bearing manufacturing process.

2.6 References

[1] P. Shenton and C. Perrin, Private communication, Dana Glacier Vandervell

[2] L.Bjerregaad, K.Geels, B.Ottesen and M.Rückert, *Metalog Guide*, Struers tech. 1992

[3] P.J. Wray, O richmond and H.L. Morrison, Use of the Dirichlet tessellation for charatcerising and modelling nonregular dispersions of second phase particles, Metallograpghy Vol 16 pp 39-58, (1983)

[4] M.T. Shehata and J.D. Boyd, Measurement of spatial distribution of inclusions. Inclusions and their influence on material behaviour (ed. R. Rungla), pp 121-31, ASM Int. Ohio, (1988)

[5] G. Burger, E. Koken, D.S. Wilkison and J.D. Embury, The influence of spatial distributions on metallurgical processess. Advances in phase transitions (ed. J.D. Embury and G.R. Purdy) pp 247-66, Pergamon press Osford, (1988)

[6] J. Boselli, P.D. Pitcher, P.J. Gregson and I. Sinclair, Secondary phase distribution analysis via finite body tessellation, J. Microscopy, Vol. 195 pt.2 pp104-112, (1999)

[7] G. Borgefors, Distance transformations in digital images, Comput. Vision Graphics Image Process, Vol.34 pp.344-71, (1986)

[8] L. Vincent and P. Soille, Watersheds in digital spaces: an efficient algorithm based on immersion simulations. IEEE Trans. Pattern Anal. Machine Intell. Vol.13 pp.583-98, (1991)

[9] BSI EN 10002-1:1990, Tensile testing of metallic materials. Method of test at ambient temperature.

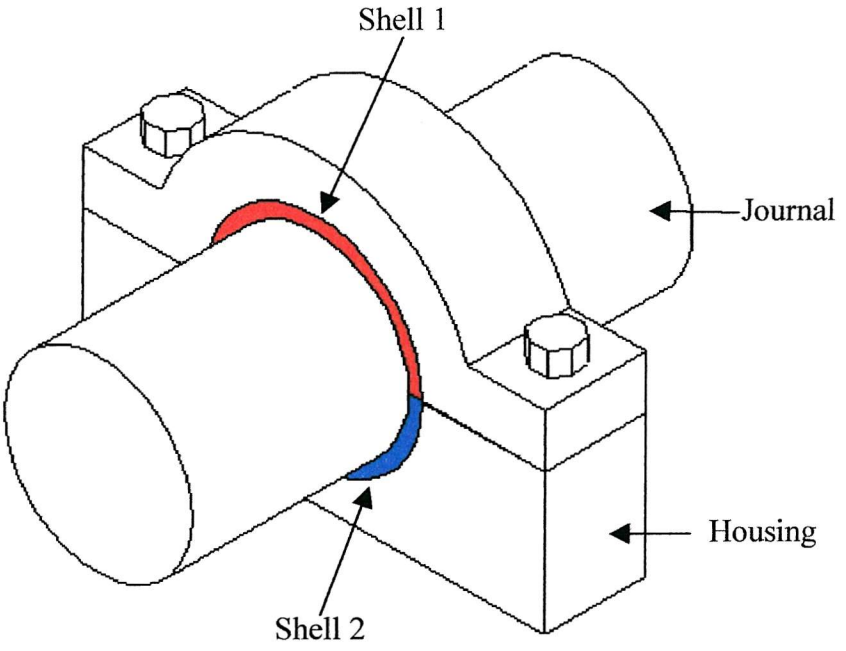

Figure 2.1: Bearing mounting

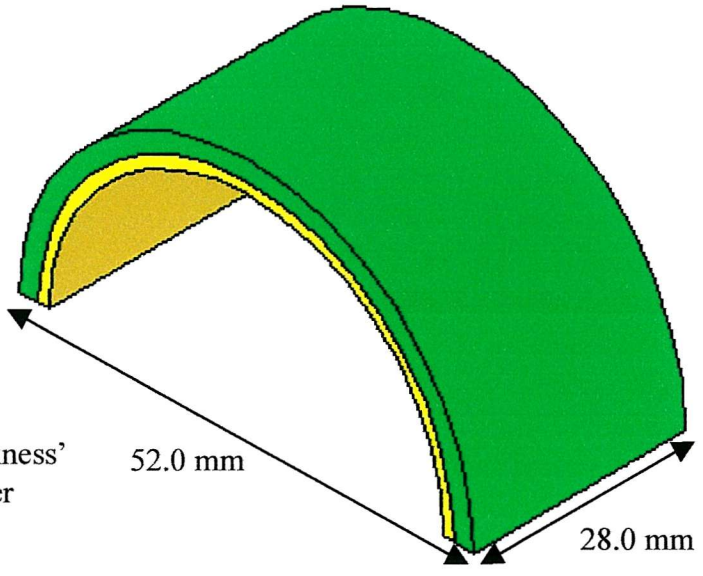

N.B. Relative layer thickness' not to scale and interlayer not shown for clarity

Figure 2.2: Bearing dimensions

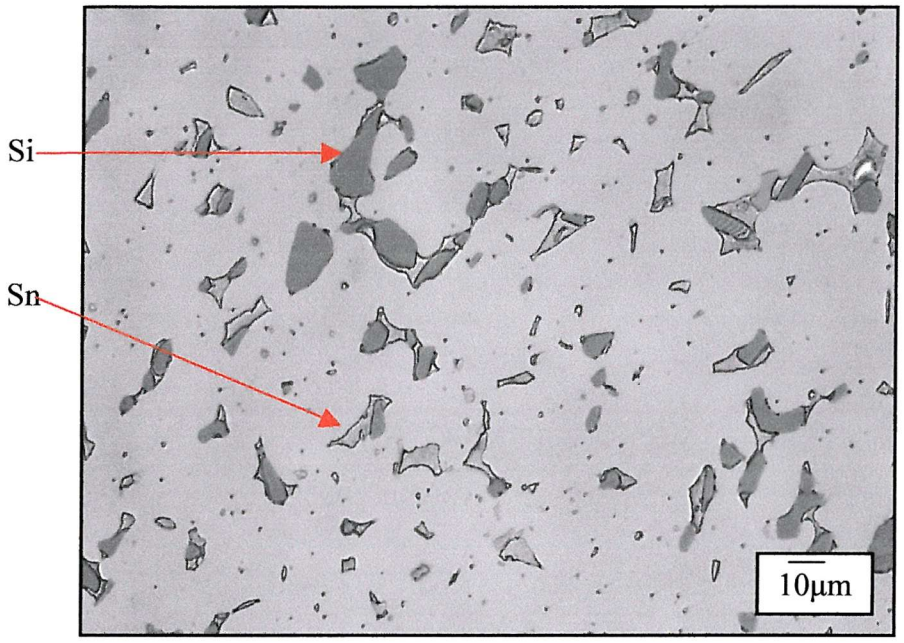

Figure 2.3:Optical micrograph of un-etched AS1241 microstructure

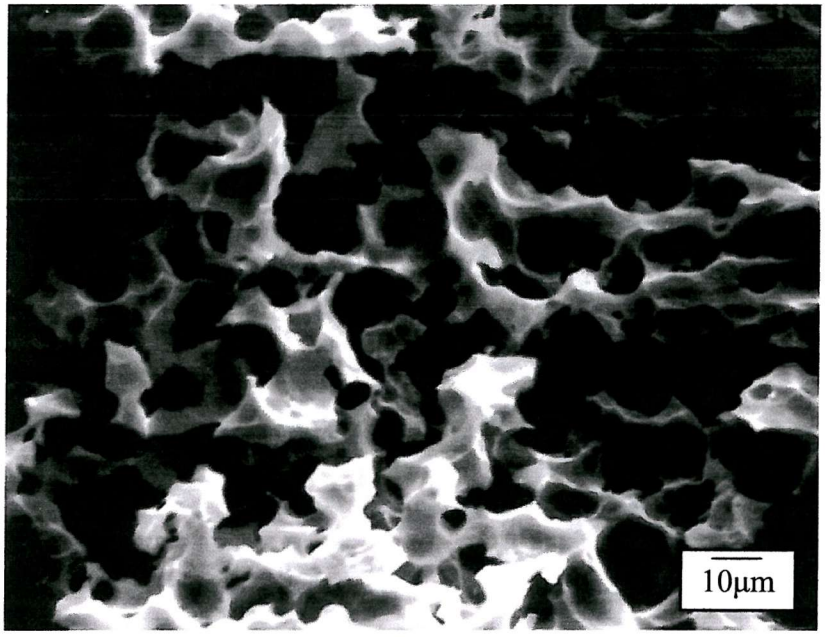

Figure 2.4: SEM micrograph of etched AS1241 lining material, showing recticular distribution of Sn secondary phase.

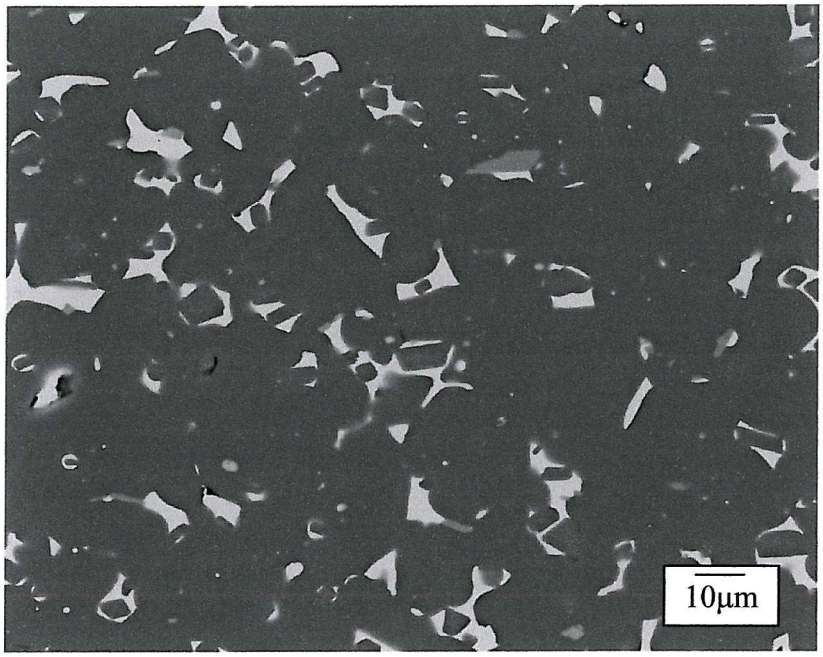

Figure 2.5: Back scattered SEM image of AS1241 microstructure

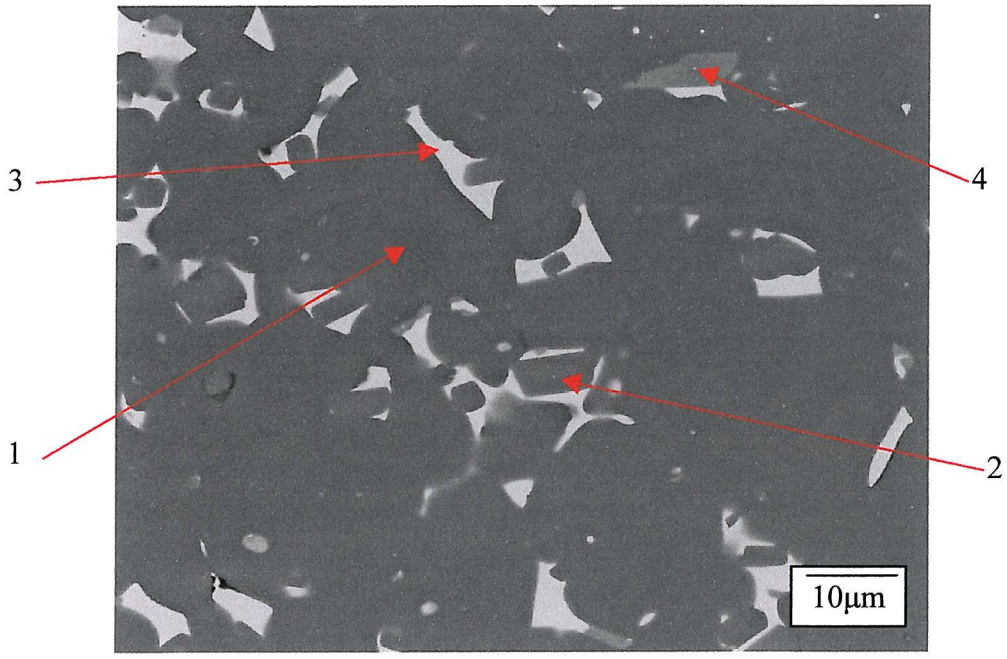

Figure 2.6: Back scattered SEM image of AS1241 microstructure showing EDX spots

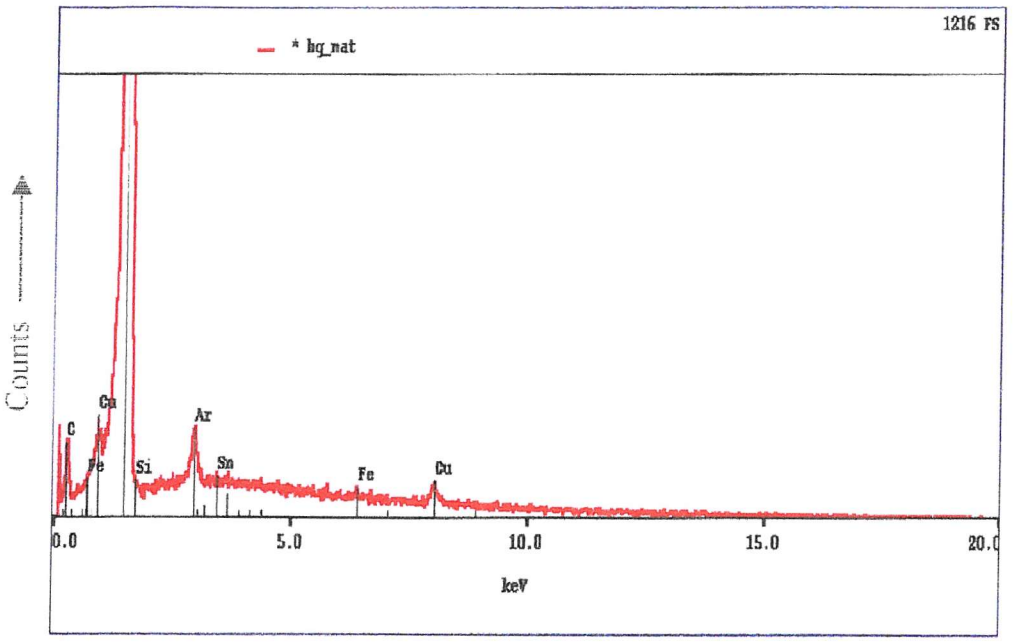

Figure 2.7: EDX spectra 1 (matrix)

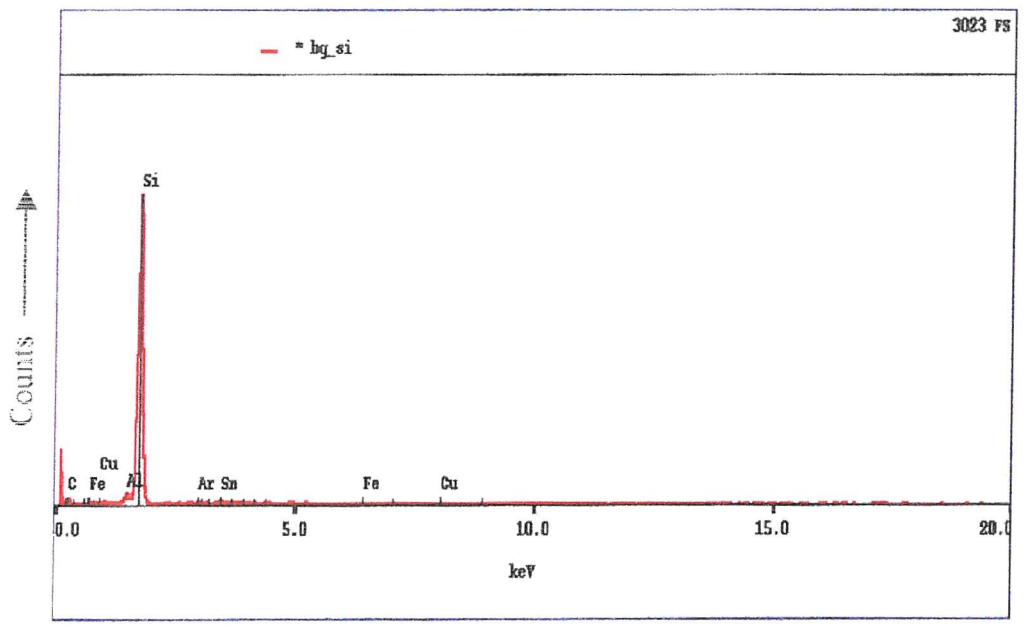

Figure 2.8: EDX spectra 2 (Si secondary phase)

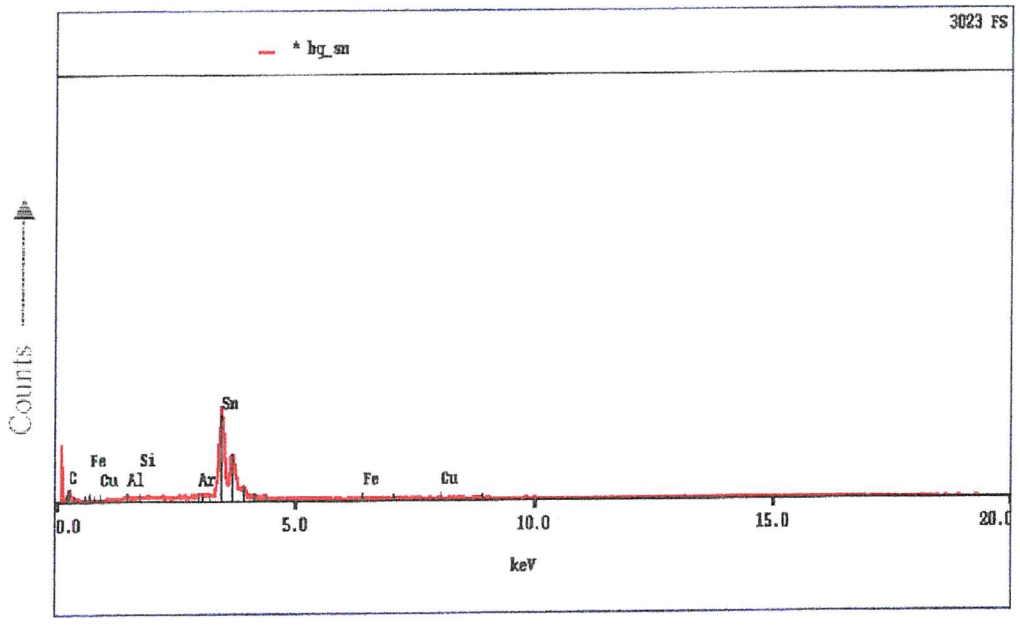

Figure 2.9: EDX spectra 3 (Sn secondary phase)

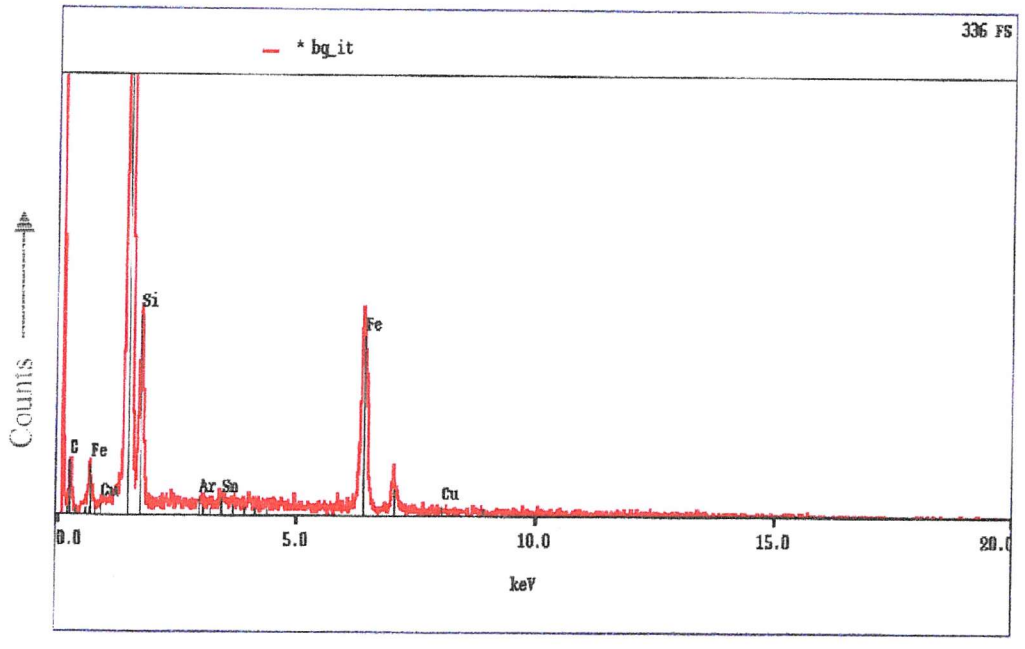

Figure 2.10: EDX spectra 4 (intermetallic particle)

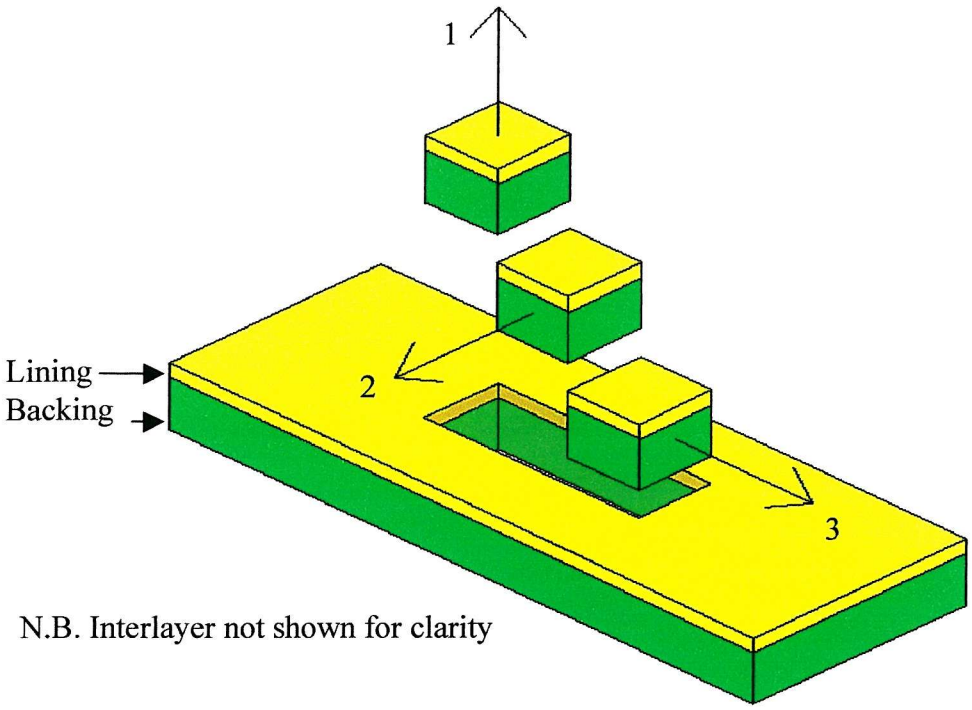

Figure 2.11: Sample orientations. Flat strip shown here, but identical orientations used for bearing and monolithic lining.

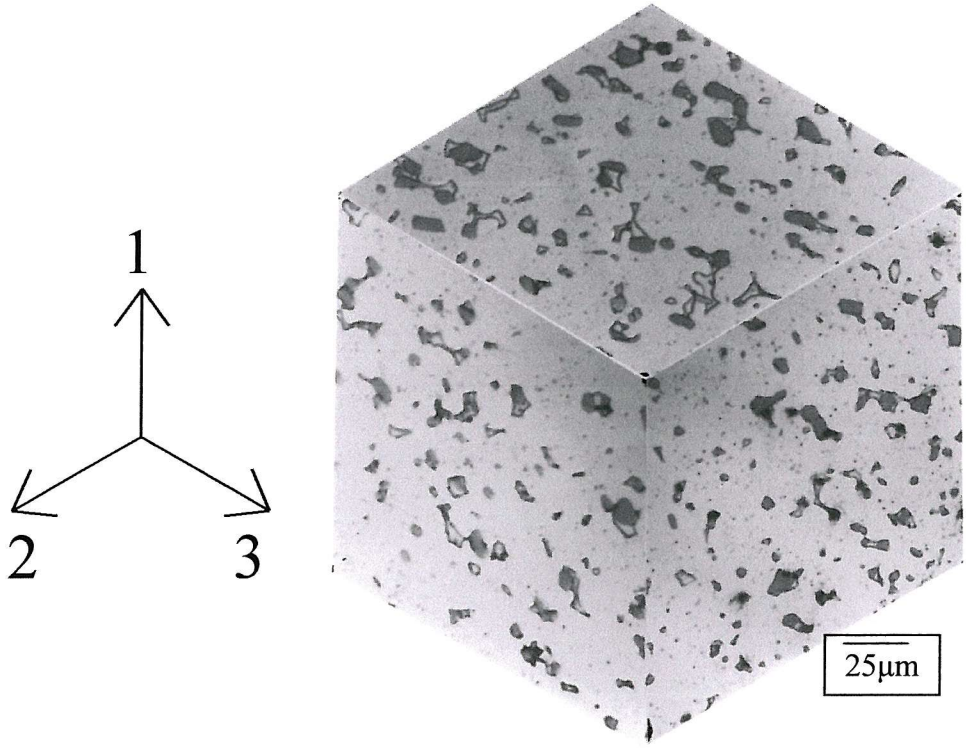

Figure 2.12: Bearing lining microstructure

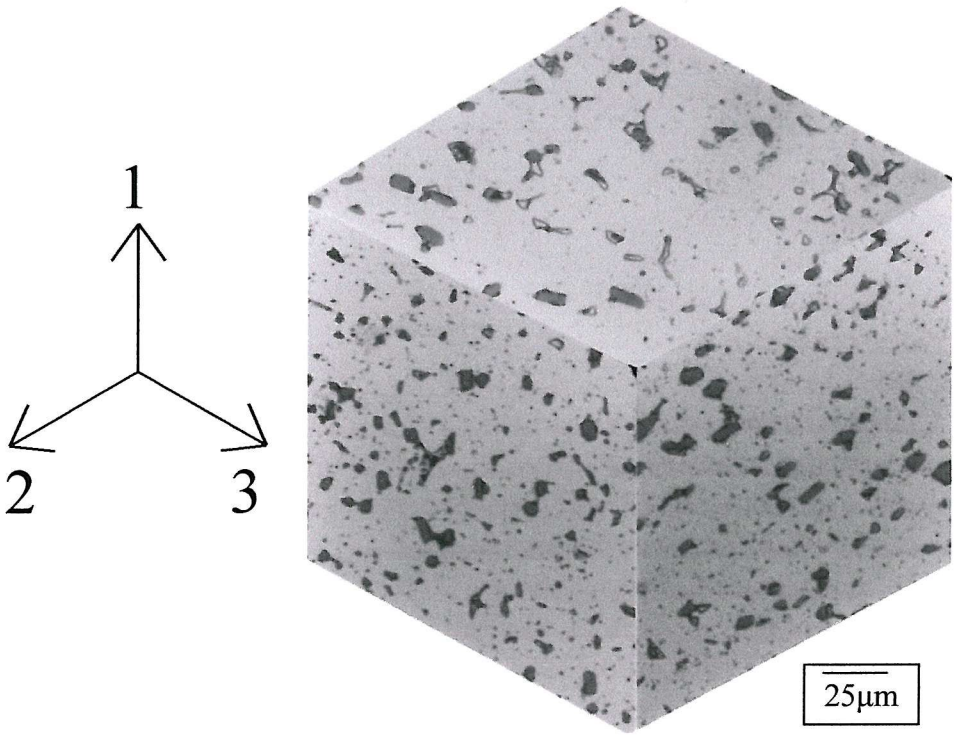

Figure 2.13: Flat strip lining material microstructure

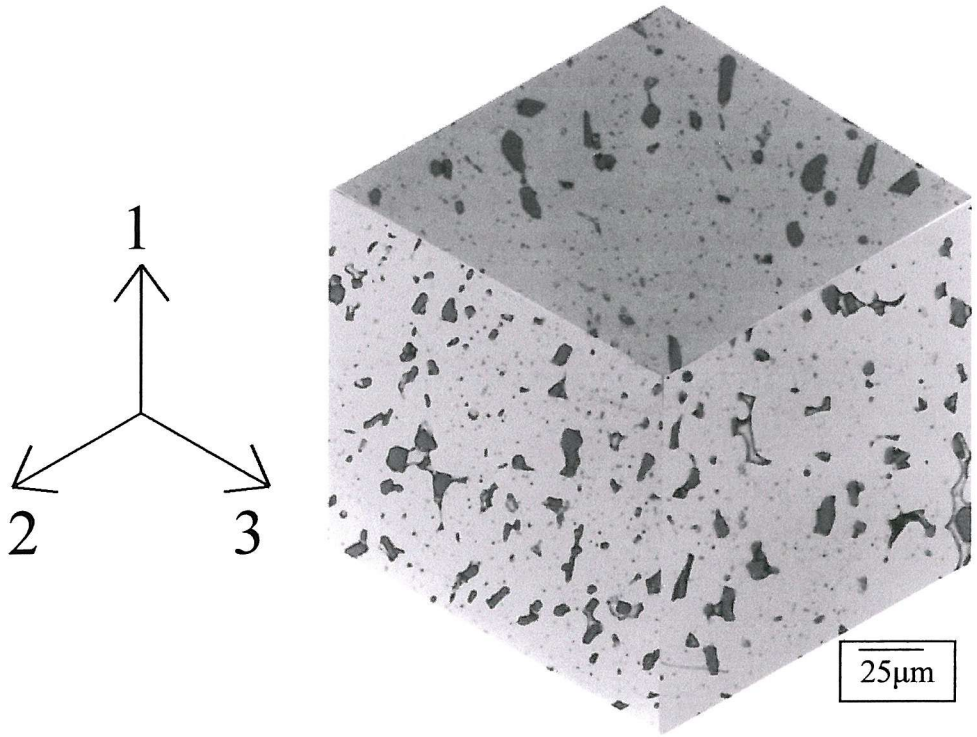

Figure 2.14: Monolithic lining material microstructure

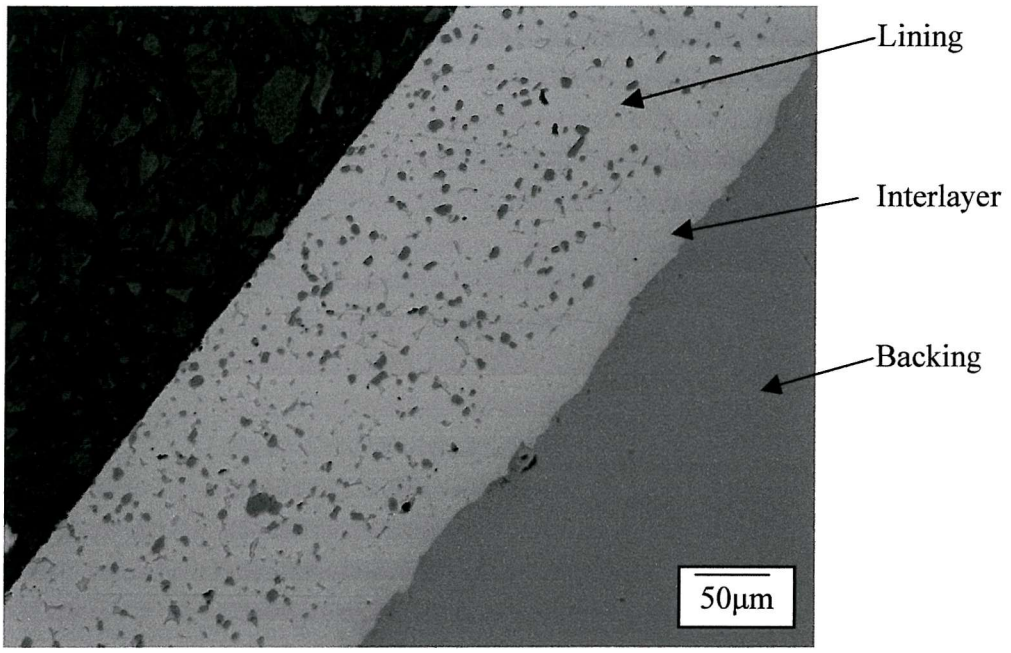

Figure 2.15: Layered structure in finished bearing

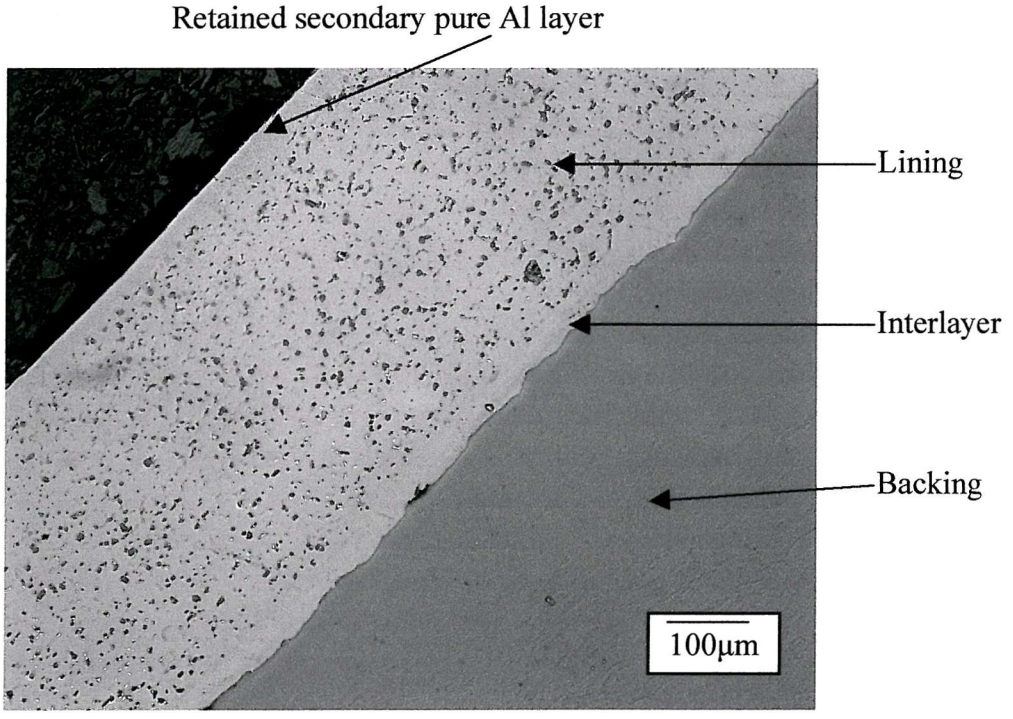

Figure 2.16: Layered structure in flat strip material (note retained Al layer and greater lining thickness)

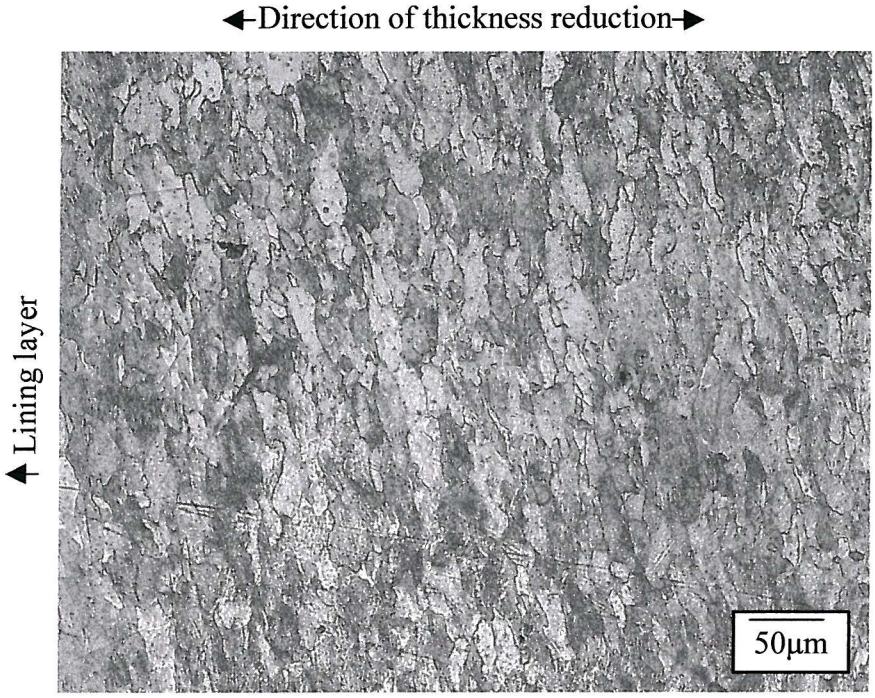

Figure 2.17: Optical micrograph of etched steel microstructure, showing flattened grains, elongated normal to the direction of thickness reduction caused by rolling during manufacture

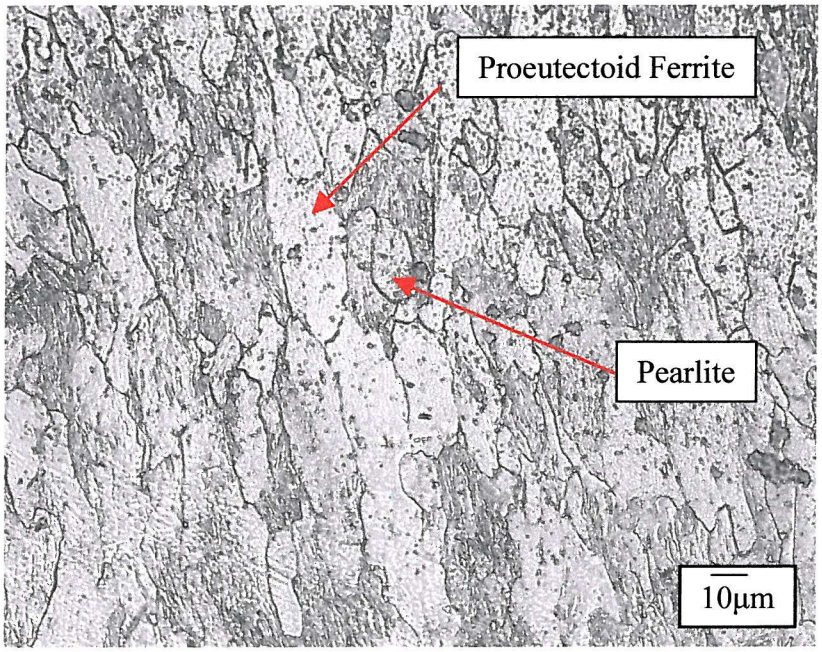

Figure 2.18: Optical micrograph of etched steel showing Ferritic/Pearlitic structure

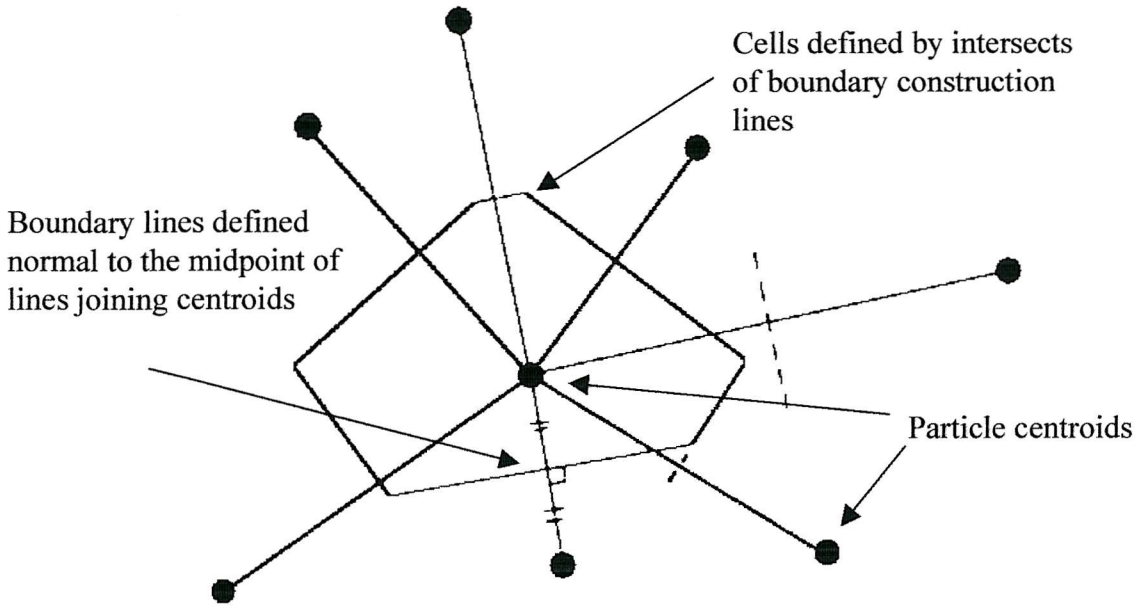

Figure 2.19: Construction of Dirichlet type tessellation

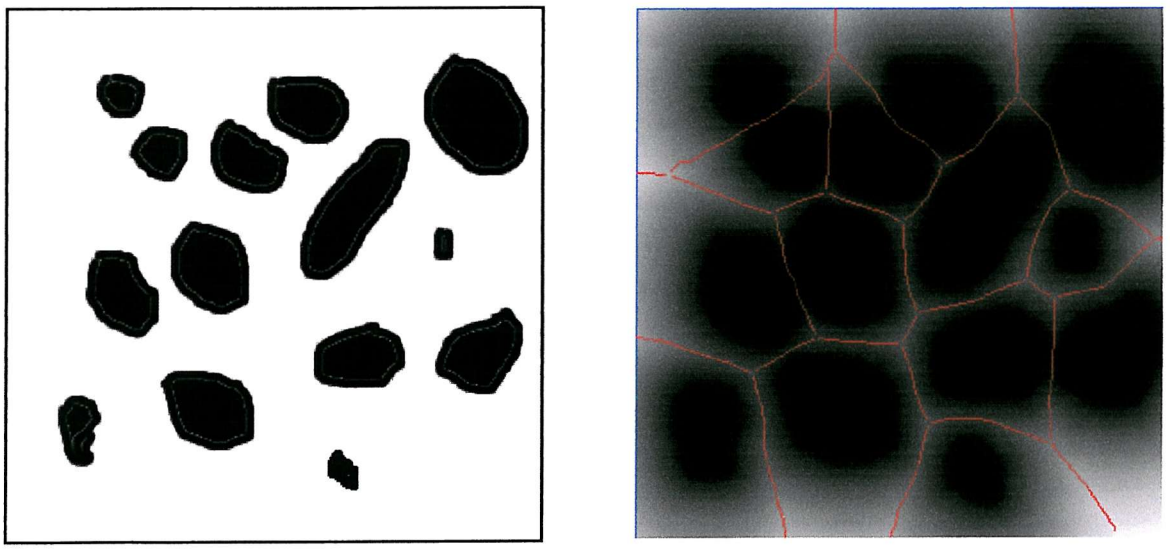

N.B. watersheds shown in red

a) Initial binary image

b) Grey scale distance transformation

Figure 2.20: Initial binary image and water shedding process

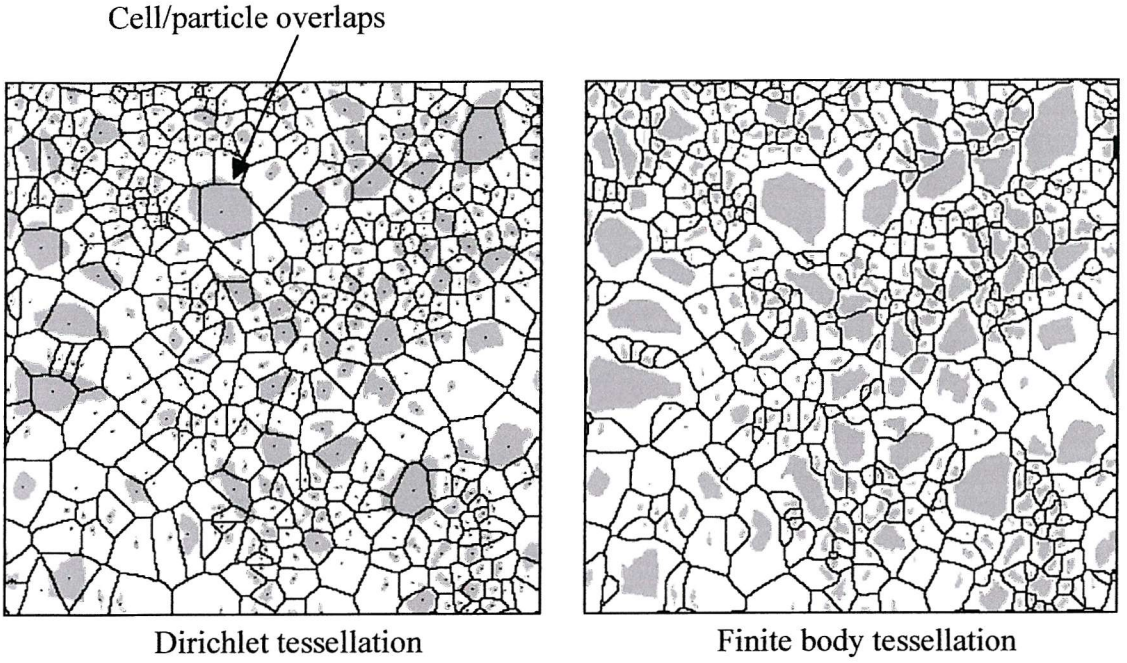

Figure 2.21: Comparison of Dirichlet and finite body tessellations on Al-SiC_p

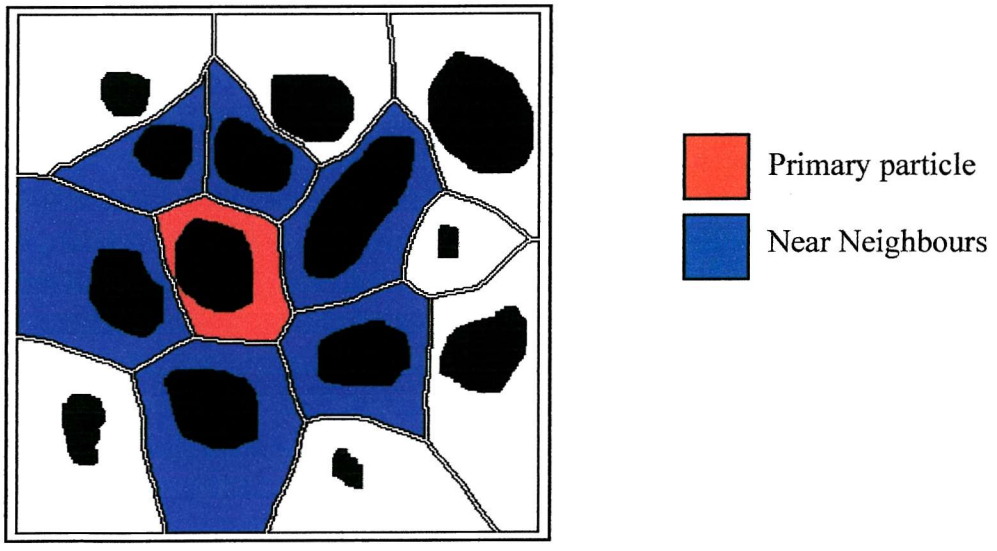

Figure 2.22: Definition of near neighbour cells, i.e. cells sharing a common boundary with the primary cell

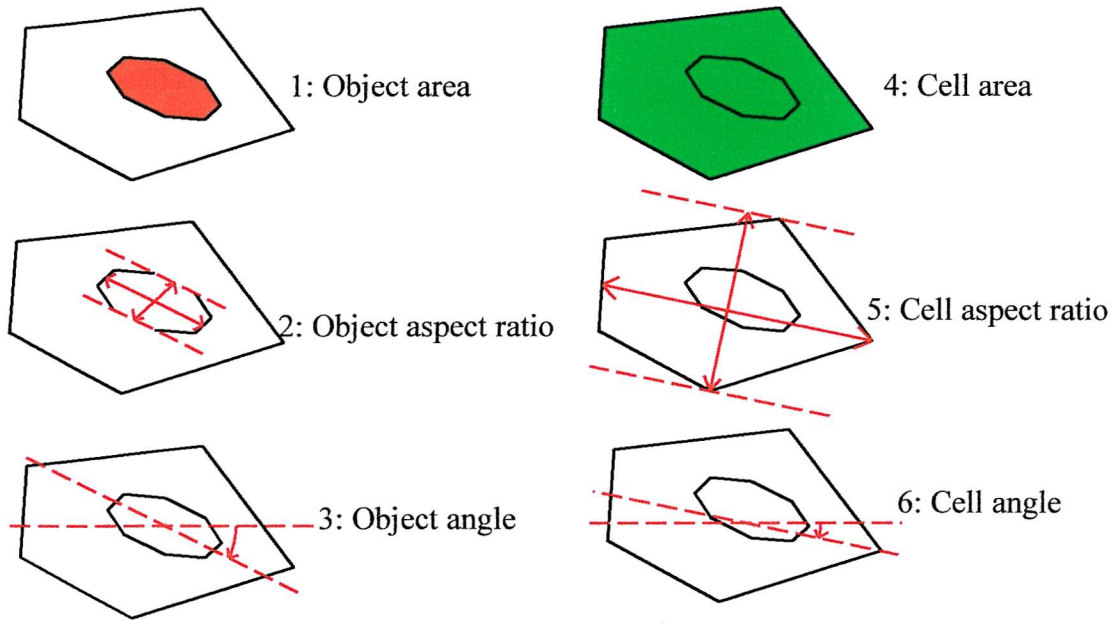

7: Local area fraction = object area (1) /cell area(4)

Figure 2.23: Single cell measures

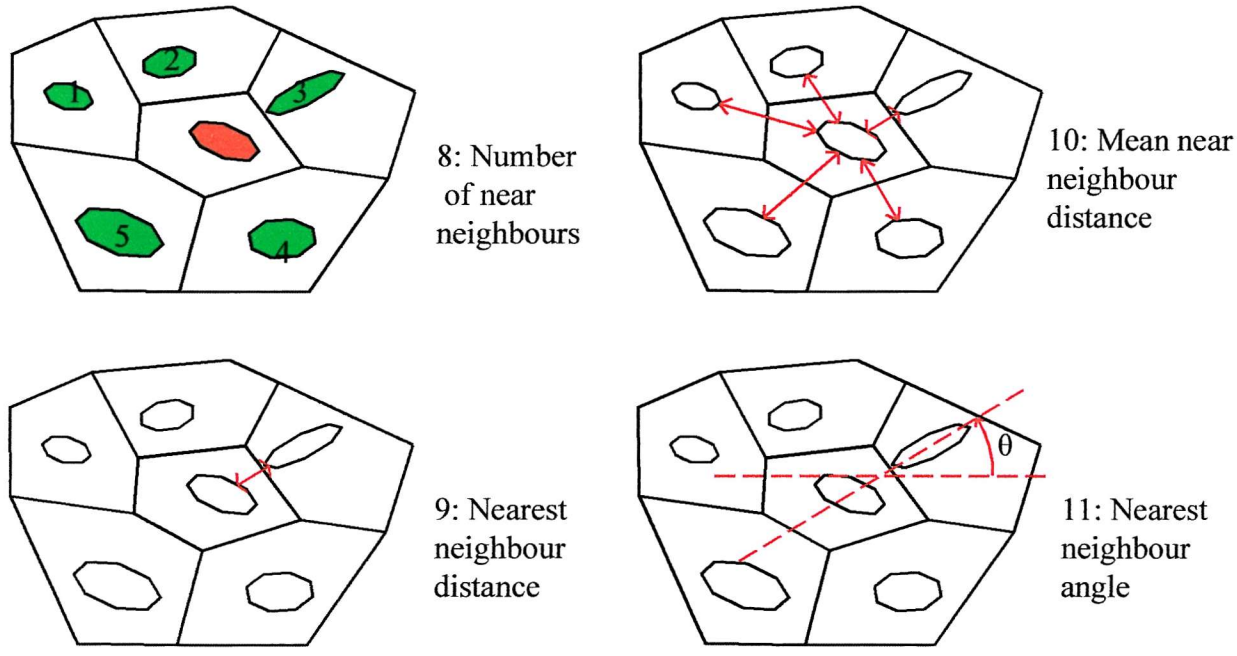

Figure 2.24: Cell and near neighbour measures

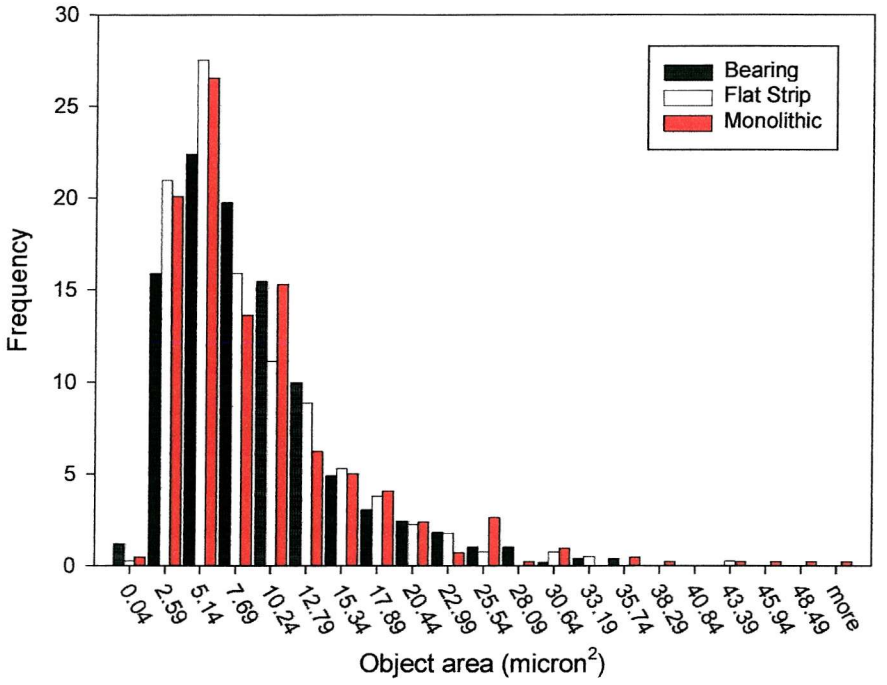

Figure 2.25:Histogram of object area

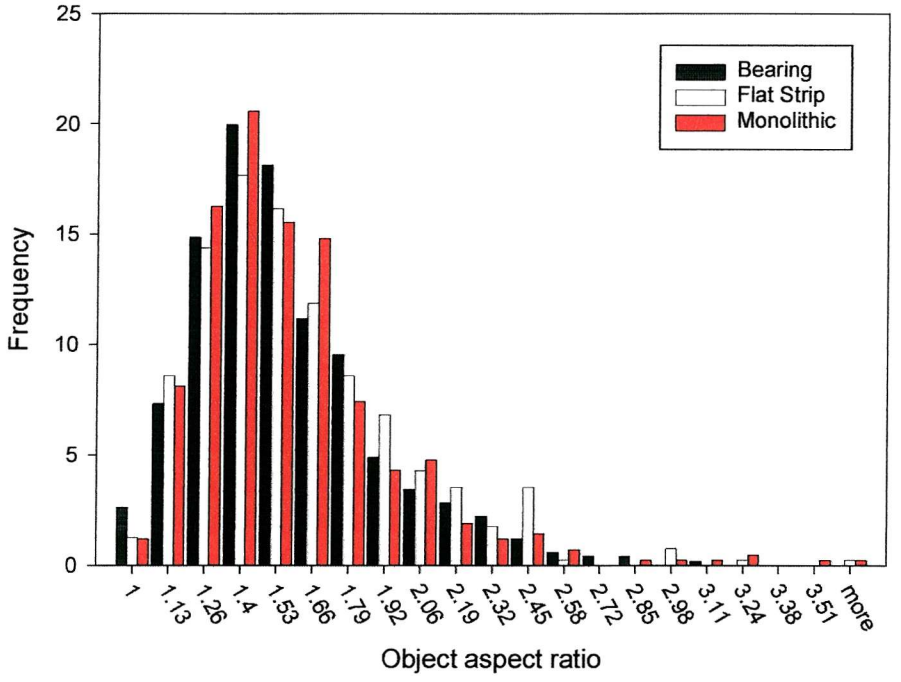

Figure 2.26: Histogram of object aspect ratio

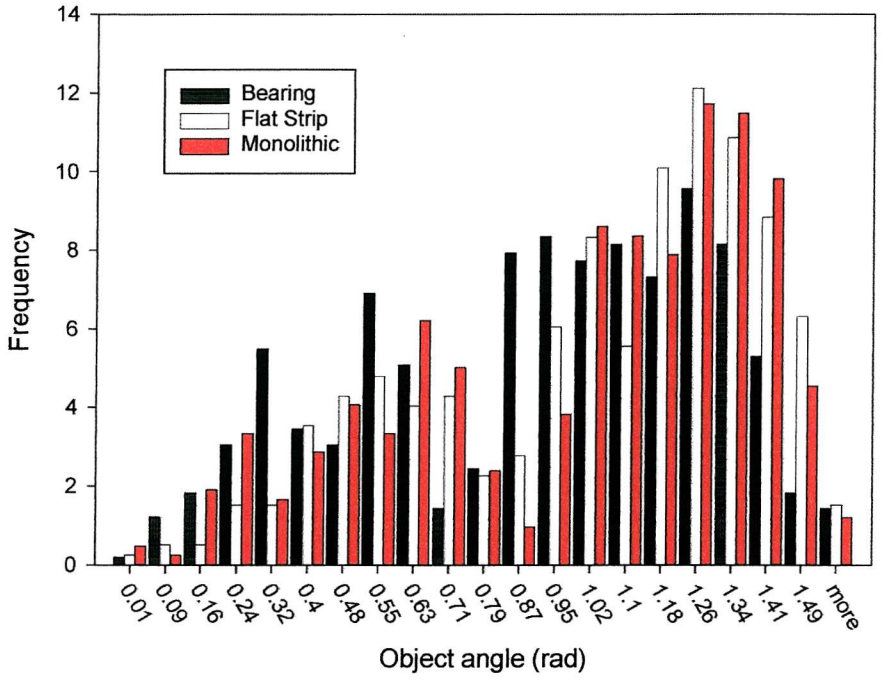

Figure 2.27: Histogram of object angle

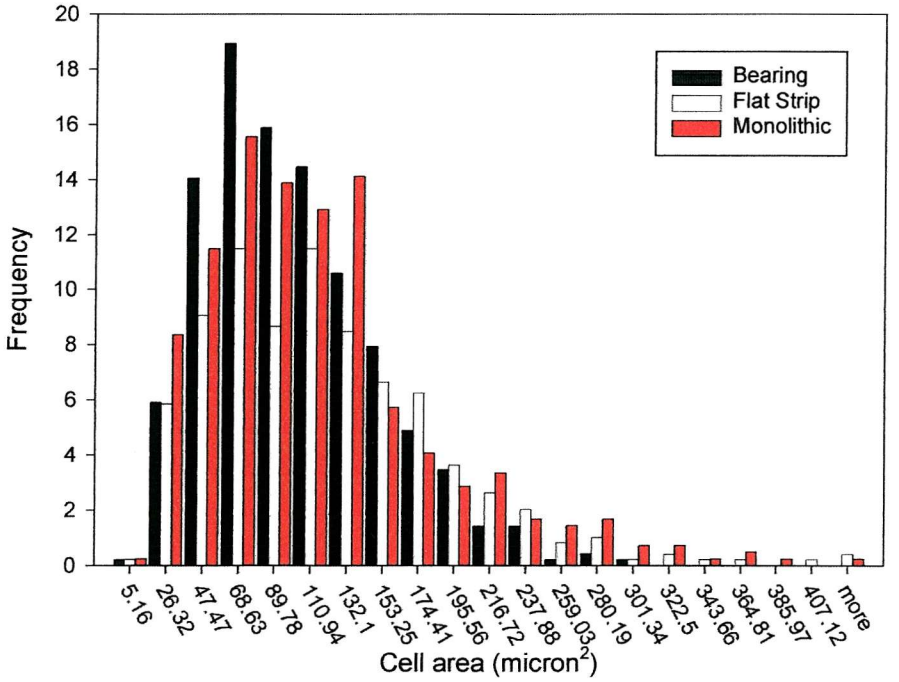

Figure 2.28: Histogram of cell area

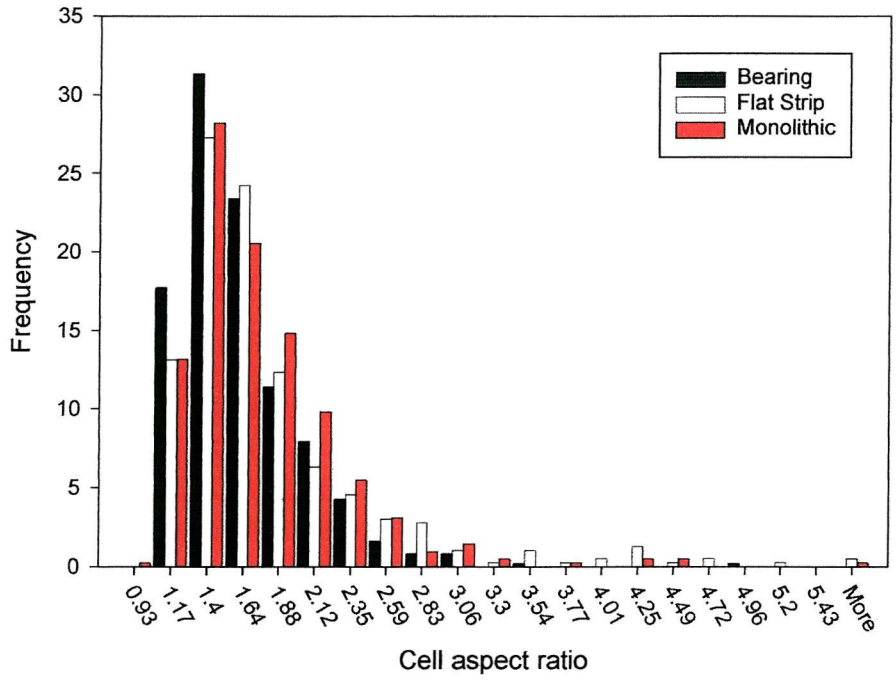

Figure 2.29: Histogram of cell aspect ratio

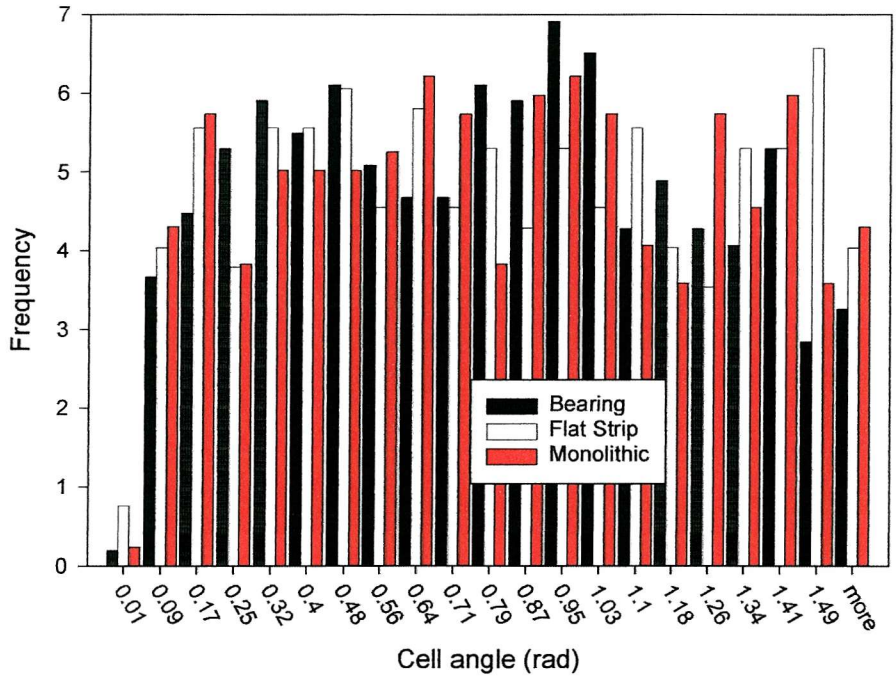

Figure 2.30: Histogram of cell angle

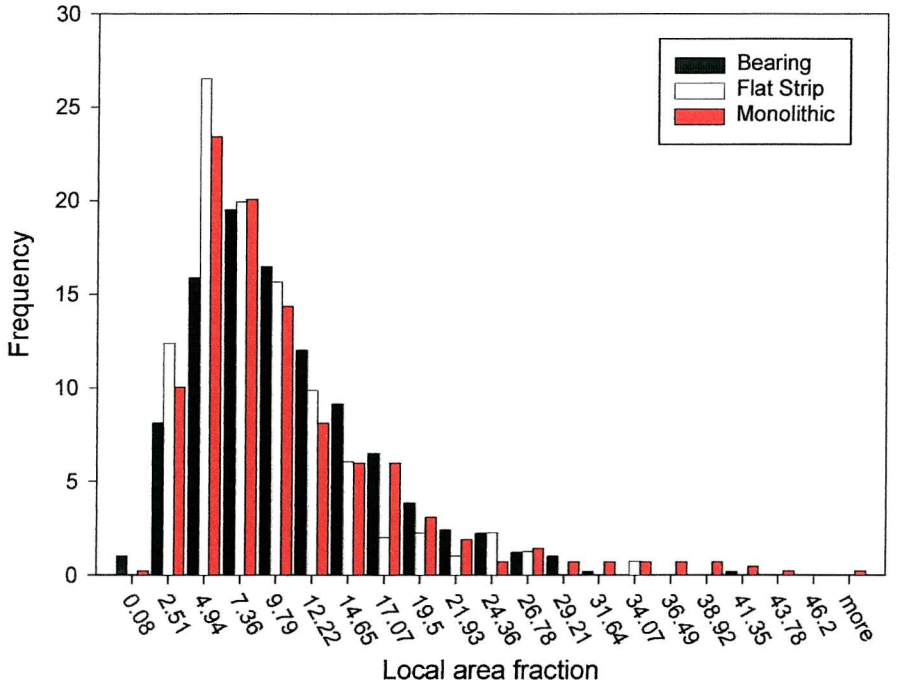

Figure 2.31: Histogram of local area fraction

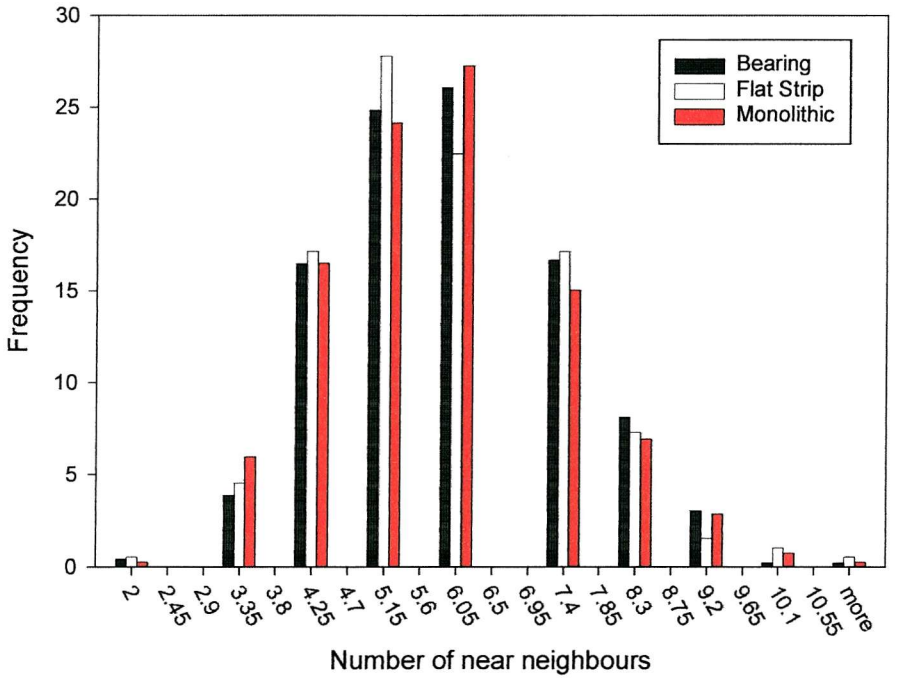

Figure 2.32: Histogram of number of near neighbours

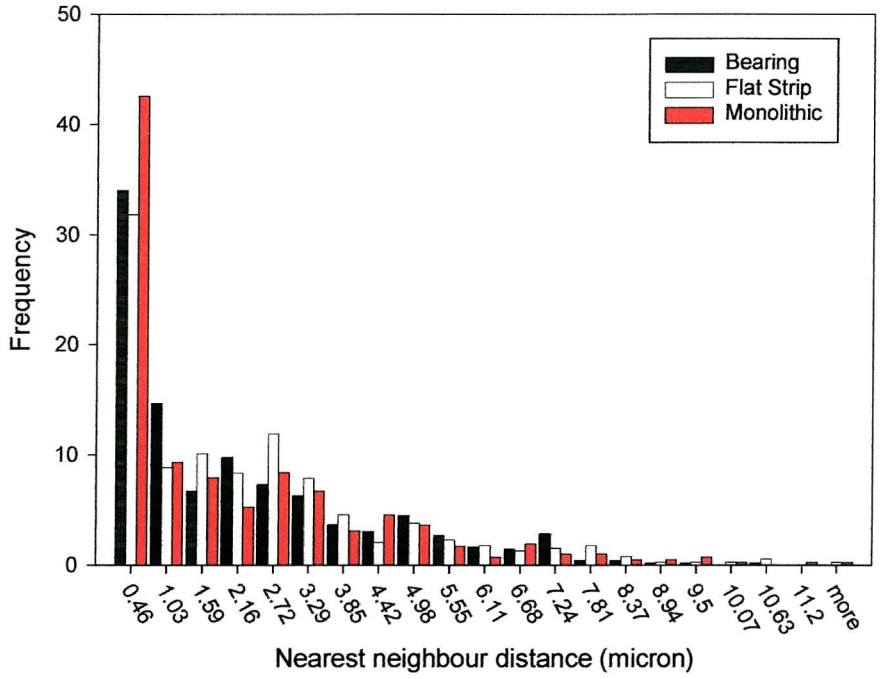

Figure 2.33: Histogram of nearest neighbour distance

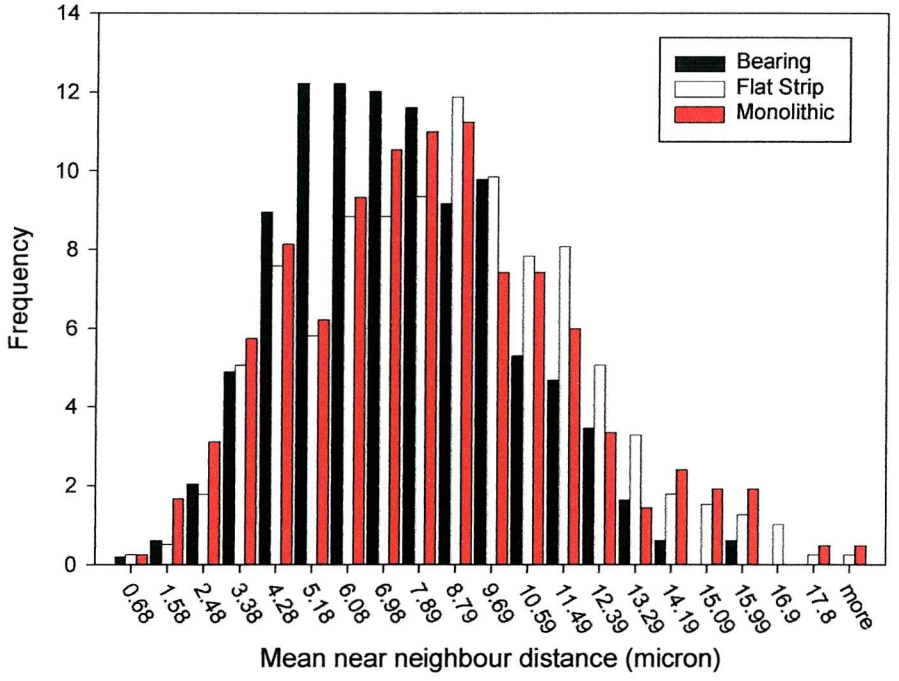

Figure 2.34: Histogram of mean near neighbour distance

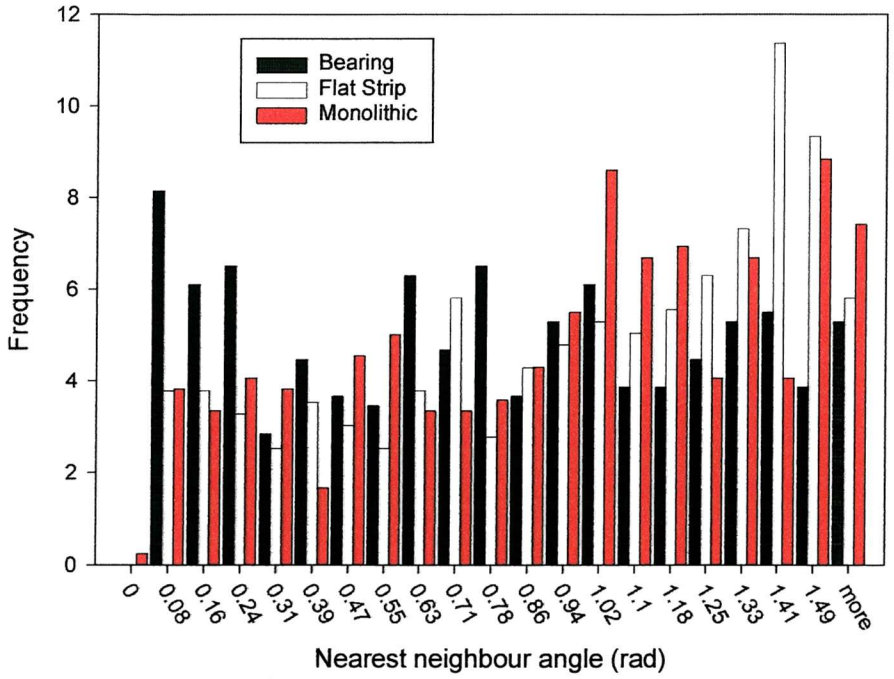

Figure 2.35: Histogram of nearest neighbour angle

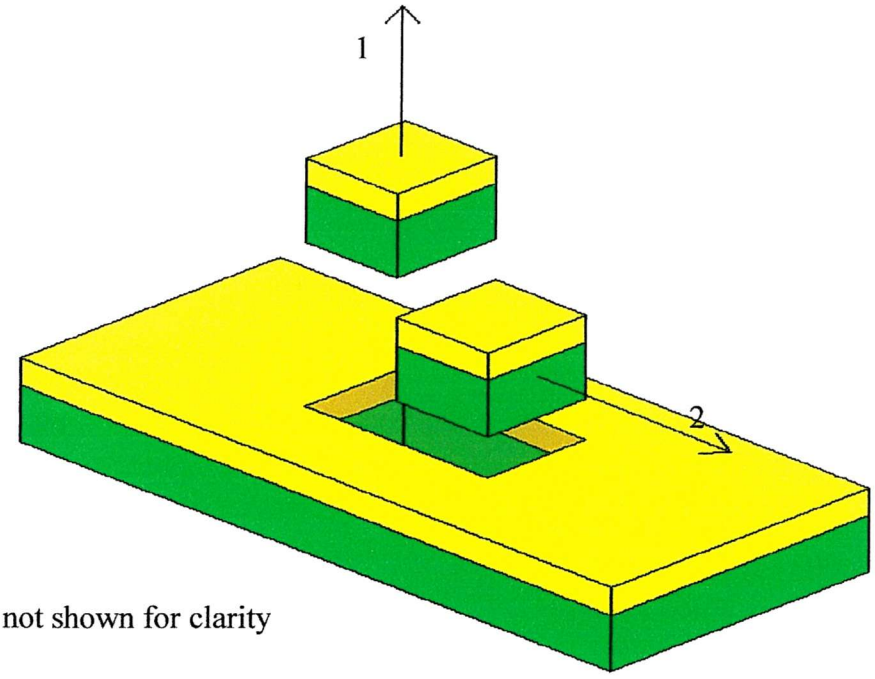

N.B. Interlayer not shown for clarity

Figure 2.36: Sample Orientations for micro-hardness indent tests. Flat strip shown here, similar orientations taken for bearing. Monolithic lining taken in orientation 1 only.

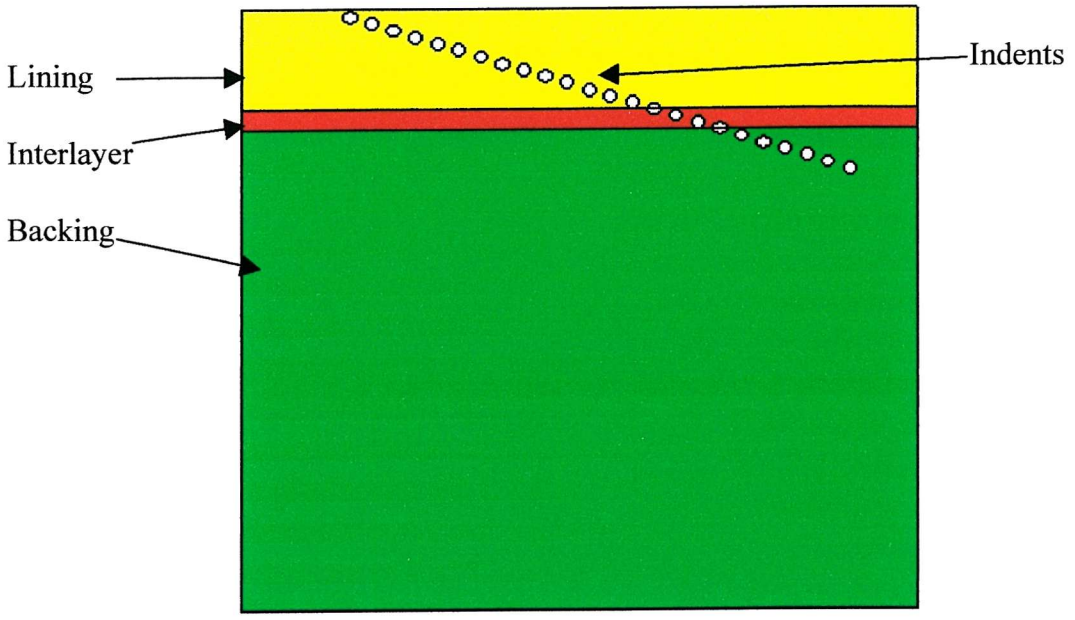

Figure 2.37: Indent locations on through thickness traverses

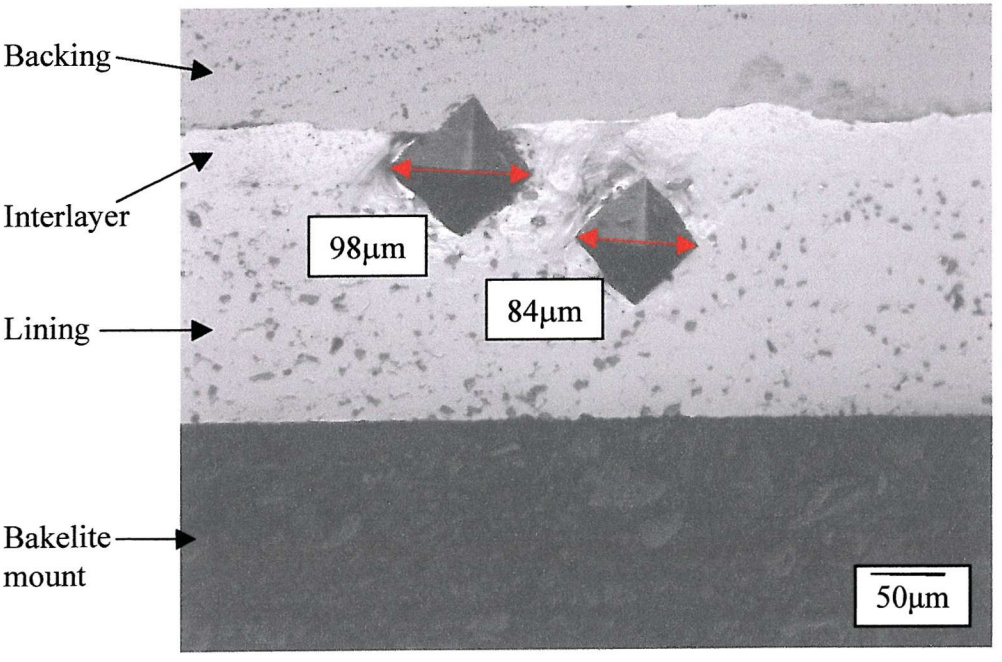

Figure 2.38: Optical micrograph showing the relative size of interlayer and lining micro-hardness indents

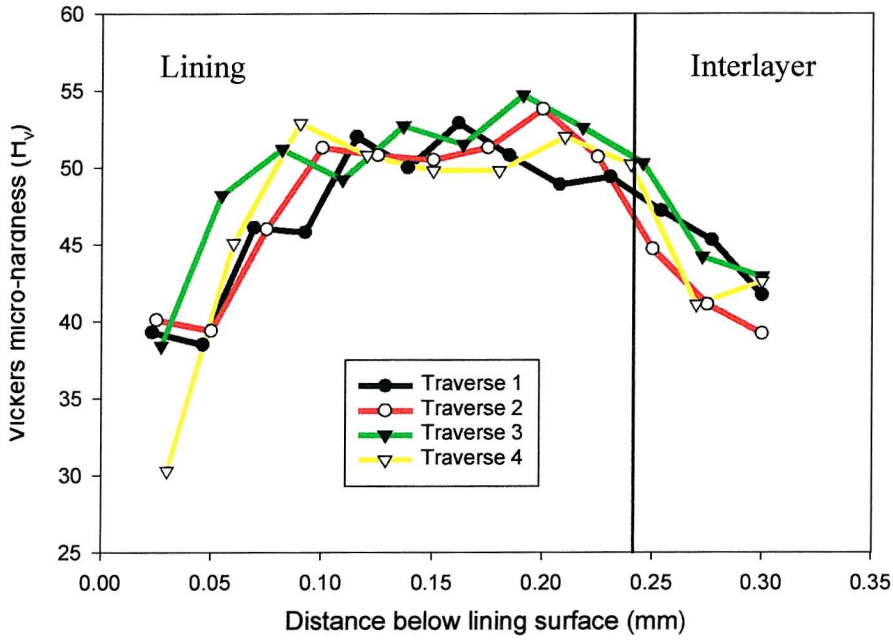

Figure 2.39: Micro-hardness results from traverse across bearing

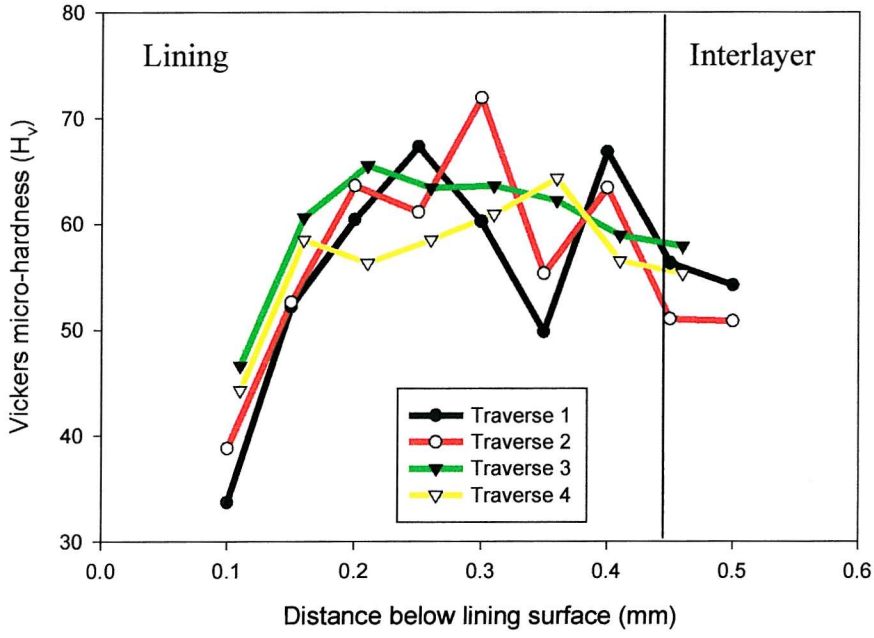

Figure 2.40: Micro-hardness results from traverse across flat strip

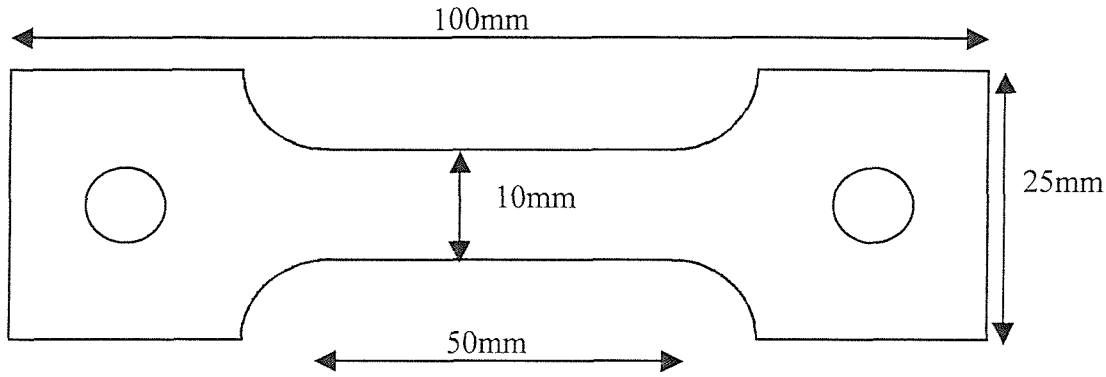

Figure 2.41: Tensile test dog-bone dimensions

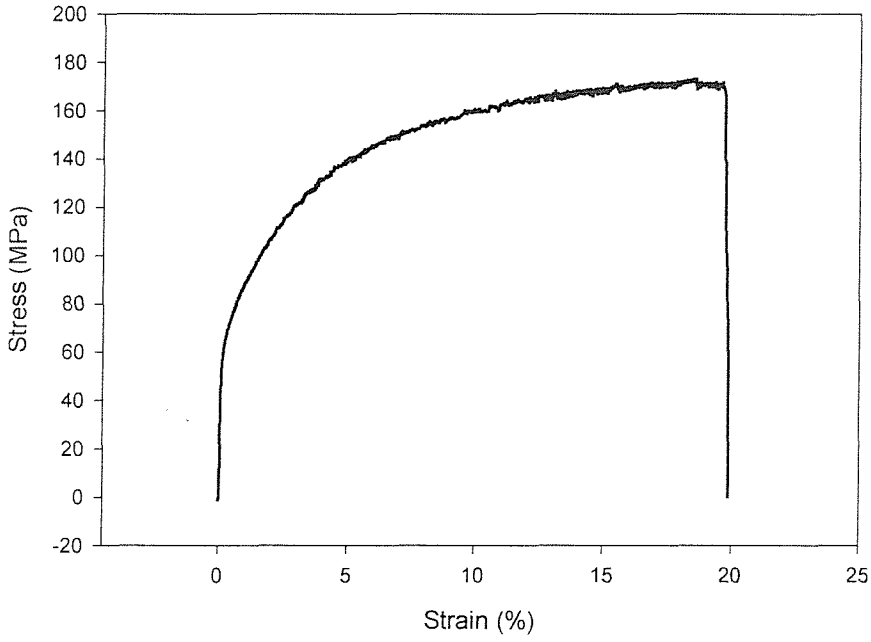

Figure 2.42: Typical tensile stress-strain curve for AS1241

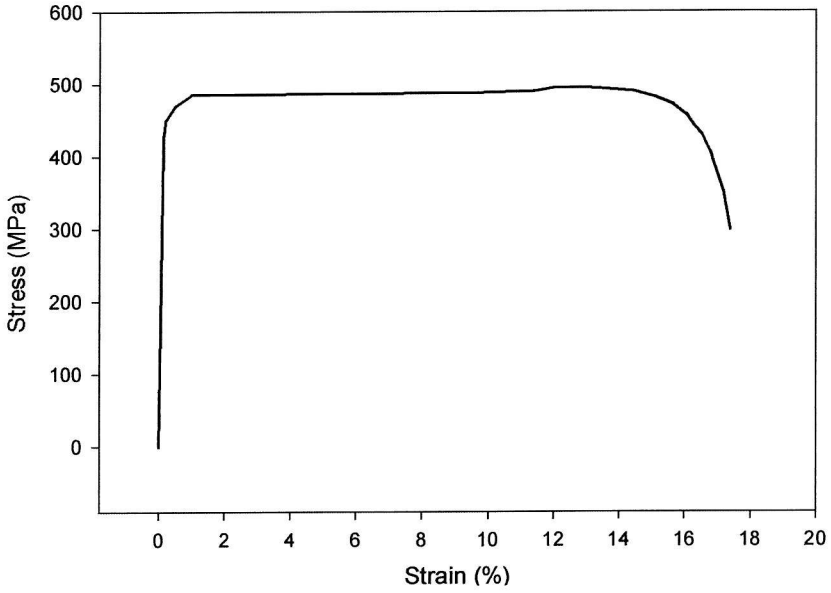

Figure 2.43: Typical tensile stress-strain curve for steel backing material.

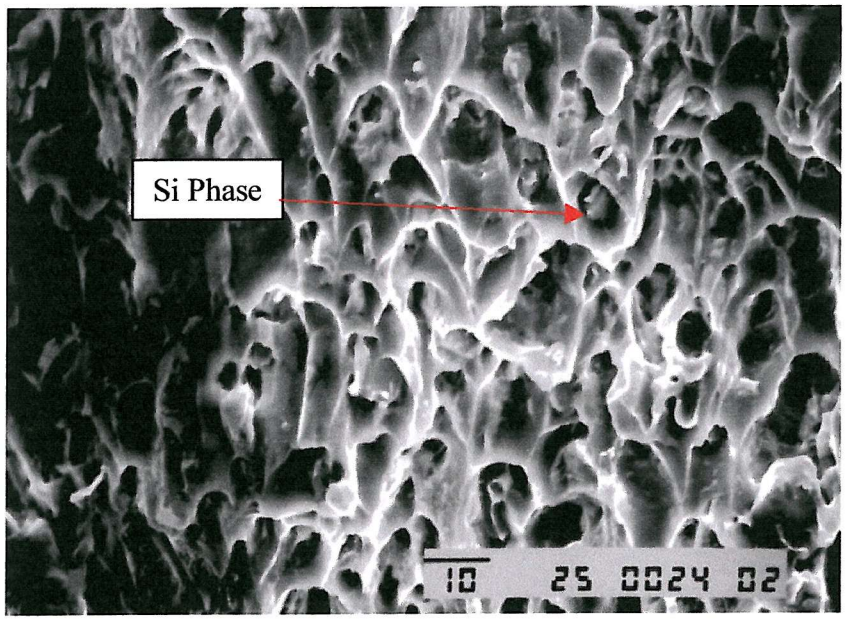

Figure 2.44: SEM micrograph showing tensile test fracture surface

3.0 FATIGUE TESTING OF BEARING MATERIALS

This chapter reports on a series of tests carried out to investigate the fatigue performance of the bearing material system discussed in the previous chapter. Throughout the testing program, no attempt was made to directly replicate the expected in-service loading, environment or constraint conditions. Rather the fundamental fatigue behaviour of the material systems was to be investigated under a series of well characterised stress states and environmental conditions. The test matrix comprised several test types:

- Centre cracked tension (CCT) fatigue tests, performed in ambient conditions, using thin sheet samples of monolithic lining material.
- Uninterrupted run out bending fatigue tests on finished bearings.
- Ambient environment short crack fatigue tests, performed in bend on flat strip samples.
- Short crack fatigue bend tests, performed on flat strip samples *in vacuo* and in an oil environment.

3.1 Long Crack CCT Tests

Long crack CCT tests were carried out to establish a baseline understanding of fatigue crack propagation behaviour with which to compare the future short crack results. Specimens were manufactured from the monolithic lining material supplied by the sponsoring company. The monolithic lining material was in short supply and of poor quality, restricting the CCT testing to a limited number of tests on small specimens having dimensions 180 mm by 60 mm. The small specimen size coupled with the material's extreme thinness (~0.5 mm) and low yield stress (56.6 MPa), resulted in the calculated crack tip plastic zones being very large. This in turn meant that insufficient material existed to allow the full da/dN-ΔK growth out curve to be established under constant load conditions in one CCT sample without violating the LEFM conditions given in Eqn 3.1.

$$(W-2a) \geq 1.25\left(\frac{P_{max}}{B\sigma_y}\right) \quad (3.1)$$

The tests were carried out using a 50kN Instron 8502 servo-hydraulic fatigue testing machine at a frequency of 10 Hz, a load ratio of 0.1 and using the Direct Current Potential Drop technique for crack monitoring, as shown in Figure 3.1. A hole and slot type notch, as shown in the magnified section of Figure 3.1, was made at the centre of each sample. This was extended by pre-cracking at ΔK = 3 MPa$\sqrt{m}$ to an overall crack length ($2a$) of 15 mm. The load was then raised incrementally, to increase ΔK in 1 MPa$\sqrt{m}$ steps after 1 mm of crack growth at each ΔK range, as shown in Table 3.1.

After failure the sample fracture surface was examined both optically and using a Jeol JSM-T300 scanning electron microscope (SEM) at an accelerating voltage of 25kV.

Table 3.1: loading levels used in CCT test

Increment	Load range (KN)	Initial ΔK (MPa$\sqrt{m}$)	Final ΔK (MPa$\sqrt{m}$)
1	0.60	3.13	3.34
2	0.70	4.01	4.38
3	0.80	4.99	5.24
4	0.92	6.02	6.44
5	1.00	6.96	7.40
6	1.08	7.97	8.48
7	1.14	8.98	9.52

3.2 Bearing Tests

A series of tests were performed on the as supplied plain bearings, to establish a fatigue life curve. These tests were carried out in a three point bend loading geometry, using a steel block to constrain the ends of the bearing, as shown in Figure 3.2. Since a large number of tests were anticipated, the use of a rig ensured an identical test set up for each sample.

The tests were carried out using a 50kN Instron 8501, at 10Hz with a load ratio of 0.1. Calculating the maximum lining stress for a given load is not a trivial task for this test geometry, therefore this was evaluated using an elasto-plastic finite

element (FE) model described in Appendix I. An initial sample was tested under an incrementally increasing load to establish a stress level at which fatigue cracks would initiate. Starting at a load calculated to give a maximum stress of $0.9\sigma_y$ (51 MPa) on the surface of the lining material, the test was allowed to run for 100,000 cycles; if no visible cracks were evident, the load was increased, to give a 10% increase in top surface stress and the test restarted. The loading regime for this initial test is given in Table 3.2. Cracks were visible on the surface of the lining material after the final load increment.

Table 3.2: Incremental loading regime for initial bearing test

Test increment	Max Load (KN)	Max lining stress (MPa)	Behaviour observed
1	0.46	51	no cracking
2	0.52	56.1	no cracking
3	0.60	61.7	no cracking
4	0.71	67.9	no cracking
5	0.91	74.7	no cracking
6	1.3	82.1	no cracking
7	1.7	90.3	no cracking
8	2.0	99.4	no cracking
9	2.2	109.3	small cracks

In order to establish sample fatigue life under various stress levels, a series of uninterrupted run out tests were carried out. To ensure that all these tests were terminated at a similar amount of fatigue damage, a failure criterion was required. Due to both the lining surface roughness and the large number of tests, acetate replication was not suitable for crack monitoring, rather a compliance method was employed. The actuator displacement at maximum load was recorded throughout the test, when this value had increased by 0.3 mm, the sample was deemed to have reached a failure point. Use of this criterion led to the tests being stopped when the samples contained visible cracks, but considerably before gross bearing failure. The test matrix comprised 18 tests and is given in Table 3.3.

Table 3.3: Bearing test matrix

Test No.	Maximum load (KN)	Maximum lining stress (MPa)	Fraction of lining UTS (%)
BT1	1.2	80.69	46.4
BT2	1.3	82.38	47.4
BT3	1.4	83.96	48.3
BT4	1.5	85.62	49.2
BT5	1.6	87.56	50.4
BT6	1.7	89.79	51.6
BT7	1.8	92.09	53.0
BT8	1.9	95.07	54.7
BT9	2.0	98.49	56.6
BT10	2.1	102.78	59.1
BT11	2.2	107.68	61.9
BT12	2.3	112.34	64.6
BT13	2.4	117.87	67.8
BT14	2.5	123.39	71.0
BT15	2.6	129.23	74.3
BT16	2.7	136.02	78.2
BT17	2.8	143.61	82.6
BT18	2.9	154.28	88.7

Post failure sectioning studies were carried out on failed samples to investigate the sub-surface behaviour caused by increased loading.

3.3 Short Crack Fatigue Test Methodology and Configuration

The behaviour of short fatigue cracks is of key importance, since long crack type behaviour is unlikely to be established before sample failure, due to the small size of the tested bearings. A program of bend fatigue tests was carried out to investigate the influence of the lining material microstructure on fatigue crack initiation and early growth behaviour. The first part of the test matrix was designed to establish a reliable test method to evaluate crack initiation and early growth behaviour. The following criteria were required:

• High surface finish must be achievable easily – Since acetate replication was to be used for crack monitoring, the microstructure must be clearly identifiable. Also since many tests were to be carried out it was preferable to automate this polishing process.

• Short test duration (~200,000 cycles) – Due to the number of tests required, and the time-consuming nature of the replication technique, short duration tests were required.

• Reasonable number of cracks – Ideally cracks should be constrained to a small region to allow reliable identification through the replica record.

• Load level within machine operating parameters. – Due to the small sample size low loads were anticipated, but it was important that they be within the Instron 8501/8502 servohydraulic's load range.

• Repeatable failure criterion.

• All short crack tests to be carried out using Instron 8501/8502 servo-hydraulics with a load ratio of 0.1 and at a frequency of 10 Hz - To allow comparison of results with baseline fatigue data established via the long crack CCT tests.

Ideally these tests would have been carried out on actual bearings, however, it was impossible to consistently achieve the quality of finish required on a curved specimen, and hence attention moved to the flat strip material.

Bend bar type specimens of dimensions 80 mm by 20 mm were produced from the flat strip material. The corners of these were bevelled off to aid the polishing process. The surface of the lining material was then ground back to remove the retained secondary interlayer and reduce the lining thickness to that of a finished bearing (~0.25 mm). This surface was then polished using the route described in Table 2.5, to ensure a good surface for replication. Since it was anticipated that a large number of specimens would be required for the testing program and to ensure repeatability, an automatic polishing jig ,shown in Figure 3.3, was manufactured.

These samples were tested in four point bend, to give a nominal constant stress field on the top surface within the centre span, using a loading span of 10 mm and a centre span of 20 mm as shown in Figure 3.4. The maximum top surface stress for a given loading was calculated by an elasto-plastic finite element model, the development of which is described in Appendix I.

In order for acetate replication to be used, the tests must be of reasonably short duration (~200,000 cycles). To establish a loading regime under which fatigue cracks would initiate and grow within this duration, a sample was tested under an incrementally increasing load in the same manner as the initial bearing test, although starting at a considerably higher initial stress. After cracks had been observed, a repeat test was performed at the maximum load increment to confirm that visible cracks were evident within the 200,000 cycle test window. It was seen that the region of high stress and hence likely crack initiation in four point bend is very large, and it was felt that this would make the analysis of any single crack through the replica

record very difficult. For this reason subsequent tests were performed using a three point bend loading geometry, shown in Figure 3.5, using a loading span of 25mm. In this geometry the peak stress is concentrated along a line directly above the central roller, thus reducing the area over which cracks may be expected to initiate when compared to a four point bend loading geometry. A further test was carried out to ensure that visible fatigue cracks were evident within the required number of cycles using this revised loading geometry. As this was the case, the remainder of the tests were carried out in three point bend. The loading and stress levels for these tests are given in Table 3.4.

Based on the behaviour of the initial three point bend test, a compliance failure criterion was defined in a similar manner to that used in the bearing tests. Failure was deemed to have occurred when the actuator displacement at maximum load had increased from its initial value by 0.5 mm. A higher value is used to define the failure of flat strip tests compared to the bearings, since the flat strip test method is more compliant than the bearing rig. A deflection increase of 0.5mm in a flat strip sample was found to correspond to a similar amount of fatigue cracking as that required to give a 0.3mm deflection increase in a bearing sample.

Table 3.4: Test regime for bend bars during identification of loading regime

Sample no.	Loading geometry	Max lining stress (MPa)	Fraction of UTS (%)	Cycles at this stress	Behaviour observed
FST1	4 – Point bend	82.6	47.5	100000	no cracking
		83.2	47.8	100000	no cracking
		84.6	48.6	100000	no cracking
		86.8	49.9	100000	no cracking
		88.7	51.0	100000	no cracking
		92.3	53.1	100000	no cracking
		95.0	54.6	100000	no cracking
		99.2	57.0	100000	no cracking
		105.2	60.5	74965	small cracks
FST2	4 – Point bend	105.2	60.5	200000	small cracks
FST3	3 – Point bend	105.3	60.6	200000	small cracks

3.4 Short Crack Fatigue Tests

A series of detailed short crack fatigue tests were carried out, to investigate the influence of the lining material microstructure on the initiation and early growth behaviour of small fatigue cracks. Tests were carried out on highly polished samples in ambient, vacuum and oil environments. The configuration for all flat strip short crack fatigue tests is given in Table 3.5. The ambient and vacuum tests were carried out using a 50kN Instron 8501, whilst due to the size of the rig, the oil tests used a larger 50kN Instron 8502 servo-hydraulic fatigue testing machine.

Table 3.5: Short crack fatigue test configuration

Loading geometry	Three point bend
Maximum lining stress	105.3 MPa
R- ratio	0.1
Span	25 mm
Frequency	10 Hz
Failure criterion	0.5 mm increase in deflection at maximum load

3.4.1 Ambient short crack fatigue tests

After a successful run-out test without interruption to establish likely sample lifetime, detailed tests were performed, with acetate replicas being taken every 1000 cycles to give a series of "snap shots" of fatigue crack initiation and growth on the specimen surface. After testing, these replicas and the top surface of the failed samples were examined using optical and SE microscopy. To allow investigation of the subsurface crack behaviour, samples were sectioned, polished and examined, again using optical and SE microscopy.

3.4.2 *In vacuo* short crack fatigue tests

Vacuum tests were carried out to investigate the effect of having an inert environment at the crack tip. These tests were carried out in an ESH environmental chamber attached to a 50kN Instron 8501 servo hydraulic fatigue testing machine. The chamber is equipped with both rotary and turbomolecular pumps, and reliably produces a vacuum level of $1.5e^{-5}$ mbar or lower at room temperature. In addition the chamber is fitted with quartz lamps capable of raising the sample temperature up to 1000 degrees Celsius, although in this program all tests were carried out at room temperature.

No attempt to monitor fatigue crack growth by replication was made during these tests, hence only fatigue lifetimes and post test observations were obtained.

3.4.3 Oil environment short crack fatigue tests

Since in service the bearing surface is not exposed to the air, but submerged in oil, several tests were performed to investigate the effect of an oil environment on fatigue crack behaviour. The oil used was Shell Rotella X 10W. This is typically used in low to medium output diesel engines, and is also used by the sponsoring company in all of their bearing accelerated test rigs. Rotella oils are paraffin based, and available in various viscosities, the 10W version used in these tests has a kinematic viscosity of 43.18 cSt and a density of 876kgm^{-3} at 40 °C.

Unlike the vacuum tests, these tests were interrupted and monitored using acetate replicas. Thus when the test rig was designed, provision had to be made to remove the oil from the test piece and allow replication of the specimen surface. A schematic of the rig is shown in Figure 3.6, demonstrating how the oil may be moved from the test chamber to a remote reservoir by adjusting their relative positions.

An uninterrupted test was run to a compliance failure condition, to establish a sample lifetime, and hence a replication schedule. A second interrupted test was then performed, acetate replicas being taken every 25000 cycles.

3.5 Fatigue Test Results

3.5.1 Long crack fatigue test results

Recalling that the CCT test was performed with an incrementally increasing load, crack growth rate data was collected in several discrete blocks of increasing ΔK. Figure 3.7 shows an example of the clear transient effects which were seen in the P.D. trace whenever the load was increased. Apparently enhanced crack growth rates were indicated immediately after load increase. The transient appears to decay leaving a reasonably linear trace. Further analysis was restricted to these linear regions only, this unfortunately reduced considerably the size of each data block. Unfortunately data could not be collected over the last load step, since the transient effects did not decay sufficiently to allow consistent crack growth rate measurements. Figure 3.8 shows the edited ΔK data plotted against crack growth rate, it can be seen that even

after removing the obvious transients, some scatter is still present within each data block. Also shown in Figure 3.8 is a typical curve for AL 2024 to provide a comparison with the AS1241 data. The growth rate of fatigue cracks appears to be faster in AS1241, which is unsurprising since AL2024 is a structural alloy noted for its fatigue resistance. AS1241 and AL2024 appear to exhibit a similar fatigue threshold of ~3MPa$\sqrt{m}$, which is typical for most aluminium alloys.

Examination of the fracture surface using scanning electron microscopy revealed evidence of different crack growth mechanisms. Figure 3.9 shows the fracture surface near threshold (ΔK=3MPa$\sqrt{m}$), this shows evidence of a highly tortuous fatigue crack path, with spheroidal silicon secondary phases clearly defined on the surface. Figure 3.10 shows the fracture surface at higher ΔK (ΔK~9MPa$\sqrt{m}$), at this point the fracture surface is flatter, the secondary phases are less evident and classical striations are visible. The striation spacing in this region was measured at 1.63 ± 0.12 μm, indicating a crack growth rate of $1.63*10^{-3}$ mm/cycle.

Although a continuous long crack growth out curve was not established, a band of baseline fatigue behaviour was characterised, to allow comparison with subsequent short crack studies.

3.5.2 Bearing test results

The failure criterion used resulted in visible fatigue cracks on the surface of the lining material, typically extending over 90-100% of the bearing width. The deflection at maximum load was seen to remain unchanged for ~95% of the specimen fatigue life, before increasing rapidly to a compliance failure condition. Figure 3.11 shows a section through a typical failed bearing. Fatigue cracks were observed to initiate at the surface and propagate towards the backing. However it appears that upon reaching the interlayer, the crack deflects or bifurcates and grows for considerable distance parallel to the interface. One of the cracks shown in Figure 3.11 is still in this condition, whilst the other shows evidence of previous propagation in this manner, although it has now penetrated the steel layer, causing final sample failure.

Figure 3.12 shows the S-N curve generated from this series of tests, using the FE model described in Appendix I to calculate the lining stress range in each case. A modified Basquin[1] relation proposed by Morrow[2] given by Eqn 3.2 was fitted to the

bearing data, using the Gerber[3] relation, given by Eqn 3.3, to determine stress amplitude.

$$\sigma_a = (\sigma'_f - \sigma_m)(2N_f)^b \tag{3.2}$$

$$\sigma_a = \sigma_a\big|_{\sigma_{m=0}} \left\{1 - \frac{\sigma_m}{\sigma_{UTS}}\right\} \tag{3.3}$$

where, σ_m and $\sigma_a\big|_{\sigma_{m=0}}$ are the mean stress and the stress amplitude for fully reversed loading (σ_m =0 and R= -1) respectively.

From the curve fit the fatigue strength coefficient σ'_f and the fatigue strength exponent b were found to have values of 150.15 MPa and -0.08 respectively. It can be seen that this relation does not fit the data particularly well. This is not surprising since stress-life approaches tend to be unreliable in cases exhibiting plastic deformation. To address this, a strain-life approach was applied; Figure 3.13 shows a graph of cycles to failure against plastic strain range (calculated by FE as described in Appendix I). Eqn 3.4, proposed by Coffin[4] and Manson[5] was then fitted to this data.

$$\frac{\Delta\varepsilon_p}{2} = \varepsilon'_f (2N_f)^e \tag{3.4}$$

where ε'_f is the fatigue ductility coefficient and e is the fatigue ductility exponent. From the curve fit, these parameters were found to have values of 4.33 and –0.89 respectively. The strain-life model fits the data rather better than the stress-life model, this is probably due to the plastic deformation of the sample, which is not accounted for in the stress-life model.

3.5.3 Ambient short crack fatigue test results

The fatigue lifetimes for the flat strip samples tested in ambient conditions in accordance with the parameters in Table 3.5 are shown in Table 3.6.

Table 3.6: Fatigue lifetimes for ambient short crack tests

Sample	Environment	Lifetime (cycles)
FSA1	Ambient	224347
FSA2	Ambient	195764
FSA3	Ambient	181986
FSA4	Ambient	229948

Sample FSA1 was run uninterrupted to a compliance failure condition, whereas subsequent tests were interrupted to allow acetate replication of the specimen surface. A compliance failure method was used to determine specimen fatigue life, and as with the bearing tests, the deflection at maximum load was seen to remain unchanged for ~95% of the specimen life, before increasing rapidly till failure, at which point fatigue cracks were seen to have propagated over 90-100% of the sample width.

After using the model described in Appendix I to calculate the plastic strain amplitude for these tests, the results were compared with the bearing tests. Figure 3.14 shows the flat strip test lifetimes plotted on the strain-life curve established from the bearing tests, it is clear that the data from the flat strip tests correlates well. The degree of lifetime variation seen in the flat strip samples is well within the band of behaviour defined by the bearing tests.

Considering the replica record, cracks were seen to initiate at multiple sites on the lining material surface, along the line of maximum bending stress. Fatigue crack initiations were first observed after less than 10000 cycles ($N/N_f < 5$ %), however cracks continued to initiate throughout the duration of the test. Unfortunately, due to the very high number of discrete cracks, counting approaches could not be applied reliably.

Figure 3.15 shows several typical initiating and very short fatigue cracks on the lining surface after 50000 cycles. The initiation sites appeared to be generally associated with the interface between the matrix and the Si phase rather than from other secondary phases or slip bands as Shenton[6] has reported. Figure 3.16 shows an SEM micro-graph of a typical initiation site at higher magnification. Several cracks have initiated from, and are propagating along the interface between the Si phase and

the matrix, causing the Si phase to practically de-cohere from the matrix. It is interesting to note that these small cracks are propagating parallel to the global applied tensile axis as well as perpendicular to it, indicating a locally complex stress state. The early growth rate of these cracks was rapid and appeared to be highly microstructurally dependent. Figure 3.17 shows the lining surface after 100000 cycles (N/N_f ~ 50 %) the crack tip appearing to preferentially propagate along slip bands, through the soft Sn phase or along the interfaces between Si phases and the matrix. In addition to obvious deviations in the path of fatigue cracks, considerable fluctuations in the growth rate were observed. Figure 3.18 shows a typical fatigue crack, exhibiting highly microstructurally sensitive crack growth; it is annotated with the instantaneous crack growth rates at several points along its length. It was found that cracks propagated slowly along the Si-Matrix interfaces and more rapidly through the tin phases. The most rapid mode of propagation was along what appears to be slip bands within the Al matrix.

Due to the large number of initiation sites, clusters of micro-cracks coalesced rapidly to form larger cracks. Coalescence events were first observed at 50,000 cycles (N/N_f ~ 25 %), although coalescence events continued to occur throughout the test as a dominant crack built up.

Figures 3.19a-e show how the crack field on the surface of sample FSA2 developed. Cracks first appeared towards one side of the sample, those on the axis of maximum bending stress coalesced to form a dominant crack, this crack then extended across the sample surface. A field of new cracks were seen to initiate rapidly ahead of the dominant crack, these grew rapidly and coalesced with the main crack, extending its length. Typically the main crack had extended over at least 90% of the sample width when a compliance failure condition was reached.

Figure 3.20 shows the growth rate of several small cracks as they neared coalescence with the main dominant crack. It appears that as the projected distance between the cracks decreased, their growth rate accelerates markedly. Many cracks were seen to approach obliquely, a typical example is shown in Figure 3.21. The cracks accelerated and grew in a direction normal to the direction of nominal stress, as the projected spacing between them decreased. However once an overlap was established (projected spacing < 0) their crack growth rate dropped markedly and they deflected towards each other, indicating a marked change in crack tip conditions.

As is shown in Figures 3.19c-e, cracks propagating off the axis of maximum stress were often overtaken by the dominant crack. When this occurred their growth rate was seen to reduce considerably, usually arresting entirely.

The growth rate of large un-coalesced cracks was also seen to decrease once they reached a critical top surface length of 0.7-1.0 mm. Sectioning studies linked this to the point when the lining material is cracked through. Figure 3.22 shows that in common with the bearing tests, a crack having grown entirely through the lining, will not penetrate into the steel. Rather it deflects abruptly, and propagates along the interlayer. As in the bearing tests, no interface failure was observed, the crack propagating along the centre of the interlayer. Such behaviour will cause a large increase in extrinsic crack tip shielding, and this will result in the observed reduction in crack growth rate at the surface. In common with the bearing tests, final failure appeared to be caused by a previously deflected crack finally penetrating the steel layer, leading to the abrupt reduction in compliance.

3.5.4 *In vacuo* and oil environment short crack fatigue test results

Using identical loading conditions to the ambient tests, 5 further tests were carried out on flat strip samples, 3 under vacuum conditions and 2 in an oil environment. No attempt was made to interrupt any of the vacuum tests, they were simply run out to failure. Unfortunately none of these tests reached a failure condition, even after a large numbers of cycles. Of the oil tests, sample FSO1 was run out to a compliance failure condition, whilst the second oil environmental test FSO2 was interrupted, and acetate replicas of the lining surface taken every 25000 cycles until failure. All the fatigue lifetimes for these tests are shown in Table 3.7

Table 3.7: Fatigue lifetimes for environmental samples

Sample	Environment	Lifetime (cycles)
FSV1	Vacuum	1300000#
FSV2	Vacuum	2576629#
FSV3	Vacuum	5039397#
FSO1	Oil	754579
FSO1	Oil	747368
Average ambient	Ambient	208011

Sample did not reach compliance failure

Figure 3.23 shows a post test micrograph of the surface of a sample tested *in vacuo*, no clearly definable fatigue cracks were observed, although a number of voids

were present on the sample surface. The lack of visible cracking, coupled with the extremely high number of cycles performed (more than 25 $N_{f\ Ambient}$), suggest that vacuum conditions severely suppress fatigue crack propagation in this material

The oil environment also increased the sample fatigue lifetime, although not to the same degree as the vacuum conditions, typically $N_{f\ Oil} \sim 3.5\ N_{f\ Ambient}$. Consequently when these results are plotted on the strain-life curve shown in Figure 3.24, they fall well outside the band of behaviour defined by the ambient tests.

Examination of the replica record showed very similar fatigue crack growth mechanisms to those observed under ambient conditions. Multiple crack initiations were observed, early in the specimen's life (N/N_f ~5%) at the Si/matrix interfaces. Early fatigue crack growth rates were seen to be considerably retarded compared to those seen under ambient conditions. Figure 3.25 shows typical microstructurally influenced crack growth of a similar nature to that observed under ambient conditions, cracks appearing to preferentially propagate along Si-matrix interfaces, through Sn phases and along slip bands in the Al matrix. A final failure crack was built up through successive coalescence events, a dominant crack being established by 400,000 cycles (N/N_f ~50%).

3.6 Crack Growth Analysis and Comparison

Compared to samples tested in air, both the oil and vacuum tested samples showed considerably higher fatigue lifetimes, an increase of 350% and >2500% respectively. Indeed no propagating fatigue cracks at all were observed *in vacuo*, even after $5*10^6$ cycles.

In the case of the oil and ambient environments, short crack growth rate data was available from the replica records. In order to compare the short crack results with the already established CCT long crack baseline data, short crack ΔK levels were calculated using Eqn 3.5 proposed by Scott and Thorpe[7], assuming the crack geometry shown in Figure 3.26.

$$K_s = \left[\left[M_{f(0)}\left(1-0.3\frac{a}{W}\right)\left(1-\left(\frac{a}{W}\right)^{12}\right)\right]+\left[0.394E(k)\left(\frac{a}{W}\right)^{12}\sqrt{\frac{c}{a}}\right]\right]\frac{\sigma_{\max}}{E(k)}\sqrt{\pi a}$$

$$\text{where: } M_{f(0)} = \left[1.21-0.1\left(\frac{a}{c}\right)+0.1\left(\frac{a}{c}\right)^4\right]\sqrt{\frac{a}{c}}$$

$$E(k) = \left[1+1.47\left(\frac{a}{c}\right)^{1.64}\right]^{1/2}$$

(3.4)

Figure 3.27 shows how the *a/c* ratio would increase with each successive coalescence event, hence only single un-coalesced cracks were considered for analysis. All crack lengths are projected and a half penny subsurface shape (*a/c*=1) was assumed.

Calculations were based on a value of far field maximum stress of 105.3 MPa (value calculated by F.E. elasto-plastic model, see Appendix I for details).

Equation 3.4 provides a semi-empirical method of predicting the ΔK values surrounding a half-penny or semi-elliptically shaped crack. However it should be noted that the short cracks considered are growing under highly elasto-plastic conditions, and hence the use of ΔK is questionable, as LEFM conditions are clearly not maintained. However ΔK has been used as a correlation parameter for purposes of comparison with long crack data (in accordance with other short crack studies in the literature).

Figures 3.28 and 3.29 show plots of crack length against cycles and crack growth rate against ΔK respectively for cracks grown in both ambient and oil environments. It can clearly be seen that the fatigue cracks in oil grow at a much reduced rate for a given ΔK level. In both cases individual crack growth rates accelerate and decelerate, despite experiencing a constant applied load range throughout the test. It was shown in section 3.6.3 that this is due to the microstructural sensitivity of the crack growth mechanism, cracks appearing to propagate quickly along slip bands, slower through Sn phase and even slower along Si/matrix interfaces.

Figure 3.30 shows the same short crack growth rate data compared with the long crack data obtained from CCT tests on monolithic lining material under ambient conditions. It appears that short cracks in both ambient and oil environments grow at ΔK levels apparently far lower than the long crack fatigue threshold.

3.7 Discussion

The CCT long crack test was used to provide baseline fatigue growth behaviour with which to compare the subsequent short crack results. Due to sample size constraints, it had be performed under an incrementally increasing load regime. This approach caused large transient effects in the p.d. trace. These transients are likely to be caused by underload effects[8]. Since when ΔK is increased, K_{max} rises immediately, but K_{cl} remains unchanged. Thus ΔK_{eff} is increased, giving enhanced crack growth rates. However, the effect is transitory, since plastic crack wake is built up at the new ΔK level, thus increasing K_{cl} until a new equilibrium is reached. This transient effect is then repeated each time the ΔK level is increased. In addition it is possible that an electrical closure mechanism is operating however, the absence of a step increase in p.d. at each point of ΔK level increase indicates that if present, this is a minor effect.

Examining the fracture surface of the CCT test two distinct regimes of crack propagation were evident. Near threshold (ΔK=3MPa$\sqrt{m}$), secondary phases were clearly evident on the fracture surface, the soft Sn phase appeared to have been propagated through, whilst the harder Si retained its spheroidal shape. This indicates that these phases are preferentially sought out by the crack tip, propagating through the Sn and around the Si. At higher ΔK levels (ΔK~9MPa$\sqrt{m}$), the fracture surface appeared much flatter, fewer secondary phases were visible and classical striations were present. The reduction in secondary phases appearing on the fracture surface suggests that the crack tip has not sought them out and indicates that crack growth at this higher ΔK is relatively microstructurally insensitive. This coupled with the presence of classical striations suggests a stage II fatigue crack growth mechanism is operating at this higher ΔK.

An S-N curve was produced using multiple run out tests on finished bearings. The use of a compliance method to define a failure point was found to be successful, terminating all tests at a similar degree of fatigue cracking. It was found that as part of a bearing system, AS1241 can apparently tolerate cyclic stresses far in excess of yield. F.E. modelling (described in Appendix I) showed that for all tests the AS1241 lining behaved plastically, and for a considerable proportion (P_{max} > 2kN), the steel backing was also well above its yield stress. Although an endurance limit to 10^7

cycles was not established, the stress range necessary to cause failure in $2*10^6$ cycles was such that its maximum stress was 142% of yield (46% UTS). Given that in this region the *S-N* curve is clearly approaching a limit, it is unlikely that the true endurance limit will be much lower.

A stress-life approach was used to fit a curve to the obtained data using Basquin's equation. The fit obtained using this relation was not particularly good, unsurprisingly since the material system is behaving highly plastically. In contrast, a strain-life approach using the Coffin-Manson equation and an F.E. model (described in Appendix I) to calculate the plastic strains was found to fit the data very well. Whilst values for the fatigue ductility coefficient and exponent were obtained and had reasonable values, no literature data is available for direct comparison.

Due to inherent problems with polishing the lining surface of a curved bearing, tests to investigate the microstructural behaviour of fatigue cracks were performed on samples of flat strip material, in the material condition immediately prior to bearing forming. Four tests using these samples were performed under ambient conditions, the first was simply run uninterrupted to a compliance failure condition, whilst the remainder were interrupted and acetate replicas taken of the sample surface. The fatigue lifetimes of these tests were plotted onto the strain-life curve determined by the bearing tests, and it was seen that they correlated well with the bearing's fatigue behaviour. The implications of this are important, since it confirms both that the two sample types are comparable, and that the two F.E. models used for predicting stress and strain levels in the two specimen types are accurate. This second point also confirms that the properties determined from the monolithic lining material, and used in the F.E. model, are very similar to the properties of the bearing and flat strip lining material.

In ambient conditions, multiple fatigue cracks were seen to initiate early in the specimen's life (N/N_f <5%), though subsequent initiations occurred throughout the specimens life. These initiations were on the lining surface in the region of maximum bending stress, primarily at the interfaces between Si secondary phases and the surrounding matrix. Shenton *et al*[6] also reported simple slip band initiation in this alloy, but initiations of this type were not observed in the current work. Close examination of typical initiation sites showed that fatigue cracks initiated and apparently grew practically right round the Si phases, and almost decohered them from the matrix before propagating away. It was also observed that multiple cracks

would initiate at a single secondary phase, some propagating normal to the remote stress field, and some parallel to it. This is an indication of a complex local stress field surrounding the Si phases during initiation; the processes governing preferential initiation sites are investigated further in Chapter 4.

Early fatigue crack growth was seen to be rapid and highly microstructurally dependent. Cracks appearing to preferentially propagate along Si/matrix interfaces, through Sn phases and along what appear to be slip bands in the matrix. This tallies with the observations of long crack behaviour at low apparent ΔK levels, where high numbers of secondary phases were evident on the fracture surface, again indicating that near threshold (at low ΔK levels) these phases are preferentially sought out by the crack tip. Similar behaviour has been reported in Al-Si cast alloys[9] and Al-SiC composites in which small fatigue cracks are seen to deflect towards, and grow along the interfaces of the very stiff SiC inclusions[10]. This behaviour was modelled by Padkin *et al*[11] who showed that particles stiffer than the surrounding matrix will tend to attract and accelerate fatigue cracks. In addition to deflecting the small fatigue cracks, secondary phases also appear to affect their growth rates. It was seen that cracks grew most rapidly along slip bands, slower through the Sn phases and slower still along the Si/matrix interfaces. These changes in crack growth rate may be seen clearly in the da/dN vs ΔK behaviour; such scatter in crack growth rates is typical of short fatigue behaviour[12].

Due to the multiplicity of crack initiations, coalescence events were inevitable. These were first observed after ~40,000 cycles ($N/N_f \sim 0.12$) in ambient tests, although as was observed for initiation events, coalescences continue to occur throughout the duration of the test. It was seen that micro-cracks coalesced quickly to form a dominant crack, a field of new cracks were then seen to initiate ahead of this. The dominant crack was then seen to propagate across the sample by coalescence with these new micro-cracks. It was observed that, as cracks neared coalescence (based on projected spacing), their growth rate increased markedly. Cracks propagating parallel to but remote from the axis of maximum bending stress were however seen to arrest when overtaken by the dominant crack. Both these phenomena indicate complex interactions between multiple cracks. Offset cracks were observed to accelerate and continue growing normal to the applied stress field until they overlapped. Subsequent to this, their growth rate decreased markedly and their tips deflected towards each other, indicating a marked change in the crack tip driving

force. This type of behaviour has been observed previously[13], and together with the other coalescence behaviour is examined in more detail in Chapter 5.

Un-coalesced cracks were observed to either reduce in growth rate or arrest entirely when they reached a critical surface length of 0.7-1.0 mm, sectioning studies were used to assess this behaviour in terms of the sub-surface behaviour. It was seen that a crack having propagated downwards through the lining material would deflect along the interlayer rather than grow into the steel backing. It appears that eventually a single previously deflected or bifurcated crack eventually penetrates the steel layer, precipitating failure in terms of an observable change in compliance. These observations together with the rapid increase in deflection at maximum load near the end of the test, indicate a rapid final failure mechanism once a crack enters the steel layer. This type of deflected sub-surface crack behaviour is investigated and the resulting implications discussed further in Chapter 6.

Deflected subsurface behaviour was seen in the flat strip samples, bearings tested in this project as well as those tested on accelerated bearing fatigue rigs by the sponsoring company. It is encouraging to observe that similar failure mechanisms are evident under a simple 3 point bend stress state as in a complex bearing fatigue rig, showing that whilst this fundamental study applies simple well defined stress states and accelerated test times, it provides a valuable and relevant mechanistic insight into bearing fatigue performance.

Short crack analysis was restricted to single un-coalesced cracks to ensure a relatively simple stress state and a constant *a/c* ratio. ΔK was used to characterise the growth of both long and short cracks, although its application to the short crack problem is questionable, since it is an elastic parameter and the short cracks are growing under highly plastic conditions. However, in line with many other short crack fatigue studies, it is used here to compare the relative growth rates of long and short cracks. Stress intensity factor values for short cracks were calculated by the equation proposed by Scott and Thorpe[7], using the maximum top surface stress predicted by the finite element model. Comparing these results with the long crack data, it was shown that as expected[14] short cracks propagated at ΔK values considerably below the apparent long crack threshold. Short crack propagation was observed at a predicted ΔK of 0.12 MPa$\sqrt{m}$, compared to a long crack threshold of 3 MPa$\sqrt{m}$.

In addition to the ambient tests, flat strip samples were tested under vacuum and in-oil conditions. Although these tests were carried out under the same loading

conditions as the ambient tests, fatigue lifetimes were considerably enhanced, indeed no failures were observed in vacuum tests even after 25 $N_{f\,Ambient}$ cycles.

No clearly distinguishable fatigue damage was evident on the surface of samples tested in vacuum, however a number of voids were observed on the sample surface. From their size and shape it is possible that these have been caused by decohered Si phases, which in common with the observations of Gall *et al*[9], were seen to occur occasionally as a result of the crack initiation mechanism in the ambient tests. However the fatigue crack propagation mechanism observed under ambient conditions appears to have been entirely suppressed in vacuum. Vacuum conditions were expected to alter the fatigue behaviour, since it is known that fatigue mechanisms in aluminium alloys are highly sensitive to environmental changes. Several authors have found that fatigue crack growth rates may be as much as an order of magnitude lower under vacuum conditions than in moist air. This has been linked to the reduction in striation formation observed in samples tested *in vacuo.* Pelloux[15,16] hypothesised that the slip process by which striations form may be more reversible in the absence of an oxide layer, hence causing lower damage accumulation and therefore lower crack growth rates. In addition hydrogen embrittlement effects should be negligible under vacuum conditions, again promoting reduced crack growth rates.

Tests performed in an oil environment also typically showed a 350% increase in lifetime compared with tests in ambient conditions. Crack initiation was first seen to occur at a similar life fraction to ambient tests (N/N_f ~5%). The initiations were again primarily associated with the Si secondary phases. Early crack growth was seen to be microstructurally sensitive and similar to that observed under ambient conditions; the crack tip appearing to preferentially propagate towards Si/matrix interfaces, through Sn phase and along slip bands. Multiple coalescence events were observed and the establishment of a dominant crack occurred at similar life fractions to ambient tests.

Comparison with the ambient short crack data revealed that the propagation rate of short cracks in an oil environment was typically an order of magnitude lower. This can be attributed to a number of factors affecting the conditions at the crack tip. Since the oil was not dehumidified, it is unlikely that it will provide an entirely inert environment at the crack tip[17], and hence some degree of hydrogen embrittlement may occur. However the oil is likely to promote a more inert crack tip environment

than that present during ambient testing. However in contrast to the vacuum tests, oxide debris are more likely to be built up in oil, promoting irreversible slip, and in addition to any hydrogen embrittlement effects, promote a faster crack growth rate compared with that seen *in vacuo*.

Tzou *et al*[17] found that oils of viscosity less than 12500 cSt reduced fatigue crack growth rates in steels and that this effect was greater in low viscosity oils. This was attributed to the low viscosity oil penetrating into the fatigue crack and exerting a closure effect. The viscosity of the oil used in the flat strip tests was very low (43.18 cSt), also being paraffin based, it has a high surface tension, thus it will easily penetrate into any fatigue cracks.

Thus considering that the tests were carried out at low load ratios, where closure mechanisms are known to have the greatest effect on fatigue crack growth rate[18], and that the oil has almost certainly penetrated into the cracks, it is likely a viscous fluid induced closure mechanism will be operating. The observed lifetime increase is therefore likely to be caused by a combination of viscous fluid induced crack closure, and reduction of both hydrogen embrittlement and irreversible slip at the crack tip. However the relative magnitudes of these effects cannot be established without further testing, which is beyond the scope of the present thesis.

3.8 Summary and Conclusions

As part of a bearing system AS1241 can tolerate cyclic stresses well above yield (but below UTS), without apparent fatigue damage. An *S-N* curve was produced using bearings tested to a compliance failure condition, this showed that the endurance limit to $2*10^6$ cycles was ~80 MPa (c.f. yield stress = 56.6 MPa, UTS = 172.9 MPa). This data when plotted using a strain-life methodology was found to fit the Coffin-Manson equation with values of the fatigue ductility coefficient and exponent of 4.33 and –0.89 respectively. These values are typical of a non-structural material of low yield stress.

Due to the difficulty in reliably polishing the curved bearing lining surface, studies to investigate the microstructural influence on fatigue crack behaviour were carried out on flat strip samples immediately prior to forming. Under ambient conditions the lifetimes of these samples were found to fit the previously determined

strain-life plot very well. This indicates the two sample types and testing approaches are comparable, and that the F.E. models used to calculate the elasto-plastic stresses and strains in both sample types tally well.

Under ambient conditions multiple fatigue crack initiations were seen along the axis of maximum bending stress early in the samples life (N/Nf <5%), although subsequent initiations occurred throughout the duration of the test. Initiations were seen to be primarily associated with the Si/matrix interfaces. Early crack growth was seen to be microstructurally dependent, the crack tip appearing to propagate preferentially along Si/matrix interfaces, through Sn phases and along what appear to be slip bands in the matrix. The relative rates of propagation were seen to be highest along slip bands, then through Sn phases, whilst Si/matrix interfaces showed the slowest crack growth. Using the equation proposed by Scott and Thorpe[7] it was shown that short cracks propagate at ΔK levels apparently far lower than the long crack threshold, although the short cracks are growing under elasto-plastic conditions, making the assumption of ΔK similitude between long and short cracks questionable.

Due to the high number of discrete cracks (>2000) multiple coalescence events were observed, starting at ~25% lifetime and continuing till failure. A dominant crack was seen to be built up through the coalescence of many pre-existing smaller cracks. A field of micro cracks was then seen to initiate ahead of this large crack. These then coalesced with the dominant crack, extending it till failure occurred. The growth rate of cracks nearing coalescence was seen to increase as their projected spacing reduced, whilst those cracks overtaken by the dominant crack were usually seen to arrest.

Un-coalesced cracks were seen to arrest at a critical length of 0.7-1 mm, this was linked to sub-surface conditions, where it was seen that having grown through the lining, the crack tip deflected along the interlayer rather than continuing to propagate into the steel backing layer. This behaviour is thought to be in response to a large increase in extrinsic shielding, and it is believed that this is responsible for the observed reduction in surface crack growth rate. Rapid final failure appears to be brought about when a previously deflected crack finally penetrates the steel layer. This sub-surface deflected behaviour was observed in bearings and flat strip tested under simple fatigue conditions and in bearings tested on accelerated bearing fatigue rigs (e.g. Sapphire).

The effect of vacuum and oil environments on fatigue crack growth behaviour was investigated. It appears that *in vacuo* fatigue crack growth is suppressed, though some evidence of fatigue crack initiation events was observed. It is likely that this is due to the promotion of reversible slip and reduction of hydrogen embrittlement at the crack tip, both of which are known to occur in Al alloys under vacuum conditions. Fatigue lifetimes in oil were seen to be increased by 350%. However the fatigue crack initiation and propagation mechanisms appeared to be unchanged from those observed under ambient conditions. Since the oil was not dehumidified, it is likely that oxide formation and hydrogen embrittlement may still be able to occur to some extent at the crack tip. It is also likely that the fatigue crack became penetrated by oil, and that a viscous closure mechanism was present during these tests. However further work is required to determine the relative contribution of these effects on the increase in fatigue life observed in oil.

3.9 References

[1] O.H. Basquin, The exponential law of endurance tests, Proc ASTM V10 pp625-30 (1910)

[2] J.D. Morrow, Fatigue design handbook – advances in engineering, V4 Sec. 3.2 pp21-29 SAE (1968)

[3] H. Gerber, Bestimmung der zulassigen spannungen in eisen-konstructionen, Zeitschrift des bayerischen architeteckten und ingenieur-vereins, V6 pp 101-10 (1874)

[4] L.F. Coffin, A study of the effect of cyclic thermal stresses on a ductile metal, Trans. ASME V76 pp15-22 (1954)

[5] S.S. Manson, Behaviour of materials under conditions of thermal stress, National advisory commission on aeronautics: report 1170 (1954)

[6] P. Shenton and C. Perrin, Private communication, Dana Glacier Vandervell

[7] P.M.Scott and T.W.Thorpe, A critical review of crack tip stress intensity factors for semi-elliptic cracks, Fatigue of Engineering Materials and Structures Vol 4 pp291-309 (1981)

[8] H. Nisitani and K. Takao, Fatigue crack acceleration and closure in rotating bending tests of 0.54% carbon steel. Eng. Fract. Mech. V10 pp855-66 (1978)

[9] K. Gall, N. Yang, M. Horstemeyer, D. McDowell and J. Fan, The dobonding and fracture of Si- particles during the fatigue of a cast Al-Si alloy, Met. Trans. Vol.30A pp. 3079-88 (1999)

[10] M. Jono, Initiation and growth mechanism of small fatigue cracks in SiC/Al composites, Proc small fatigue cracks: mechanics, mechanisms and applications, Oahu Hawaii pp289-301 (1998)

[11] A.J.Padkin, M.F.Bereton and W.J.Plumbridge, Fatigue crack growth in two phase alloys, Mat Sci and Tech V3 pp217-223 (1987)

[12] J. Lankford, The growth of samll fatigue cracks in 7075-T6 aluminium, Fat. Engng Mat. Struct. V5 pp233-48 (1982)

[13] P.J.E. Forsyth, Fatigue- damage and crack growth in aluminium alloys, Acta Met. V2 pp 702-71 (1963)

[14] S.Pearson, Initiation of fatigue cracks in commercial aluminium alloy and the subsequent propagation of very small cracks, Eng Fract Mech 7 pp235-47 (1975)

[15] R.M.N. Pelloux, Mechanisms of formation of ductile fatigue striations, Trans A.S.M.E. V62 pp 281-5 (1969).

[16] R.M.N. Pelloux, Crack extension by alternating shear, Engng. Fract. Mech. V1 pp697-704 (1970).

[17] J.L.Tzou, S.Suresh and R.O.Ritchie, Fatigue crack propagation in oil environments- I. Crack growth behaviour in silicone and paraffin oils, Acta Met v33 pp105-116 (1985)

[18] W.Elber, The significance of fatigue crack closure, In damage tolerant aircraft structure, special technical publication 486 pp230-42 (1971)

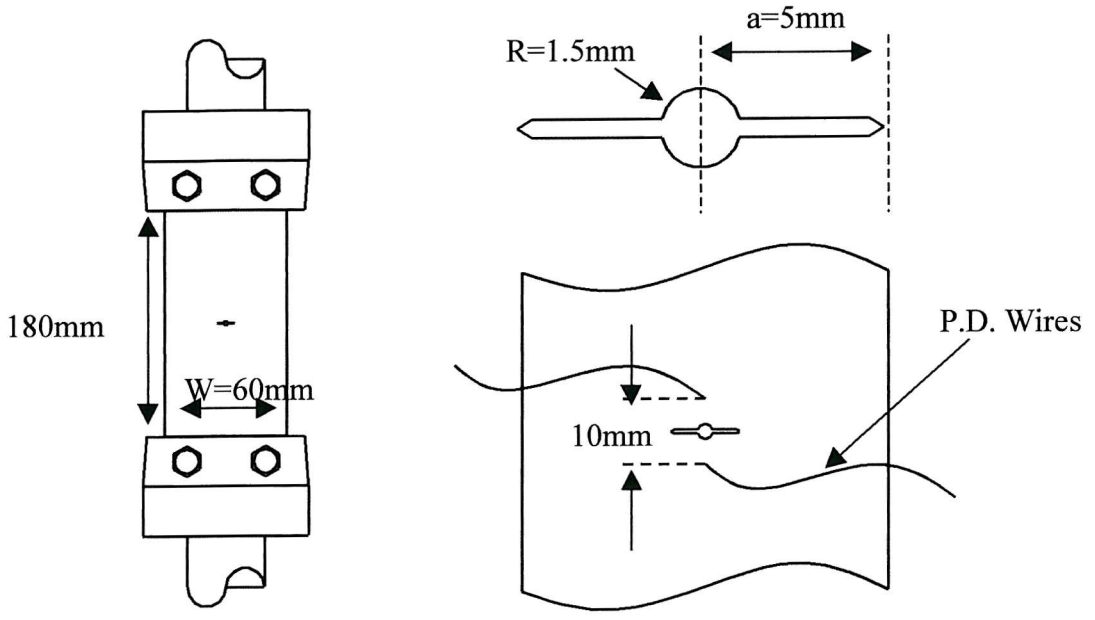

Figure 3.1: Long crack CCT geometry and notch dimensions

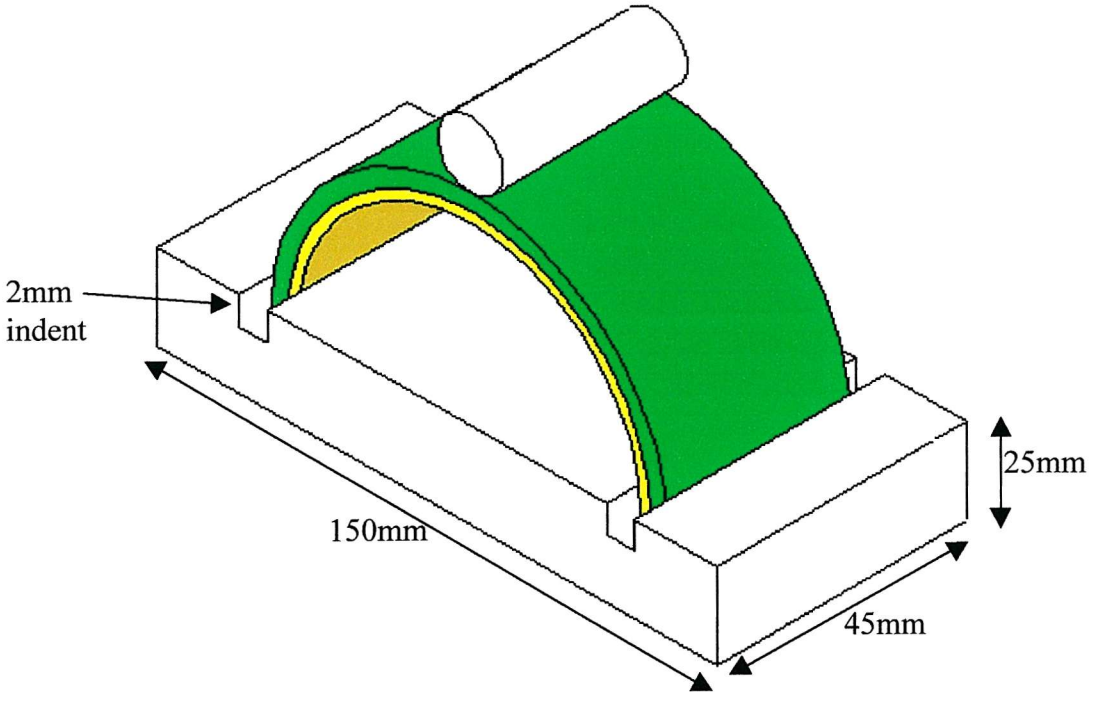

Figure 3.2: Bearing short crack test geometry and rig

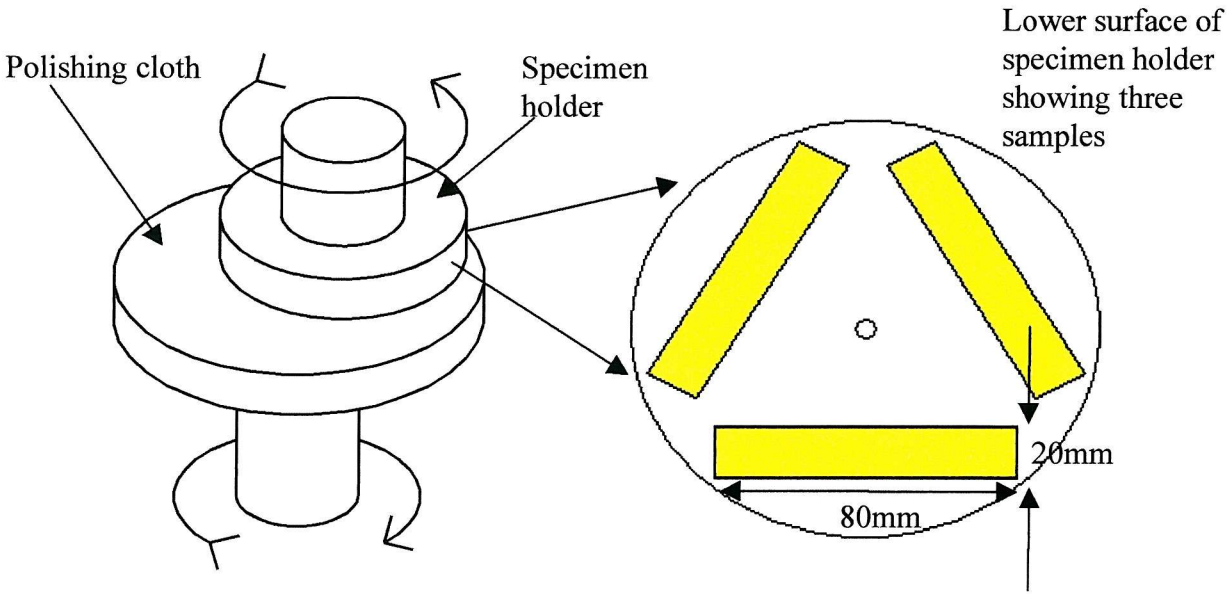

Figure 3.3: Automatic polishing jig and typical flat strip sample

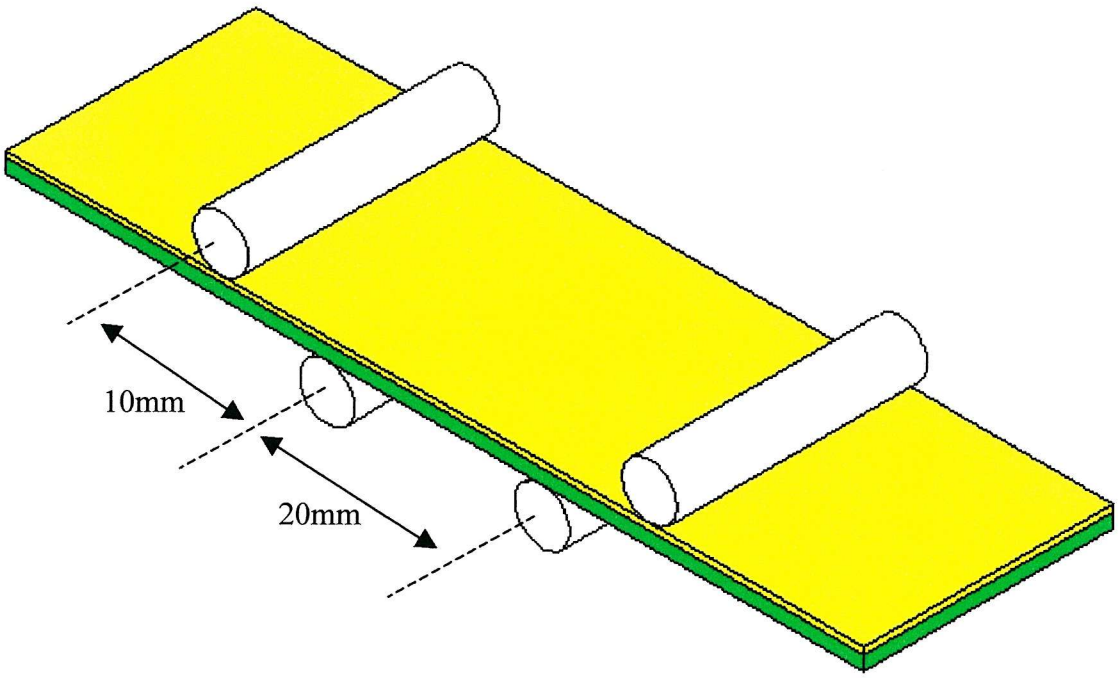

Figure 3.4: Four point bend geometry for flat strip samples

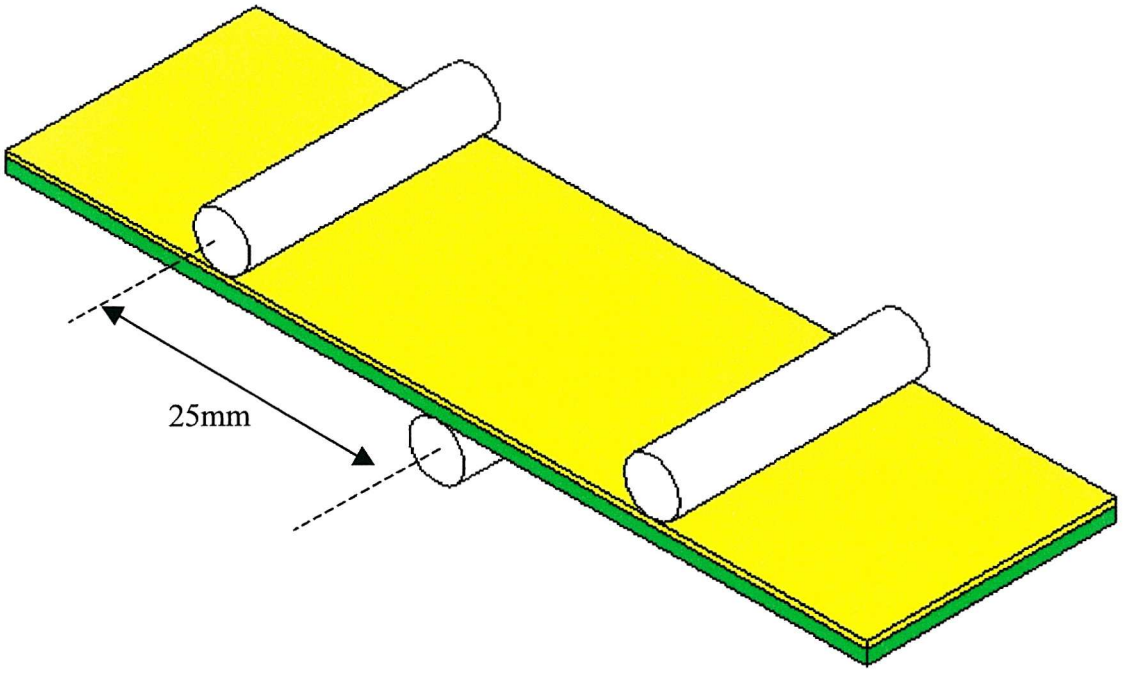

Figure 3.5: Three point bend short crack fatigue test geometry

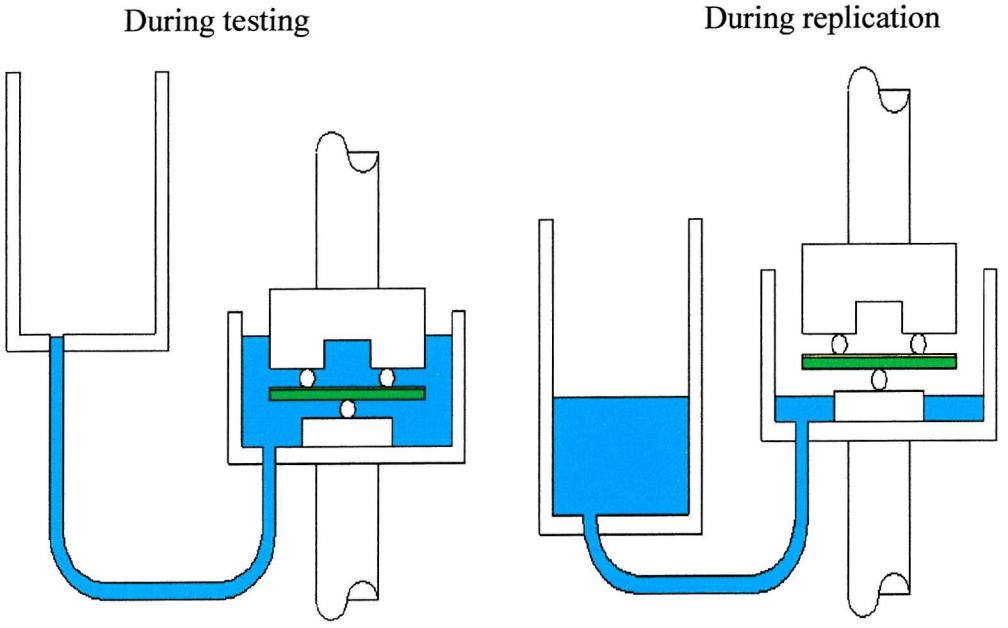

Figure 3.6: Oil environmental test rig

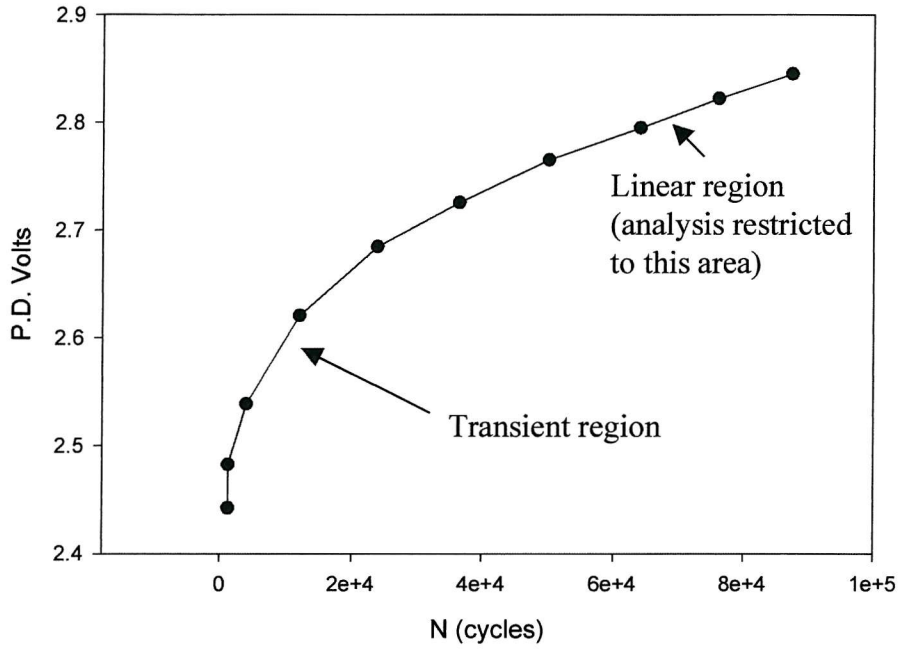

Figure 3.7: Typical transient effect seen after increasing load to raise ΔK, in this case from 3 to 4MPa$\sqrt{m}$

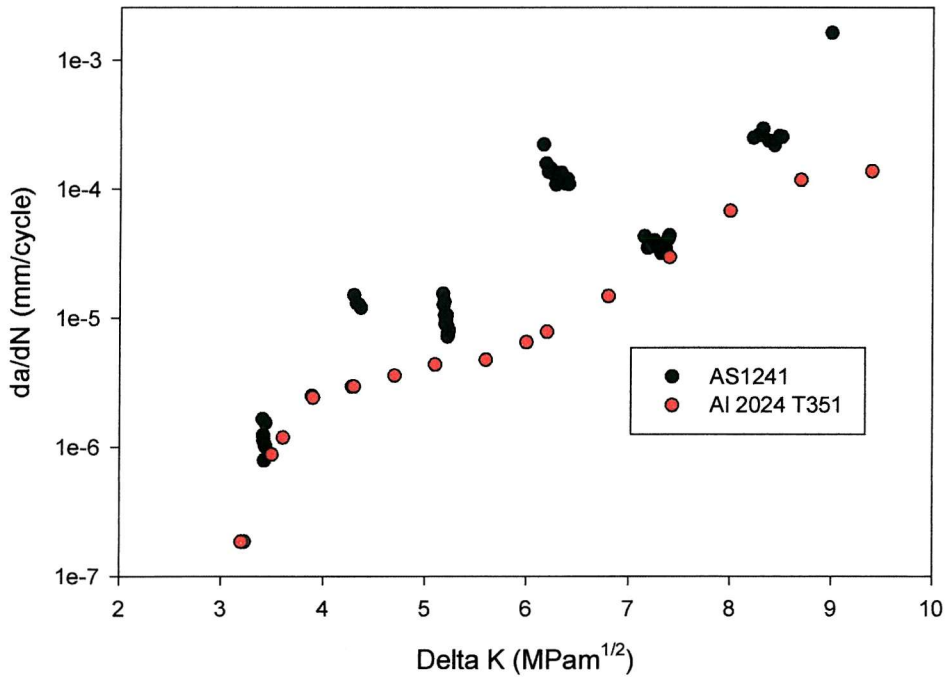

Figure 3.8: AS1241 Long crack data from CCT test, Al 2024 (Xu et al) shown for comparison

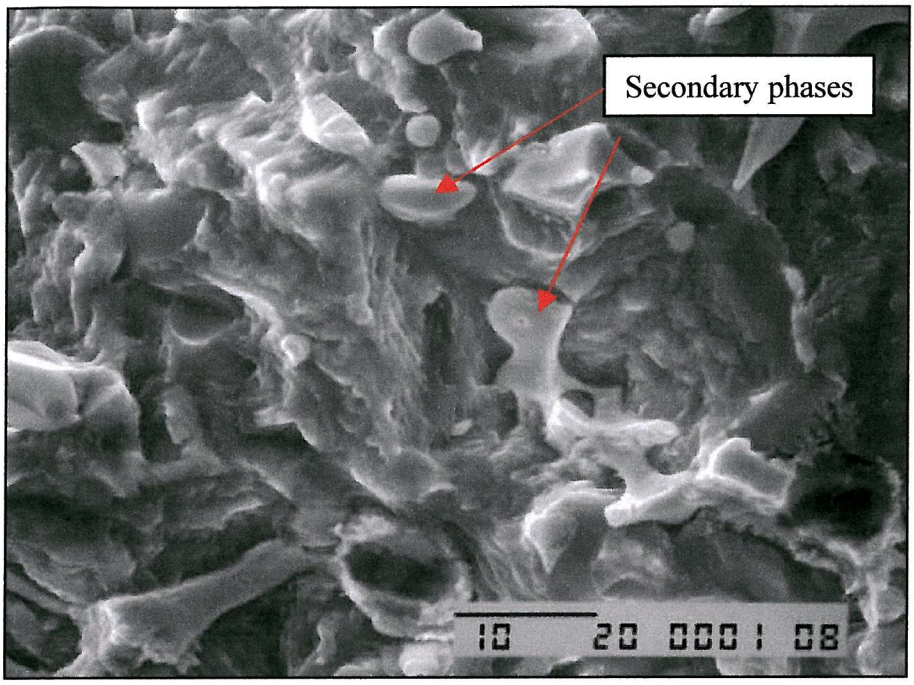

Figure 3.9: SEM micrograph showing long crack fracture surface near threshold (ΔK=3MPa$\sqrt{m}$)

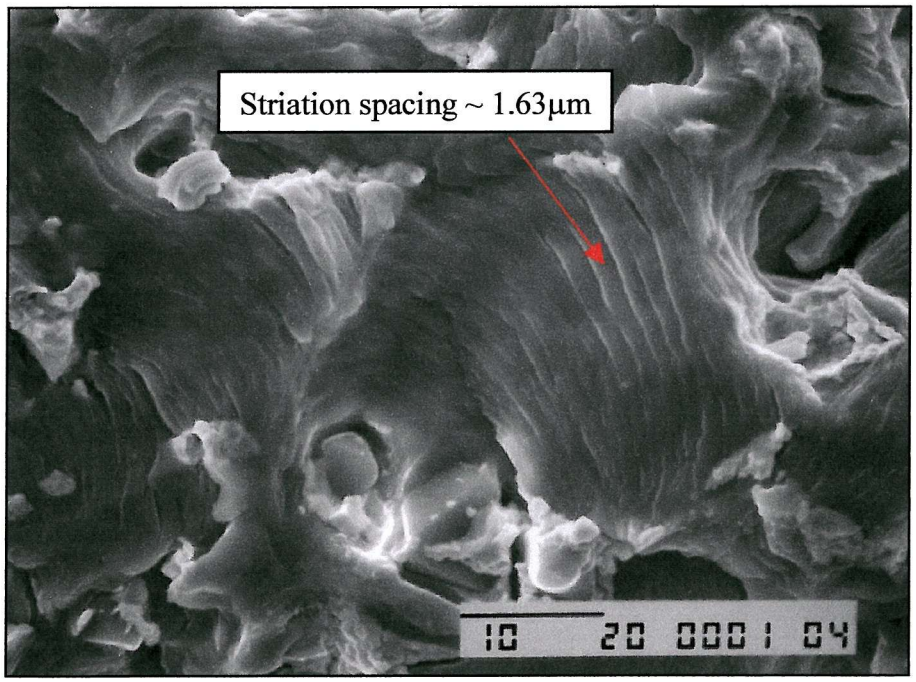

Figure 3.10: SEM micrograph showing long crack fracture surface at higher ΔK (ΔK~9MPa$\sqrt{m}$)

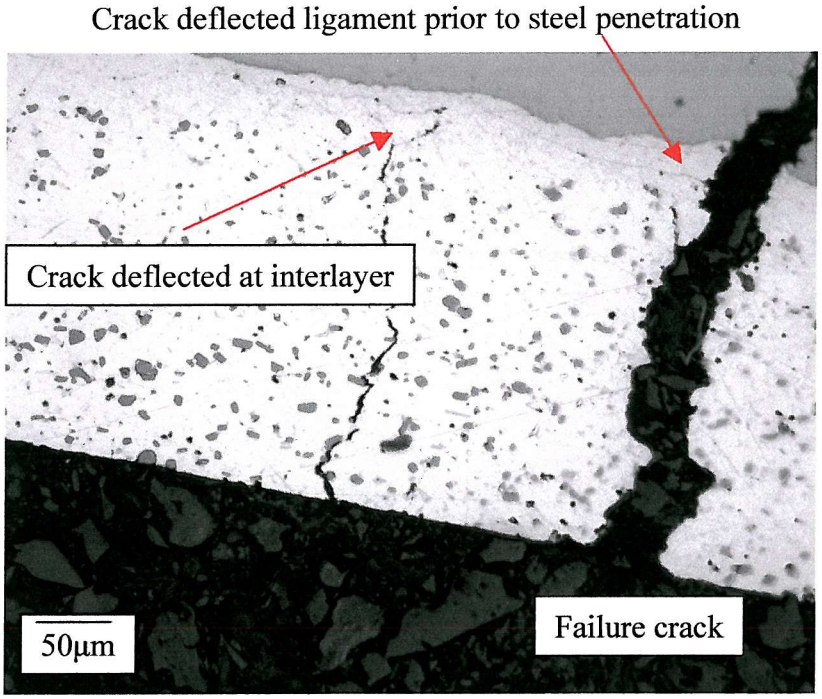

Figure 3.11: Optical micrograph showing section through failed bearing showing deflected crack, and failure crack with previous deflected behaviour

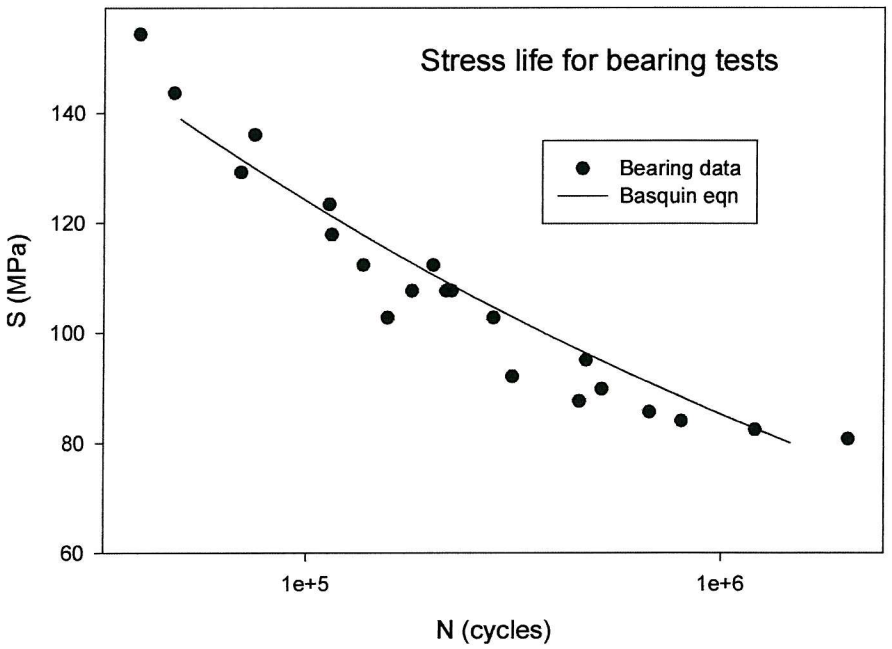

Figure 3.12:Basquin relation fitted to stress life data produced by bearing tests

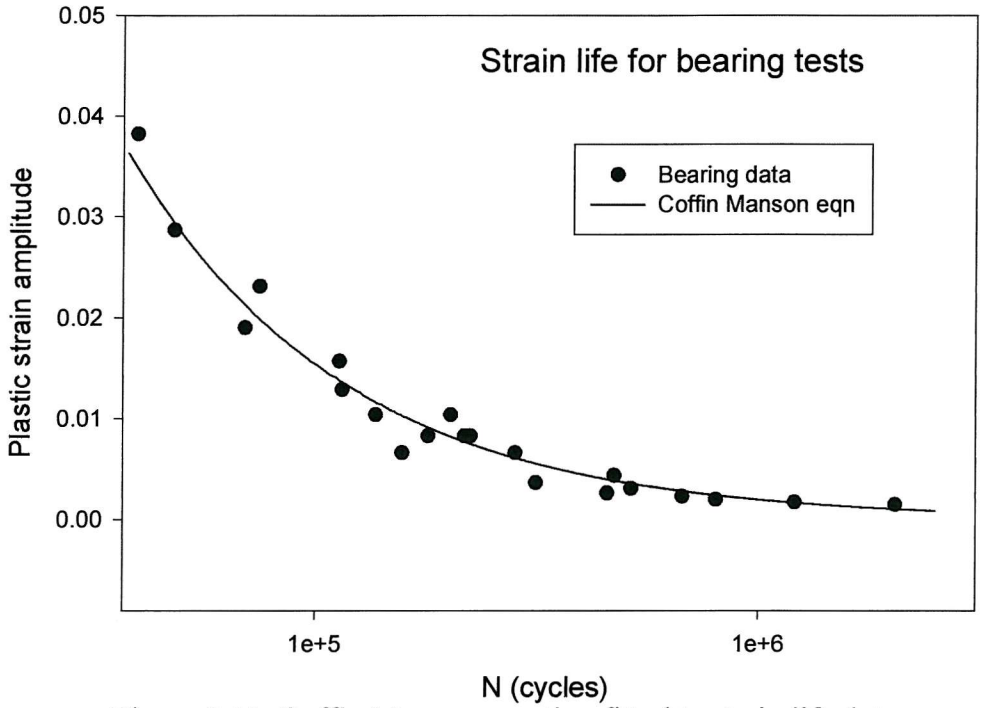

Figure 3.13: Coffin Manson equation fitted to strain life data produced by bearing tests

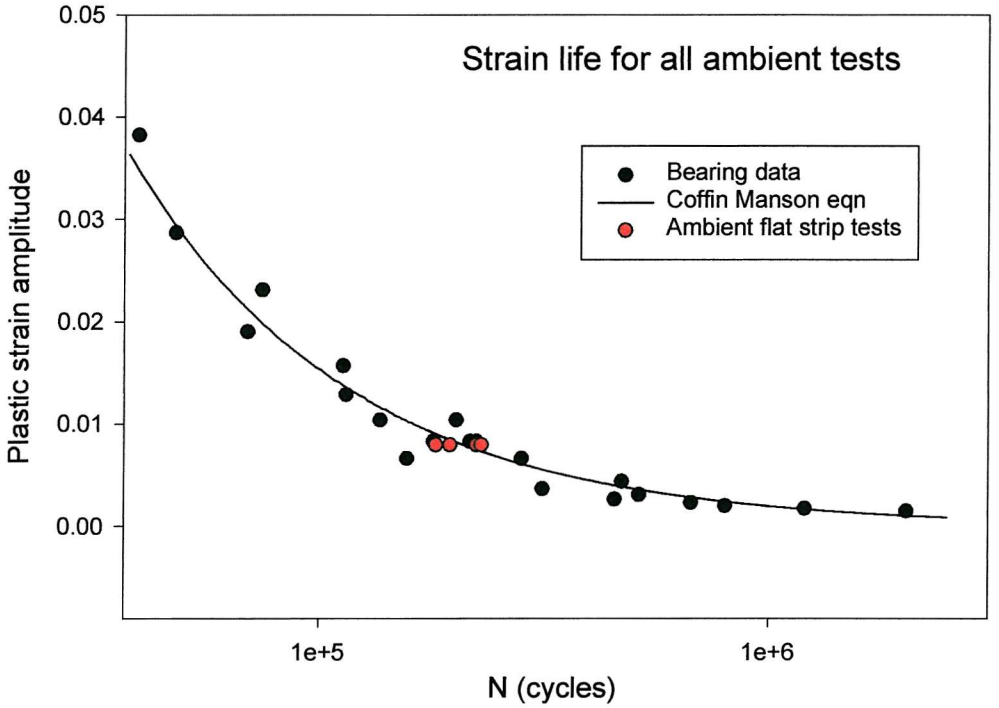

Figure 3.14: Correlation seen between ambient flat strip tests and previously established strain life curve

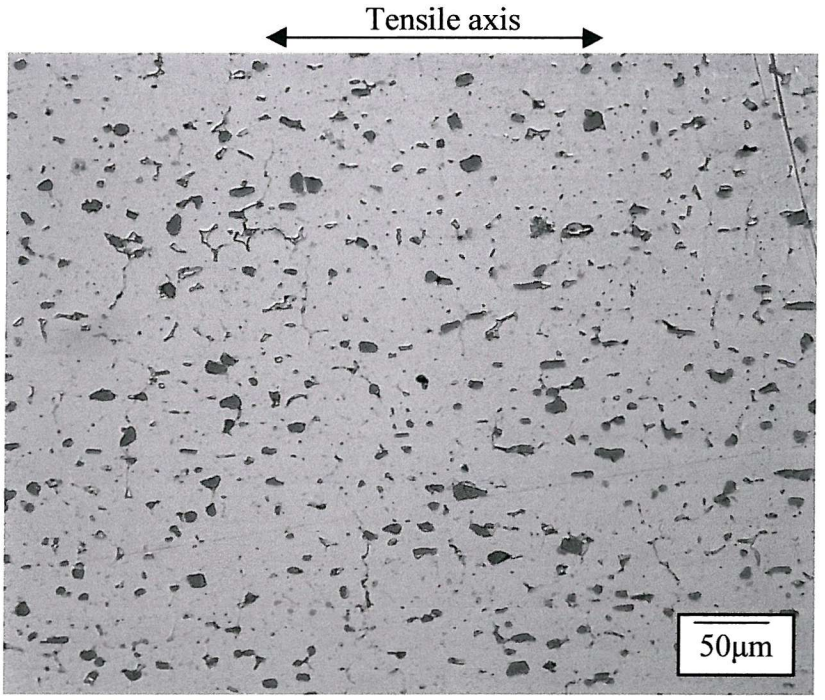

Figure 3.15:Specimen surface after 50,000 cycles, showing multiple crack initiation sites

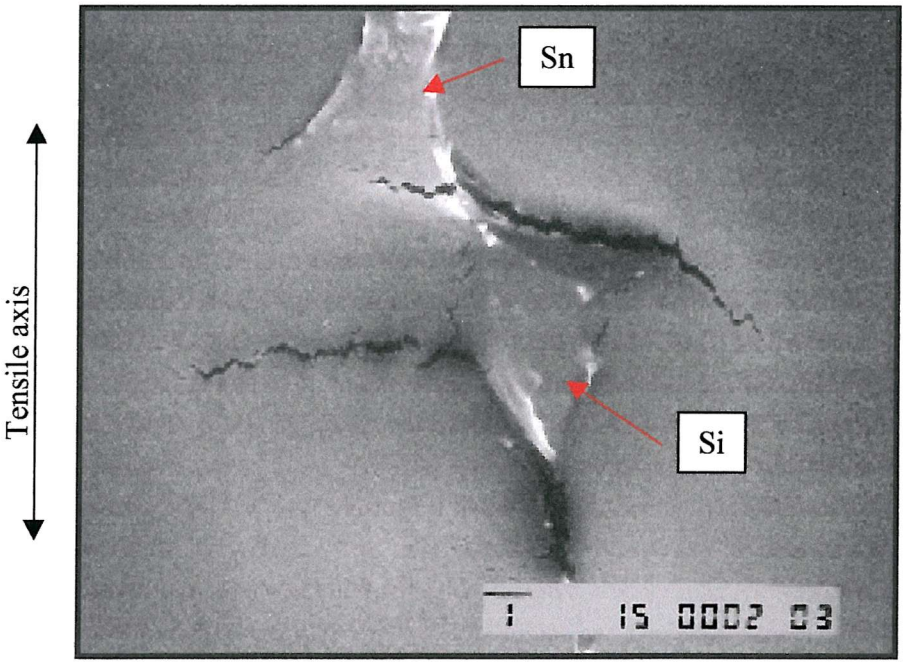

Figure 3.16: SEM image of acetate replica showing typical initiation site, giving evidence of a complex local stress state during initiation

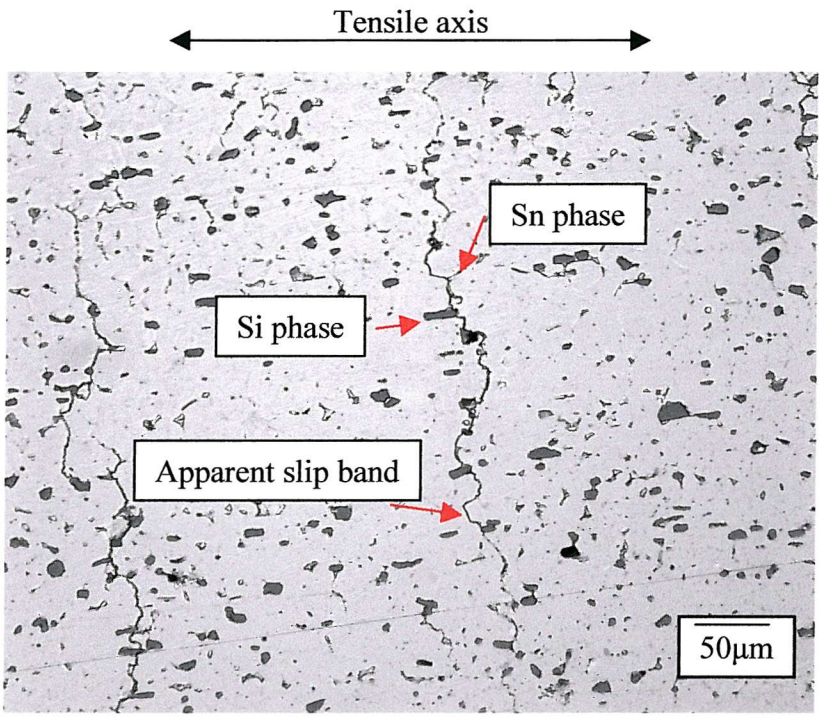

Figure 3.17: Specimen surface at 100,000 cycles, showing typical microstructural fatigue crack growth

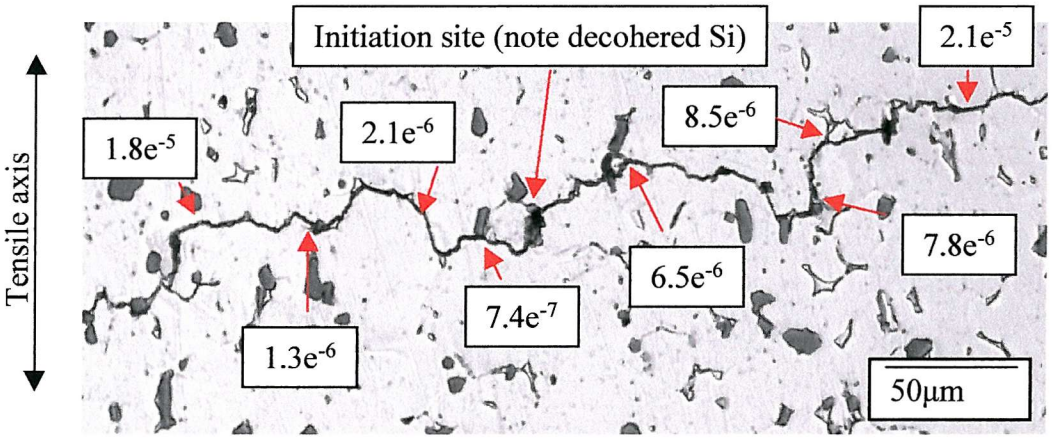

N.B. All crack growth rates given in mm/cycle

Figure 3.18: Individual crack and associated crack growth rates indicating microstructural influence on short fatigue crack growth rate

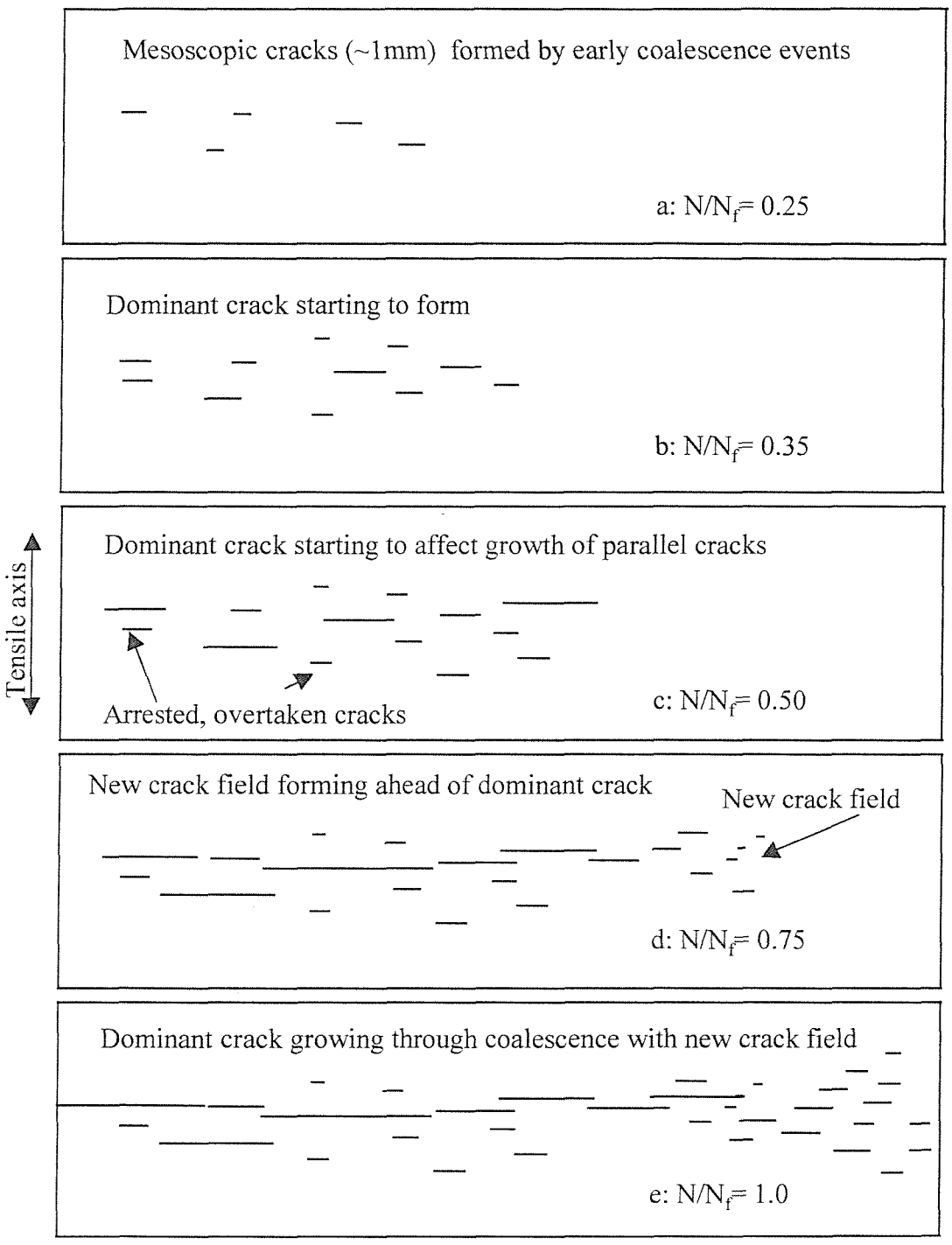

Figure 3.19: Crack field development on the surface sample FSA2

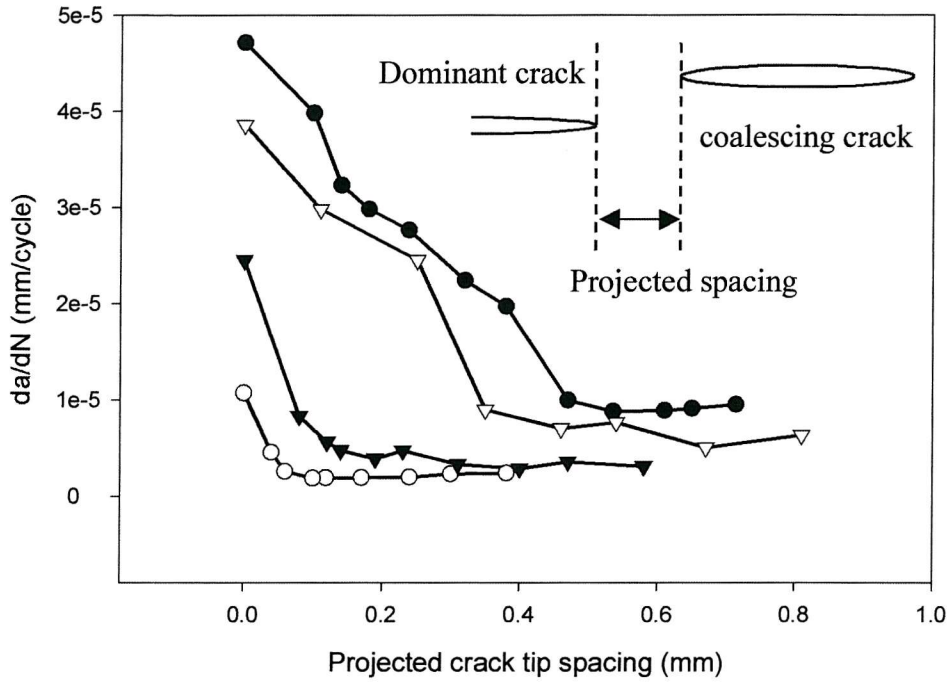

Figure 3.20: Crack growth rate variation as cracks approach coalescence with the main dominant crack

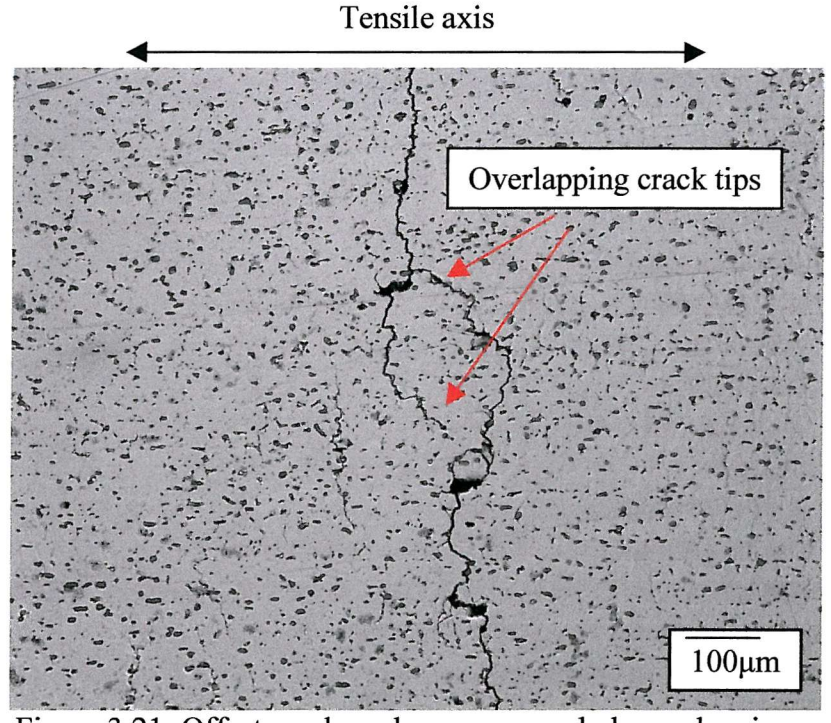

Figure 3.21: Offset crack coalescence morphology, showing how cracks tend to overlap before deflecting towards each other

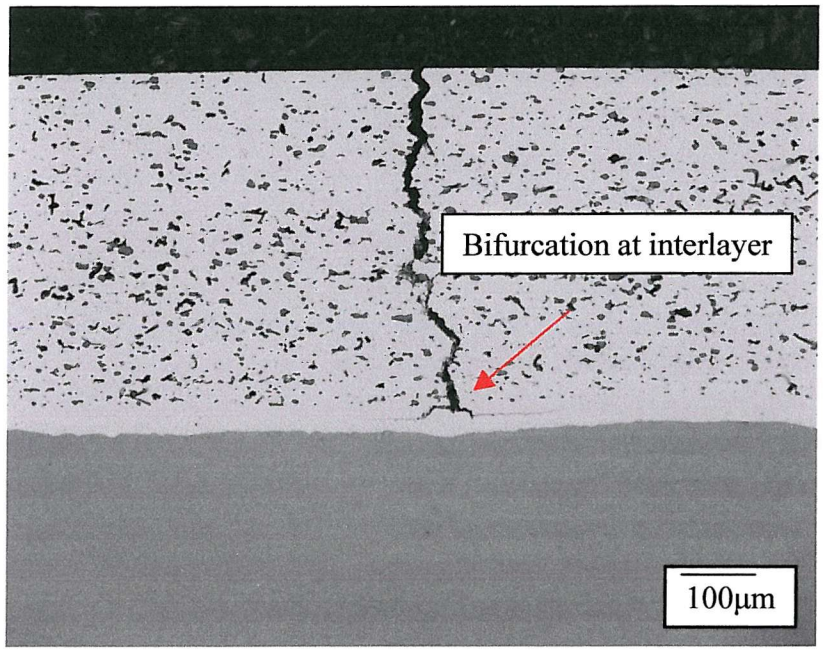

Figure 3.22: Subsurface behaviour seen in ambient flat strip tests.

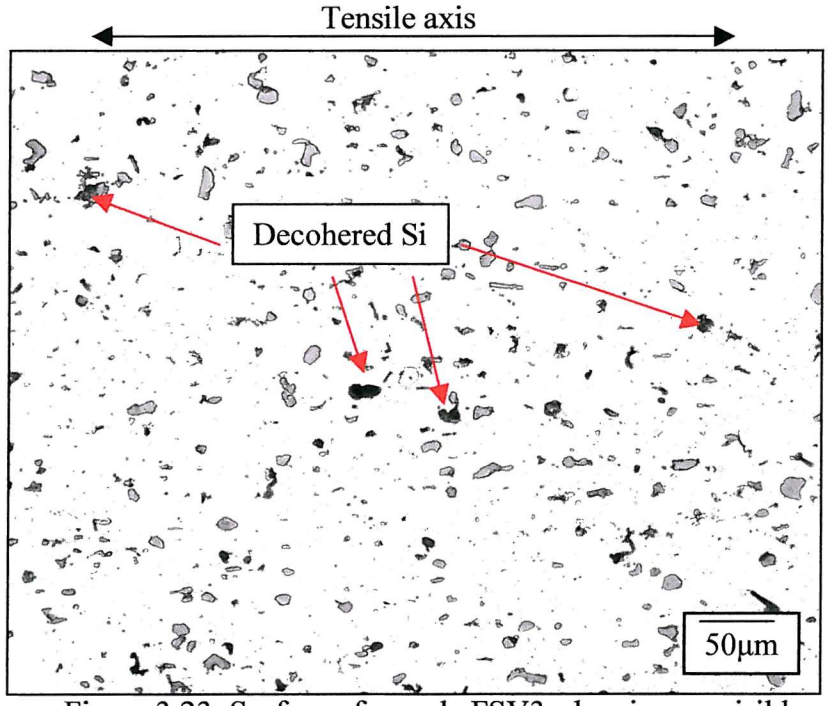

Figure 3.23: Surface of sample FSV3, showing no visible cracking, but several decohered Si-phases

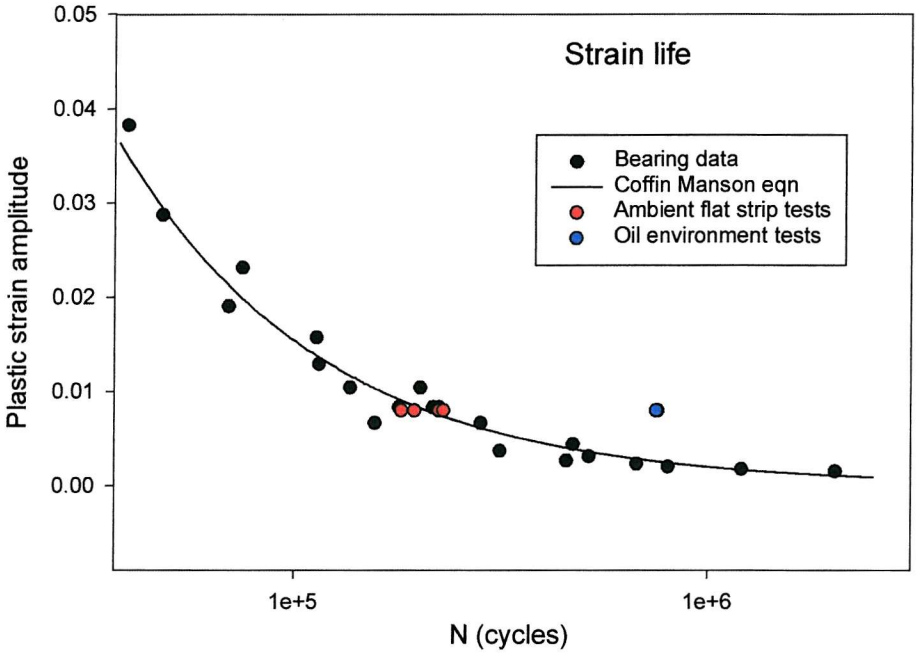

Figure 3.24: Oil environment flat strip test results plotted on strain life curve determined from bearing tests

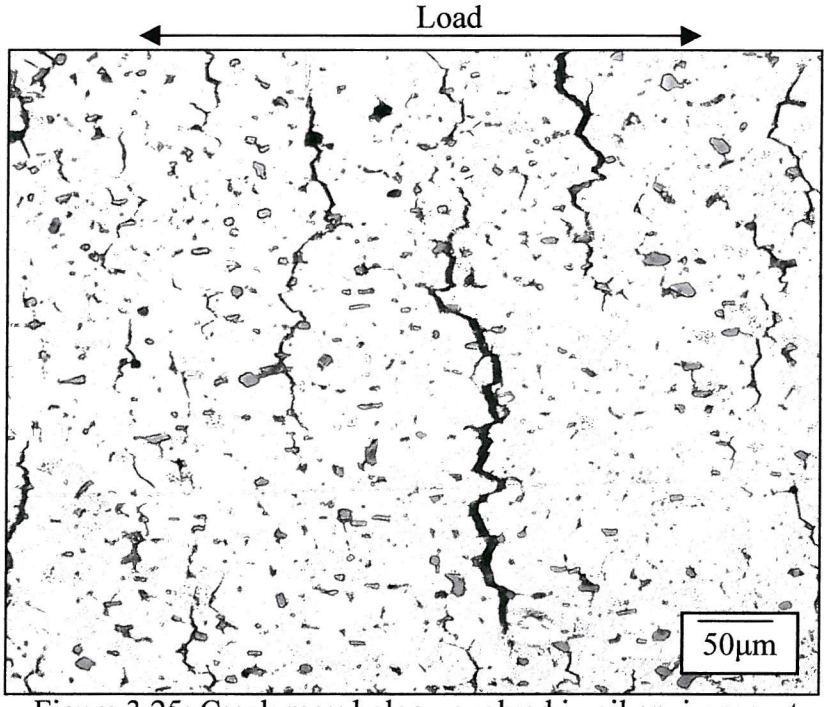

Figure 3.25: Crack morphology evolved in oil environment tests, very similar to that produced under ambient conditions

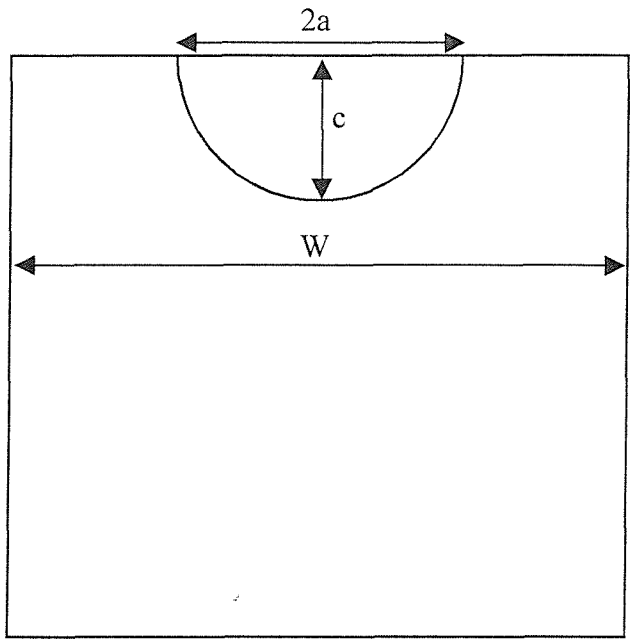

Figure 3.26:Crack geometry used for short crack ΔK calculations using the equation proposed by Scott and Thorpe

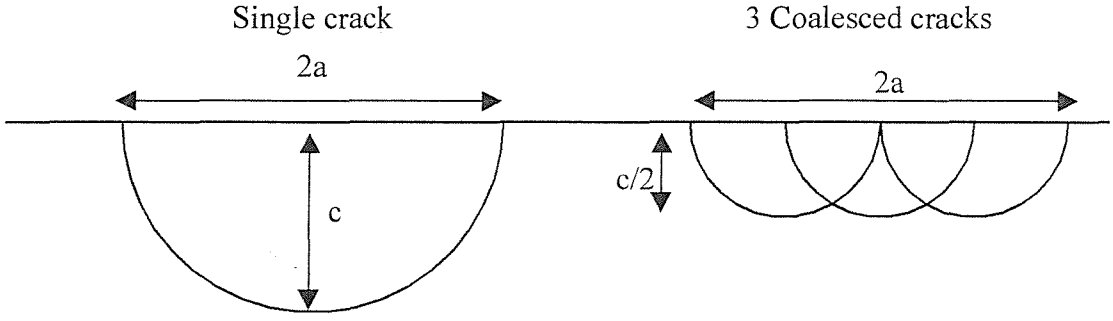

The greater the number of coalesced cracks, the greater the surface length (a) for a given depth (c). Hence as cracks coalesce the a/c ratio increases.

Figure 3.27: Effect of multiple crack coalescences on short crack a/c ratio

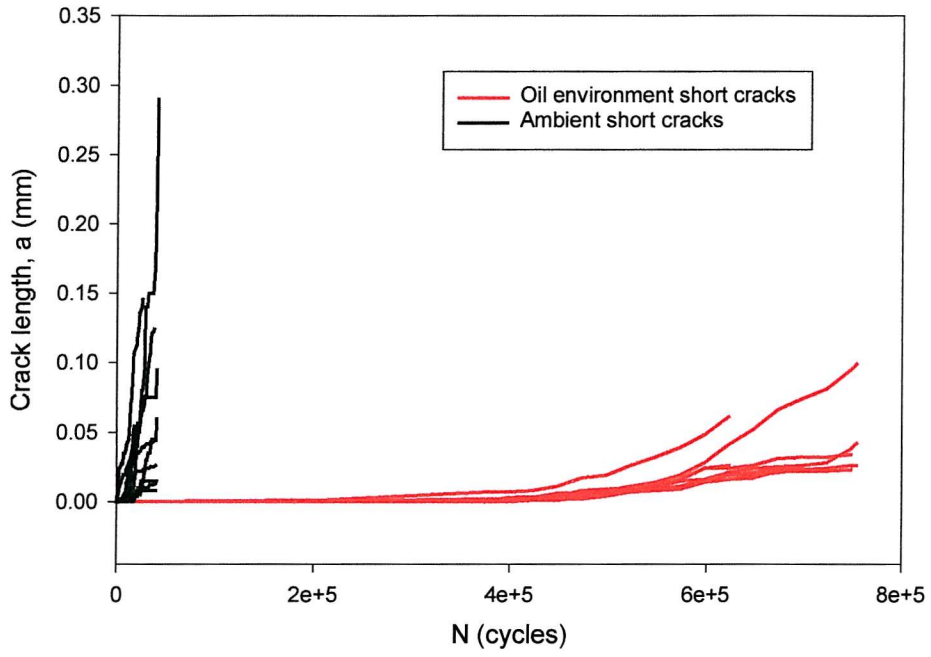

Figure 3.28: a vs. N plot showing retarded crack growth in samples tested in oil

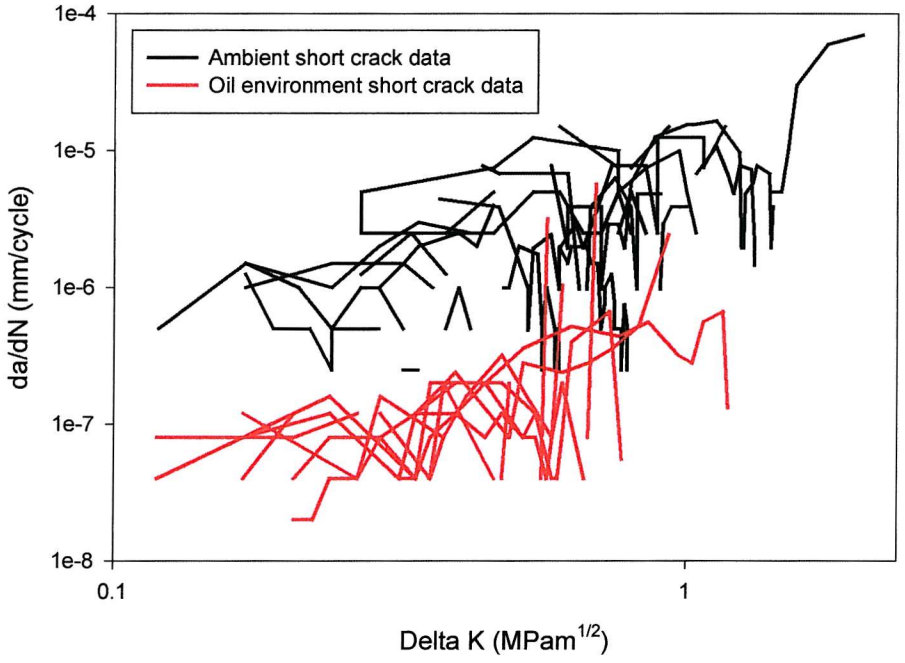

Figure 3.29: Short crack growth rate vs ΔK again showing retarded growth rate in oil samples

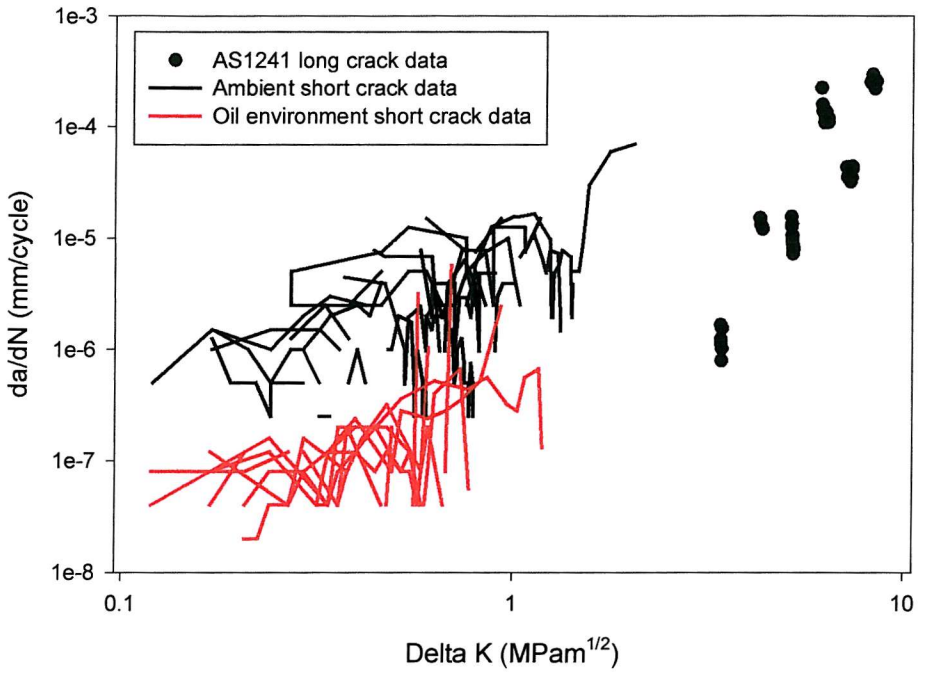

Figure 3.31: Comparison of short crack growth rate data with CCT long crack behaviour

4.0 INVESTIGATION OF PREFERENTIAL INITIATION SITE LOCATION

This chapter reports on analytical techniques applied to investigate preferential initiation site location. It was apparent from the experimental studies that generally points of fatigue crack initiation are associated with the interfaces between the Si secondary phases and the matrix. Using first tessellation approaches and subsequently microstructural scale finite element modelling, it was hoped to further refine this understanding.

4.1 Statistical Characterisation of Initiation Sites

Using the replica record collected for the ambient flat strip short crack fatigue tests, it was possible to identify areas of microstructure containing crack initiations. A total of 10 regions were randomly selected, each containing approximately 300 discrete Si secondary phases. As with the earlier tessellation work, these were converted to binary images by hand. Tessellated structures were constructed using the finite body tessellation approach developed by Boselli *et al*[1]. The cells produced by this method were divided into three populations according to behaviour of the contained particle, as shown in Figure 4.1.

- Initiating Cells – those cells containing a particle at which a fatigue crack initiated
- Bordering Cells – those cells sharing a common boundary with an initiating cell (near neighbours of initiating particles)
- Background Cell – those cells neither containing nor sharing a boundary with a cell containing a fatigue crack initiation.

Subdividing the cell population in this manner gave a total of 163 initiating, 810 bordering and 1965 background cells. The same measures as described earlier in Section 2.3.2 were then applied to these cells, the mean and standard deviations for each measure are given in Table 4.1, whilst frequency histograms are given in Figures 4.2 to 4.12.

Table 4.1: Mean values and standard deviation for tessellation measurement on initiating, bordering and background cells.

Type	Object area (μm^2)	Object aspect ratio	Object angle (rad)
Initiating	12.17 ± 11.54	1.49 ± 0.36	0.90 ± 0.41
Bordering	6.22 ± 6.73	1.50 ± 0.41	0.88 ± 0.42
Background	4.24 ± 5.19	1.48 ± 0.50	0.87 ± 0.4

Type	Cell area (μm^2)	Cell aspect ratio	Cell angle (rad)
Initiating	113.65 ± 58.59	1.48 ± 0.42	0.88 ± 0.42
Bordering	87.59 ± 53.45	1.61 ± 1.22	0.79 ± 0.44
Background	62.46 ± 43.21	1.70 ± 1.51	0.77 ± 0.44

Type	Local area fraction	Number of near neighbours	Nearest neighbour distance (μm)
Initiating	10.48 ± 6.41	6.39 ± 1.38	2.61 ± 1.87
Bordering	6.98 ± 5.34	6.00 ± 1.45	2.53 ± 1.92
Background	6.93 ± 5.73	5.52 ± 1.42	1.94 ± 1.7

Type	Mean near neighbour distance (μm)	Nearest neighbour angle (rad)
Initiating	7.59 ± 2.5	0.73 ± 0.44
Bordering	7.30 ± 2.64	0.79 ± 0.46
Background	6.03 ± 2.56	0.83 ± 0.45

First considering the object area, it was seen that generally the object area (Si particle size) is higher in initiating cells than bordering cells and that this in turn is higher than background cells. Similar observations were made for cell area, where again the initiating cells were found to be generally larger than the bordering cells, and these in turn larger than the background cells. These trends were revealed in terms of both higher mean values and as discernible shifts in the frequency distribution. Given these results, it is unsurprising to see a similar trend in the distributions of mean near neighbour distance.

When considering the local area fraction (object area/cell area), it was seen that the values for the bordering and background cells were very similar, whilst that for the initiating cells was considerably higher (c.f. L.A.F initiating cells =10.5, L.A.F bordering/background cells ~6.95). These results indicate that initiating particles tend to be larger than the background population and more distant from their immediate neighbours.

No discernible differences were seen in the histograms of the angle or aspect ratio measures, other than roughness in the initiating cell distributions caused by the small number of initiating cells compared to the other two populations.

4.2 Multiphase Microstructure Characterisation Techniques.

In addition to the tessellation approaches discussed in Chapter 2, further insight into nucleation type events may be obtained through microstructural scale modelling. Historically the majority of research in this area has focussed on so called mean field approaches and using these techniques to predict the bulk properties of inhomogeneous materials. Generally these methods aim to approximate a section of the real inhomogeneous material with a "virtual" homogeneous material having the same macroscopic properties. This reference volume can then be used to predict the overall material response to external loading. These approaches have little value in the current work, where bulk material "homogeneous" properties are already determined, and rather it is the highly localised stress and strain fields surrounding individual secondary phases or inclusions which are of interest. These fields may be evaluated using some of the finite element micro-mechanical approaches discussed in subsequent sections

4.2.1 Classic mean field methods.

Early approaches to modelling inhomogeneous materials are usually based on the work of Eshelby[2,3] who evaluated the stress and strain fields of a homogeneous material in which a sub-region undergoes a transformation such that it no longer fits into its previous space in the parent material. Eshelby showed that if a homogeneous elastic inclusion in an infinite matrix is subjected to a uniform "stress free" strain ε_t, then uniform stress and strain fields are set up within the constrained inclusion. The constrained strain ε_c is given by the expression in Eqn 4.1.

$$\varepsilon_c = S_e \varepsilon_t \tag{4.1}$$

where S_e is the Eshelby tensor. This result can be used to model the stress fields within a typical matrix-inclusion composite. The approach is to replace each inclusion

with a region of matrix material of identical size and shape, on which a fictitious "equivalent" strain is made to act. Hence, by superposition, the total strain in the inclusion will be the applied strain and an additional term ε_c due to the constraining effects of the surrounding matrix. Unfortunately this approach is only easily applicable to elliptical inclusions, and evaluating the effect of several particles is extremely complex. More complex methods are required to evaluate the stress/strain interactions of multiple particles of realistic geometry.

4.2.2 Periodic or unit cell models.

Periodic microfield approaches (PMA) aim to describe both the macroscale and microscale behaviour of an infinite sheet of inhomogeneous material by creating a model material based on a periodic phase arrangement. Commonly the stress and strain fields are examined by dividing the microgeometry into periodically repeating unit cells. The analysis may then be limited to a single cell without loss of information. Herein lies the major disadvantage of this approach; since the geometry is periodic, by definition the loading, deformation and constraint must also be periodic. Hence it is not possible to model macroscopic features such as free boundaries, cracks or highly random (non periodic) phase arrangements using PMA.

The unit cells themselves may be of generic phase arrangement or be based as closely as possible on the phase arrangement of a given sample and may vary widely in complexity; two simple cells are shown in Figure 4.13, whilst a more complex example is shown in Figure 4.14. Several methods are available for evaluating the microfields within such a cell, the most common being the finite element method, since it affords the greatest flexibility in specifying material behaviour.

Studies in the literature which apply FEM to PMA unit cells typically fall into one of three approaches. Most commonly the cell is broken down into a large number of standard continuum elements, and the mesh designed in such a way that element boundaries fall at the interfaces between constituent phases. Figure 4.15 shows an example of this method applied to a complex unit cell proposed by Nakamura and Suresh[4]. This approach has the advantage that almost any commercially available FE package may be used for its solution, and in principle any microgeometry may be modelled. However the success of the model is dependent on the quality of the mesh produced, which, due to its complexity is likely to require considerable time and

complex pre-processing. Further examples of this approach are given in the work of Plankensteiner *et al*[5] and Sangani *et al*[6].

A second approach involves breaking the cell down into a small number of complex hybrid elements specifically formulated for the problem. Typically each element of this type consists of a single inclusion surrounded by a region of matrix. An early example of this approach is given in the work of Accorsi[7]. However the approach was considerably enhanced by Ghosh *et al*[8], who proposed the Voronoi element method. In this approach the finite element mesh is generated directly from the results of a Dirichlet tessellation, making it one of the most advanced and flexible methods available. A typical mesh generated using the Voronoi element method is shown in Figure 4.16.

A third method is applied to meshes generated from digital images of the actual sample microgeometry. It involves using a simple square mesh of the same resolution as the digital image, each element is then assigned to one of the phases as indicated by the grey value of the corresponding pixel. This approach is easy to implement, however it does lead to the meshed phases having ragged edges, although Guldberg *et al*[9] report that this leads to acceptably small errors. Using this approach periodic cell models have also been developed in 3D using a hexahedral mesh, built up from a series of digital images produced after careful sectioning of the sample. Models of this type are often solved using Finite Difference (FD) or Fast Fourier Transform (FFT) methods, due to the simplicity and regularity of their meshing strategies; an example of this approach is given by the work of Moulinec & Suquet[10].

4.2.3 Embedded cell techniques.

Whilst PMA cells allow investigation of the microfields around individual phases, they are limited by periodicity constraints. Embedded cell approaches (ECA) overcome these whilst continuing to allow the investigation of the impact of macroscopic features on the intra cell microfields. ECA use a core region in which the material phases are modelled discretely, rather like a unit cell. Then, rather than applying periodic boundary conditions, the core region is surrounded by a large region of material of bulk material properties, to which far field loading is applied. An overall schematic of this type of model, as used by Chimani *et al*[11] is shown in Figure 4.17. Whilst the cores used in embedded cell models look similar to periodic cells,

they are not required to represent a periodic distribution. Hence they are applicable to a wider range of particle shapes and arrangements.

The outer embedding region serves to transfer the loading onto the core; Dong *et al*[12] report that this should be made approximately 25 times the area of the core, as is shown in Figure 4.18. Whilst ECA are not as computationally elegant as PMA, they do allow any microgeometry to be modelled whilst maintaining validity. Another advantage is that they allow investigation of the impact of macroscopic features on the microscopic stress/strain fields. Several researchers including Fischmeister *et al*[13] have created crack models with the crack body in the embedding region and the tip within the core, as shown in Figure 4.19, hence allowing investigation of the effect of secondary phases on the crack tip plastic zone.

4.3 Considerations for Microstructural FE Models

It has been demonstrated by previous researchers that the use of microstructural finite element modelling can provide a valuable insight into the local material behaviour under far field loading. Of the modelling approaches discussed, both PMA and ECA are capable of investigating the local stress/strain fields in a multiphase microstructure. Both approaches have advantages and disadvantages, PMA are more computationally efficient, since they do not require redundant elements in the form of an embedding zone, however they are limited in terms of periodicity constraints. ECA require more elements and may suffer from transient interface effects between core and embedding region (especially under elasto plastic conditions), although they allow any microgeometry to be modelled.

PMA were originally developed for fibre reinforced composites, which comprise reasonably periodic arrangements of identical inclusions. The secondary phases in the AS1241 material are neither periodic in distribution or regular in shape. A very large unit cell would be required to come close to representing this material on a pseudo periodic basis. This lack of regularity makes the AS1241 system unsuitable for PMA. Embedded cells are capable of modelling a smaller region of material whilst maintaining validity (due to the large amount of homogeneous material to provide constraint). This smaller core region may then be meshed at a high density to create a good representation of the complex microgeometry present in this material.

Since the success of a microstructural model is primarily dependent on it being an accurate representation of the sample material, and it was not felt this could be achieved using PMA, an ECA was adopted for the microstructural modelling program undertaken. To ensure a representative section of matrix is modelled together with each secondary phase a tessellation approach was adopted. This is similar to the Dirichlet method proposed by Ghosh *et al*[8], but without the restrictions on particle size and shape imposed by the Voronoi element. The implementation of this procedure is described further in the subsequent sections.

4.4 Embedded Cell Microstructural Model Methodology

Using the same terminology as for the earlier tessellation studies, it was hoped to investigate the microfields surrounding the initiating particles, and compare these with those produced around the bordering and background cells. To achieve this core regions based upon the tessellation results were created, comprising one or more initiating cells, the associated bordering cells, and a single loop of background cells. Typically this resulted in models comprising 30-40 particles, two examples of these models are shown in Figure 4.20. The model geometry was determined by approximating each particle and cell boundary by a polygon. A smoothing routine was then applied to the polygons approximating the secondary phases to round off the sharp corners, this process is shown in Figure 4.21. The smoothing process was achieved by filleting adjoining pairs of lines with a fillet radius equal to a quarter of the length of the shorter line. This filleting factor appears to approximate the shapes of the spheroidal or cuboidal Si secondary phases reasonably well.

In this preliminary investigation no attempt was made to model the properties of the interface between Si phase and the matrix, these components were assumed to be perfectly bonded. The models were meshed using 8 node quadrilateral elements formulated for plane stress (to simulate a free surface). Figure 4.22 shows the mesh refinement along the interfaces between the Si phases and the matrix, the mesh was increased at these points, since they represent sites of likely crack initiation. Recalling that the tessellation, and hence the modelled geometry only considered the Si secondary phase distribution, the Sn phases were added by altering the properties of the predefined elements to simulate the Sn phases associated with the Si phases, as

shown in Figure 4.23. Typically each completed core region required ~6000 elements, an example is shown in Figure 4.24.

Multi-linear isotropic hardening curves, the construction of which is described in Appendix II, were used to govern the behaviour of the Sn phase and the matrix, whilst it was recognised that the Si, due to its high yield point (c.f σ_y Si ~345MPa (compressive), σ_y other constituent phases 21-56MPa) would remain elastic throughout the analysis. The material properties used for each material are summarised in Table 4.2.

Table 4.2: Material properties used for embedded cell models

Material	Elastic modulus (GPa)	Poisson's ratio	Yield stress (MPa)	Ultimate tensile stress (MPa)	Elongation to failure (%)
Al alloy matrix	70	0.3	56	172	21
Si secondary phase	420	0.14	N/A material remains elastic throughout the analysis		
Sn secondary phase	41.4	0.33	21	220	39
AS1241 embedding material	69.8	0.33	56	172	19

N.B. AS1241 data obtained from sponsoring company and tensile testing program described in Chapter 2, mechanical property data for other materials is taken from the Metallic materials specification handbook[14] and the Metals handbook Vol.2[15].

An embedding region is required to transfer the load and constraint to the central core. This was made 25 times the size of the core cell in line with the recommendations of Dong *et al*[12]. This region was again meshed using 8 node quadrilaterals, although at a considerably lower density than in the core region. Since the material in this region has the properties of monolithic AS1241, its response was governed by the experimentally determined hardening curve shown in Figure 2.42.

At this preliminary stage it was not necessary to precisely simulate the loading applied during the fatigue testing, rather it was intended to observe effects of the particle population on the intra core stress/strain microfields under arbitrary loading. Hence the model was loaded monotonically in the direction shown in Figure 4.24, the

nodal displacement being calculated to give an overall strain in the y direction of 0.2%. This is just sufficient to initiate plastic yielding in the AS1241, Sn secondary phases and the Al alloy matrix material. The model was then solved incrementally using the ANSYS5.5 finite element package, typically requiring ~80 increments before reaching convergence.

4.5 Initial Results From Embedded Cell Modelling

Figure 4.25 shows the Von Mises stress fields produced within the Al alloy matrix in the core region. It is clear that the secondary phases have an impact on this distribution. However it is also clear that some interference is caused by the interface between core and embedding region. This type of interface effect is to be expected when using ECA to model elasto-plastic situations. Following the advice of Bohm[16], the results from the edge cells (i.e. the ring of background cells) were ignored. Figure 4.26 shows the same stress fields after the results from the outer row of background cells are removed, this considerably reduces the interference caused by interface effects, thus making the particle interactions clearer. Comparing the resultant stress field with the position of crack initiations, some correlation can be seen between points of high stress and crack initiation sites, however it can also be seen that several points of high stress are not associated with initiation events.

It is known that fatigue crack initiation is generally caused by high shear deformation along slip bands[17], hence a correlation between shear strain and crack nucleation points may be evident. Figure 4.27 shows the plastic x-y shear strain evolved in the core region matrix, comparing this with the pattern of crack initiation sites and directions of subsequent growth a reasonable correlation is observed. Further examples comparing the positions of crack initiation sites with point of high positive plastic shear strain are shown in Figures 4.28 and 4.29.

It can be seen that the Si-secondary phases appear to cause considerable strain concentrations in the core region matrix. Figures 4.30 and 4.31 show the stress and strain fields surrounding a single particle. It can be seen that a large stress discontinuity is present along the Si/matrix interface, and that this in turn is causing high strain levels, as the matrix stretches around the harder Si phase. It appears that this stretching effect was more pronounced around larger Si secondary phases.

4.6 Investigation of Si Phase Size on Matrix Stress/Strain Fields

The magnitude of the matrix strain caused by a given individual Si secondary phase appears to be linked to the size of that phase. To investigate the dependence of matrix strain on Si secondary phase size, a very simple ECA finite element model was constructed. Shown in schematic form in Figure 4.32, each model comprised a simple circular core region of fixed radius 20μm containing a single circular Si phase of variable radius. This core was embedded in material of bulk AS1241 properties. A series of models were solved to investigate the effect of varying the size of the Si particle over the range seen in experimental samples (1-10μm in radius). In each case the model was loaded monotonically to give a 0.2% strain in the y direction (as with the earlier embedded cell models).

Figures 4.33 and 4.34 shown stress and strain fields in the core region produced with a 10μm radius Si phase. It is clear from the stress plot that large discontinuities are present due to the difference in properties between the Si phase and the core matrix. It can also be seen that considerable core matrix strains are produced as it is stretched around the harder Si. At a Si phase radius of 10 μm the maximum matrix strain is more than 500% applied strain (c.f. $\varepsilon_{app} = 0.2\%$, $\varepsilon_{max} = 1.1\%$).

For each secondary phase size the maximum matrix stress and strain results were recorded and normalised against the values produced for a 1μm radius Si phase (smallest particle evaluated). The normalised matrix maximum stress and strain results are shown in Figure 4.35. It can be seen that increasing the secondary phase radius has little effect on the magnitude of the stress concentration caused produced in the matrix. In contrast the maximum strain was seen to rise considerably with increasing secondary phase radius.

4.7 Discussion

Using the tessellation package developed by Boselli *et al*[1], measurable differences were found between particles associated with fatigue crack initiation sites, the near neighbours of initiating particles and the background particle population. It was found that in general particles associated with crack initiation sites were larger,

and had a larger local area fraction than bordering and background particles. This larger local area fraction in initiating particles also results in a generally larger mean near neighbour distance. Thus it was seen that initiating particles tended to be large Si particles in reasonably Si-free areas of matrix.

A series of microstructural finite element models were created using an ECA and the geometric recommendations of Dong *et al*[12]. Initially these were created using tessellated sections of microstructure surrounding initiation sites as core regions. As these models were solved using elasto-plastic material models, some interface anomalies were seen between the core and embedding region. These make the results in the outer row of cells questionable, and hence they were ignored as recommended by Bohm[16]. It was seen that the secondary phases were exerting a considerable effect on the core matrix strain field, with high strain values being present where the matrix is stretched around the much stiffer Si phases. Although the loading used in these models was monotonic, and hence unrepresentative of the cyclic loading necessary to cause fatigue, a reasonable correlation was observed between points of high core matrix plastic shear strain and fatigue crack initiation sites. It is likely that the points of high plastic strain under monotonic loading are equivalent to the points at which plastic strain would be accumulated in the case of cyclic loading.

To investigate the effect of particle size on the magnitude of core stress and strain concentration, a further series of models were created and solved. These were much simpler than the previous set, comprising of a single circular Si phase in a circular core region. Whilst the size of the core region remained constant, a series of particle sizes were evaluated, in the radius range 1-10μm (equivalent to size range seen in actual microstructure). Comparing the results of this series of models it was shown that whilst the matrix strain remained fairly constant with increasing particle radius, the matrix strain increased markedly.

It is likely that the initiation of fatigue cracks is linked to this behaviour, since under cyclic loading, plastic strain will be accumulated at points along the interfaces between Si phases and the matrix. The magnitude of this strain has been shown to be related to particle size, hence generally larger particles will accumulate sufficient strain to cause crack initiation before smaller particles. This hypothesis is backed up by the tessellation results, which showed that initiating particles are generally considerably larger than the bordering and background populations.

4.8 Preliminary Conclusions

It was found using a tessellation approach that the Si secondary phases causing fatigue crack initiation in experimental samples were generally larger and more widely spaced than the background population. No effects of alignment or aspect ratio were detected. These observations were linked to the results of a number of microstructural finite element models, where it was shown that under loading the matrix material is stretched around the Si secondary phases causing high strain levels. It was further shown that the magnitude of this matrix strain surrounding a given particle is related to the size of that particle, higher strains being created by larger particles. This indicates that large Si particles are more likely to cause fatigue crack initiation since they create higher strains in the surrounding matrix.

Embedded cell models of section of microstructure were used to establish that a fair correlation exists between crack initiation sites and points of high matrix plastic strain. Further work is required on this subject to investigate the effects of cyclic loading and the resultant accumulation of plastic damage.

4.9 References

[1] J. Boselli, P.D. Pitcher, P.J. Gregson and I. Sinclair, Secondary phase distribution analysis via finite body tessellation, J. Microscopy, Vol. 195 pt.2 pp104-112, (1999)

[2] J.D.Eshelby, The determination of the elastic field of an ellipsoidal inclusion, and related problems, Proc roy soc V.241 pp376-396 (1957)

[3] J.D.Eshelby, The elastic field outside an ellipsoidal inclusion, Proc Roy soc pp561-569 (1959)

[4] T. Nakamura and S. Suresh, Effect of thermal residual stresses and fibre packing on deformation of metal matrix composites, Acta. Met. Vol.41 pp1665-81, (1993)

[5] A.F.Plankensteiner, H.J.Bohm, F.G.Rammerstorfer, V.A.Buryenko and G.Hackl, Modelling of layer structured high speed steel, Acta Mat V45 pp1875-87 (1996)

[6] A. Sangani and W. Lu, Elastic coefficients of composites containing spherical inclusions in a periodic array, J. Mech. Phys. Sol. Vol.35 pp.1-21 (1987)

[7] M.L.Accorsi, A method for modelling microstructural material discontinuities in a finite element analysis, *Int J num meth engng* 26 pp 2187-97 (1988)

[8] S.Ghosh, Z.Nowak and K.Lee, Quantitative characterisation and modelling of composite microstructures by voronoi cells, Acta mater V45 No6 pp2215-34 (1996)

[9] R.E.Guldberg, S.J.Hollister and G.T.Charras, The accuracy of digital image based finite element models, J.Biomech Eng 120 pp 289-95 (1998)

[10] H. Moulinec and P.Suquet, A fast numerical method for computing the linear and non linear mechanical properties of composites. C.R.Acad. Sci. Paris, serie II Vol. 318, pp 1417-1423, (1994)

[11] C.M. Chimani, H.J. Bohm and F.G. Rammerstorfer, On stress singularities at free edges of bimaterial junctions – A micromechanical study, Scripta mater. Vol.36, pp.943-947. (1997)

[12] M.Dong and S.Schmauder, Modelling of metal matrix composites by a self consistent embedded cell model, Acta Mat V44 No6 pp2465-78 (1996)

[13] H.F. Fischmeister, S. Schmauder and L.S. Sigl, Finite element modelling of crack propagation in WC-Co hard metals, Mat. Sci. Eng. Vol.106 pp.305-11, (1988)

[14] Metallic Materials Specification Handbook, Fourth Ed., Robert B. Ross, Chapman & Hall, London, (1992)

[15] ASM Metals Handbook Vol.2 - Properties and Selection: Nonferrous Alloys and Special-Purpose Materials, ASM International 10th Ed. (1990)

[16] H.J. Bohm, A short introduction to basic aspects of continuum micromechanics, Proc Frontiers for computational micromechanics in industrial and engineering materials: Ambient and high temperature deformation and fracture, Nat. Uni. Ireland, Galway, (1998)

[17] W.A. Woods, Formation of fatigue cracks, Philosophical magazine Vol.3 pp692-9, (1958)

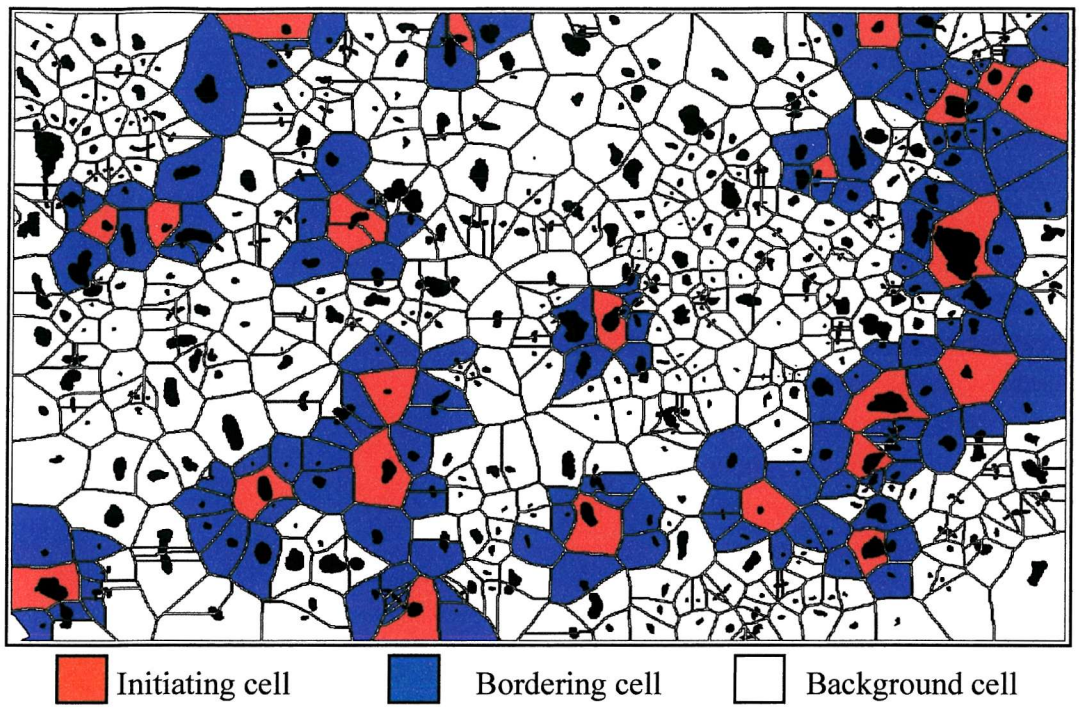

Figure 4.1: Typical post test region of tessellated microstructure, showing terminology used to describe three populations of Si secondary phases

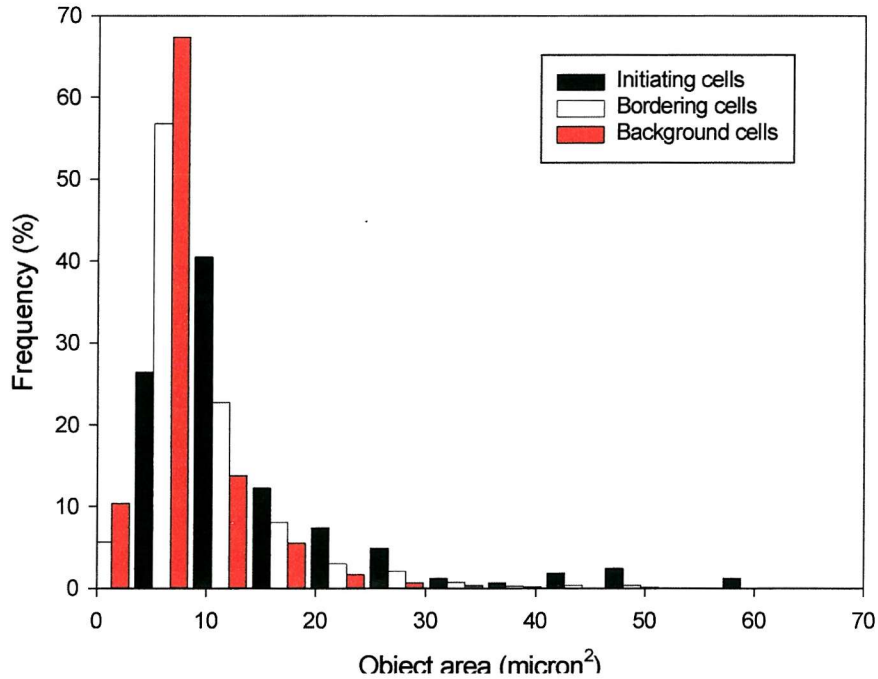

Figure 4.2: Histogram of object area

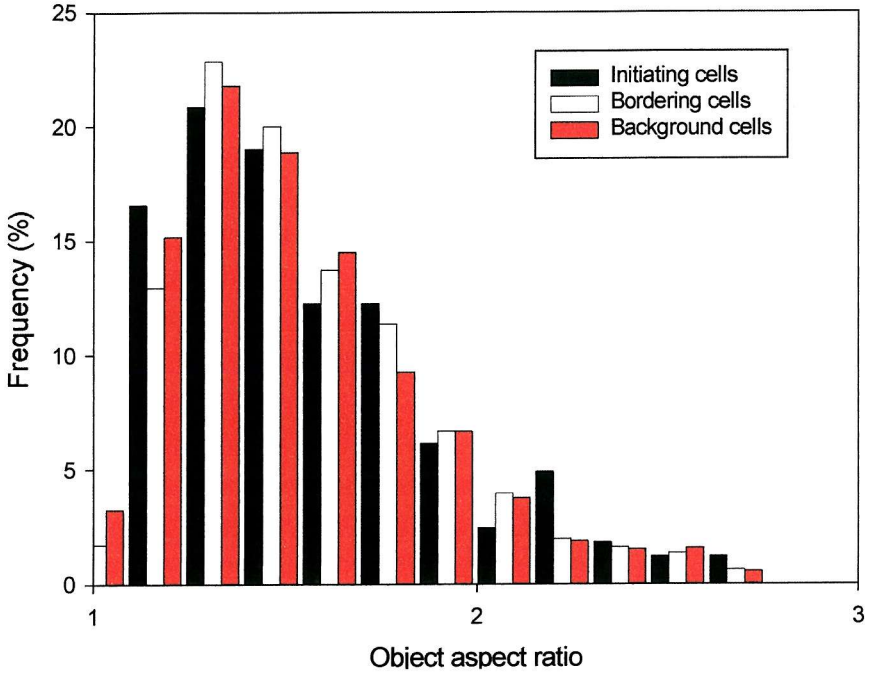

Figure 4.3: Histogram of object aspect ratio

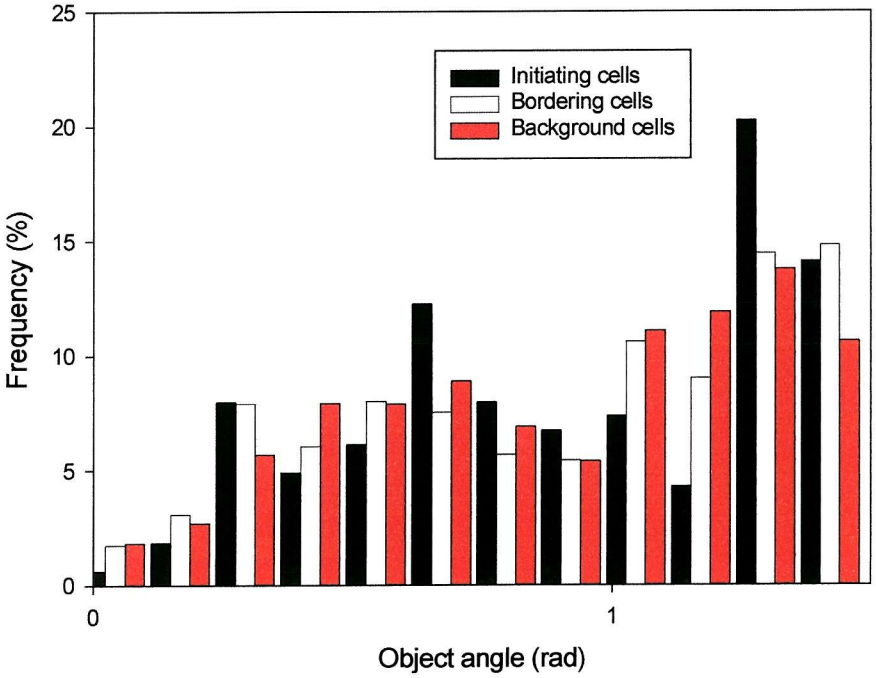

Figure 4.4: Histogram of object angle

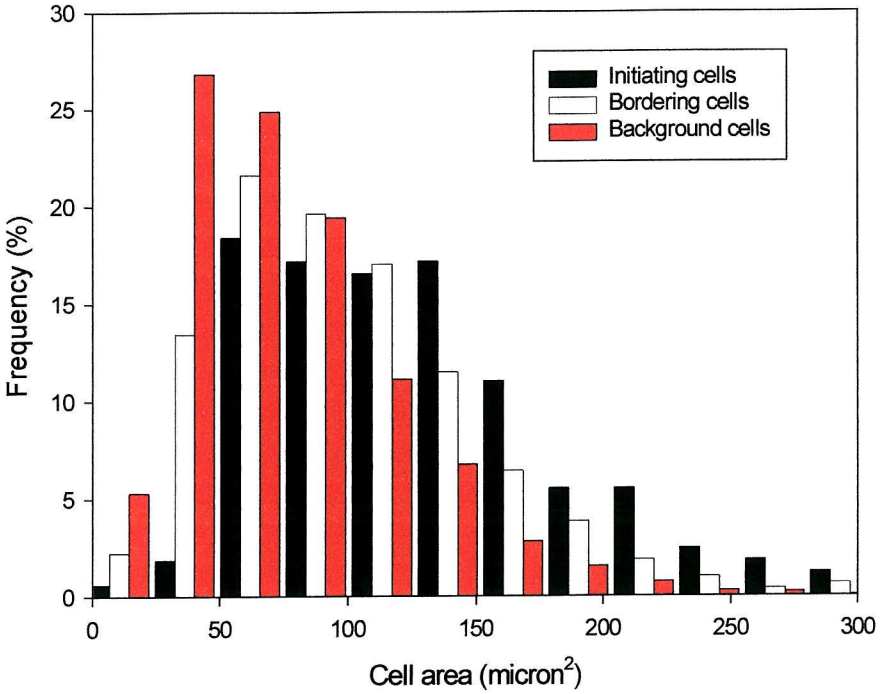

Figure 4.5: Histogram of cell area

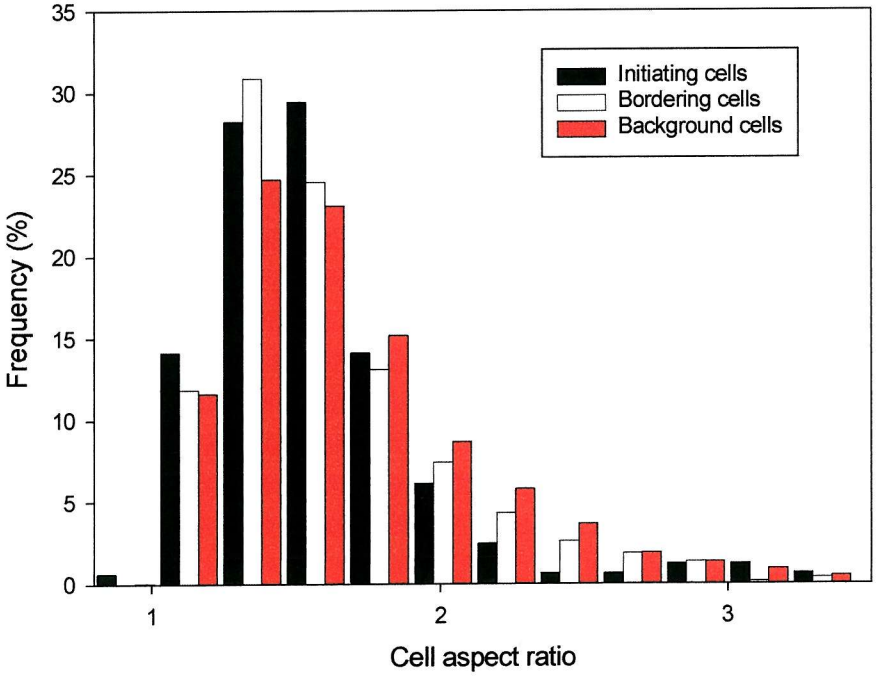

Figure 4.6: Histogram of cell aspect ratio

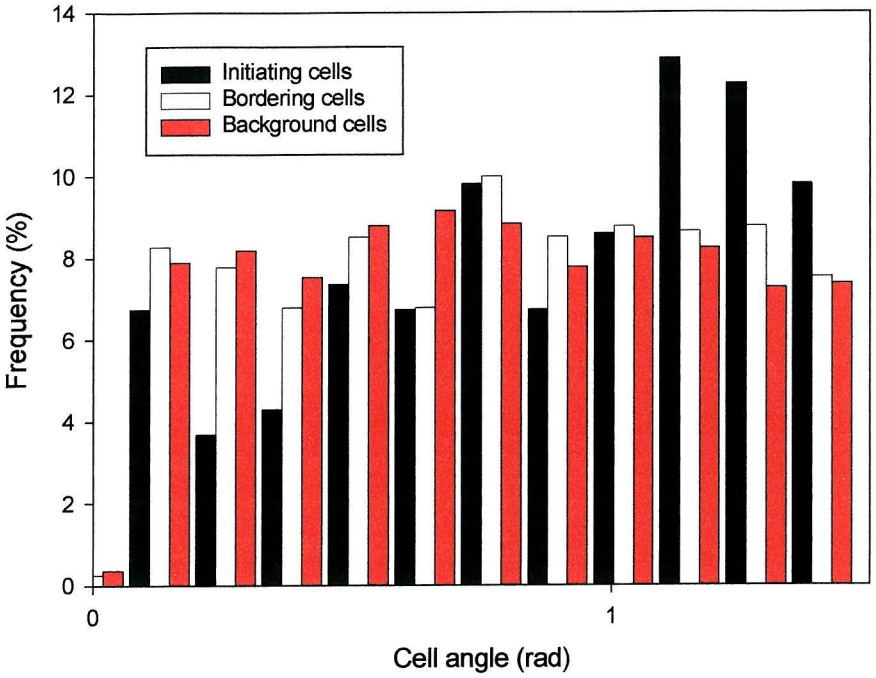

Figure 4.7: Histogram of cell angle

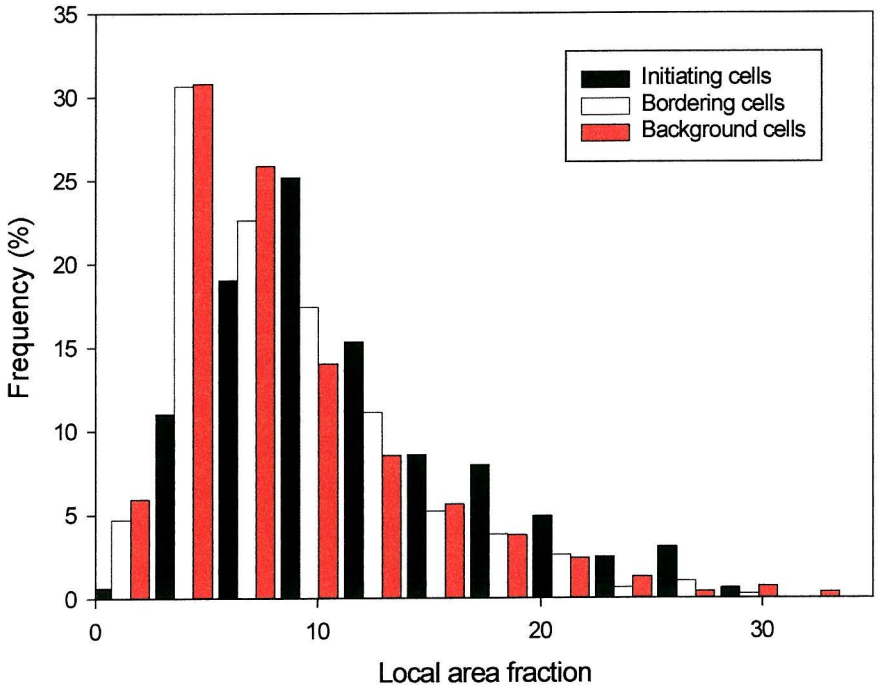

Figure 4.8: Histogram of local area fraction

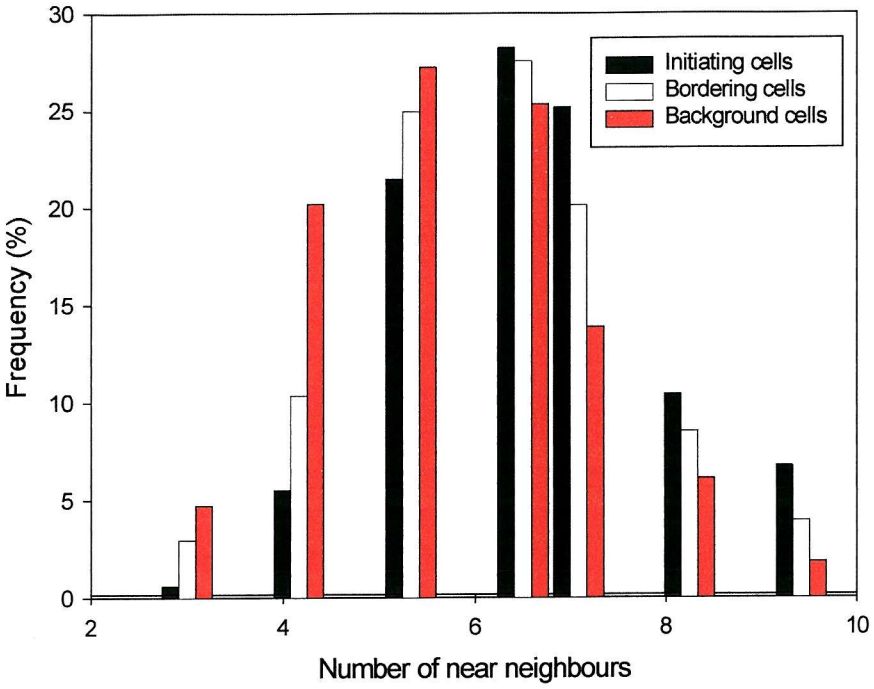

Figure 4.9: Histogram of number of near neighbours

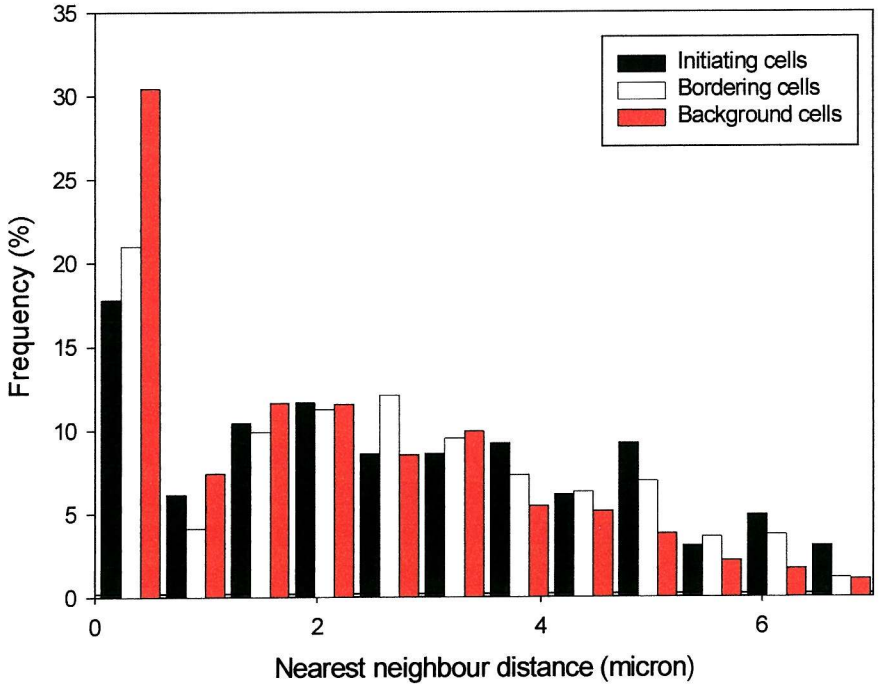

Figure 4.10: Histogram of nearest neighbour distance

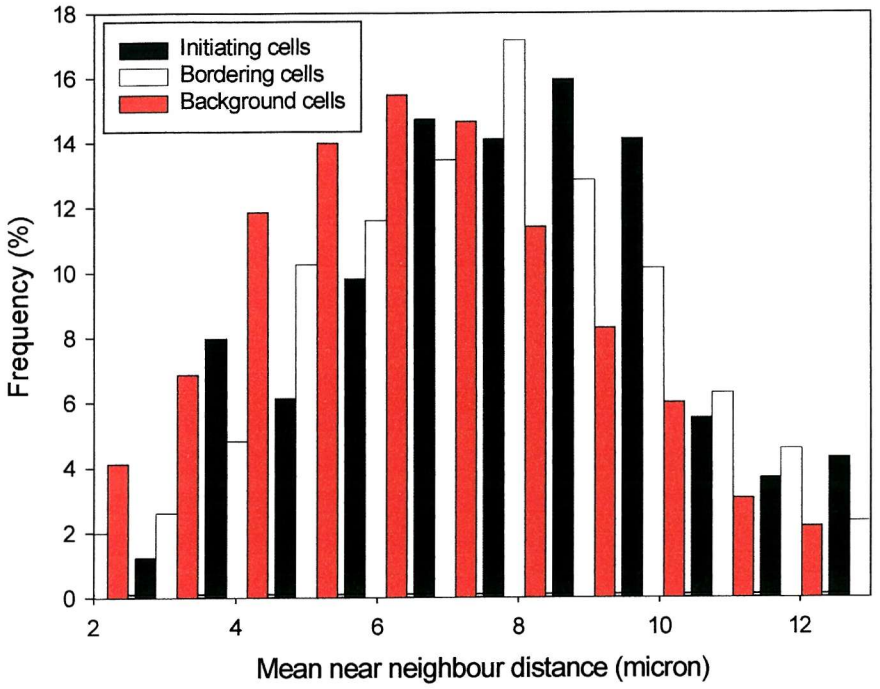

Figure 4.11: Histogram of mean near neighbour distance

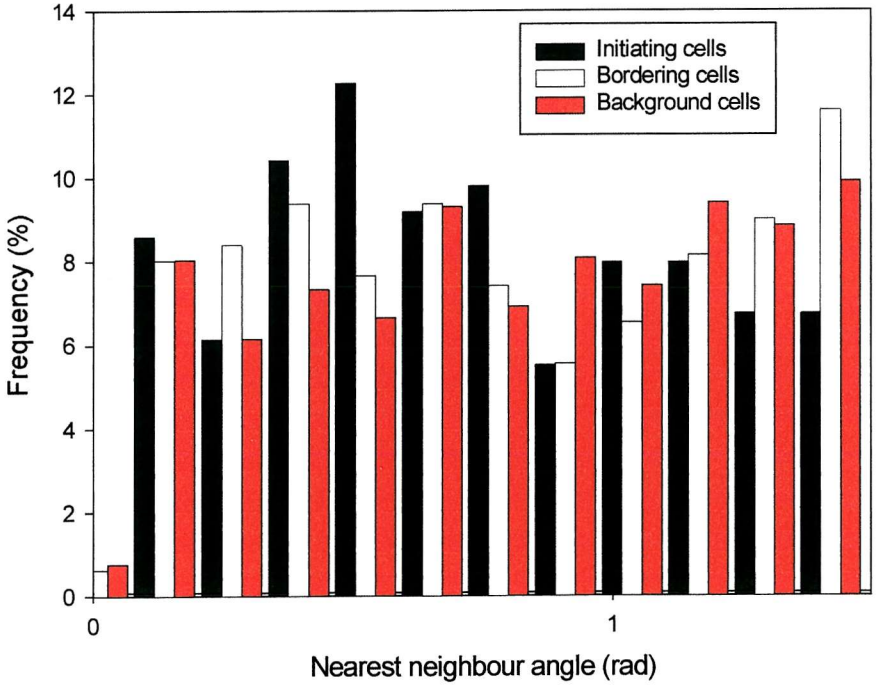

Figure 4.12: Histogram of nearest neighbour distance

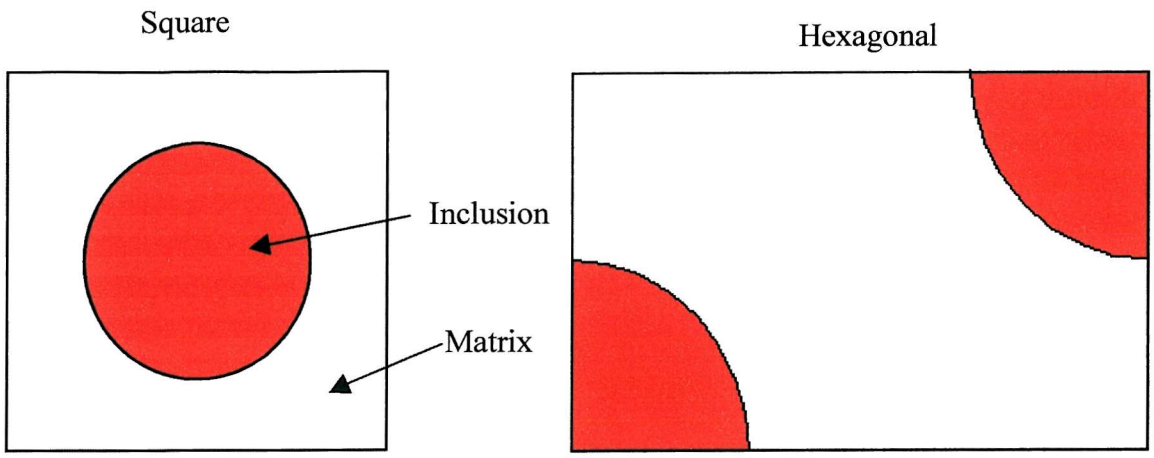

Figure 4.13: Simple periodic unit cells

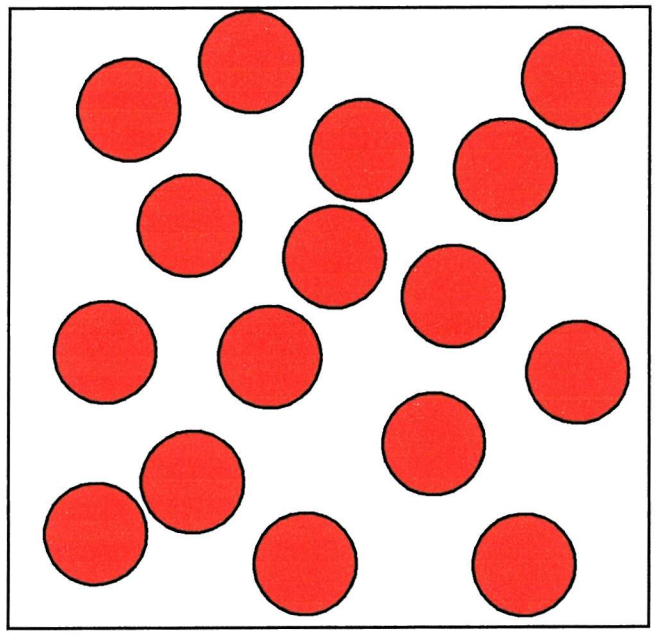

Figure 4.14: Example of complex unit cell

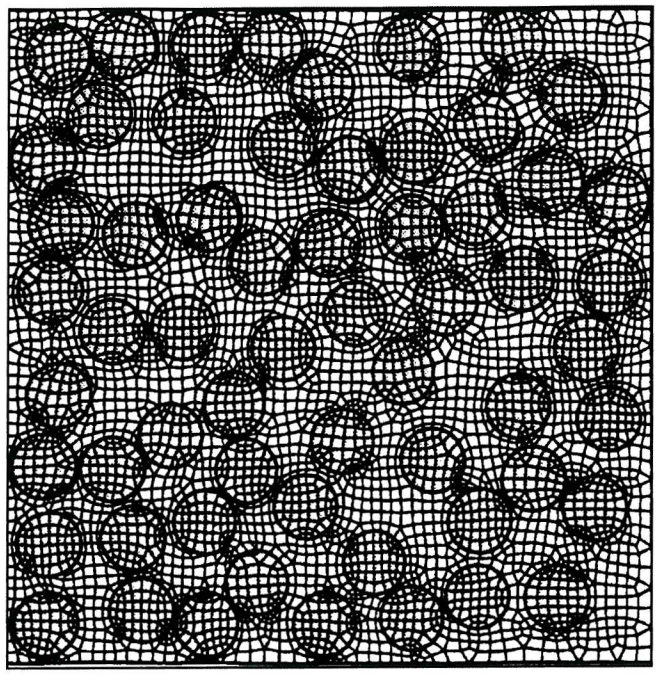

Figure 4.15: Complex unit cell meshed using conventional finite elements (Nakamura & Suresh 1993)

Voronoi element meshes often created on the basis of Dirichlet tessellations (Ghosh et al 1996)

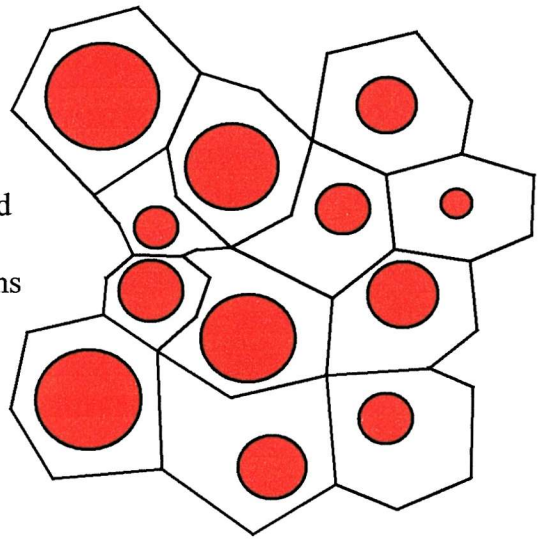

Each Voronoi element comprises a single inclusion and a section of matrix material

Figure 4.16: Typical mesh created using Voronoi elements

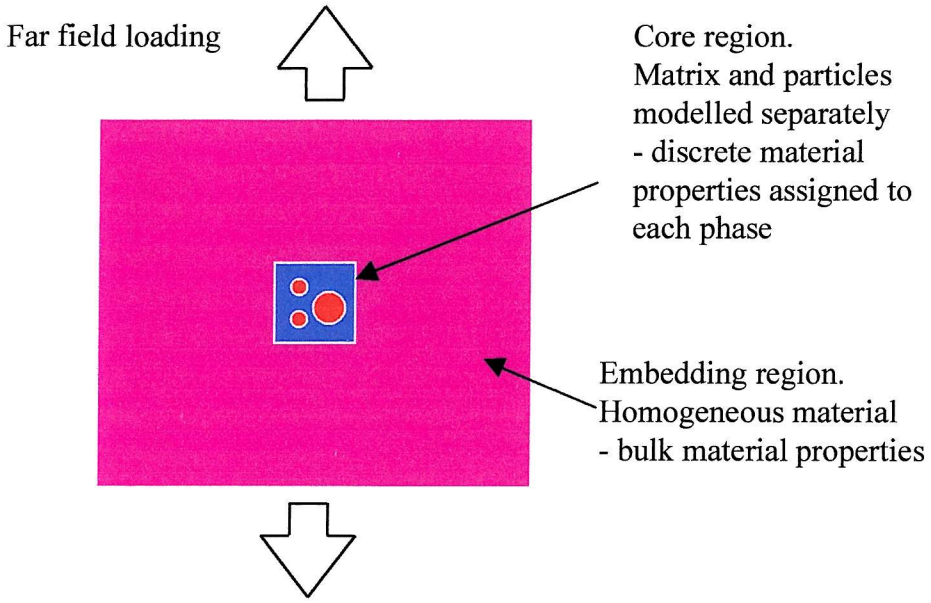

Figure 4.17: Embedded cell model geometry

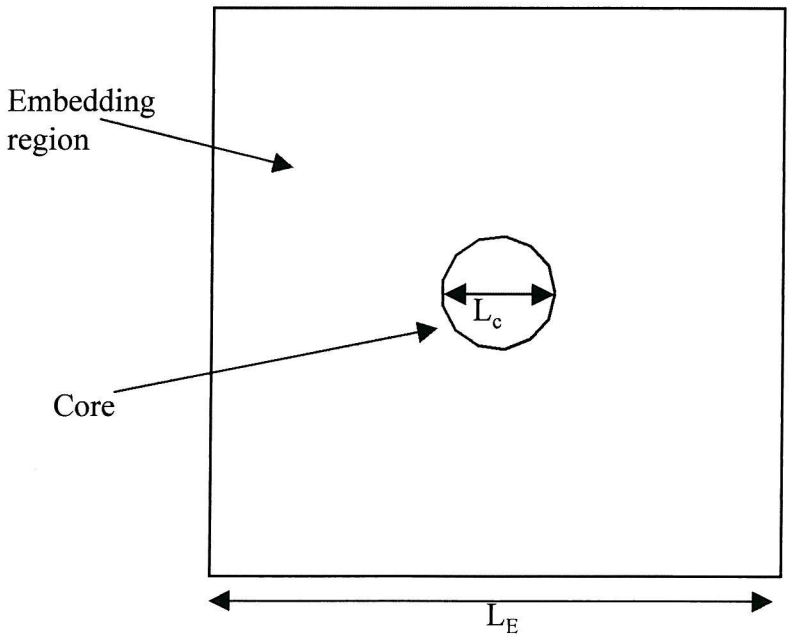

Figure 4.18: Relative sizes of core and embedding regions should be arranged such that $L_E/L_C = 5$

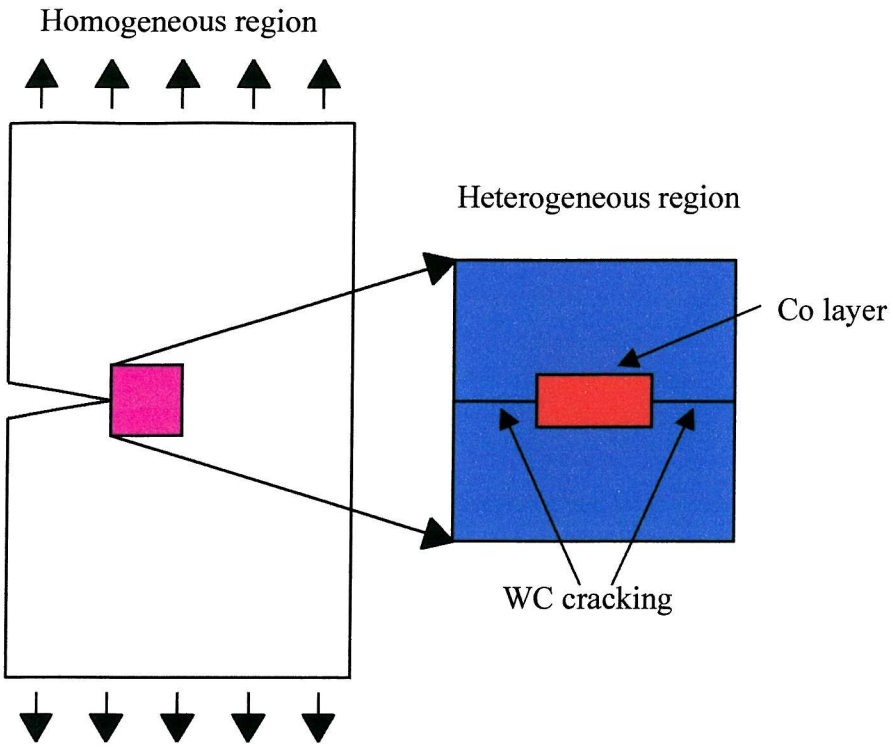

Figure 4.19: Embedded cell model of crack propagation in WC-Co (Fischmeister et al 1988)

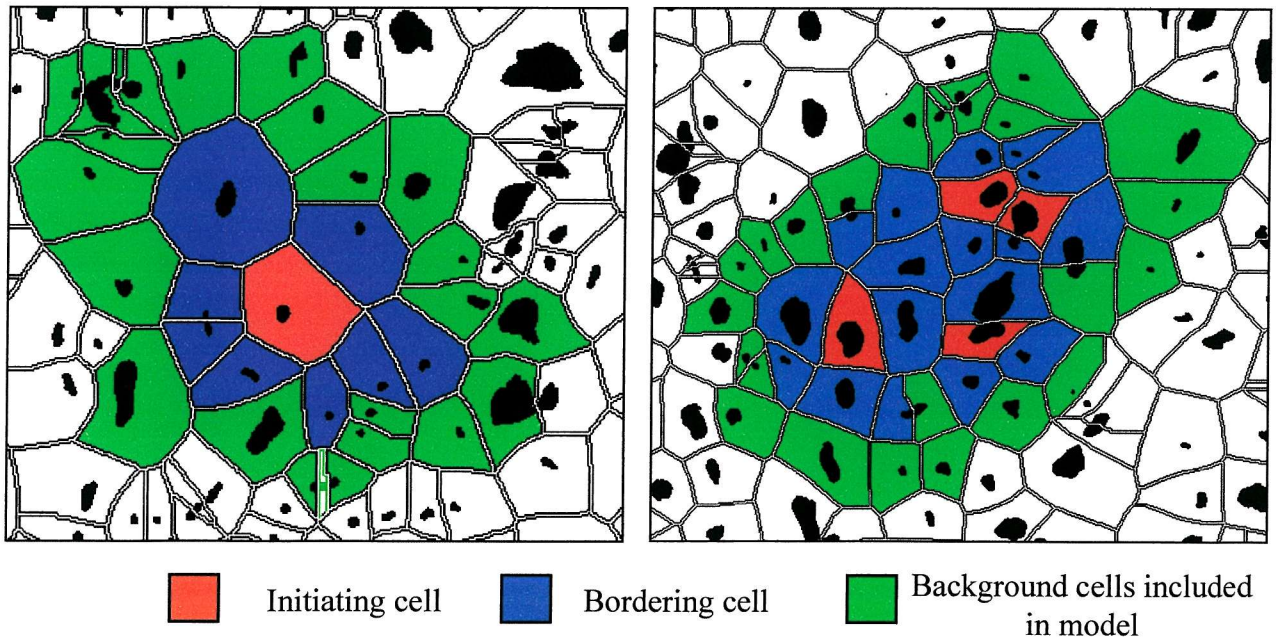

Figure 4.20: Two examples of core regions used in embedded cell microstructural finite element modelling

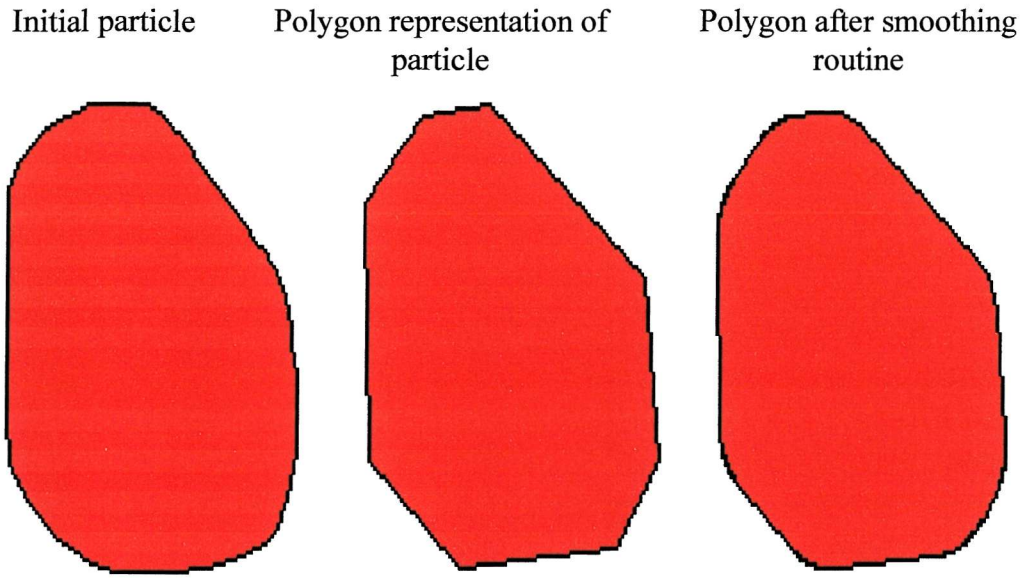

Figure 4.21: Routine used for creating FE representation of secondary phases

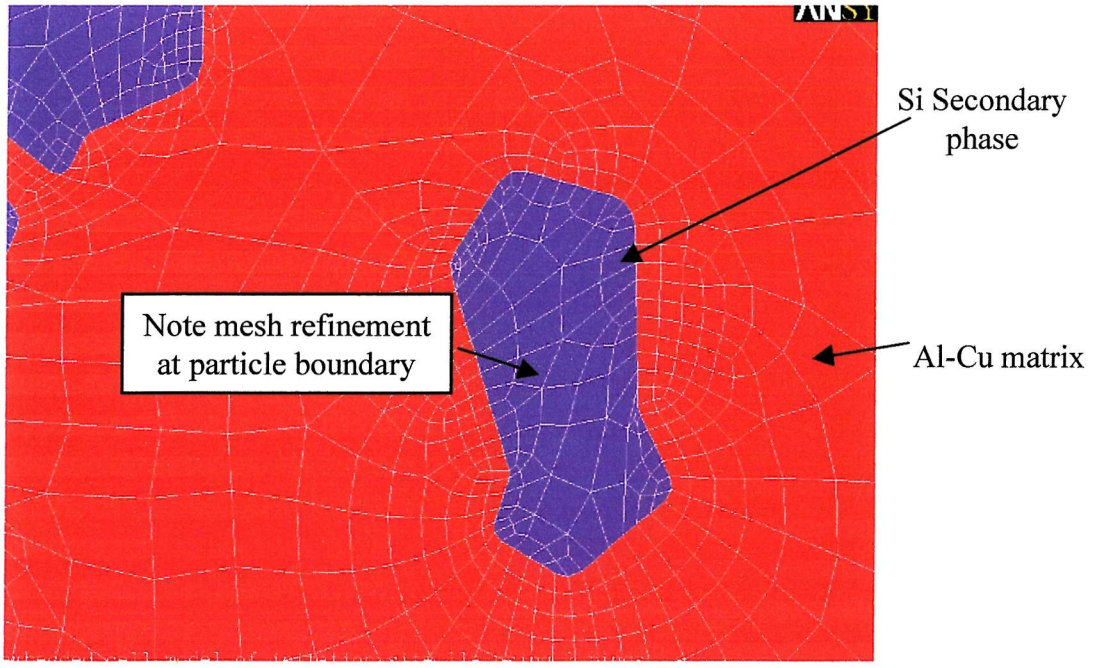

Figure 4.22: Meshing strategy, showing refinement at interfaces between matrix and Si secondary phases

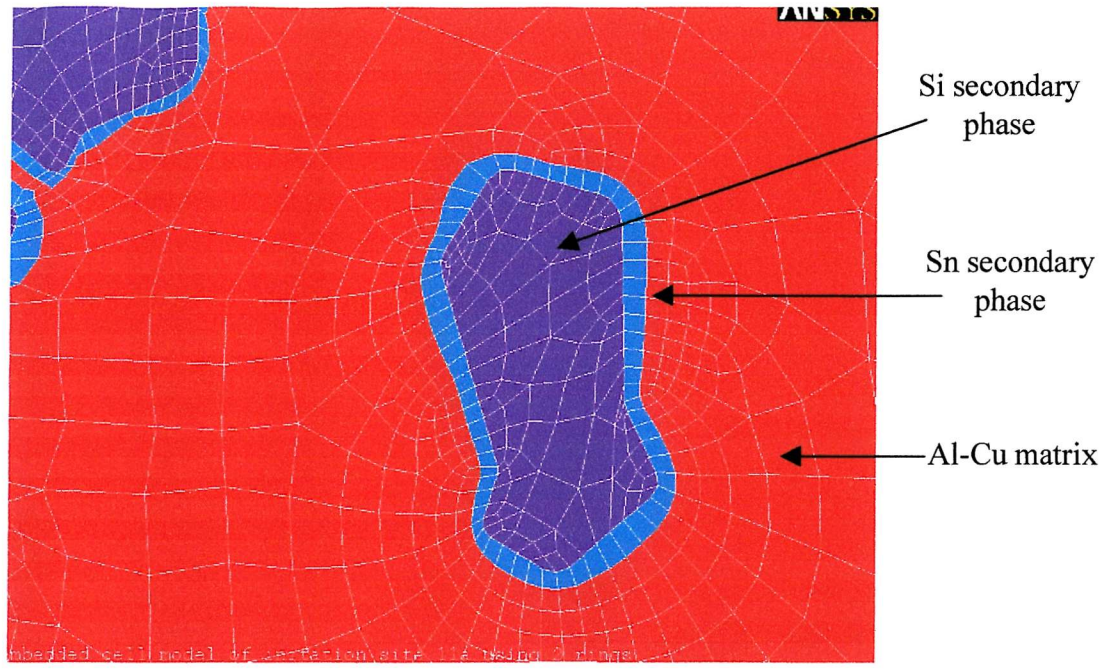

Figure 4.23: Method for representing Sn secondary phase associated with Si

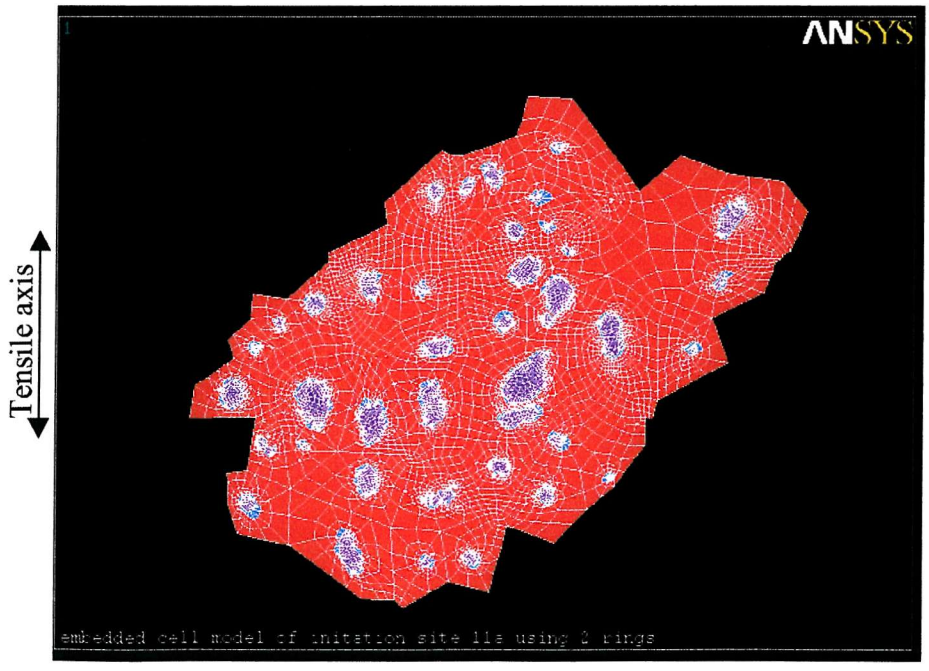

Figure 4.24: Example of core region, showing completed mesh ~6000 elements

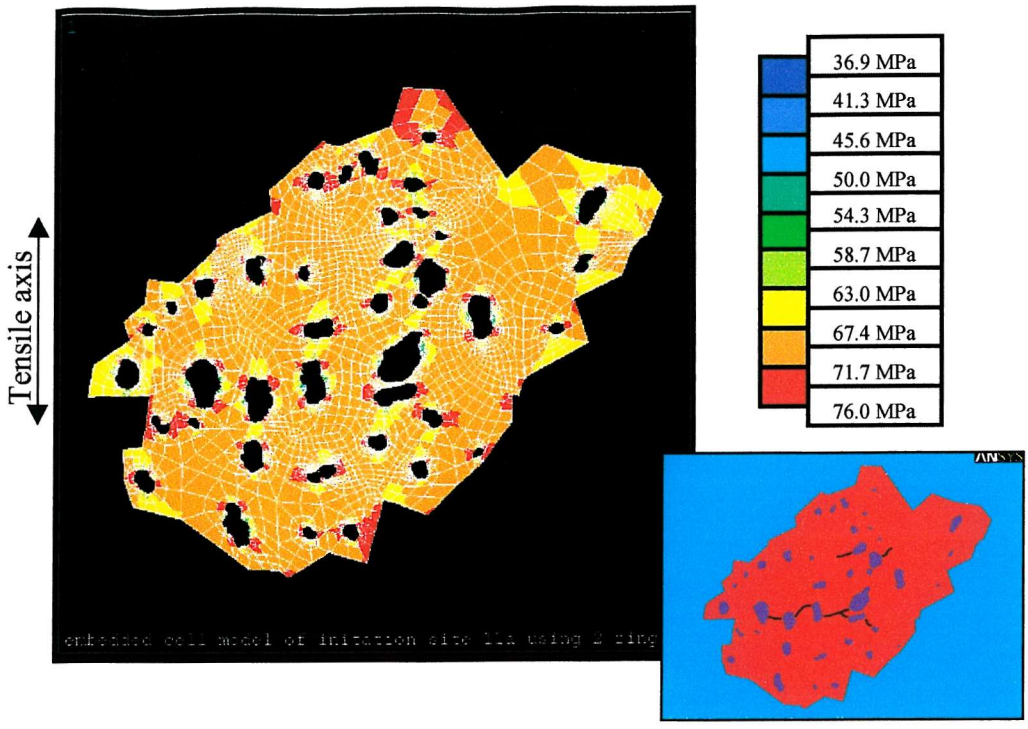

Figure 4.25: Von Mises stress in overall model

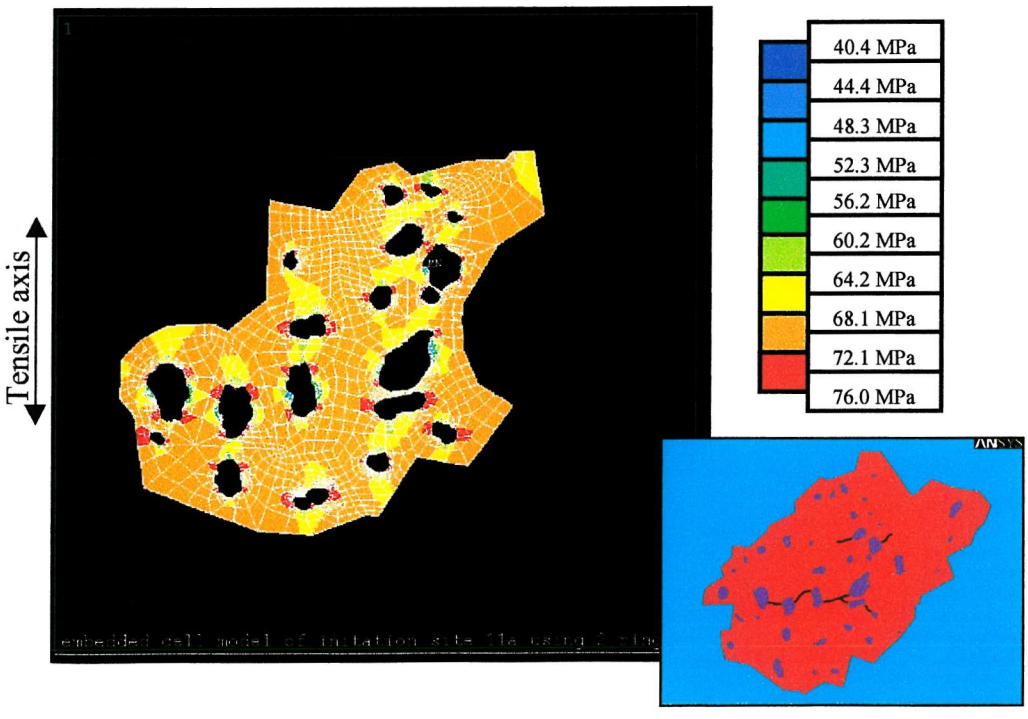

Figure 4.26: Von Mises stress in model after removing outer ring of background cells

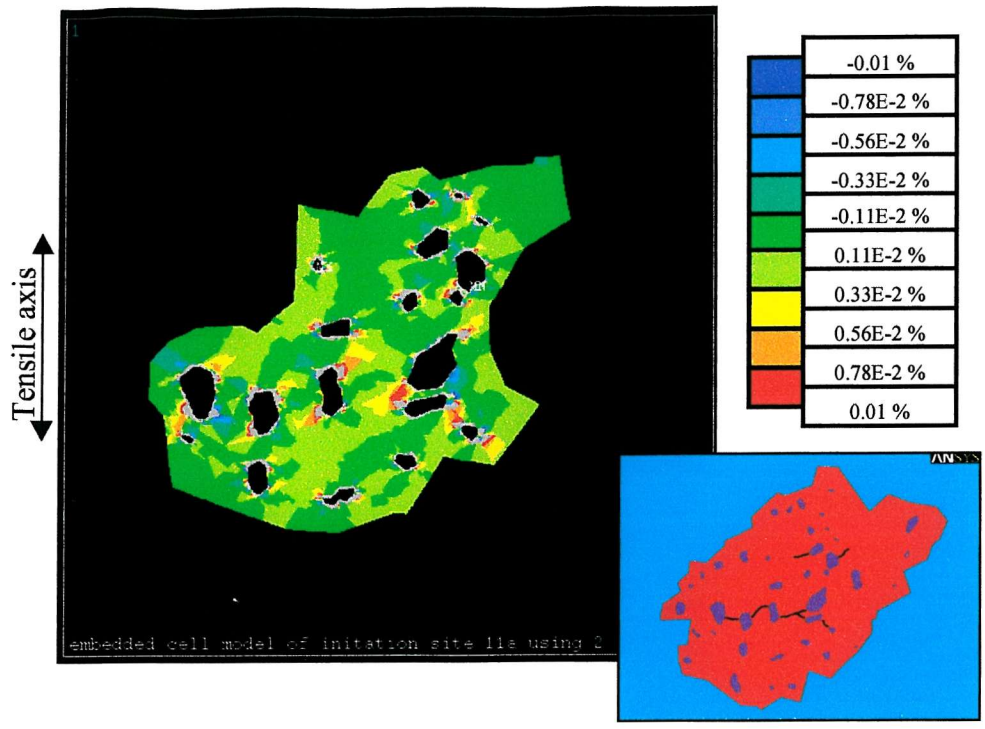

Figure 4.27: Comparison of crack initiation sites, and points of high plastic x-y shear strain

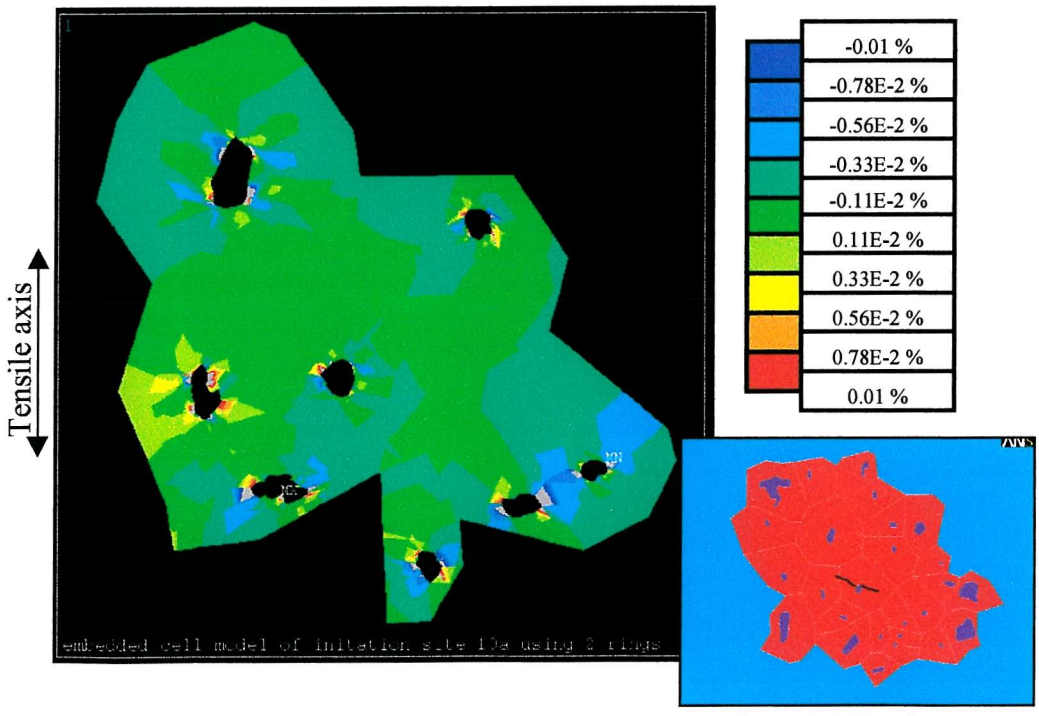

Figure 4.28: Second example of comparison of crack initiation sites, and points of high plastic x-y shear strain

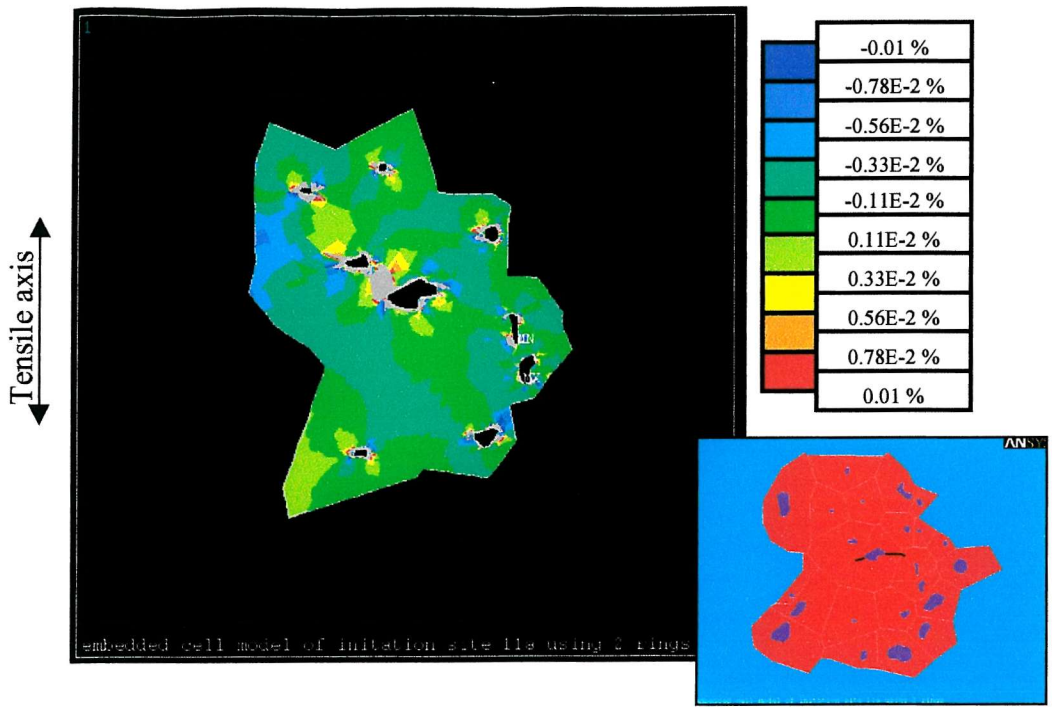

Figure 4.29: Third example of comparison of crack initiation sites, and points of high plastic x-y shear strain

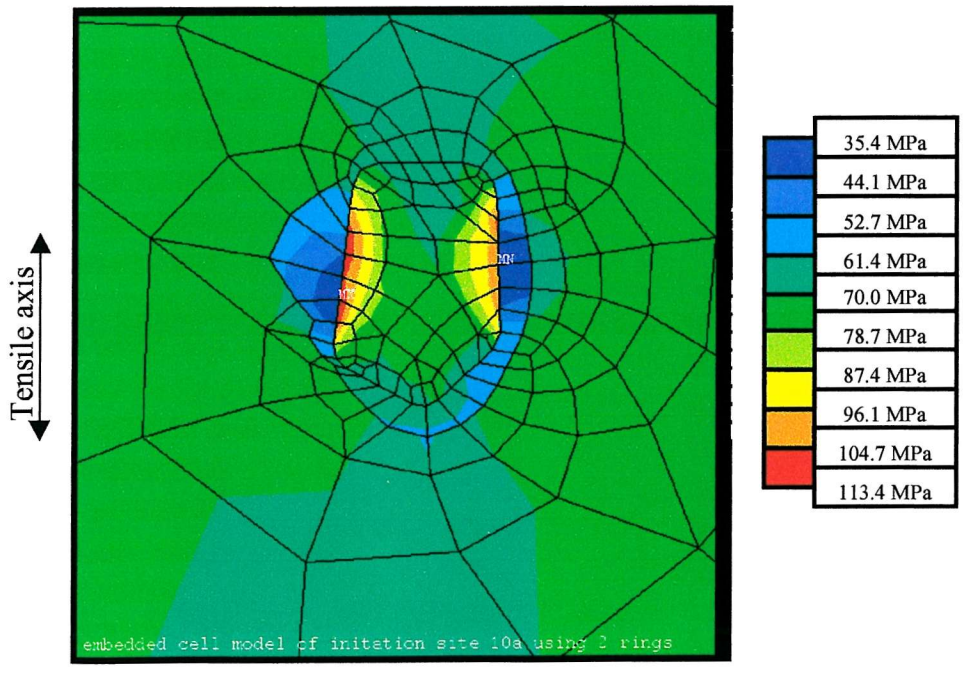

Figure 4.30: Von Mises stress field surrounding a single Si secondary phase

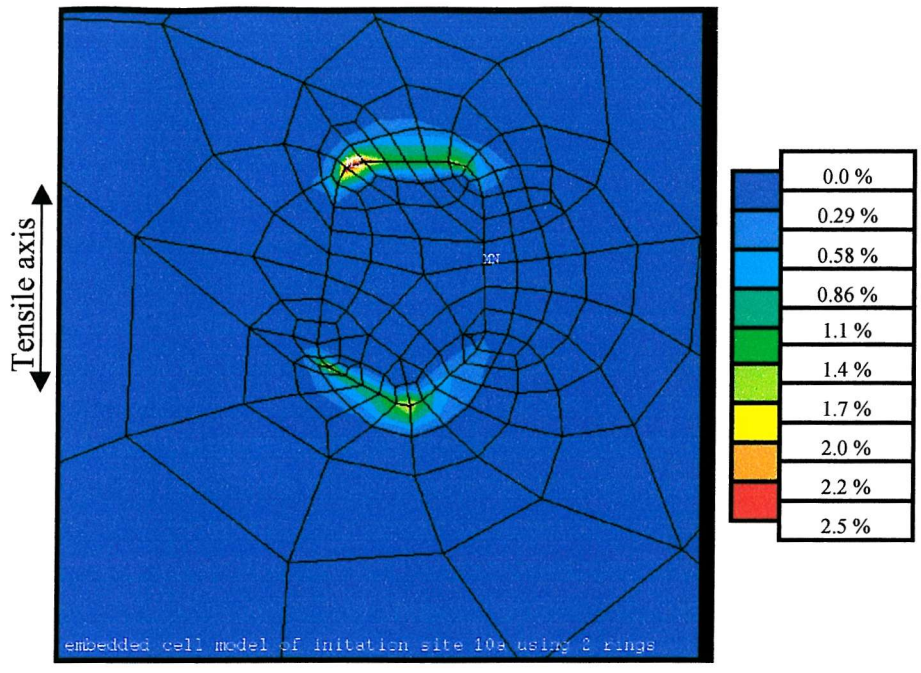

Figure 4.31: Von Mises plastic strain field surrounding a single Si secondary phase

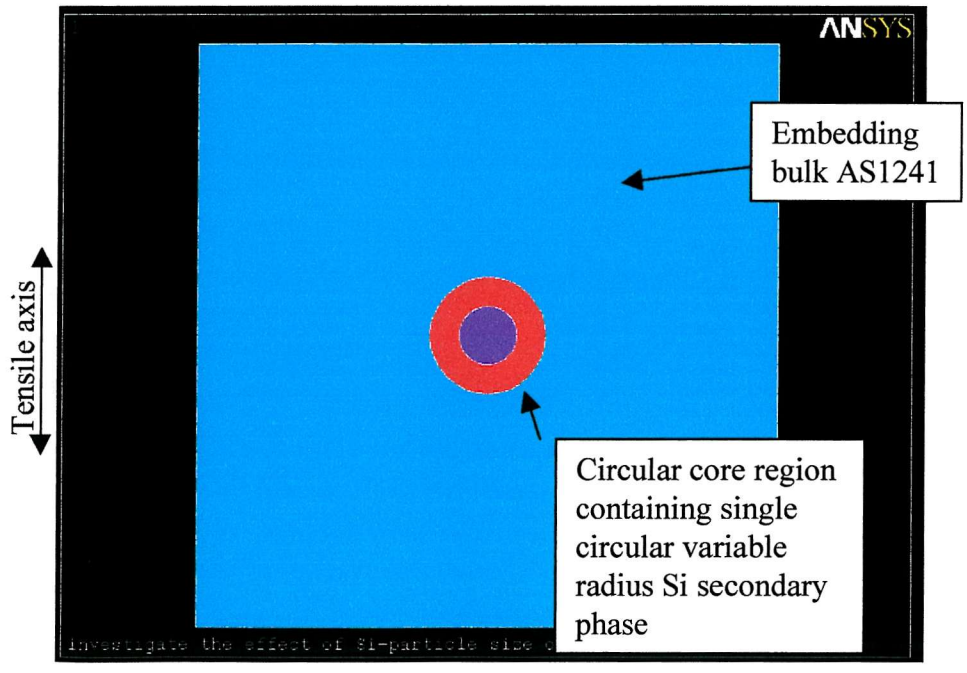

Figure 4.32: Schematic of model used to investigate the effect of inclusion size on stress and strain in core matrix

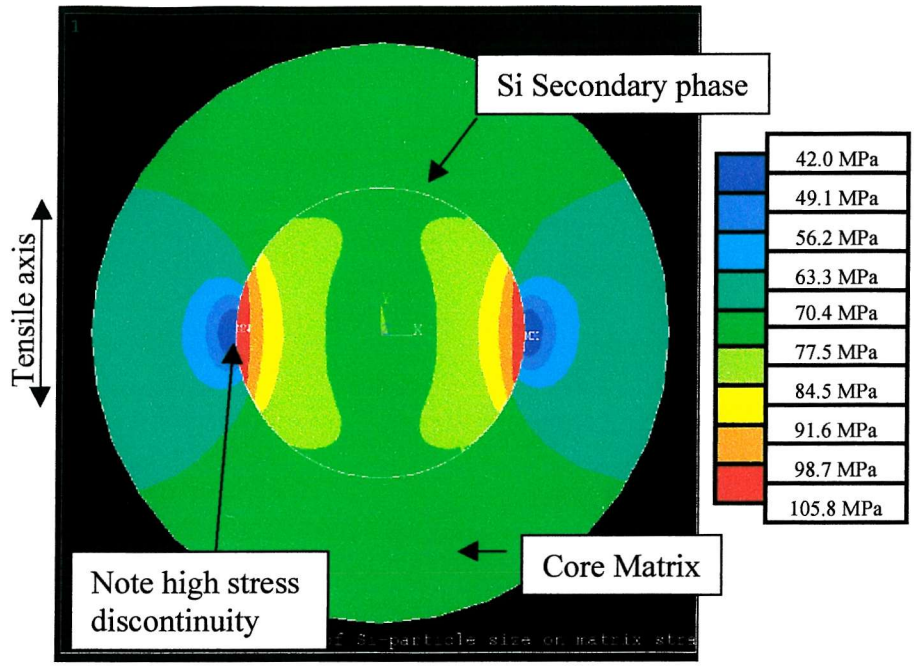

Figure 4.33: Example of Von Mises stress field in the core region

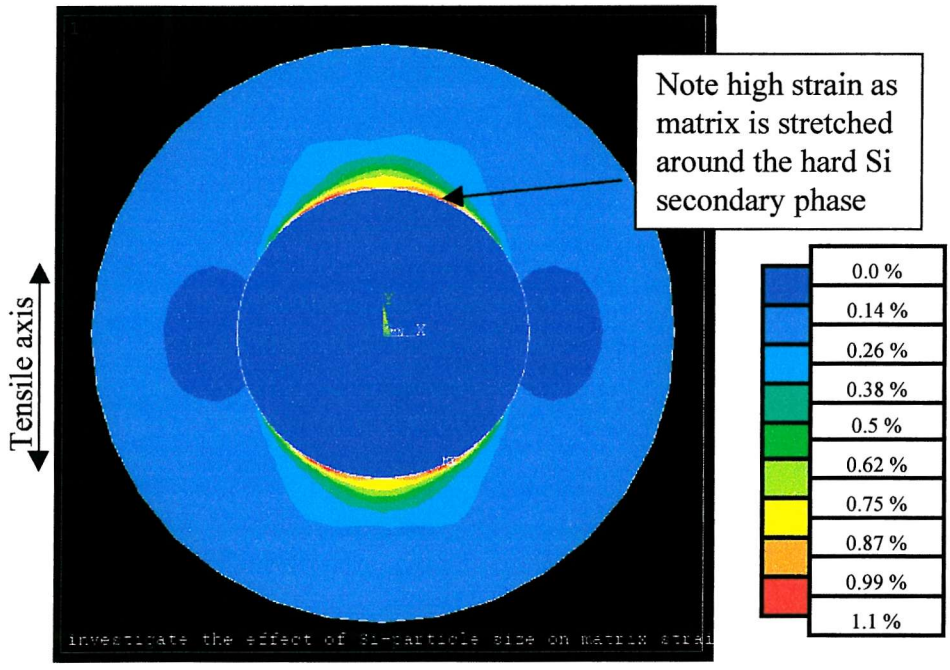

Figure 4.34: Example of Von Mises strain field in core region

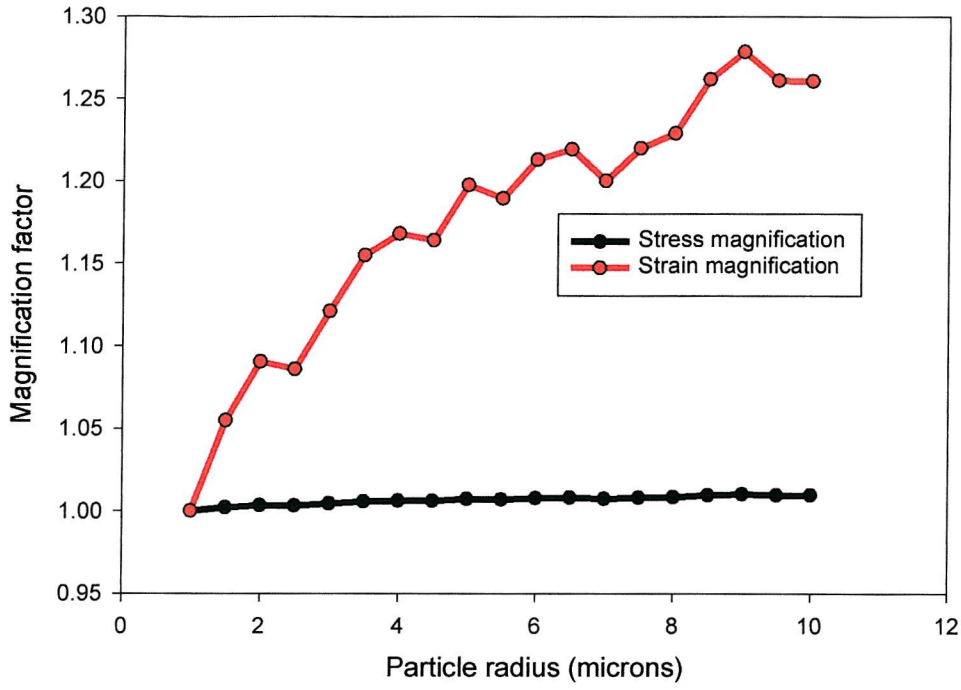

Figure 4.35: Normalised results from model, showing rapid increase in matrix strain with increasing Si secondary phase size.

5.0 FATIGUE CRACK COALESCENCE EFFECTS

It was seen in the experimental program, that multiple fatigue cracks would initiate and grow in the region of maximum bending stress, as shown in Figure 5.1. These cracks typically formed a complex field of micro-cracks on the specimen surface. Due to the sheer multiplicity of these cracks, coalescence events were seen to be inevitable and frequent, eventually leading to the formation of a dominant "failure crack", built up through successive coalescence events. It was also noted that a degree of crack interaction was present between micro-cracks propagating in the same region of material. Both crack acceleration and deceleration events were observed as pairs of cracks approached each other.

This chapter reports on a series of finite element models created as a preliminary investigation to further characterise these observed crack interactions.

5.1 Crack Coalescence Modelling Approaches

The behaviour of multiple fatigue cracks has been the subject of some interest in the literature. It has long been recognised that coalescing cracks exhibit complex behaviour, due to the apparent mode mixity produced by crack tip plastic zone interactions. Several attempts have been made to characterise this behaviour, ranging from Forsyth's[1] early approaches based on K, to complex finite element approaches based on mixed mode fracture mechanics, for example Wang *et al*[2].

Due to the complexity of creating suitable finite element models, much of this literature concentrates on the interactions of just two cracks. Soboyejo and co-workers[3,4] used a three dimensional FE approach to investigate the behaviour of a pair of symmetric half penny shaped co-linear cracks as they coalesced. They used this information to predict the subsurface shapes of co-linear cracks produced in double ridged bend bar samples. Using a similar approach Soboyejo and Knott[5] also considered the interactions between two parallel cracks. However their approach could not be applied to problems comprising cracks of unequal size due to the symmetric model methodology adopted.

Whilst very realistic, the three dimensional finite element approaches required to investigate cracks under bending loading are very complex to formulate, hence many finite element studies consider the interactions of cracks under simple tensile loading, which may be represented in two dimensions. Such studies include Kuang and Chen[6] who investigated the plastic zone interactions between coalescing cracks, and Meyer *et al*[7] who investigated the criteria for crack coalescence based on the results of finite element modelling and neural networks.

It is recognised that in order to study the interactions between more than two or three cracks, a more advanced approach may be required. One such approach is given by Isida *et al*[8] who report results from a technique capable of modelling any number of parallel cracks arranged in an array. A more general approach is given by the probabilistic work of Chen *et al*[9], who used Monte Carlo type approaches to simulate the arrest and coalescence behaviour of a field of micro-cracks.

5.2 Crack Field Geometries

In common with the majority of studies in the literature, the crack field geometries produced in experimental samples were deemed too complex on which to develop modelling techniques, rather this study considers a series of simpler fundamental crack field geometries, consisting of pairs of interacting cracks. It was proposed to model the mesoscopic crack behaviour (100-1000μm crack length) in AS1241, an example of this is shown in Figure 5.2. It can be seen that as a first order approximation, the general propagation mode of these cracks may be considered as normal to the applied loading. Hence in the first instance, it was unnecessary to consider cracks propagating along axes other than that normal to the far field stress. With these restrictions in place, the arrangements of interacting cracks may be generalised into the three types shown in Figure 5.3;

- Co-linear – Crack midpoints displaced along an axis normal to applied loading
- Parallel – Crack midpoints displaced along an axis parallel to applied loading, with axis of symmetry through their midpoints
- Oblique – Crack midpoints displaced along an axis inclined at an arbitrary angle to applied loading

In reality the majority of coalescence events observed were of the third or oblique type, however considering the other two simpler orientations allowed a greater understanding of the crack tip interactions to be obtained.

5.3 General Finite Element Model Methodology and Formulation

To simulate the crack pairs in a three point bend loading geometry would require a three dimensional model similar to, but more complex than that of Soboyejo *et al*[3,4]. As a preliminary investigation a model of this complexity was considered inappropriate; rather, in line with other studies, it was proposed to consider only the surface behaviour in a simple two dimensional manner. Figure 5.4 shows the modelled geometry and loading for the three cases considered. These comprised a sheet of material under monotonic tensile loading containing two elliptical cracks in the required orientation. The dimensions of the sheet were made large with respect to those of the cracks, such that small scale yielding conditions were maintained throughout the loading cycle.

Finite element models were created using the general purpose finite element code ANSYS5.5. The model geometry was arranged such that whilst one crack was held at a fixed length, the other's length could be incrementally increased, the two cracks are therefore referred to as the "*free crack*" and the "*growing crack*". Such a geometry allows many discrete solutions to be obtained in a single program run, as the length of the *growing crack* is incrementally increased. However this process does not truly simulate crack growth, since only tensile monotonic loading is repeatedly applied, and residual plastic strain is not predicted and carried into subsequent analyses. Typically the length of the *growing crack* was increased to reduce the spacing between the two cracks (as crack midpoints are fixed) and hence investigate the interactions between them.

The models were created using 8 node quadrilateral elements in plane stress, therefore simulating the surface condition. The mesh was considerably refined at all crack tips, and contours for J-integral evaluation provided. These contours however limit the minimum distance between the cracks, since due to meshing constraints the contours may not cross each other. A multi-linear isotropic elasto-plastic model based on the experimentally derived AS1241 stress/strain curve shown in Figure 2.42 was

used to model the sheet material response. The models were loaded by a uniform strain of 0.05% applied directly to the edge nodes. At the end of each loading step, the crack tip driving force was evaluated using the J-integral. In its current form ANSYS cannot calculate this parameter directly, rather it must be found from other solution parameters; this process is implemented within a macro, which together with its validation is described in Appendix III.

5.4 Co–Linear Cracks Model

A schematic of the Co-linear model is shown in Figure 5.5, the symmetrical nature of this arrangement is an advantage since only half of the problem requires meshing, hence reducing the model's computational expense. Figure 5.6 shows the mesh refinement at the crack tips, and the circular contours used for the evaluation of the J-integral.

Whilst the *free crack* was held at a constant length of 1mm, the *growing crack* was extended from a length of 0.5mm to a final length of 2.5mm in increments of 0.1mm. Since the midpoint of the *growing crack* remains at a constant position, the spacing between the cracks reduces from 1.25mm to 0.25mm. The cracks could not be allowed to come closer than this due to meshing constraints, caused by the circular J-integral contours. Figures 5.7a-e show the development of the plastic zones ahead of the cracks. It can be seen that initially the crack tip plastic zones are small and a considerable region of elastic material exists between them. As the length on the *growing crack* is increased, the plastic zones appear to converge, forming an annular plastic region between the converging crack tips, containing a small elastic nugget. Further extension of the *growing crack* made the inter crack region entirely plastic, as the two opposing crack tip plastic zones merge completely.

J-integral solutions were obtained for both ends of the *growing crack*, using the macro described in Appendix III. Solutions for the *Free crack* were not obtained in this instance. These results are plotted in Figure 5.8, together with an analytical solution for a single crack in a semi-infinite plate, highlighting the effect of a second crack ahead of the *growing crack*. Figure 5.8 is also annotated to correlate with Figures 5.7a-e showing the plastic zone development.

It can be seen that the driving force at the closing tip begins to deviate from the analytical solution at a crack length of ~1.5mm, this corresponds to the behaviour shown in Figure 5.7c, in which the annular plastic region is starting to form, whilst the material within this region is not itself deforming plastically, it is clear that this region is being formed through the interaction of the converging crack tip plastic zones. When the annular region does become plastic (*growing crack* length = ~2mm), the driving force at the closing tip is ~60% higher than the analytical solution, also the driving force at the free tip is starting to rise above the predicted value. At minimum spacing (0.25mm), the plastic zones have entirely merged, at this point the driving force at the closing and free tips are 170% and 30% greater respectively than values predicted for a single crack.

5.5 Parallel Cracks Model

The model shown in schematic form in Figure 5.9 was used to investigate the behaviour of parallel cracks. This was created using an identical methodology to the co-linear crack model, though obviously the axis of symmetry is normal to that of the previous model.

As before the *free crack* was held at a constant length of 1mm, whilst the *growing crack* was extended from an initial length of 0.2mm to a final length of 2mm in increments of 0.2mm. The vertical crack spacing was held constant at 1mm. Crack driving force was evaluated at the tips of both the *free crack* and the *growing crack* using the macro given in Appendix III. Figures 5.10a-c show the plastic zone interactions as the length of the *growing crack* was increased, whilst the crack tip driving force results are plotted in Figure 5.11.

It can be seen in Figure 5.10a that, initially the *growing crack* is considerably shielded by the larger *free crack*, whilst a large plastic region exists ahead of the *free crack*. This shielding is very evident in terms of crack tip driving force, where J_{free} is more than 50 times greater than $J_{growing}$. As the length of the *growing crack* is increased, its driving force increases, whilst at the same time the driving force of the *free crack* is seen to reduce, until the point where the cracks are of equal length, there driving forces are comparable. Figure 5.10b shows the crack tip plastic zone

interactions at this point. Whilst the plastic zones are not actually overlapped, their converging lobes are distorted towards each other, producing a region of higher stress. Increasing the length of the *growing crack* further such that it overtakes the *free crack*, continues the trend of increased *growing crack* driving force at the expense of the *free crack* driving force. Figure 5.10c shows that at a *growing crack* length of 1.5mm the *free crack* is almost entirely shielded, whilst a large plastic zone is present ahead of the *growing crack*, reversing the initial position.

5.6 Oblique Cracks Model

The oblique case, combines the effects of a co-linear and a parallel offset between the crack mid-points. This form of crack arrangement represents the most numerous of the coalescence events seen in experimental samples. The model is rather more complex than the previous two, since no axis of symmetry exists, thus the two cracks are modelled fully, and J-integral solutions are obtained at all four crack tips. A schematic of this model is shown in Figure 5.12.

As before, the *free crack* was held at a constant length of 1mm, whilst the length of the *growing crack* was increased from an initial length of 1mm to a final length of 5mm. Whilst this increase in length reduces the initial projected crack tip spacing of 1.5mm to an overlap of 0.5mm, the vertical spacing remains constant at 0.5mm for all analyses. Figures 5.13a-e show the stress fields formed between the two cracks as the *growing crack* approaches and then overtakes the *free crack*, whilst Figures 5.14 and 5.15 show the driving forces and analytical solutions for single cracks at the tips of the growing and closing cracks respectively. In Figure 5.13a it can be seen that initially the two cracks have small and distinct plastic zones ahead of them. Figure 5.13b shows that as the length of the *growing crack* is increased, the inner plastic zone lobes distend towards each other, creating a ligament of increased stress. Figure 5.13c shows that increasing the length of the *growing crack* further, causes the plastic zones to merge along this ligament. Figure 5.14 shows that at this point the driving force at the *growing crack* closing tip is starting to increase above the analytical solution.

Figure 5.13d shows the situation when the projected spacing is zero, the two closing tip plastic zones appear completely merged, however the *growing crack*

closing tip already appears to be becoming shielded. This can also be seen in Figure 5.14 where the driving force value for the closing tip is dropping below the level predicted by the analytical solution. Extending the *growing crack* further, such that the two cracks become severely overlapped, causes both closing crack tips to become severely shielded. Figure 5.13e shows the stress field surrounding the cracks at maximum *growing crack* length, at this point the *free crack* closing tip is completely shielded, whilst Figure 5.14 shows that the *growing crack* closing tip appears to be increasing in driving force as its plastic zone moves out of the shadow of the *free crack*. Figure 5.15 shows that at the same time the driving force at the *free crack* free tip is reducing, as it begins to be shielded by the overtaking *growing crack*.

Figure 5.15 shows the driving force behaviour at the *free crack* tips. Obviously the analytical solution is constant as this crack is of fixed length, and thus should maintain a constant driving force in the absence of a second crack. It can be seen that the driving force at the closing tip increases as the *growing crack* approaches, however shortly before overlap occurs the driving force drops off. This shielding increases until, at maximum *growing crack* length, the growing tip driving force is almost zero. The driving force at the free tip rises constantly as the *growing crack* length increases until shortly before maximum length is reached, when a small drop is shown.

5.7 Discussion

Figure 5.16 shows typical examples of the experimentally observed growth rate variation of small fatigue cracks as they approached coalescence with a large dominant crack. It can be seen that as the projected crack tip spacing reduces, their growth rate increases markedly. It was shown both in the co-linear, and to a lesser extent in the oblique model that, as projected crack tip spacing reduces, crack tip driving force increases to levels far in excess of the values expected for a given crack length. It was shown that this effect is apparently caused by the overlapping of the closing crack tip plastic zones. The lobes of the converging plastic zones appear to deform towards each other forming an annular plastic region considerably larger than the expected monotonic plastic zone size. Such plastic zone deformation was also reported by Kuang and Chen[6]. The predicted large increase in crack tip driving force,

is likely to be linked to the measured increased in crack growth rates in coalescing cracks.

It was also observed experimentally that fatigue cracks propagating parallel to the main dominant crack would tend to arrest when overtaken by it. This was investigated by a second FE model, where it was shown that a long crack is capable of entirely shielding a smaller crack propagating parallel to it. Some degree of plastic zone interaction was also seen in this model's results, but not to the same extent as the co-linear model.

Finally the effects of the parallel and co-linear models were combined in a single model to investigate the behaviour of cracks converging obliquely. Again elevated crack tip driving force were seen at the converging crack tips, although to a lesser extent than the co-linear model. Presumably this is due to the greater spacing between the crack tips (due to the vertical misalignment), and hence the plastic zones did not merge to the same extent. When the length of the *growing crack* was increased such that the two cracks overlapped, the driving force at both closing tips was seen to reduce, indicating a shielding mechanism was present. In reality it was observed that under such circumstances, the two closing tips would deflect towards each other as shown in Figure 5.17. This deflection is likely to be linked to the measured reduction in driving force, which indicates that it may be unfavourable for the crack to continue propagating normal to the nominal far field applied stress field.

5.8 Summary and Preliminary Conclusions

It was shown that as coalescing fatigue cracks converge, their respective plastic zones appear to merge to form a region of enhanced plasticity caused by the superimposed singular stress fields between their crack tips. It is predicted that this effect causes a considerable increase in crack tip driving force, and that this is responsible for the experimentally observed enhanced crack growth rates immediately prior to coalescence. It was also shown that, in the case of cracks converging obliquely, that crack tip driving force appears to increase until an overlap is established. Continued length increase subsequent to this causes the cracks to begin to shield each other, apparently making continued propagation normal to the nominal

loading unfavourable, since after this point the cracks are seen to deflect towards one another before arresting.

In the case of parallel cracks, it was shown that a large dominant crack is capable of entirely shielding smaller cracks, hence accounting for the observed arrest events associated with cracks propagating parallel to the dominant crack in experimental samples.

5.9 References

[1] P.J.E. Forsyth, Fatigue – damage and crack growth in aluminium alloys, acta met Vol.2 pp.703-71 (1963)

[2] Y.Z. Wang, J.D. Atkinson, R.Akid and R.N. Parkins, Crack interaction, coalescence and mixed mode fracture mechanics, Fat. Fract. Engng. Mater. Struct. Vol.19 pp51-63, (1996)

[3] W.O. Soboyejo, J.F. Knott, M.J. Walsh and K.R. Cropper, Fatigue crack propagation of coplanar semi-elliptical cracks in pure bending, Engng. Fract. Mech. Vol.37 pp.323-40, (1990)

[4] W.O Soboyejo, K. Kishimoto, R.A. Smith and J.F. Knott, A study of the interaction and coalescence of two coplanar fatigue cracks in bending, Fat. Fract. Engng. Mater. Struct. Vol.12 pp.167-174 (1989)

[5] W.O. Soboyejo and J.F. Knott, The propagation of non-coplanar semi-elliptical fatigue cracks, Fat. Fract. Engng. Mater. Struct. Vol.14 pp37-49, (1991)

[6] K.H. Kuang and C.K. Chen, Alternating iteration method for interacting multiple crack problems, Fat. Fract. Engng. Mater. Struct. Vol.22 pp743-752, (1999)

[7] S. Meyer, E. Diegele, A. Buchner-Foit and A. Moslang, Crack interaction modelling, Fat. Fract. Engng. Mater. Struct. Vol.23 pp315-23 (2000)

[8] M. Isida, T. Yoshida and H. Noguchi, Parallel array of semi-elliptical surface cracks in semi-infinite solid under tension, Engng. Fract. Mech. Vol.39 pp.845-50, (1991)

[9] E.Y. Chen, L. Lawson and M. Meshii, Comparison of the growth of individual and average microcracks in the fatigue of Al-SiC composites, Met. Trans. Vol.26A pp. 3173-76 (1995)

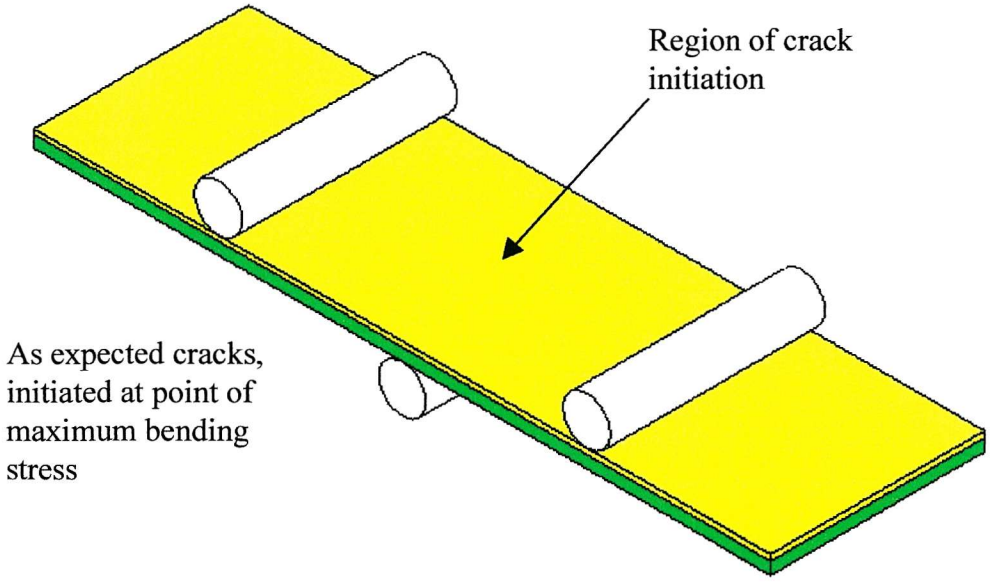

Figure 5.1: Crack initiation region in three point bend loading geometry

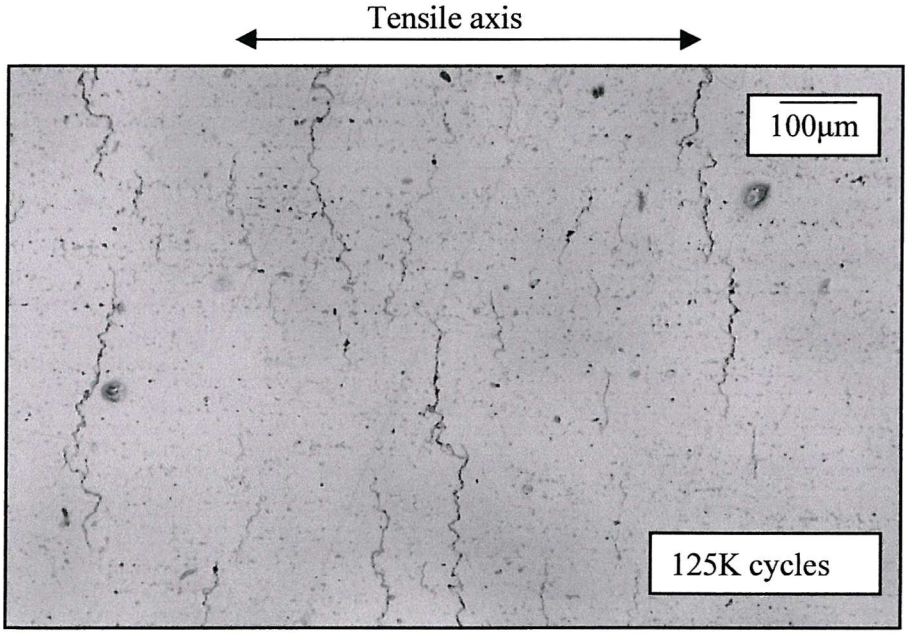

Figure 5.2: Typical mature crack morphology on sample surface, showing multiple cracks propagating normal to the far field loading direction.

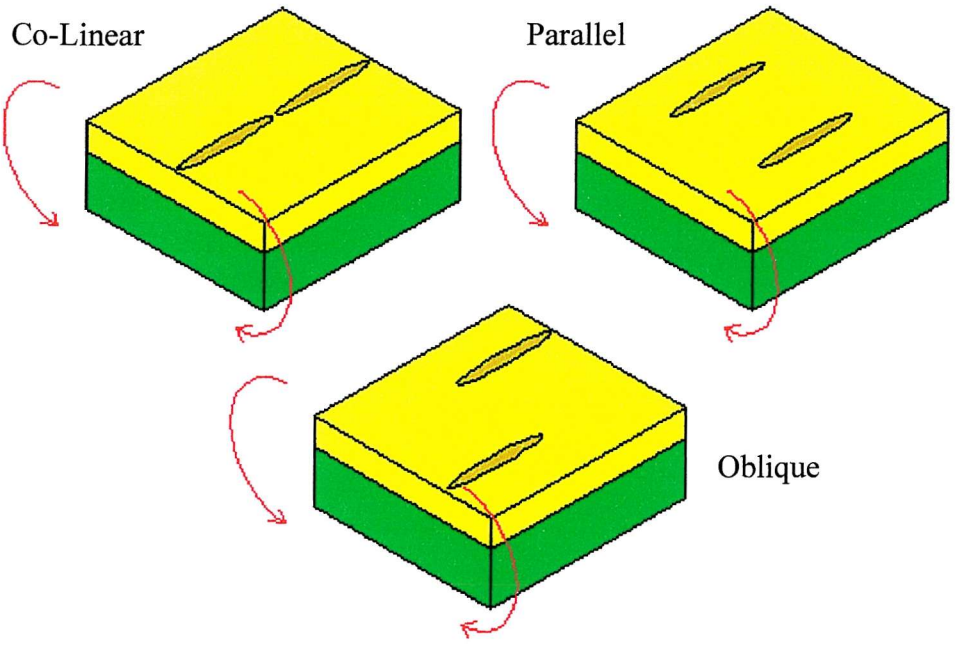

Figure 5.3: Three crack pair orientations adopted, assuming all cracks propagate normal to the far field loading

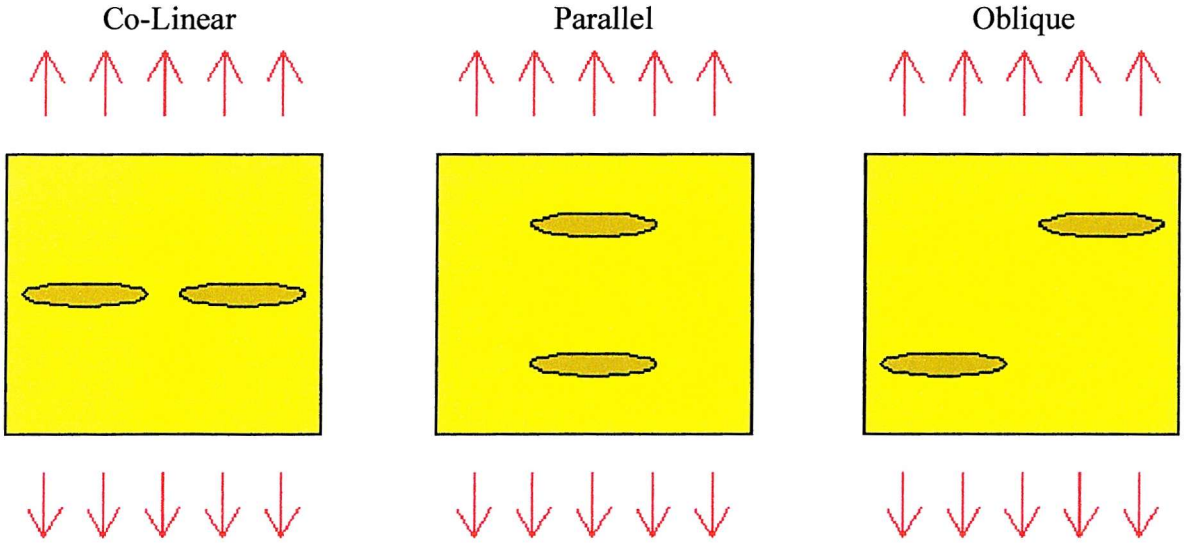

Figure 5.4: Two dimensional representations used for FE modelling study

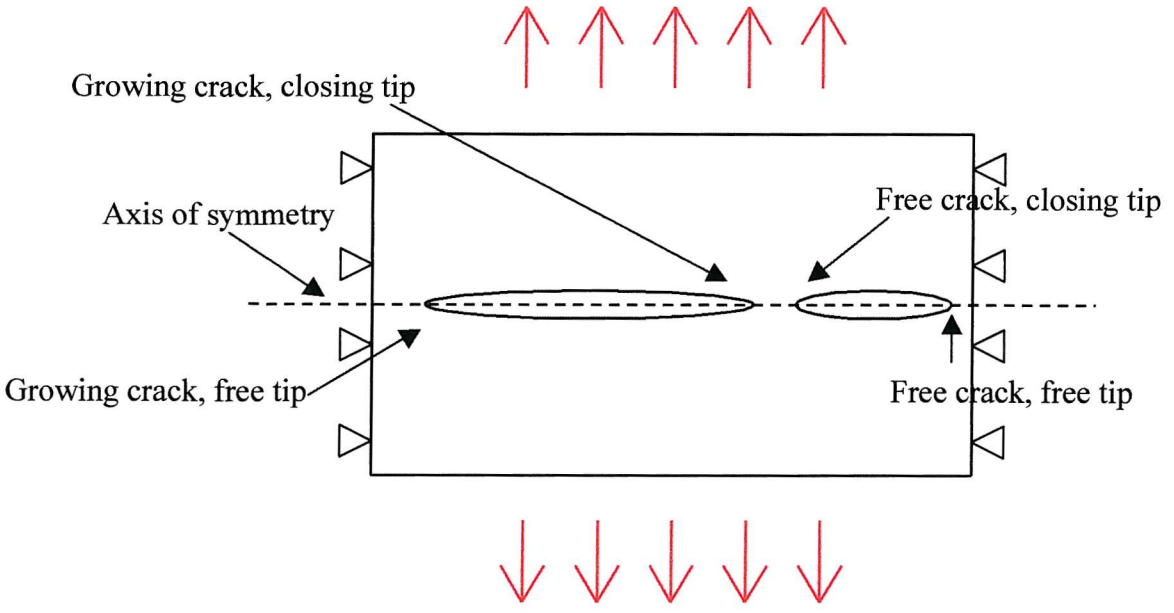

Figure 5.5: Schematic of co-linear crack model

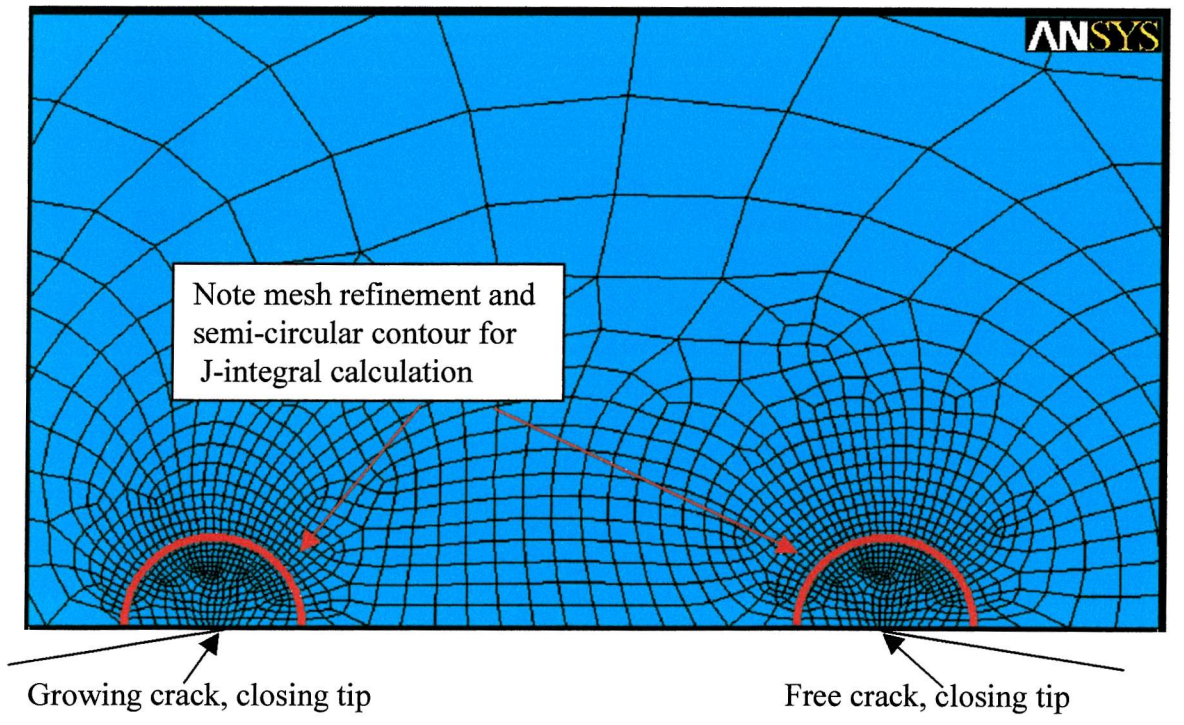

Figure 5.6: Detail of co-linear model showing mesh refinement at crack tips, including contours used for J-integral calculation

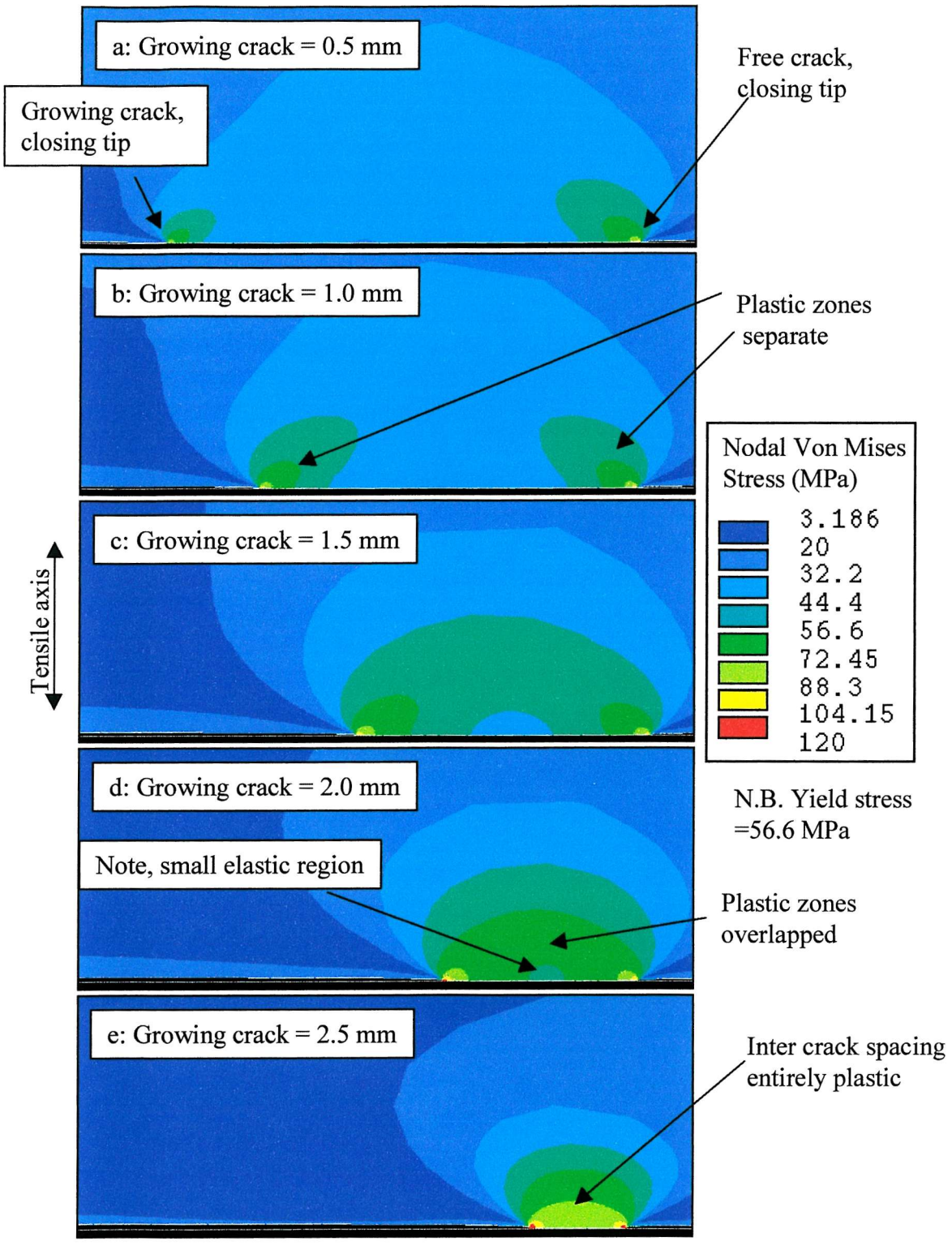

Figure 5.7: Plastic zone development as Co-linear cracks converge (Free crack held at a constant length of 1mm).

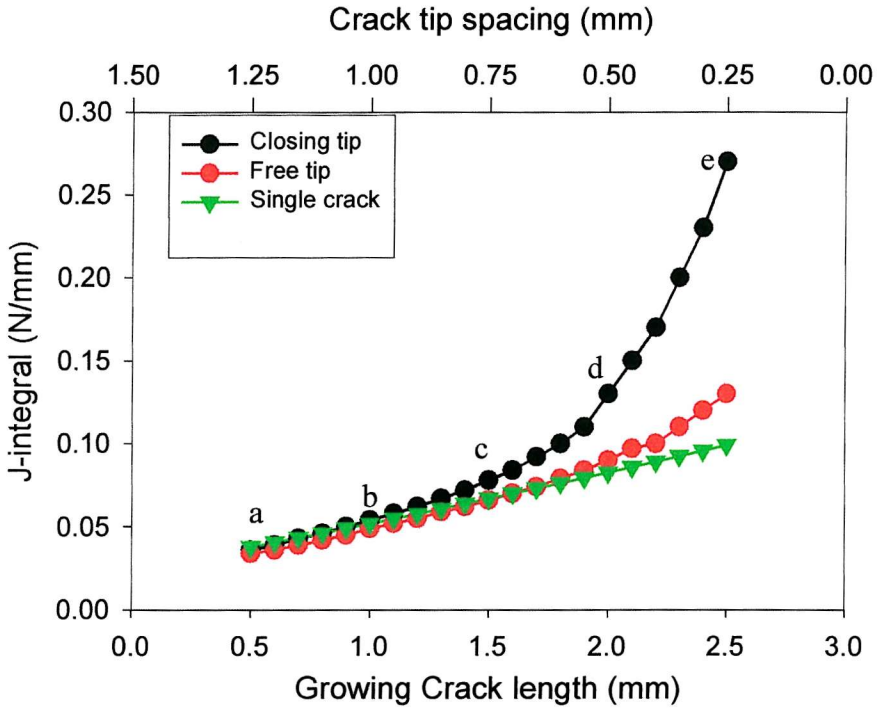

Figure 5.8: J-integral results for free and closing tips of growing crack in co-linear model

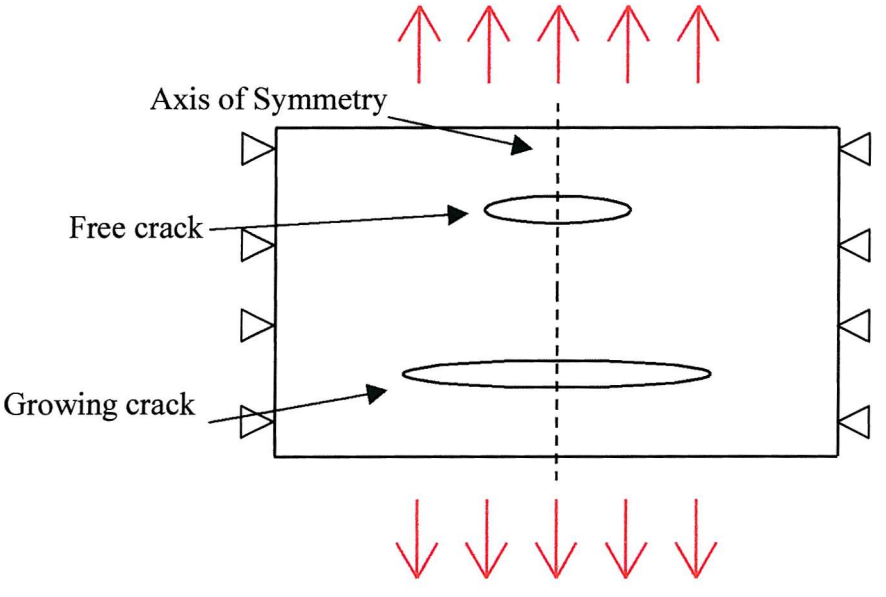

Figure 5.9: Schematic of parallel crack model

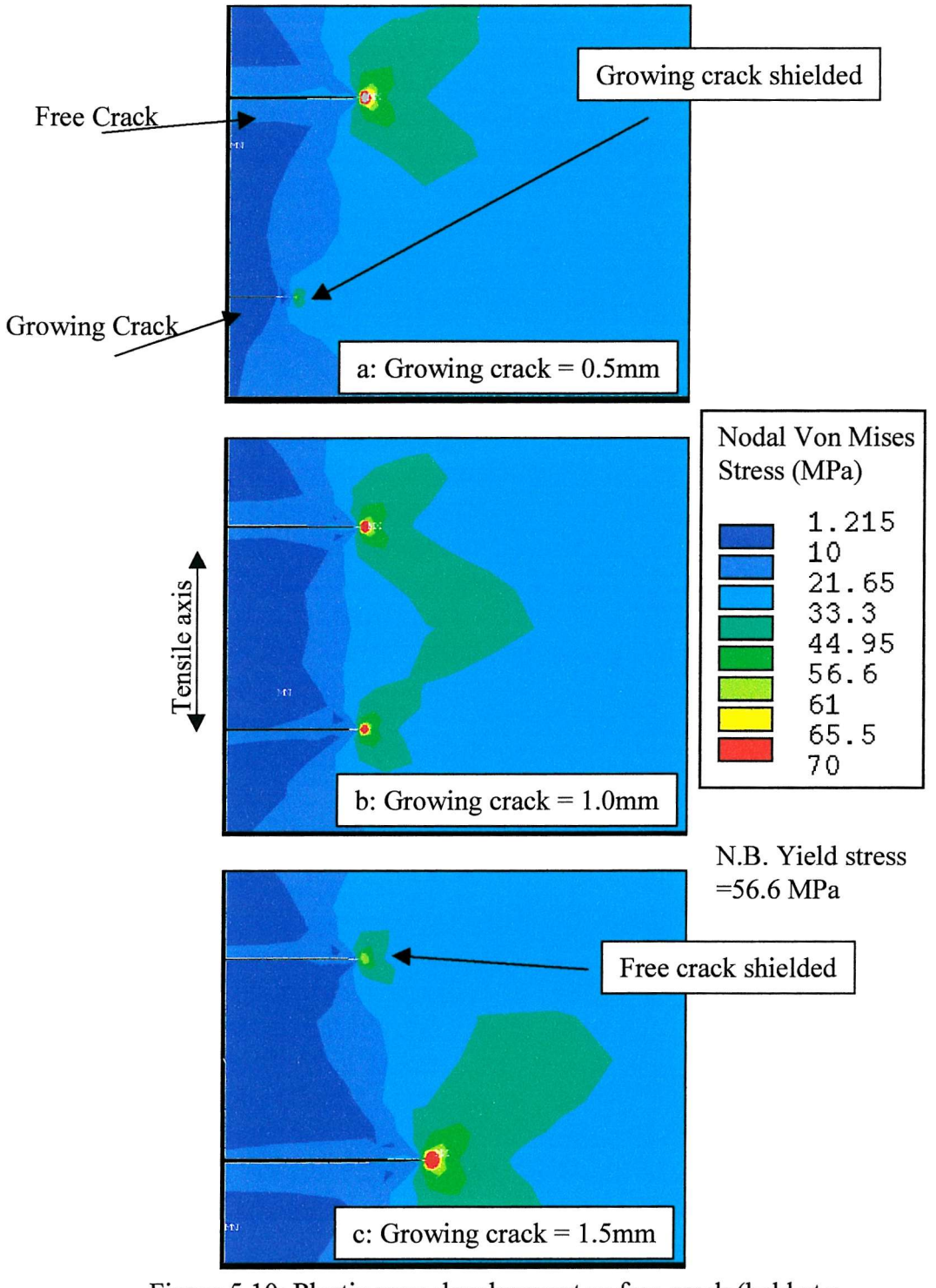

Figure 5.10: Plastic zone development as free crack (held at a constant length of 1mm) is overtaken by growing crack

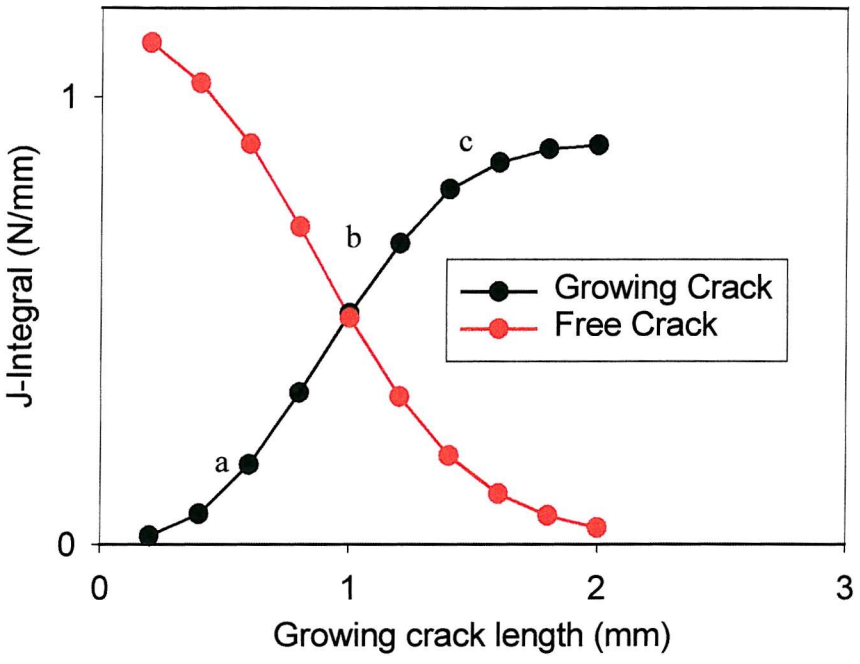

Figure 5.11: J-integral results for growing and free cracks in the parallel crack model

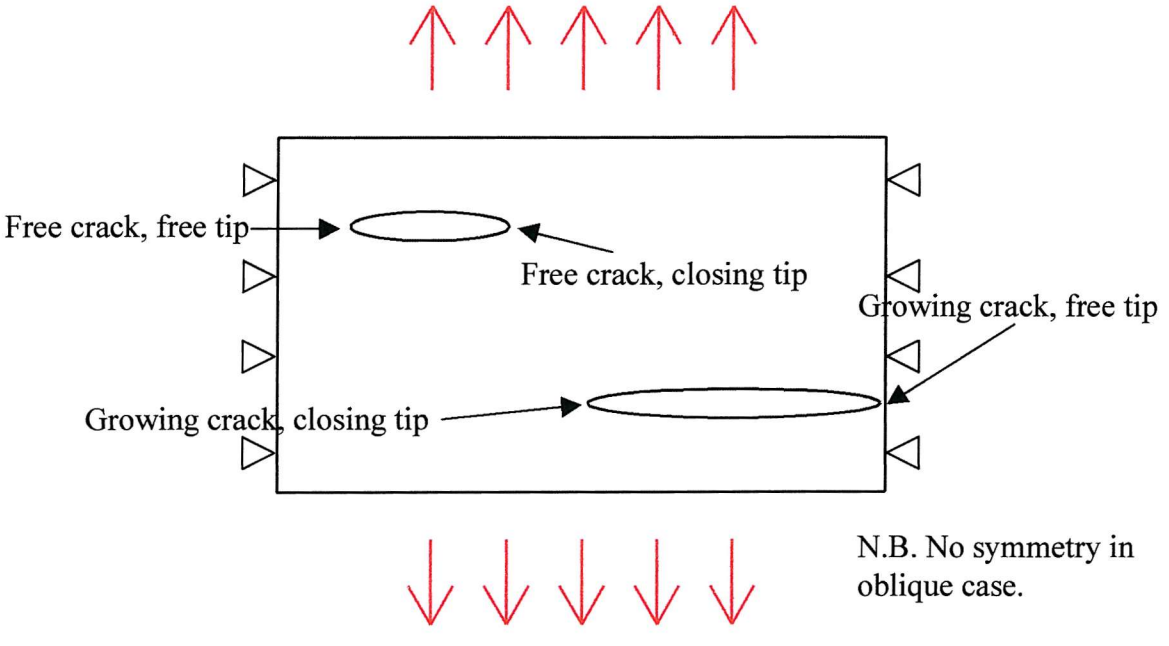

Figure 5.12: Schematic of the oblique crack model

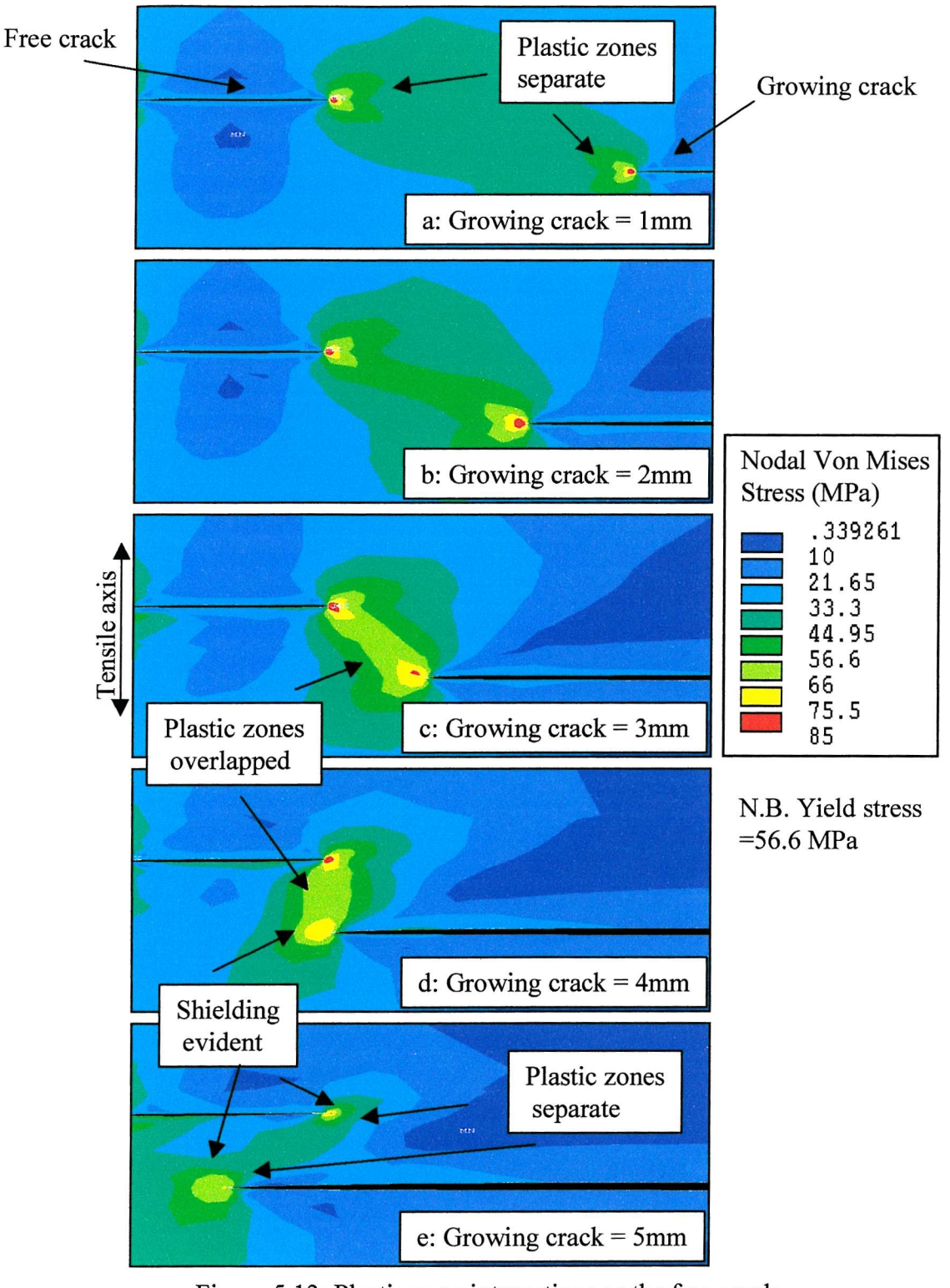

Figure 5.13: Plastic zone interactions as the free crack converges with and then is overtaken by the growing crack

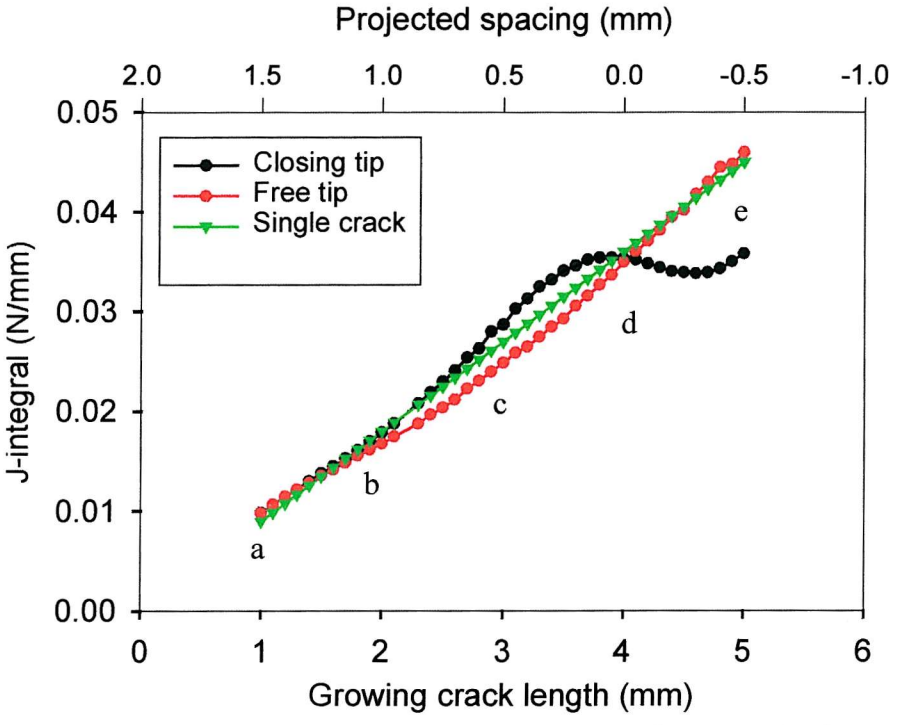

Figure 5.14: J-Integral results for the growing crack in the oblique model

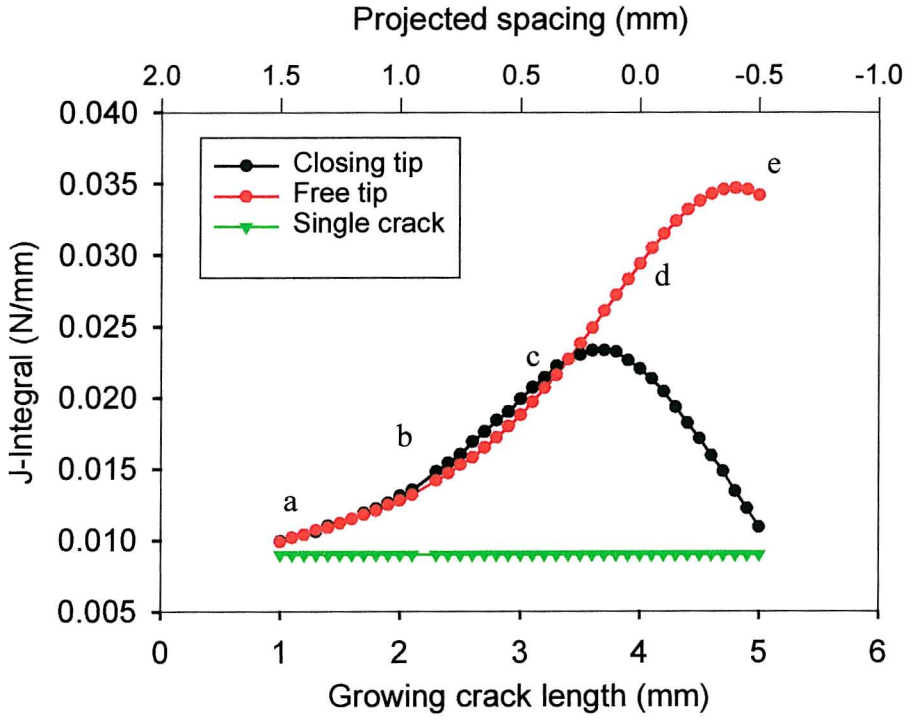

Figure 5.15: J-integral results for the free crack in the oblique model

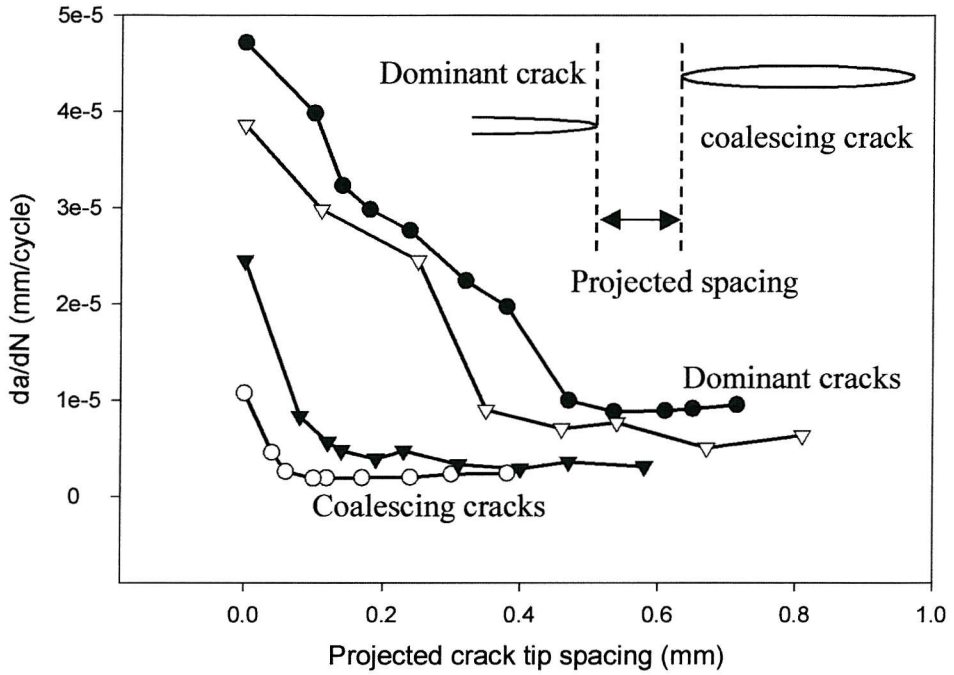

Figure 5.16: Crack growth rate variation as cracks approach coalescence with the main dominant crack

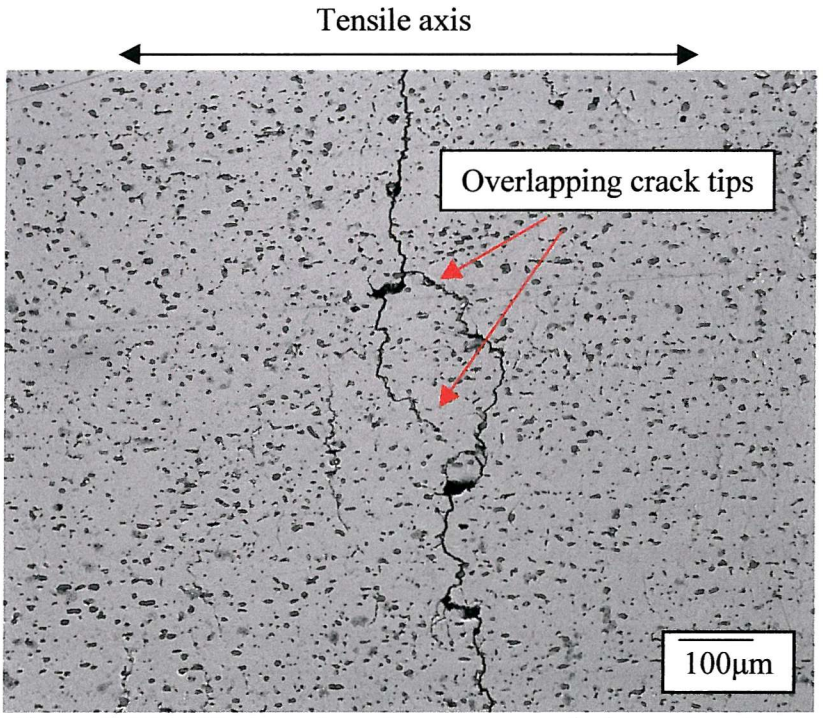

Figure 5.17: Offset crack coalescence morphology, showing how cracks tend to overlap before deflecting towards each other

6.0 DEFLECTED CRACKS IN MULTI-LAYER MATERIAL SYSTEMS

Sectional studies of experimental samples have shown that fatigue cracks growing in multi-layer bearing material systems show considerable deviation from the nominal mode I direction as shown in Figure 6.1. It is thought that the multi-layer nature of the sample is responsible for these deflections. This section reviews the general literature concerning classical approaches to deflected crack growth, before concentrating on the behaviour of cracks approaching bi-material interfaces and the criteria proposed for characterising the growth behaviour of cracks under such mixed mode conditions. A series of finite element models are proposed to explain the behaviour observed in experimental samples tested at Southampton. These models are then extended to characterise some of the features believed to cause the observed behaviour in a parametric manner. Finally several conceptual bearing designs are modelled, and assessments made as to their likely fatigue performance.

6.1 General Deflected Crack Literature

Factors which cause a fatigue crack to deviate from its nominal growth plane are of interest since they may suggest a method by which a component's fatigue life may be extended. The causes and consequences of crack deflection are examined in this Section. It can be shown that even a small deflection in a nominally mode I crack can lead to a large reduction in effective near tip crack driving force.

Suresh and Shih[1] suggested that deflection affects crack growth rate in monolithic materials in three ways:

- When the crack deflects, the effective stress intensity factor at the crack tip is typically smaller than that in a straight crack of the same total (projected) length
- If crack length is measured along the mode I growth direction, a deflected crack propagates at an apparently slower rate than a straight crack subjected to the same effective driving force.
- During the closing of the fatigue crack, even a small shear offset between the mating crack faces can lead to premature contact at far-field tensile stresses. This closure

effect will further amplify the apparent driving force required for continued propagation at the same rate as an equivalent straight crack.

Cotterell and Rice[2] showed that the local stress intensity factors at the deflected crack tip as shown in Figure 6.2 can be expressed by Eqn 6.1.

$$k_1 = a_{11}(\phi)K_I + a_{12}(\phi)K_{II}$$
$$k_2 = a_{21}(\phi)K_I + a_{22}(\phi)K_{II} \tag{6.1}$$

where ϕ is the angle through which the crack is deflected and the dimensionless parameters $a_{ij}(\phi)$ are given in Eqn 6.2.

$$a_{11}(\phi) = \frac{1}{4}\left(3\cos\frac{\phi}{2} + \cos\frac{3\phi}{2}\right)$$
$$a_{12}(\phi) = -\frac{3}{4}\left(\sin\frac{\phi}{2} + \sin\frac{3\phi}{2}\right)$$
$$a_{21}(\phi) = \frac{1}{4}\left(\sin\frac{\phi}{2} + \sin\frac{3\phi}{2}\right)$$
$$a_{22}(\phi) = \frac{1}{4}\left(\cos\frac{\phi}{2} + \cos\frac{3\phi}{2}\right) \tag{6.2}$$

If multiple crack deflections occur, the local crack driving force is reduced even further. Suresh[3] considered an idealised case of a crack containing periodic sections of length D, deflected at an angle α, separated by undeflected sections of length Q, as shown in Figure 6.3. According to this model, the elastic solutions for the local mode I and mode II stress intensity factors, k_1 and k_2 respectively, along the kink of span D are given in Eqn 6.3.

$$k_1 = \cos^3\left(\frac{\phi}{2}\right)K_I$$
$$k_2 = \sin\left(\frac{\phi}{2}\right)\cos^2\left(\frac{\phi}{2}\right)K_I \tag{6.3}$$

where K_I is the instantaneous value of the mode I stress intensity. The weighted average of the local stress intensity factors $\overline{\Delta k}$ for the periodically deflected crack is then given by Eqn 6.4.

$$\overline{\Delta k} = \left\{ \frac{D\cos^2\left(\frac{\phi}{2}\right) + Q}{D+Q} \right\} \Delta K_I = \left\{ \hat{D}\cos^2\left(\frac{\phi}{2}\right) + \left(1-\hat{D}\right) \right\} \Delta K_I \qquad (6.4)$$

where $\hat{D} = \dfrac{D}{(D+Q)}$.

Eqn 6.4 describes the modification to stress intensity factor range due to crack deflection alone, without considering any closure effects.

6.2 Cracks Approaching Bi-Metal Interfaces

Components made up from a number of layers of different materials exhibit different fatigue crack growth behaviour than those made up of monolithic construction. The behaviour of a fatigue crack as it approaches a bi-material interface has been the subject of much work. Erdogan and co-workers[4 5] investigated the near tip stress and strain fields of a crack impinging normally onto an interface between two dissimilar elastic materials. This work was extended by He and Hutchinson[6], who investigated the factors determining whether an impinging crack would deflect along an interface or pass through it..

The behaviour of fatigue cracks approaching an interface was experimentally investigated by Suresh at al[7 8], who considered a bi-material comprising a ferritic and an austenitic steel, these materials having similar elastic properties and yield stress, but differing strain hardening rates, ultimate tensile stress and hence hardness (c.f. austenitic H_v ~200, ferritic H_v ~125). They observed that a fatigue crack approaching normal to the interface from the harder side, would pass through the interface undeflected. Whilst an approaching crack from the softer side showed reduced crack growth rate, crack deflection and finally arrest. Thereby demonstrating that a plastically dissimilar interface had the potential to severely affect the propagation behaviour of an approaching fatigue crack. Suresh *et al*[7] proposed two mechanisms to explain this behaviour.

On a continuum mechanics basis, it was proposed that the local compliance ahead of the crack is raised in the case of a crack approaching the interface from the

softer side, and reduced when the crack approaches from the harder side. It was argued that an increase in local compliance precludes continued crack propagation in the nominal mode I direction, hence the crack deflects. Using a micro mechanics approach, it is argued that when a crack approaches an interface from the softer side, cyclic slip into the harder material becomes more difficult and the crack deflects as it seeks material with a lower resistance to fracture, the crack deflection then causing a marked reduction in crack tip driving force, and hence arrest.

The same material system was considered by Sugimura *et al*[9], who repeated much of the experimental work of Suresh *et al*[7] , but who also carried out a finite element investigation using the *J*-integral to characterise the driving force variation of an approaching crack under quasi-static conditions. A schematic of their model is shown in Figure 6.4.

The model was created such that one material was exclusively elastic, and the other elasto-plastic with isotropic hardening, such that the materials obeys Eqn 6.5.

$$\varepsilon = \frac{\sigma}{E}, \qquad \sigma < \sigma_y$$

$$\varepsilon = \frac{\sigma_y}{E}\left(\frac{\sigma}{\sigma_y}\right)^{\frac{1}{n}}, \qquad \sigma \geq \sigma_y \tag{6.5}$$

For validation purposes solutions were also found using a J_2 deformation theory of plasticity based on a Ramberg-Osgood type description of material response, given by Eqn 6.6.

$$\varepsilon = \frac{\sigma}{E} + \alpha\frac{\sigma}{E}\left(\frac{\sigma}{\sigma_y}\right)^{\frac{(1-n)}{n}} \tag{6.6}$$

The *J*-integral was calculated via the domain-integral formulation proposed by Li *et al*[10], using two separate contours around the crack tip, J_{tip} was found from a contour embedded entirely within the plastic zone, whilst J_{app} was found from a contour of larger radius, within the elastic region. Sugimura *et al*[9] propose that providing this outer contour is outside the plastic zone, it may exist in both materials, whilst preserving the validity and path independence of the *J*-integral. It should also be noted that this remote *J* is also given by Eqn 6.7, the Rice-Irwin relation.

$$J_{app} = \frac{1-\nu^2}{E} K^2$$

(6.7)

The crack length was incrementally increased to bring the crack towards the interface, using the ratio J_{tip}/J_{app} to represent the degree of shielding evolved. It was found that a crack approaching the interface from the softer side experienced a considerable drop in driving force as it neared the interface, it is this shielding that causes the reduction in growth rate. When a crack embedded within the harder material was considered, anti-shielding was observed as the crack approached the interface. Sugimura *et al*[9] were able to link this phenomenon to a small experimentally observed increase in growth rate as such a crack crossed into the softer material.

This work was further extended by Kim and Suresh[11] who again considered the same material system and methodology, but with the addition of an interlayer, rather than the distinct interface of earlier work. This interlayer was made either homogeneous, having the averaged properties of the two primary layers, or graded, its properties varying linearly from the primary layers as extremes. It was found that for a given interlayer thickness, a homogeneous interlayer exhibited greater shielding (crack approaching form softer side) and greater amplification (crack approaching from the harder side) than did the graded interlayer. However for both interlayer types, the effects on crack tip driving force are greater than those observed for a bi-layer, as considered by Sugimura *et al*[9].

6.3 Parameters For Defining Preferential Crack Paths

The behaviour of cracks growing under mixed mode conditions has received considerable interest, and several criteria have been proposed which attempt to characterise the preferential growth direction of a propagating fatigue crack. The majority of these approaches come from workers considering the propagation behaviour of fatigue cracks growing under mixed mode loading conditions. Several of these are discussed in the remainder of this section.

6.3.1 Maximum tangential stress criterion (MTS criterion)

This was first proposed by Erdogan and Sih[12] who considered a straight crack in a thin infinite plate of an ideally brittle material. In the plane problem, the crack tip stresses as shown in Figure 6.5, may be expressed in polar co-ordinates as in Eqn 6.8.

$$\sigma_r = \frac{1}{(2r)^{\frac{1}{2}}}\cos\frac{\theta}{2}\left[K_1\left(1+\sin^2\frac{\theta}{2}\right)+\frac{3}{2}K_2\sin\theta-2K_2\tan\frac{\theta}{2}\right]$$

$$\sigma_\theta = \frac{1}{(2r)^{\frac{1}{2}}}\cos\frac{\theta}{2}\left[K_1\cos^2\frac{\theta}{2}-\frac{3}{2}K_2\sin\theta\right]$$

$$\tau_{r\theta} = \frac{1}{2(2r)^{\frac{1}{2}}}\cos\frac{\theta}{2}\left[K_1\sin\theta+K_2(3\cos\theta-1)\right]$$

(6.8)

Griffith[13] hypothesised a mechanism for crack extension in which the crack grows radially from the tip and at an angle such that the initial growth is in the plane perpendicular to the direction of greatest tension. These conditions imply that a crack will grow from the tip in the direction in which the tangential stress, σ_θ is maximum and which the shear stress $\tau_{r\theta}$ is zero. It was also been proposed that fracture will start when the tangential stress reaches a critical value, $\sigma_{\theta c}$. Erdogan and Sih[12] hypothesised that the angle of this crack extension could be calculated from the expressions given in Eqn 6.8. They considered two special cases, namely pure mode I and pure mode II loading. In each case the angle of crack propagation θ_0 was found by setting the derivative of the tangential component of the crack tip stress field σ_θ with respect to θ equal to zero. Thus giving

Mode 1: $k_2 = 0$: $\theta_0 = 0$

Mode 2: $k_1 = 0$: θ_0 = -arc cos 1/3 = -70.5 deg

These results were experimentally verified by Erdogan and Sih[12] who performed a series of tests using large sheets of Plexiglas, which were found to behave as an ideally brittle material.

Although their analysis was based on strictly elastic assumptions and assumed an ideally brittle material, it does appear to be valid providing Griffith theory is used to explain the behaviour of the propagating crack. It can then be said that the crack will grow in the direction along which the elastic energy release per unit crack extension will be maximum, and that the crack will start to grow when this energy reaches a critical value. In this form the MTS criterion has been used successfully by

many researchers[14,15,16], though its grounding in Griffith type LEFM makes its validity in highly plastic conditions questionable. Sih[17] reports that the apparent value of θ_0 can vary substantially depending on the critical distance from the crack tip where the measurement of propagation angle is made. He found that this distance is strongly influenced by the sharpness of the crack tip.

6.3.2 Maximum tangential strain criterion

Following similar lines to the maximum tangential stress criterion, this was proposed by Chambers *et al*[18], and is based on the plastic blunting mechanism of crack advance proposed by Laird and Smith[19]. It is argued that the magnitude of this blunting is linked to the tangential strain, and that in small scale yielding conditions the near tip strains are compatible with the those further away (i.e. within the elastic region). Hence following a similar methodology to the MTS criterion the direction of maximum tangential strain may be determined from a contour outside the plastic zone, and that this gives the preferential crack propagation direction.

6.3.3 Minimum strain energy density criterion (*S*-criterion)

This criterion was first proposed by Sih[17] and is based upon the local density of the strain energy field surrounding the crack tip. It assumes that the crack propagates in the direction along which the strain energy density, w, is minimum, and that fracture will occur when this parameter reaches a critical value w_c.

Sih[17] noted that both the Griffith[13] and the Irwin[20] approaches to fracture mechanics are both limited to mode I crack extension, where the direction of crack propagation, along the axis of symmetry, is known in advance. In the case of mixed mode loading, the initial angle of crack propagation is unknown, and hence scalar parameters such as G_I and k_I cannot completely predict mixed mode crack extension behaviour.

The strain energy density, w, is calculated along a circular contour at an arbitrary distance r_0 from the crack tip. r_0 is chosen such that the contour is outside the plastic zone at the crack tip, since this method is based on LEFM assumptions. The strain energy density, w, ahead of a crack tip is given in Eqn 6.9.

$$w = a_{11}k_1^2 + 2a_{12}k_1k_2 + a_{22}k_2^2 \tag{6.9}$$

where

$$a_{11} = \frac{1}{16\mu}[(1+\cos\theta)(\kappa-\cos\theta)]$$

$$a_{12} = \frac{1}{16\mu}\sin\theta[2\cos\theta-(\kappa-1)]$$

$$a_{22} = \frac{1}{16\mu}[(\kappa+1)(1-\cos\theta)+(1+\cos\theta)(3\cos\theta-1)]$$

μ is the shear modulus and κ is an elastic constant dependent on ν

According to Sih`s[17] hypothesis, the crack tip propagation direction could be evaluated by differentiating the strain energy density with respect to propagation angle, the critical propagation angle being given when w satisfies the conditions given in Eqn 6.10.

$$\frac{\partial w}{\partial\theta} = 0, \text{ and } \frac{\partial^2 w}{\partial\theta^2} > 0 \tag{6.10}$$

Several authors have used the S criterion, since it can account for complex loading schemes, however some contradictory reports have also been made [Tanaka[21], Theocaris and Andrianopoulos[22]]. These criticisms are directed at the lack of theoretical basis of the criterion. Theocaris and Andrianopoulos[22] argue that the strain energy density criterion is invalid since it is based on the summation of the distortional and dilatational strain energy densities, which in their view are entirely different physical quantities and should not be grouped together.

In Sih's[17] formulation the contour along which w is calculated is circular, and set at an arbitrary distance from the crack tip, the assumption of the circular form of the so called core region has not been justified. Yan *et al*[23] suggest that the elastic/plastic boundary is used instead of the circular contour.

6.3.4 Dilatational strain energy density criterion (*T*-criterion)

In order to justify their comments on the theoretical validity of the S criterion, Theocaris and Andrianopoulos[22] proposed a similar criterion, separating the strain energy density into its distortional and dilatational components, T_D and T_V respectively. They also attempted to satisfy the criticisms of Yan *et al*[23] by using the

Mises elastic-plastic boundary to define the extent of the core region. Theocaris and Andrianopoulos[22] argue that this core region has a physical meaning, as obviously the LEFM assumptions of both the S and T criterion are invalid within the plastic zone at the crack tip.

Theocaris and Andrianopoulos[22] hypothesised that the point at which crack extension occurs is when the dilatational strain energy T_V reaches a critical value $T_{V,cr}$. Using the Mises criterion to define the extent of the core region, results in T_V being calculated along a contour of constant distortion strain energy T_D (the elastic-plastic boundary). Hence in order to find the direction of crack propagation the mathematics reduces to finding the maximum value of T_V along a contour of constant T_D.

Theocaris and Andrianopoulos[22] have successfully applied the T criterion to a simple problem, comprising a single crack included at a given angle to the tensile axis. For this problem the dilatational and distortional component of the strain energy density are given by Eqns 6.11 and 6.12 respectively.

$$T_V = \frac{1-2\nu}{6E}(\sigma_X + \sigma_Y)^2 \tag{6.11}$$

$$T_D = \frac{1+\nu}{3E}\left(\sigma_X^2 + \sigma_Y^2 - \sigma_X\sigma_Y + 3\tau_{XY}^2\right) \tag{6.12}$$

where σ_x, σ_y and τ_{xy} are the singular stresses around the crack tip.

6.3.5 J – Integral criterion

This was proposed by Hellen and Blackburn[24] using the path independent integral proposed by Rice[25] to investigate the behaviour of cracks existing in mixed mode stress fields. They proposed a series of angled "virtual crack extensions" with the J integral being calculated at each deflected point. This would then allow the preferential propagation angle to be determined. This criterion was found to be successful under mode I dominated cases[26], however Gdoutos[27] found significant deviations from experimental results in cases where the loading was predominantly mode II. Unlike the criteria discussed earlier, the J-integral may be evaluated within the plastic zone. However, since any elastic unloading would invalidate the method, this may only be carried out under quasi-static conditions.

6.3.6 Crack tip vector method (CTOD/CTSD – criterion)

This criterion was proposed by Li[28] and based on the concept that the crack tip displacement vector (CTD) is the driving force for fatigue crack growth. This parameter is the vector summation of the crack tip opening displacement (CTOD) and the crack tip shear displacement (CTSD). The crack tip is then assumed to propagate in the direction of this vector. Li reported that good correlation was found when using this criterion to predict experimental data. As with the *J*-integral, the CTD remains valid when evaluated within the plastic zone. Validity is also maintained after unloading steps, and thus evaluating the effect of cyclic plasticity is possible using this criterion.

6.3.7 Summary

All the criteria discussed have been used by various authors to successfully characterise the preferential propagation direction of a fatigue crack under mixed mode conditions. Many of the criteria rely on elastic assumptions, and hence are applied along a contour which must by definition exist along or outside the elastic-plastic boundary. Generally these approaches are used in cases of limiting plasticity where the size of the plastic zone is small compared to the crack length. However in the models considered in this thesis this is not the case due to the high loading, thus a purely elastic contour will be of considerable radius. It is then questionable whether any effect measured so remotely from the crack tip has any bearing on the true crack tip behaviour. The issue of contour size makes the maximum tangential stress, *S* and *T* criterions unsuitable for the current work. Whilst the *J*-integral also requires a contour within a homogeneous material, it is not required to be outside the plastic zone. Hence throughout this work the *J*-integral is used to characterise both crack tip driving force and directional propensity. Criteria based on the crack tip vector method, show considerable promise, since they can account for the effect of fatigue, also as no contour is required the crack may cross from one material to another with impunity. Implementation of this criterion is difficult in highly plastic situations using the ANSYS code, since numerical errors in the crack tip elements tend to swamp true results.

6.4 General Modelling Strategy

A series of models were created to investigate the fatigue crack behaviour seen in experimental samples. The material tests were performed in three point bend and result in elliptical cracks propagating though the lining along the line of maximum bending stress as shown in Figure 6.6.

Thus the geometry required consisted of a half penny shaped or elliptical crack propagating from the surface of the lining material until its lower point begins to interact with the interlayer or backing material as shown in Figure 6.7. In order to truly represent this situation a fully three dimensional model would have been appropriate. However it was noted that due to the effects of multiple crack coalescences the crack would adopt a shape such that it could be approximated by a two dimensional section through the centre of the sample, normal to the plane of maximum bending stress, as shown in Figure 6.8. This geometry allowed investigation of the behaviour of the crack tip as it approached the backing layer or layers. As shown in Figure 6.8, in this orientation both the specimen geometry and the observed crack behaviour (bifurcation rather than single deflection) are symmetric, therefore a symmetric model may be employed, reducing computational cost.

The major drawback of this approach is that it was not possible to investigate the driving force variation along the crack front, this could only be evaluated at the lowest point. Experimental observations of sections of a real bearing have shown that the interfaces between the layers are not smooth as modelled here, rather they are fairly irregular. It was thought however that the omission of this feature would not compromise the integrity of the model, since the deviations from smoothness are small compared to the model dimensions.

In order to assess the effect of interface proximity on the near tip stress and strain fields, it is necessary to grow the crack through the material in some manner. Ideally this would be performed in a cyclic manner in order to build up a true plastic wake behind the crack tip (as in fatigue). This however would have been very time consuming and beyond the scope of the current work. Rather the crack was modelled at a number of discrete lengths and a monotonic load applied to it, therefore no effect of past loading history (i.e. closure) is accounted for in the results presented.

The models were designed to enable two parameters to be investigated, the first of these was simply the crack tip driving force, the second being the preferential

deflection angle. The former simply required a single undeflected crack to be "propagated" through the material in a number of steps, at each increment of growth the J-integral at the crack tip was assessed.

A schematic of the model is shown in Figure 6.9; it comprises an undeflected ligament of variable length, and a small fixed length ligament which may be deflected at any arbitrary angle. In order to assess directional propensity at each increment of crack length, the analysis is applied several times for different deflected angles. Typically solutions were obtained for deflected ligament angles of 0 degrees and 20-90 degrees in 10 degree increments, these values were denoted J_0, J_{20}, etc. After these iterations, the length of the undeflected ligament would be increased to bring the crack tip nearer the interface, and a new set of deflected angle increments started. This incremental process was implemented using a series of FORTRAN commands within the input ANSYS batch file allowing looping and incremental parameter value change. In this way it was possible to perform several hundred distinct analyses sequentially without requiring user input. This contributed considerably to the speed at which results could be produced.

It is proposed that the *J*-integral found in this manner can be thought of as analogous to crack tip driving force and that crack directional propensity may be determined from the series of angled crack extensions. It was assumed that the crack will propagate in the direction which produced the highest *J*, that is, the highest crack tip driving force.

A mixture of free and mapped meshing using 8 node quadrilaterals is used to control the mesh density and reduce the model's computational expense. Approximately 800 elements were required to mesh each model, though this figure changed slightly with each iteration. Several notable features of a typical model are shown in Figure 6.10, which shows the mesh surrounding the crack tip and deflected ligament. Firstly the elements at the crack tip are collapsed to form triangles, though the mid-side nodes are not moved to impose a $1/\sqrt{r}$ singularity. Secondly the semi circular region surrounding the deflected ligament is used as the basis for the *J*-integral contour. The disadvantage of this strategy for assessing the crack tip fields is that the crack tip cannot be brought into very close proximity with an interface. Since the contour cannot cross the bi-material boundary, sufficient material must remain ahead of the crack in order to include the semicircular contour. In practice it was found that this was not a great problem when modelling cracks solely within the

lining, it did however restrict the number of cases which could be investigated when the crack tip existed within the interlayer.

All models are loaded identically, in a manner to simulate the three point bend loading used in the experimental tests. Figure 6.11 shows the applied loads and constraints, which comprised, a symmetric boundary constraint along the base and a pin contact as labelled representing the lower fixed roller. Load is applied directly to the nodes as a point load in the position shown. It should be noted that the additional material outside these loading points is not modelled, as it is unstressed and would only add to the computational expense of the model, without providing any extra information.

It had been observed in experimental samples that crack bifurcation occurred within the interlayer. Considering the length of the crack at this point (~0.45mm) and the high loading, it is reasonable to assume that the material in the region of the crack tip will be highly plastic. Hence it was felt that the plastic behaviour of the material could not be discounted when attempting to investigate the observed phenomena, thus all the finite element models incorporate full elasto-plastic material models. These are provided as isotropic hardening curves, based upon yield stress and strain hardening rate data, created as described in Appendix II. The behaviour of the AS1241 lining material was described by the stress-strain curve provided by earlier experimental tensile testing, and shown in Figure 2.42. However generally the only material data available was in the form of yield stress and tangent modulus data; this is especially true when graded layers are considered, where a great number of nominal materials are involved. The values used for the key parameters are given in Table 6.1. It should be noted that unlike Sugimura *et al*[9], the material layers considered here have differing elastic properties in addition to their plastic dissimilarity.

Table 6.1: Material properties used in finite element modelling

Material	Young's Modulus (GPa)	Poisson's Ratio	Yield Stress (MPa)	Ultimate Tensile Stress (MPa)
AS1241 Lining	69.8	0.33	56.6	187.5
Pure Al Interlayer (when used)	70	0.3	28	76
Mild Steel Backing	207	0.3	N/A	N/A

N.B. No plastic properties are provided for the steel backing, since at all time during the analysis, its behaviour was well within its elastic limit. (c.f. $\sigma_{max,steel}$ = 145MPa, $\sigma_{y,steel}$ = 420MPa.)

Subsequent to the generation of material response curves, the model was solved incrementally, with the plastic strain being resolved at each step, it was found that typically 50-60 iterations are required to reach convergence. After solution the crack tip *J*-integral was calculated using the circular contour provided, this process is described in Appendix III.

6.5 Modelling of AS1241 Bearing as a Bi-layer

Before considering tri-layer systems such as the one tested at Southampton, it was decided to establish the necessary modelling techniques on a simpler bi-layer material system.

Considering the properties of the AS1241 tri-layer bearings, it is seen that the AS1241 lining material and the pure aluminium used for the interlayer have very similar elastic properties, hence it was thought a reasonable assumption that these materials could be combined together in a single layer, using common properties. Further examination will reveal that whilst elastically similar, these materials have very dissimilar plastic behaviour. The implications of this are shown subsequently.

6.5.1 Crack tip driving force variation in bi-layer representation

A graph of crack length against apparent crack tip driving force is given in Figure 6.12. In the first instance, the analysis was only intended to investigate the driving force variation as the crack approached the interface between lining material and backing, it was therefore unnecessary to complicate the model with a deflectable crack tip. The undeflected crack was forced to propagate along the direction normal to the interface in 0.025 mm steps from an initial length of 0.1 mm to a final length of 0.475 mm. As expected, initially the apparent crack tip driving force increased fairly linearly with crack length, before reaching a maximum value at a crack length equivalent to ~75% lining thickness. After this point, the crack tip driving force was seen to drop increasingly rapidly with continued propagation towards the interface.

This trend continued until the crack reached its maximum length, the final value of crack tip driving force being almost 20% lower than its maximum.

6.5.2 Crack tip deflection behaviour in bi-layer representation

It had been noted from the previous model that as the crack tip approached the interface the apparent crack tip driving force reduced. This effect has been observed before; Sugimura *et al*[9] linked this effect to a propensity for crack tip deflection. In order to investigate this hypothesis, the bi-layer model was reformulated to include a deflected ligament as described in Section 6.4. As before the crack was propagated from a length of 20% to a length of 95% lining thickness. However on this occasion larger steps were used (c.f. 12.5% rather than 5%). At each increment of crack length, the crack tip deflection angle was varied from 20 to 100 degrees in 5 degree increments, and the crack tip driving force evaluated. Smaller deflection angles than 20 degrees were not considered since they would result in a very distorted mesh between the deflected ligament and the axis of symmetry. It was felt that this poor meshing would compromise the accuracy of any solutions acquired at low deflection angles.

For each crack length the normalised apparent crack tip driving force (J_ϕ/J_0) was plotted against deflection angle. This graph is shown in Figure 6.13, where it can be seen that at short crack lengths higher crack tip driving forces were recorded at small deflection angles. Whilst when the crack is approaching the interface, the maximum crack tip driving force was recorded at the maximum deflection angle of 90 degrees. It is interesting to note that the change from a propensity for continued straight propagation to one for deflection occurs at a similar crack length to that at which the crack tip driving force is seen to begin to drop. However this transition occurs at considerably shorter crack lengths than was observed in experimental samples indicating that the omission of a discrete interlayer in the model was a poor assumption.

6.6 Modelling of AS1241 Bearing as a Tri-layer System Including Interlayer

The behaviour predicted by the bi-layer representation of the AS1241 bearing does not match up particularly well with the experimental observations of sub-surface crack behaviour. In order to bring the model closer to true material system, the interlayer was incorporated as a separate layer of distinct properties, creating a tri-layer model. This layer had been omitted in the bi-layer model since its elastic properties are very similar to the AS1241 lining material. At the time it was noted that a large discrepancy existed between the plastic properties of the two materials (see Table 6.1). The bi-layer model was extended to include the interlayer by adding a layer of elements with the properties of pure aluminium, and reducing the thickness of the lining by a corresponding amount. The rest of the model was left unchanged including the crack tip contour and deflected ligament.

As before a single crack was artificially "propagated" through the material with the same small deflections being made at each crack length. The crack driving force was evaluated in the same manner as with the bi-layer model.

It was possible to grow the crack through the lining material as before, however due to the small thickness of the interlayer compared with the size of the crack tip contour (c.f. interlayer thickness = 0.05 mm, contour radius = 0.015 mm), it was not possible to get many results with the crack penetrated into the interlayer.

6.6.1 Crack driving force variation in tri-layer representation

A crack was propagated from an initial length of 0.22mm (corresponding to ~48% lining thickness) to a final length of 0.42mm (~93% lining thickness), with no crack tip deflection being considered during this initial stage. This process brought the crack tip as close as possible to the interface between the lining and the interlayer, before the crack tip contour began to interfere with the interface. It was seen that as the crack extended through the lining material, the apparent crack tip driving force continued to rise, indeed at an increased rate when the crack tip approached the interlayer, rather than dropping off as had been the case in the earlier bi-layer models. The graph of crack tip driving force against crack length is given in Figure 6.14 .

A second modelling run was performed with the crack tip penetrated into the interlayer. Due to the limitations posed by the size of the *J*-integral contour, it was only possible to obtain results at crack lengths between 0.46mm and 0.485mm, which

correspond to 20% to 70% of the interlayer thickness. The results are given in Figure 6.15 and show a steep downward trend in the crack tip driving force, indicating severe shielding with continued propagation towards the steel backing.

6.6.2 Crack directional propensity in tri-layer representation

As with the bi-layer case the deflection behaviour of the crack tip was investigated in the tri-layer material system. This was done in the same manner as before, using virtual crack extensions of between 20 and 90 degrees at each crack length. This process was carried out for both the case of a crack existing solely within the lining, and for the case when interlayer penetration had occurred. The same limitations on crack length were applied as in the analysis of driving force alone, hence results were obtained for crack lengths between 0.22mm and 0.42mm and for cracks 0.46mm to 0.485mm in length. The results for lining only and interlayer penetrating cracks are given in Figures 6.16 and 6.17 respectively.

It can be seen that for cracks growing solely within the lining material, it appeared more favourable for the crack to propagate directly towards the interface. Indeed if the driving force results may be linked to crack growth rate, the crack appears to accelerate. Once the crack tip had penetrated into the interlayer, over the limited range of the measurements it appears more favourable for the crack tip to deflect away from the mode I direction. These deflection measurements are consistent with the reduction in driving force predicted when the crack tip was forced to grow directly towards the backing.

6.7 Behaviour Comparisons of Bi and Tri-layer Representations of AS1241 Bearing

Considerable difference was seen between the bi layer and tri-layer finite element model representations of the AS1241 bearing tested at Southampton. The tri-layer model showed enhanced crack tip driving force as the crack approached the interlayer. No propensity for deflection was noted until the crack had penetrated this layer, at which point crack shielding also became apparent. This predicted behaviour is consistent with the behaviour seen in experimental samples.

In contrast, the predicted crack shape in the bi-layer case, exhibits considerably earlier deflection, and a marked decrease in crack tip driving force as the crack tip approaches the interface with the steel backing. This decrease in driving force and the corresponding propensity for deflection are first noted at a crack length corresponding to ~75% lining thickness. These findings are in line with those of Sugimura *et al*[9] who report similar reductions in driving force of cracks approaching a bi-material interface from the softer side. Although none of the experimental tests at Southampton were performed on bi-layer materials, a considerable amount of previous work has been undertaken by Shenton *et al*[29] and his results are used for comparison with the current analytical findings. Figure 6.18 shows a section through a cracked bi-layer bearing. The crack in this case exhibits earlier deflection as predicted by the model.

The difference in crack tip driving force during the time when the crack exists solely within the lining can be seen clearly in Figure 6.19, which illustrates the higher driving forces seen in the tri-layer representation of the bearing material system. The crack shapes predicted by the two models are shown schematically in Figure 6.20 to allow comparison.

These fundamental differences in behaviour can be attributed solely to the inclusion of the soft interlayer, showing that this feature has a strong influence on the overall behaviour of propagating fatigue cracks in this type of material system. Hence a series of parametric studies was undertaken to investigate the influence of both interlayer properties and thickness; these studies are presented in Section 6.9.

6.8 Parametric Feature Studies

A number of conceptual bearing designs were proposed by the sponsoring company. These were used to study the effect of varying the interlayer thickness and material properties in a parametric manner. It was hoped to use the techniques described in earlier sections to attempt to predict the likely fatigue crack behaviour in these material systems and possibly make some assessment of fatigue life. Seven bearing systems were considered, which are summarised in Table 6.2 and the schematic structures of which are given in Figure 6.21.

Table 6.2: Conceptual bearing details

Case	Lining Material	Lining Thickness (mm)	Interlayer Material	Interlayer Thickness (mm)
1	AS1241	0.45	1xxx Al	0.05
2	AS1241	0.45	AS1241	0.05
3	AS1241	0.45	CL154	0.05
4	AS1241	0.45	2xxx Al	0.05
5	AS1241	0.475	1xxx Al	0.025
6	AS1241	0.25	1xxx Al	0.25
7	AS1241	0.475	CL154	0.025
8	AS1241	0.25	CL154	0.25

N.B. In all cases the backing consisted of 1.5 mm of steel.

The material designated CL154, an AL-Si-Mg-Cu system is considered as a replacement for the 1xxx Al in interlayer applications; its properties along with those of the other candidate interlayer materials are given in Table 6.3.

Table 6.3: Interlayer Properties

Material	Young's Modulus (GPa)	Poisson's Ratio	Yield Stress (MPa)	UTS (MPa)	Elongation at UTS (%)
1xxx	70	0.3	17	55	25
AS1241	69.8	0.33	56.6	173	17.4
CL154	70	0.3	74	152	21
2xxx	70	0.3	97	186	18

6.8.1 Case 1 and Case 2 – standard bearing

These are the tri-layer and bi-layer representations respectively of the standard AS1241 bearing. The results from these models were discussed in depth in sections 6.7 and 6.6, respectively.

6.8.2 Case 3 – bearing with standard thickness CL154 Interlayer

The results for this model, shown in Figures 6.22 and 6.23, indicate that initially the crack tip driving force increases with crack length, as was the case with the standard bearing. At this stage with a small crack existing within the lining only there is no propensity for crack deflection. When the crack length is increased to a length of 0.37mm a reduction of crack driving force was noted and this was accompanied by a tendency for crack deflection. This reduction in driving force continued until the test was halted at a crack length of 0.42mm

6.8.3 Case 4 – bearing with standard thickness 2xxx Al interlayer

The result for this model are shown in Figures 6.24 and 6.25. This model was run in order to assess the effect of a very hard interlayer on the predicted fatigue crack behaviour, in this case a material having the properties of a 2xxx series Aluminium alloy was used. The results obtained were very similar to those for case 2, except the drop in driving force associated with the crack tip approaching the interlayer was more pronounced and accompanied by a very strong propensity for crack deflection.

6.8.4 Case 5 – bearing with reduced thickness 1xxx Al interlayer

In addition to varying the properties of the interlayer the sponsoring company were also interested in the effect of varying the thickness of the interlayer relative to the lining material. Results for crack tip driving force and deflection propensity are shown in Figures 6.26 and 6.27. In this case the interlayer was reduced to half its original thickness, whilst the lining thickness was increased by a corresponding amount. Compared with the results for a bearing containing the standard thickness pure aluminium interlayer within the crack range modelled (0.22mm to 0.42mm), the previously observed crack tip amplification was not observed, rather a very slight decrease in crack tip driving force coupled with a propensity for deflection was predicted as the crack reached its maximum length.

6.8.5 Case 6 - bearing with increased thickness 1xxx Al interlayer

It is also possible to increase the thickness of the interlayer, in this case it is made half the total lining thickness, with a corresponding reduction in lining thickness. The results shown in Figures 6.28 and 6.29 show that a short crack existing in the lining only appears to have a much higher driving force than a similar crack in a standard bearing system. Once the crack was allowed to extending into the interlayer, the driving force dropped off markedly and a propensity for deflection became evident almost immediately.

6.8.6 Case 7 – bearing with reduced thickness CL154 interlayer

This model was used to investigate the combined effect of increasing the hardness of the lining material whilst at the same time reducing its thickness. The model has the same geometry as case 4 however the interlayer is modelled as CL154. The results shown in Figures 6.30 and 6.31 show a trend similar to that obtained with

the standard thickness CL154 interlayer, with the crack tip driving force reducing as the crack tip approached the interface. It was intriguing to note that this reduction is less pronounced with the thinner interlayer, as the opposite trend was observed when the thickness of the pure aluminium interlayer was reduced in thickness.

6.8.7 Case 8 – bearing with increased thickness CL154 Interlayer

This model combines the effect of an increase in interlayer hardness coupled with an increase in thickness until the interlayer comprises half the total lining thickness. The results are shown in Figure 6.32 and 6.33 and show that whilst the crack existed only in the lining the crack driving force was very low, compared to other material systems, upon crossing into the interlayer the crack tip experiences rapidly increasing driving force until the crack approaches the steel backing. Interestingly the propensity for deflection occurs at a much shorter crack length than that at which a reduction in crack tip driving force is observed.

6.8.8 Summary of parametric behaviour studies

Considering first the effect of altering the material properties of the interlayer. In the case of the interlayer being softer than the lining (Case 1), crack driving force amplification was predicted when the crack tip approaches the interlayer. The effect of increasing the yield stress of the interlayer can be seen in Figure 6.34. In the case of a Bi-layer, effectively an AS1241 interlayer (Case 2), some degree of shielding can be seen, increasing the interlayer yield stress further to that of CL1534 (Case 3) and then to that of a 2xxx Al (Case 4) causes the magnitude of this shielding to rise with increasing interlayer yield stress.

The effect of reducing the interlayer thickness can be seen in Figure 6.35 which shows the driving force plots for the reduced thickness 1xxx (Case 5) and CL154 (Case 7) interlayer plotted against those of standard thickness interlayers (Cases 1 and 3 respectively). In the case of the soft 1xxx Al interlayer, the reduction in thickness appears to cause a reduction in the observed amplification effect, whereas in the case of the CL154 interlayer, a reduction in thickness reduces the magnitude of the shielding effect.

The trends in the increased thickness interlayers are harder to see, Figure 6.36 shows the apparent crack tip driving force plots for the increased thickness 1xxx Al (Case 6) and Cl154 (Case 8) interlayers, plotted with those of standard thickness for

comparison (Cases 1 and 3 respectively). Compared with a standard layer, the increased thickness 1xxx Al interlayer shows initially greatly enhanced crack tip driving force, however after interlayer penetration occurs, shielding becomes evident fairly quickly. The increased thickness CL154 interlayer shows initially much lower driving forces than a standard thickness CL154 interlayer, however less shielding is evident when the crack tip approaches the backing as indicated by the slightly higher driving force at this point.

6.9 Evaluation of Conceptual Bearing Designs

In addition to the parametric studies, two other bearing designs were considered, the construction of which are shown schematically in Figure 6.21. The first of these is a sputter coated bearing used in high load applications, the second is an advanced conceptual design, comprising a lining of graded material properties and no interlayer.

6.9.1 Sputter coated CL154 bearing

This type of bearing has been extensively tested by the sponsoring company using a Sapphire type accelerated test rig[30], where it was found to have excellent fatigue resistance. The bearing comprises a CL154 lining with a sputtered Al coating, a standard steel backing and no discrete interlayer. Due to the extreme thinness of the sputtered layer (15-20 μm) it was not possible to model cracks existing solely within the coating. Therefore the results shown in Figures 6.37 and 6.38 relate to cracks penetrated well into the CL154 layer. Their behaviour was consistent with that of a CL154/steel bi-layer, in that a propensity for deflection, coupled with a drop in crack tip driving force was first noted at a crack length of 0.4 mm and continued until maximum crack length was reached.

6.9.2 Bearing with graded lining and no interlayer

The final case considered was a possible future bearing design comprising a steel backing and a graded lining with no discrete interlayer. The lining was to vary from a very soft pure aluminium type material at the surface to a material with

properties such that it was 20% stronger than AS1241 at the interface with the steel backing as shown in Table 6.4.

Table 6.4: Variable property extremes used for graded lining material

Position	Young's Modulus (GPa)	Poisson's Ratio	Yield Stress (MPa)	Ultimate Tensile Stress (MPa)
Surface	70	0.3	33.8	77.8
Interface with steel	69.8	0.33	68.0	225.0

It should be noted that, for modelling purposes the lining properties were assumed to vary linearly between the lining surface and the interface with the steel backing, though this need not be the case.

Modelling the graded lining could be approached in two ways, either it could be modelled as a number of distinct strips, or as a continuous grade with each element having its own properties. It was felt that the former would lead to problems, since the number of "virtual interfaces" would severely limit the number of crack lengths which could be evaluated due to problems fitting in the contour. It would however lead to a homogenous grading along the length of the strip. The second approach is to give each element individual properties based upon its position. This approach results in a vast number of material properties, but does allow any crack length to be used, since there are no interfaces to interfere with the crack tip contour. For these reasons, this second approach was selected..

The graded lining model was based on the bi-layer model since no distinct interlayer was required. The *J*-integral contour and the ability to model deflection of a small crack tip ligament is retained, since it was required to investigate the deflection behaviour as well as the driving force variation through the sample. The model was initially meshed assuming that it consists of a homogeneous material. Then each element in the lining is selected in turn, and given material properties based on the x co-ordinate of its centroid. This results in a constant gradation of material properties from the surface to the interface, the smoothness of which is limited only by the element density. The absence of "virtual interfaces" puts little restriction on the position of the crack tip within the lining and hence allows the behaviour of a full set of crack lengths to be investigated. This approach results in the crack tip J-integral being calculated over a region on non-homogeneous material, thereby making the

evaluation of this parameter strictly invalid. However since the radius of the J-integral contour is very small, the change in material properties across it is negligible (~0.06%), and hence it is argued that material within the contour maybe considered homogeneous.

Several points were noted from the results of this model. Firstly the crack tip driving force at minimum crack length was ~10% lower than all of the other cases except the thick CL154 case. Secondly the increase of crack tip driving force with crack length occurred at a slower rate than with the homogeneous lining cases. Thirdly, and most notably the driving force dropped off much earlier than had been observed in the other cases, a severe drop in crack tip driving force and a corresponding increase in deflection propensity being predicted at a crack length of 0.32mm. The crack tip driving force results for the graded layer bearing are shown in Figure 6.39, a plot for the standard bearing is included for comparison. Considering the crack deflectional propensity graph shown in Figure 6.40, it is interesting to note that for much of its growth there seems to be no strong propensity for deflection or for straight crack growth, unlike all the other cases studied.

6.10 Discussion

6.10.1 Implication and validity of selected methodology

Models based on a 2-dimensional approximation of the real crack shape have been found to produce results consistent with experimental observations in the cases of the tri-layer AS1241 bearing and the bi-layer AS78 bearing.

For the current quasi-static fracture mechanics-based study of crack behaviour in bearing materials systems, the *J*-integral was shown to be valid. It was then used to characterise both the crack tip driving force and the propensity for crack deflection. The driving force had to be found directly from a near tip contour, a far field contour being invalid due to the constraints of the layered structure. Hence it was not possible to evaluate the effects of the elastic and plastic behaviour separately as in the Sugimura *et al*[9] approach. This is in part due to the current work relating to a realistic system rather than an idealised case. However it was possible to re-create the trends observed by earlier workers using the selected approach.

The macro used to calculate the integral was found to perform well, and was accurate when compared with a standard solution. As expected the integral was shown to be path independent, even within the quasi-plastic region, providing the contour was remote from the very near tip elements, which were found to give inaccurate results.

It should be noted that due to the monotonic loading history, the results obtained are essentially based upon a fracture mechanics approach, rather than considering the effect of cyclic fatigue loading. It is however encouraging to see that the trends predicted by this simplified approach do correlate well with experimental observations.

In this study the quoted values for crack tip driving force are based upon the value of the near tip *J*-integral evaluated at maximum load. In the case of fatigue, the crack tip driving force should be related to the *J* integral range. To fully model fatigue, cyclic loading must be applied, and residual plasticity allowed to form within the crack wake. This will undoubtedly cause closure effects, and will be particularly important when crack deflection is considered. Under these dynamic conditions the *J*-integral would not be theoretically valid, since the material would have undergone some degree of elastic unloading. However the use of the cyclic *J*-integral was proposed by Dowling *et al*[31] for characterising crack growth rates. Used in a semi empirical manner as given by Eqn 6.13 it was found to be successful, but the method's lack of theoretical basis, has inhibited its adoption.

$$J^C \approx 3.2(\Delta w_e)a + 5.0(\Delta w_p)a = \frac{1.6(\Delta\sigma)^2 a}{E} + \frac{5.0(\Delta\sigma)(\Delta\varepsilon_p)a}{\left(\frac{n+1}{n}\right)} \qquad (6.13)$$

A more valid method would be to evaluate the crack tip behaviour using the crack tip opening displacement (CTOD). This parameter in conjunction with the crack tip sliding displacement (CTSD) may be used to fully characterise the behaviour of the crack tip during both loading and unloading steps, thus accounting for the effect of accumulated plastic damage. Moreover it is valid under highly plastic conditions and in all materials. It was not used in the current work since it was found that the ANSYS solution near the crack tip was not accurate enough under elasto-plastic conditions to allow its reliable use. In any future work a move to a more advanced finite element code (e.g. ABAQUS) should be considered if this criterion is to be adopted.

6.10.2 Modelling of standard AS1241 bearing system

Initially the standard AS1241 bearing as tested at Southampton was modelled as a bi-layer (the interlayer being ignored and the lining increased in thickness by a corresponding amount). This was done to attempt to validate several of the techniques required on a simpler system first.

It was seen for small cracks, that crack tip driving force increased proportionally with crack length as one would expect, however as the crack tip plastic zone approached the interface, its driving force began to reduce. It appears that the interaction between the plastic zone of the approaching crack and the interface leads to a rapid increase in the extrinsic shielding experienced by the crack tip. It appears that remote from the interface, it is more favourable for the crack to continue propagating towards the interface. However at the point when shielding begins to evolve, there appears to be a marked tendency for the crack to bifurcate. This propensity for bifurcation appears to occur simultaneously with the onset of reduced crack tip driving forces.

In the bi-layer model, the lining is much softer than the steel, and it appears that the plastic zone created in this softer material is incapable of penetrating into the steel, indeed the steel remains elastic at all points during the analysis. This causes the shape of the plastic zone ahead of a crack approaching the interface to become highly distorted causing the predicted large increase in extrinsic crack tip shielding.

The transition from a propensity for continued straight propagation, to one for 90 degree deflection takes some time to evolve, typically about 10% lining thickness. It is thought that this is due to the increase in shielding with increasing crack length being fairly slow and hence it is believed that in reality this would lead to a gradual bifurcation to the crack tip. This type of behaviour has been observed in early AS78 bearings comprising a steel backing and an Al-Si system lining material, post failure micro-graphs of this were provided by Dana Glacier Vandervell and are shown in Figure 6.18.

The behaviour of the bi-layer representation of the AS1241 bearing, was considerably different from the experimental observations, hence the model was extended to include the interlayer, which is noted to be very thin and very soft, compared to the rest of the lining. It was seen that as a crack (existing solely within the lining), approached the interlayer, the apparent crack tip driving force increased, in contrast to the previously observed reduction in the bi-layer case. It was also noted

that no propensity for deflection away from the far field mode I direction was detected for cracks prior to interlayer penetration. This trend was reversed when the crack was allowed to penetrate into the interlayer. The *J*-integral showed a marked drop with further propagation towards the backing, and this was coupled with a rapid change to a propensity for 90 degree deflection.

For a crack existing solely within the lining, the model predicts anti-shielding as the crack approaches the interlayer. It appears that the close proximity of the soft interlayer reduces the local compliance near the crack tip (similar to a free surface condition). Causing an increase in both crack tip plastic zone size (which penetrates well into the interlayer) and in crack tip driving force. Essentially this is completely the opposite effect to the previously observed shielding, evolved when the crack was approaching the interface from the softer side (as in the bi-layer case). This so called "crack amplification" or anti-shielding was commented on by Sugimura *et al* who described this effect as a crack approached an interface from the less compliant side. Sugimura *et al*[9] were able to measure an increase in crack growth rate associated with the predicted point of crack amplification, demonstrating that it is a real effect. Unsurprisingly, given the increase in crack tip driving force, no propensity for crack tip deflection was predicted for a crack existing solely within the lining. This was not the case when the crack was allowed to propagate into the interlayer. It was not possible to model very small penetrations due to meshing constraints, however it was possible to observe a radical behaviour change. It appears that the material system now behaves as a highly compressed bi-layer, the plastic zone formed in the very soft interlayer being highly compressed by the proximity of the elastic backing, causing shielding. As was observed earlier these high levels of extrinsic crack tip shielding are associated with a propensity for deflection. In this case the change from 0 degree to 90 degree is very sharp, conforming to experimental observations.

6.10.3 Role of interlayer material properties

A major topic for discussion with the sponsoring company was the role played by the material properties of the interlayer on the fatigue performance of the whole bearing system. It appears that the yield stress of this layer is critical in determining the point at which crack deflection occurs. For this reason a parametric study to investigate the role of interlayer yield stress was carried out. It should be noted that all

the materials considered as interlayer candidates had identical elastic properties, only the yield stress and strain hardening values were altered.

Four different interlayer materials were investigated as described in Section 6.9. It was seen that a bearing containing an interlayer softer than the lining, would exhibit crack amplification as the crack tip approaches the interlayer, and that crack deflection would occur only after interlayer penetration. Increasing the strength of the interlayer to that of the lining was seen to remove the crack amplification. Further increases in interlayer strength were seen to promote increased shielding and earlier crack deflection.

These effects can be explained by the compliance mismatch between the lining and the interlayer. In the case of a soft interlayer, the approaching crack encounters a area of reduced compliance, which causes an increased plastic zone size and hence increased crack tip driving force. When the interlayer is made harder than the lining the reverse is true, the plastic zone of the approaching crack is compressed by the increased compliance form the hard interlayer, hence causing shielding and crack deflection. The magnitude of this shielding appears to be related to the compliance mismatch between the lining and the interlayer materials.

It therefore appears that the inclusion of an interlayer material having a yield stress considerably lower than that of the lining material may be detrimental to the overall fatigue performance of the bearing, since such an interlayer will promote increased crack tip driving forces in its vicinity and this has been linked to considerably later deflection.

6.10.4 Layer geometry effects

The second feature investigated was the role of interlayer thickness. The total thickness of the lining and interlayer was kept constant, however the ratio between them was altered considerably. The effect of reducing the thickness of the interlayer to half its standard thickness was investigated first.

In the case of a standard 1xxx Al interlayer, reducing the thickness removes the previously observed anti shielding as a crack approaches the interlayer. This is attributed to the thinner soft interlayer no longer being able to buffer the approaching crack from the shielding effects of the very stiff steel backing. Hence local compliance just prior to interlayer penetration will be higher in this case than in the standard bearing, leading to some degree of shielding being evolved.

The effect of reducing the thickness of a interlayer stiffer than the lining was also investigated, a bearing containing a reduced thickness CL154 interlayer was shown to exhibit less shielding at a given crack length than that of a standard CL154 bearing. This was attributed to the thinner interlayer producing a smaller region of raised local compliance within the lining adjacent to the interlayer.

Overall it was seen that to promote early deflection, the local compliance in the lining material must be increased; in the case of a soft interlayer this may be achieved by reducing its thickness, whereas a harder layer should be kept at its maximum thickness.

This view was given further credence when the effect of increasing the interlayer thickness to half the overall lining thickness was considered. In the case of a soft interlayer, initially greatly enhanced crack driving force was observed. Of course once the crack had penetrated the interlayer the very high compliance of the steel caused high levels of shielding to be evolved quickly. In the case of the thick CL154 layer it was harder to assess what the overall effect may be, since initially the crack tip driving force is very low due to the high local compliance in the lining caused by the thick interlayer. But the values of crack tip driving force near the interface with the steel are quite high. However it can be seen that almost immediately after interlayer penetration a propensity for crack deflection is developed. This particular conceptual bearing may well be worthy of further experimental study to investigate the predicted performance benefits over a standard bearing.

A more extreme version of the thick CL154 interlayer bearing, which essentially exhibits the same behaviour, is the proposed sputter coated bearing. Unfortunately due to the extreme thinness of the sputtered layer it was not possible to investigate the behaviour of crack existing solely within this layer using the current model geometry. Since it is known from experimental studies performed by the sponsoring company, that cracks do not penetrate into the CL154 layer, this is precisely the region of interest. It is however possible to postulate the likely behaviour of a small fatigue crack – since it should be analogous to some of the other systems examined. Since the sputtered layer is very soft compared to the CL154 layer adjacent to it, it can be assumed that a crack tip approaching the interface between the layers will experience a shielding effect. If the magnitude of this shielding effect is great enough then the crack will bifurcate rather than penetrating further into the bearing. This may be considered as highly compressed bi-layer behaviour. There is

evidence for this type of behaviour from experimental samples, which show no macroscopic fatigue damage after testing[29]. It is unlikely that no cracks have initiated, but rather their presence has been obscured by the smearing of the soft Al layer. This has been compounded by the cracks inability to penetrate into the CL154 layer making their detection difficult.

The predicted behaviour from the finite element model of this system, thus applies to a scenario which will not occur, i.e. a crack penetrating deep into the CL154 layer and as one would expect, the predicted behaviour is very similar to that of a simple CL154-Steel bi-layer material system.

6.10.5 Behaviour of graded layers

The bearing featuring a graded lining material is a possible future design under development by the sponsoring company. The behaviour of a crack within this lining material was studied to investigate any potential fatigue performance gains. The graded lining was modelled by assigning material properties to individual elements based upon their position. Thus the accuracy to which the grading of the layer is modelled is dependent entirely on the mesh density. The results showed generally lower crack tip driving forces and an early propensity for crack tip bifurcation. It was also seen that the rate at which crack tip driving force increased with crack length was also lower than in monolithic cases. This can be attributed to the material ahead of the crack being harder at all times, thus the crack tip experiences a shielding effect at all crack lengths. The presence of this intrinsic shielding effect means that far less extrinsic shielding from an interface effect is required for crack bifurcation to occur, hence leading to earlier crack tip deflection. It is believed that these effects will lead to longer fatigue lifetimes in experimental samples. As was noted earlier, for several of the crack lengths investigated, no definite directional propensity was observed. It is believed that in reality this will cause the crack to become extremely microstructurally dependent. This feature could in turn be used to increase fatigue lifetimes via carefully chosen secondary phases to cause a highly deflected crack path (hence reduce crack tip driving force via additional microstructural scale shielding and closure effects).

6.11 Summary and Conclusions

It has been shown that the layered material structure employed in plain bearings exerts a considerable influence on the mesoscopic growth of fatigue cracks. It has been shown that in the case of the standard AS1241 bearing a fatigue crack will undergo a marked behaviour change from a nominally mode I direction, when it enters the 1xxx Al interlayer. The cause of this radical bifurcation has been linked to a severe increase in local compliance ahead of the crack tip preventing its penetration into the steel backing. This increase in near tip shielding has also been conclusively linked to a propensity for crack deflection, correlating well with experimental observation.

The role of the interlayer in fatigue crack behaviour has been characterised, showing that the 1xxx Al material in the tested bearings will tend to accelerate cracks prior to interlayer penetration, deflection only occurring after this event. Finite element models of cracks in bearings employing harder interlayer materials relative to the lining, display increased shielding and earlier crack deflection than the standard bearing. The magnitude of this shielding was shown to be proportional to the hardness ratio of the two materials.

The role of interlayer thickness was also quantified, showing that in the case of soft interlayers, a reduced thickness gives increased shielding and hence earlier deflection. The converse being true of hard interlayer material, where it was found to be more beneficial to increase the interlayer thickness to its maximum amount. This view was confirmed by experimental tests on a sputter coated bearing, which showed no fatigue damage at even extreme stress levels.

Predictions were made about the likely fatigue behaviour of a bearing containing a lining material of graded material properties. It was seen that such a material appeared to exhibit intrinsic shielding, and hence required little extrinsic shielding to bring about severe crack deflection. It was also noted that for much of its life a crack in such a material showed little definite directional propensity. This was considered evidence that micro-structural influences on fatigue behaviour in this material system would be important.

Overall it is felt that the bearings worthy of further study are the graded lining bearing, the thick interlayer CL154 bearing and the sputter coated conceptual bearing,

as all of these show possible performance gains over the standard AS1241 type tested at Southampton.

6.12 References

[1] S. Suresh and C.F. Shih, Plastic near tip fields for branched cracks, Int. J. Fracture V30 pp237-259 (1986)

[2] B. Cotterell and J.R. Rice, Slightly curved or kinked cracks, Int. J fracture 16 pp 155-69 (1980)

[3] S. Suresh, Crack deflection: Implications for the growth of long and short fatigue cracks, Met Trans 14A pp2375-85 (1983)

[4] T.S. Cook and F. Erdogan, Stresses in bonded materials with a crack perpendicular to the interface, Int. j. Engng Sci 10 pp677-97 (1972)

[5] F. Erdogan and V. Biricikoglu, Two bonded half planes with a crack going through the interface, Int. j. Engng Sci. 11 pp745-66 (1973)

[6] M He and J.W. Hutchinson, Crack deflection at an interface between dissimilar elastic materials, Int. j. Solids Structures V25 No9 pp 1053-67 (1989)

[7] S. Suresh, Y. Sugimura and E.K. Tschegg, The growth of a fatigue crack approaching a perpendicularly-orientated bimaterial interface, Scripta Met and Mat V27 pp1189-1194 (1992)

[8] S. Suresh, Y. Sugimura and T. Ogawa, Fatigue cracking in materials with brittle surface coatings, Scripta Met. et Mat. V29 pp237-242 (1993)

[9] Y. Sugimura, P.G. Lim, C.F. Shih and S. Suresh, Fracture normal to a bimaterial interface: effects of plasticity on crack tip shielding and amplification, Acta Met V43 No3 pp1157-69 (1995)

[10] F.Z. Li, F. Shih and A. Needleman, A comparison of methods for calculating energy release rates, Eng Fract Mech V21 No2 pp 405-21 (1985)

[11] A.S. Kim and S. Suresh, Plasticity effects on fracture normal to interfaces with homogeneous and graded compositions, Int J. Solids Structs V34 No26 pp 3415-32. (1997)

[12] F. Erdogan and G.C. Sih, On the crack extension in plates under plane loading and transverse shear, J. Bas. Eng. ASME Trans 85 pp519-25 (1963)

[13] A.A. Griffth, The phenomenon of rupture and flow in solids, Trans Roy Soc. A221 pp 163-97 (1921)

[14] A.T. Yokobori, T. Yokobori, K. Sato and K. Syoli, Fatigue crack growth under mixed modes I and III, Fatigue Fract. Engng. Mater. Structures, 8 pp315-25 (1985)

[15] L.P. Pook, The fatigue crack direction and threshold behaviour of mild steel under mixed mode I and III loading, Int. J. Fatigue, 7 pp21-30 (1985)

[16] T.H. Hyde and A.C. Chambers, A compact mixed mode (CMM) fracture specimen, J. Strain Analysis, 23 pp 61-66 (1988)

[17] G.C. Sih, Strain energy density factor applied to mixed mode crack problems, Int. J. Fracture 10 pp305-21 (1974)

[18] A.C. Chambers, T.H. Hyde and J.J. Webster, Mixed mode fatigue crack growth at 550°C under plane stress conditions in jethete M152, Engng fract. Mech V39 pp 603-19. (1991)

[19] C.Laird and G.C.Smith, Crack propagation in high stress fatigue, Philosophical magazine 8 pp 847-57 (1962)

[20] G.R. Irwin, Analysis of stresses and strain at the end of a crack traversing a plate, J. App Mech. 24 pp 361-4 (1957)

[21] K. Tanaka, Fatigue crack propagation from a crack inclined to the cyclic tensile axis, Engng. Fracture Mech., 6 pp493-507, (1974)

[22] P.S. Theocaris and N.P. Adrianopoulos, The T-criterion applied to ductile fracture, Int. J. Fracture 20 R125-30 (1980)

[23] X. Yan, Z. Zhang and S. Du, Mixed mode fracture criteria for the materials with different yield strengths in tension and compression, Engng. Fracture Mech. 42 pp109-16 (1992)

[24] T.K. Hellen and W.S. Blackburn, The calculation of stress intensity factors for combined tensile and shear loading, Int. J. Fracture, 11 pp 605-17 (1975)

[25] J.R. Rice, A path independent integral and the approximate analysis of strain concentration by notches and cracks, Trans ASME J of Applied mechanics V pp379-386 (1968)

[26] Y. Dai and G.H. Zheng, On fatigue crack growth under mixed mode cyclic loading, Numerical methods in fracture mechanics, Proc. Fourth Int. Conf. Texas USA pp658-76 (1987)

[27] E.E. Gdoutos, Fracture mechanics criteria and applications. Kluwer, The Netherlands

[28] C. Li., Vector CTD criterion applied to mixed mode fatigue crack growth., Fatigue Fracture Engng. Mater. Structures 12 pp 59-65 (1989)

[29] P. Shenton and C. Perrin, Private communication, Dana Glacier Vandervell

[30] W.H. Wilson, A test machine for assessing the fatigue propoerties of impulsively loaded plain bearings, Proc I. Mech E. V182 pp129-131 (1967)

[31] N.E. Dowling, W.R. Brose and W.K. Wilson, Notched member fatigue life predictions by local strain approach. In fatigue under complex loading pp55-84 (1977)

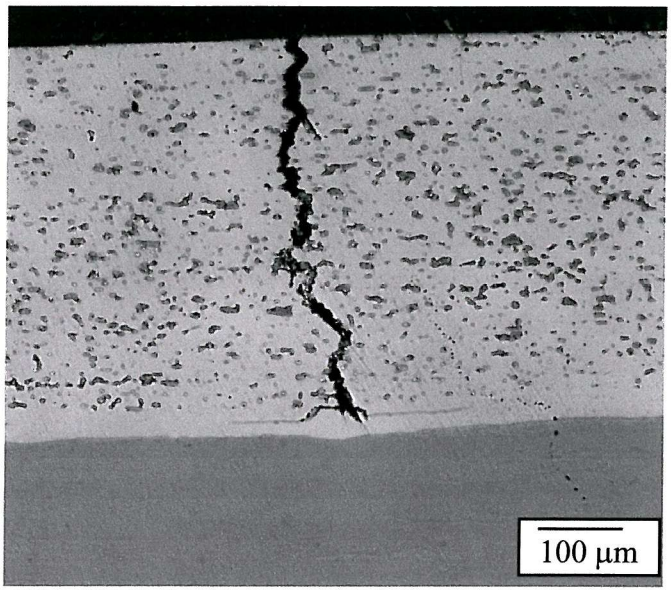

Figure 6.1: Typical sub surface crack behaviour seen in bearing materials tested in ambient conditions at Southampton

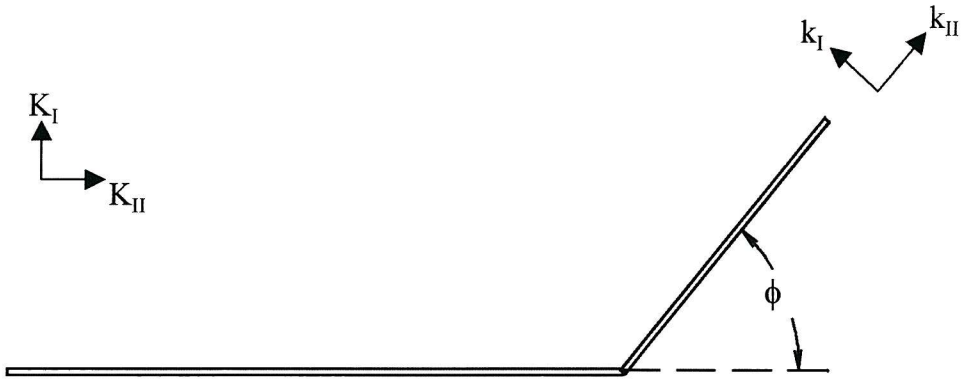

Figure 6.2: Crack containing single deflection

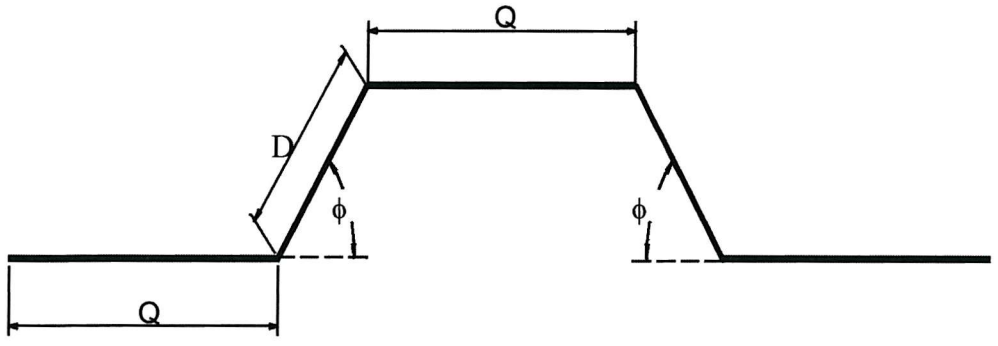

Figure 6.3: Crack containing periodic deflections

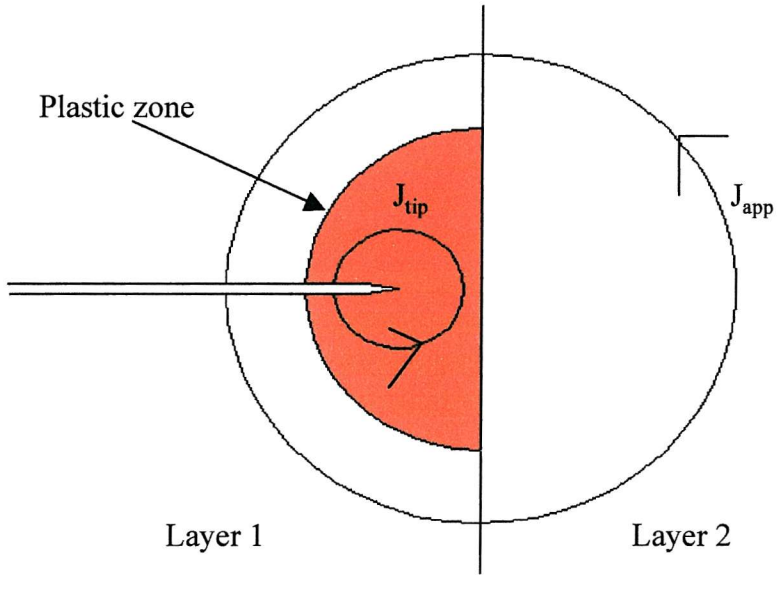

Figure 6.4: Contours used for J-integral calculation in Suresh model

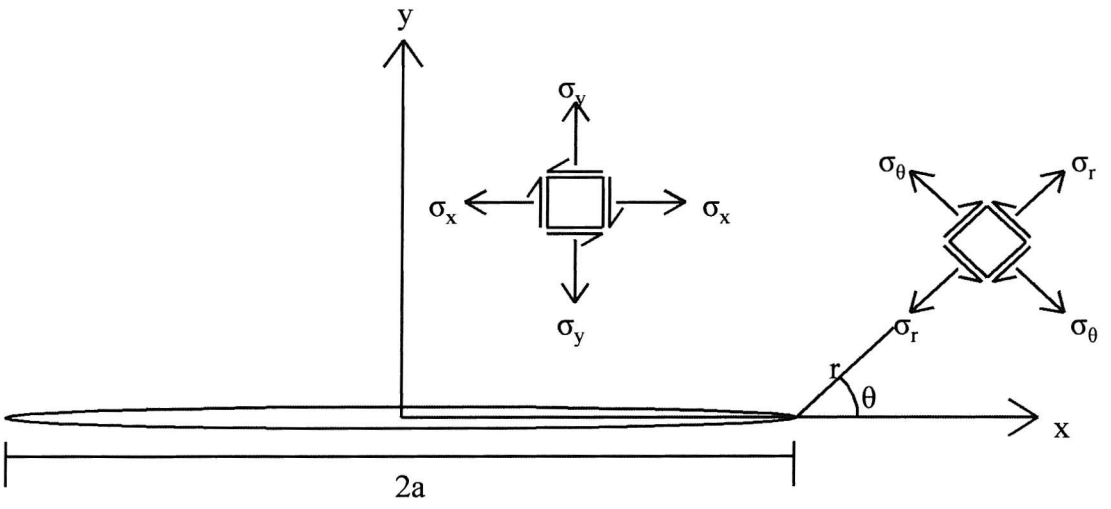

Figure 6.5: Nomenclature used to describe stresses in an infinite plate containing semi-infinite crack

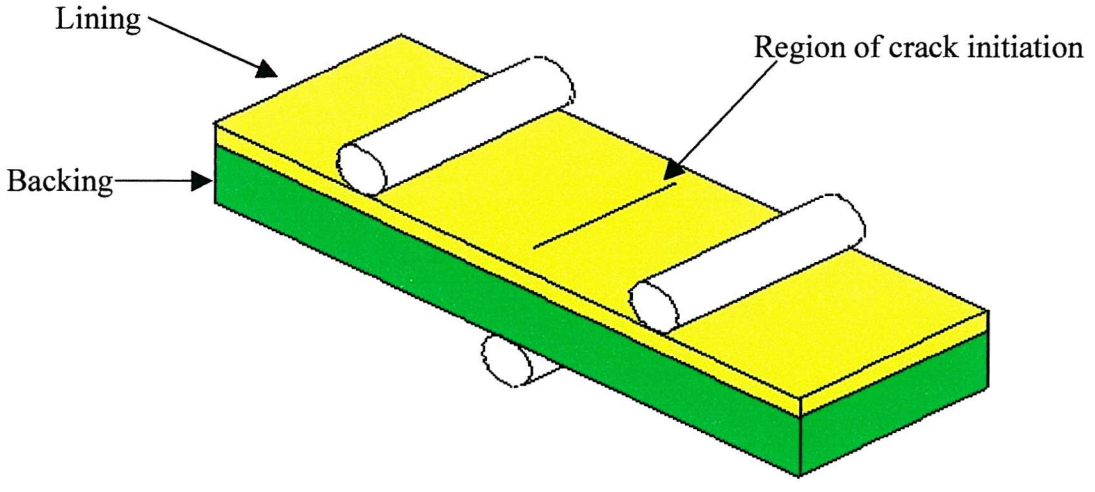

Figure 6.6: Experimental specimen geometry and crack initiation region

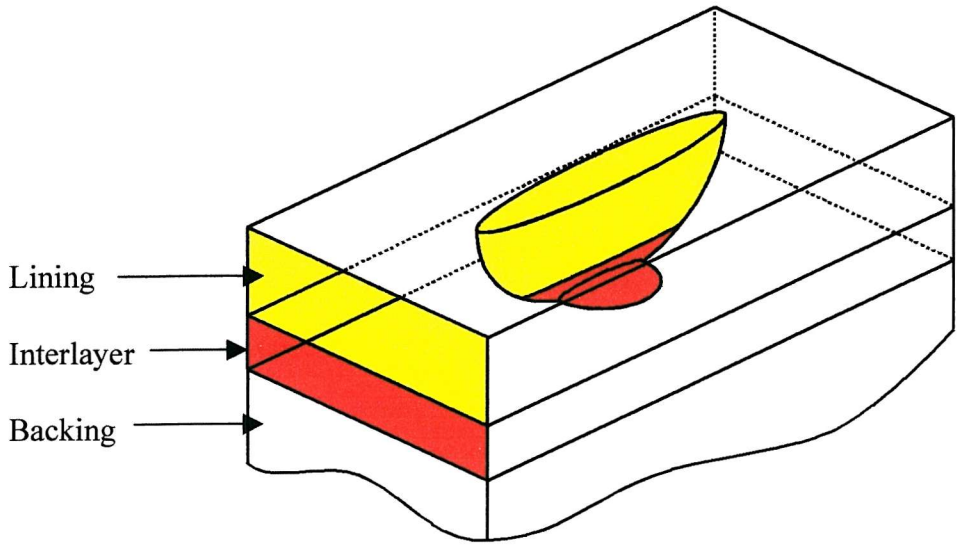

Figure 6.7: 3D crack geometry after interlayer penetration

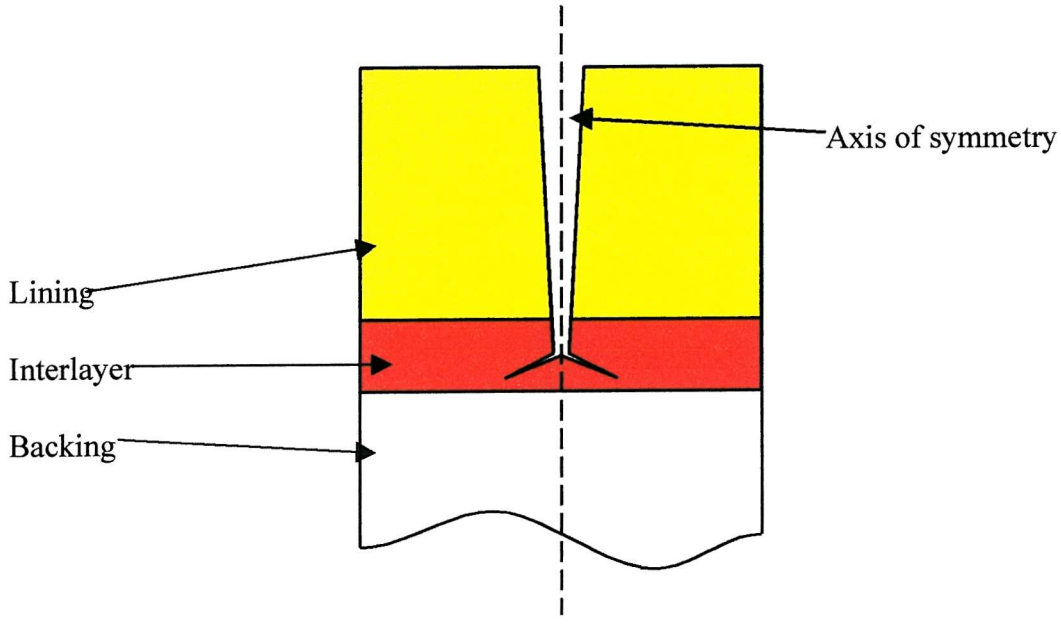

Figure 6.8: 2D representation of crack, used for modelling

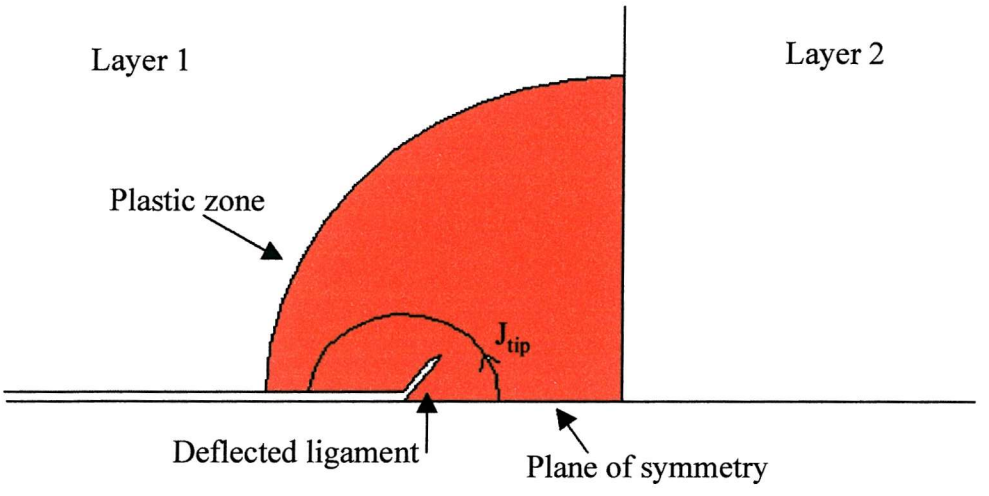

Figure 6.9: Model Schematic

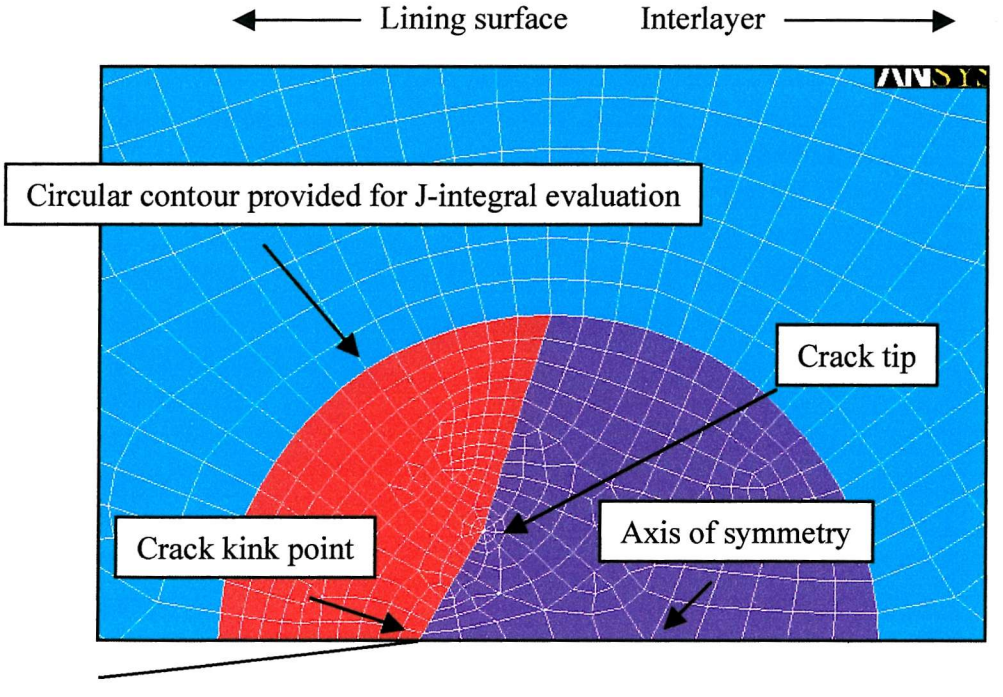

Figure 6.10: Crack tip mesh

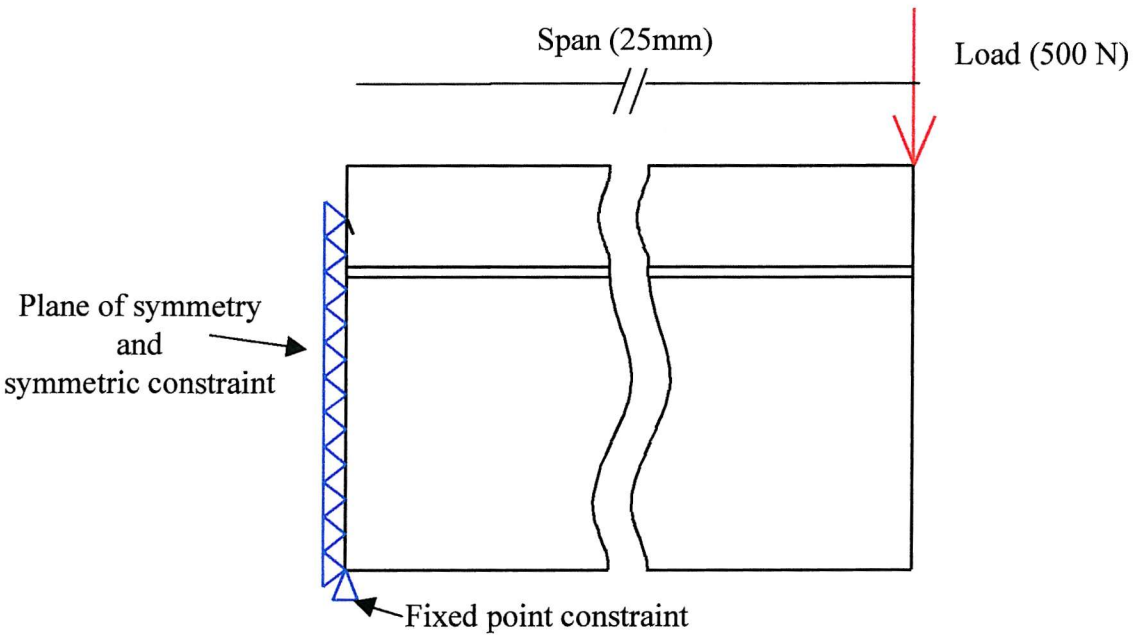

Figure 6.11: Constraints and loads as applied to model

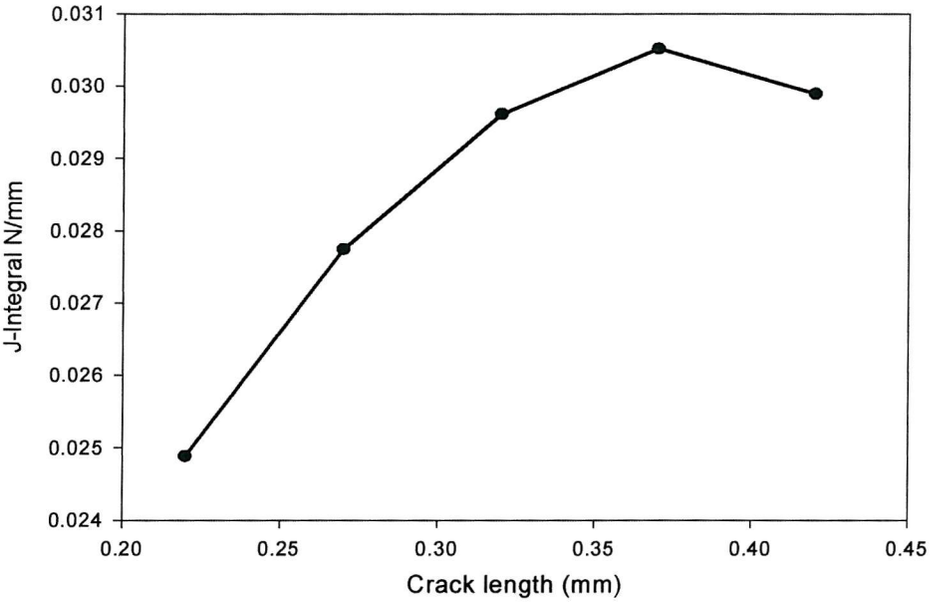

Figure 6.12: Crack tip driving force against crack length in bi-layer representation of AS1241 bearing material

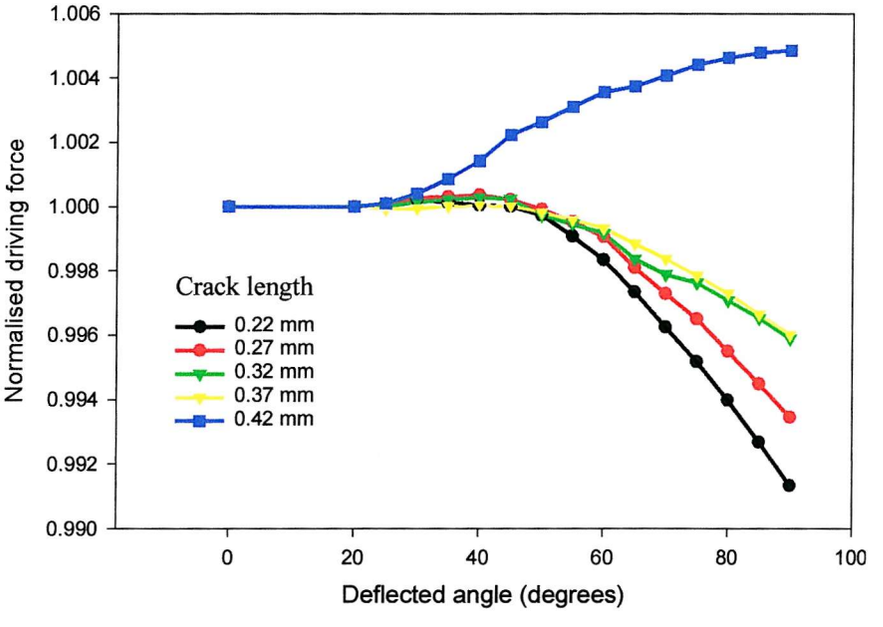

Figure 6.13:Deflectional propensity for crack in bi-layer representation of AS1241 bearing material

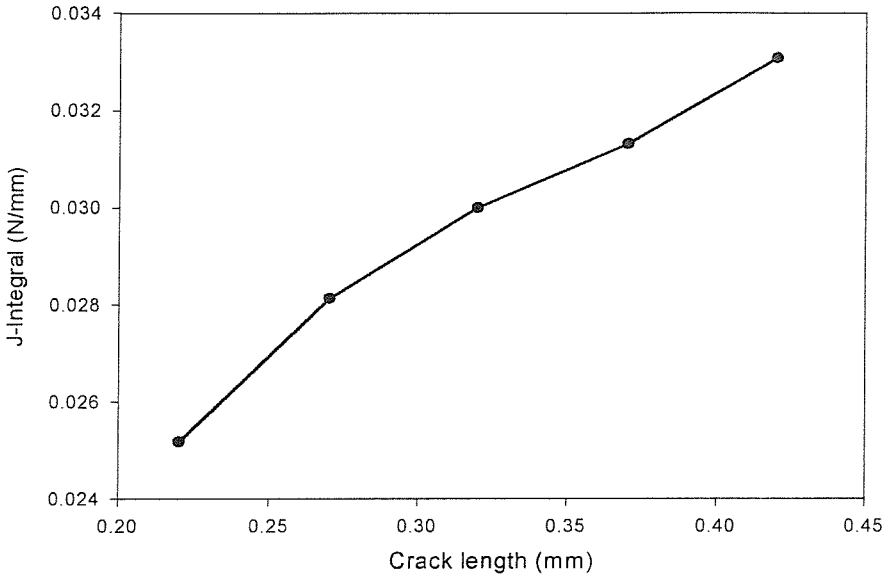

Figure 6.14: Crack tip driving force of crack existing solely within the lining of tri-layer representation of AS1241 bearing material

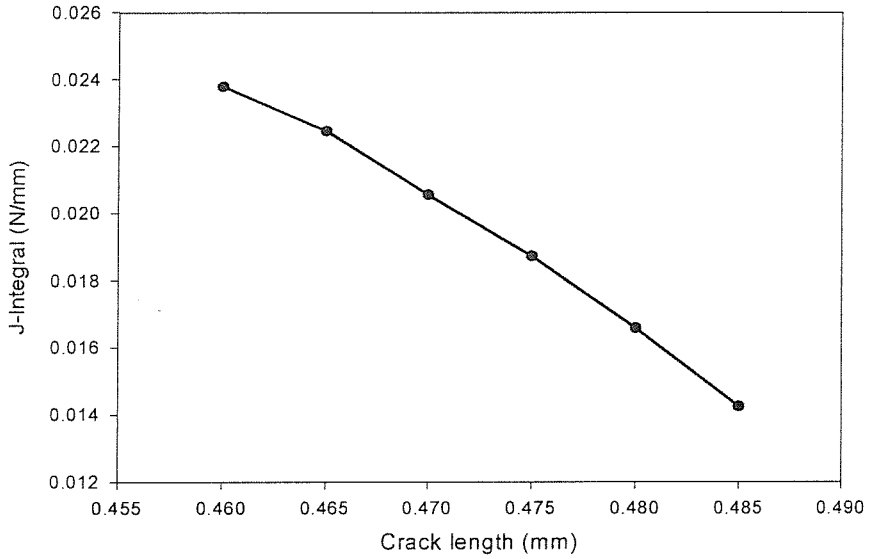

Figure 6.15: Crack tip driving force of interlayer penetrating crack in tri-layer representation of AS1241 bearing material

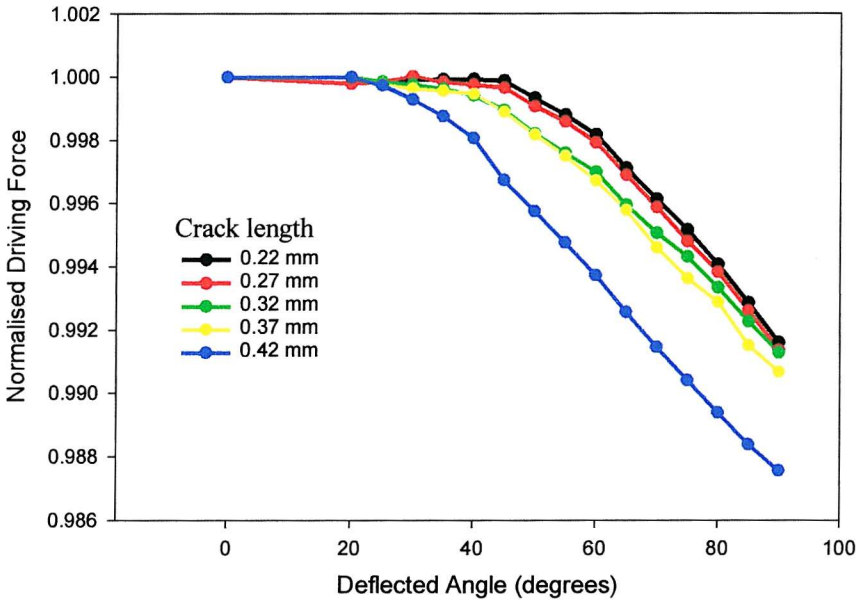

Figure 6.16:Crack tip directional propensity for crack existing solely within the lining of tri-layer representation of AS1241 bearing material.

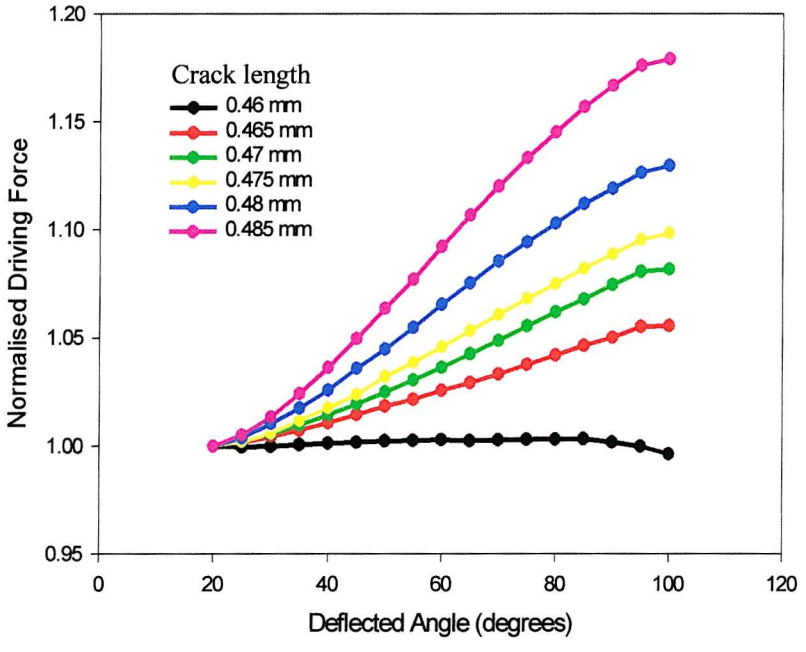

Figure 6.17:Crack tip directional propensity of interlayer penetrating crack in tri-layer representation of AS1241 bearing material

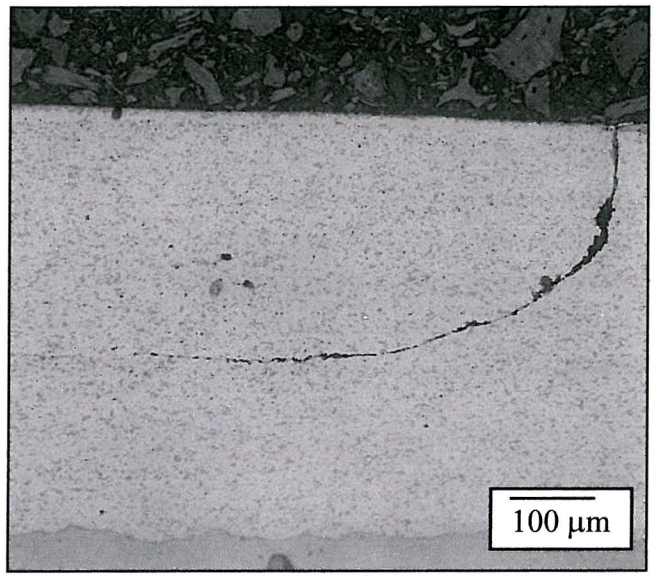

Figure 6.18: Section through bi-layer AS78 bearing showing early crack deflection (Shenton et al 1998)

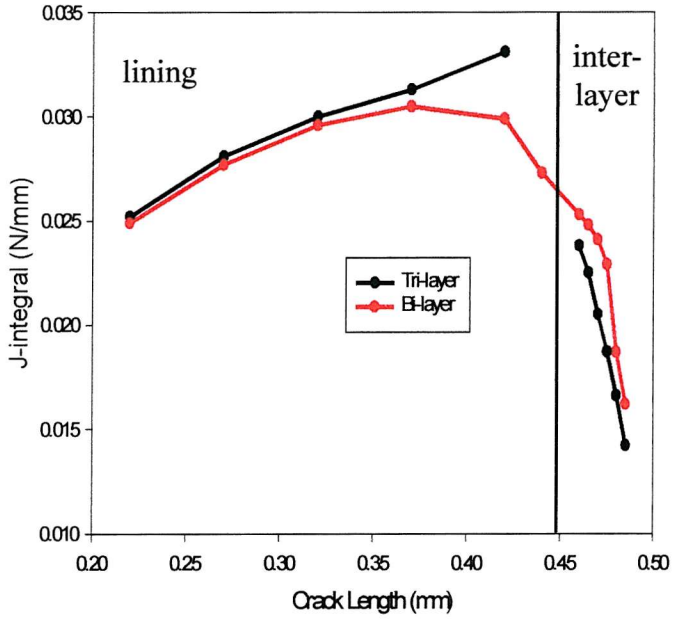

Note apparent driving force amplification prior to interlayer penetration in tri-layer case

Figure 6.19: Comparison of driving force variation in the bi-layer and tri-layer representations of AS1241 bearing material

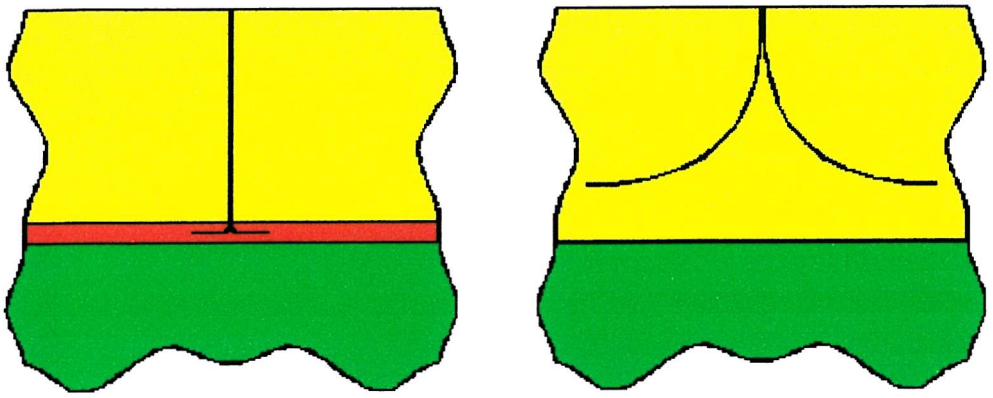

a) Tri-layer b) Bi-layer

Figure 6.20: Crack shapes predicted by bi-layer and tri-layer representations of AS1241 bearing materials

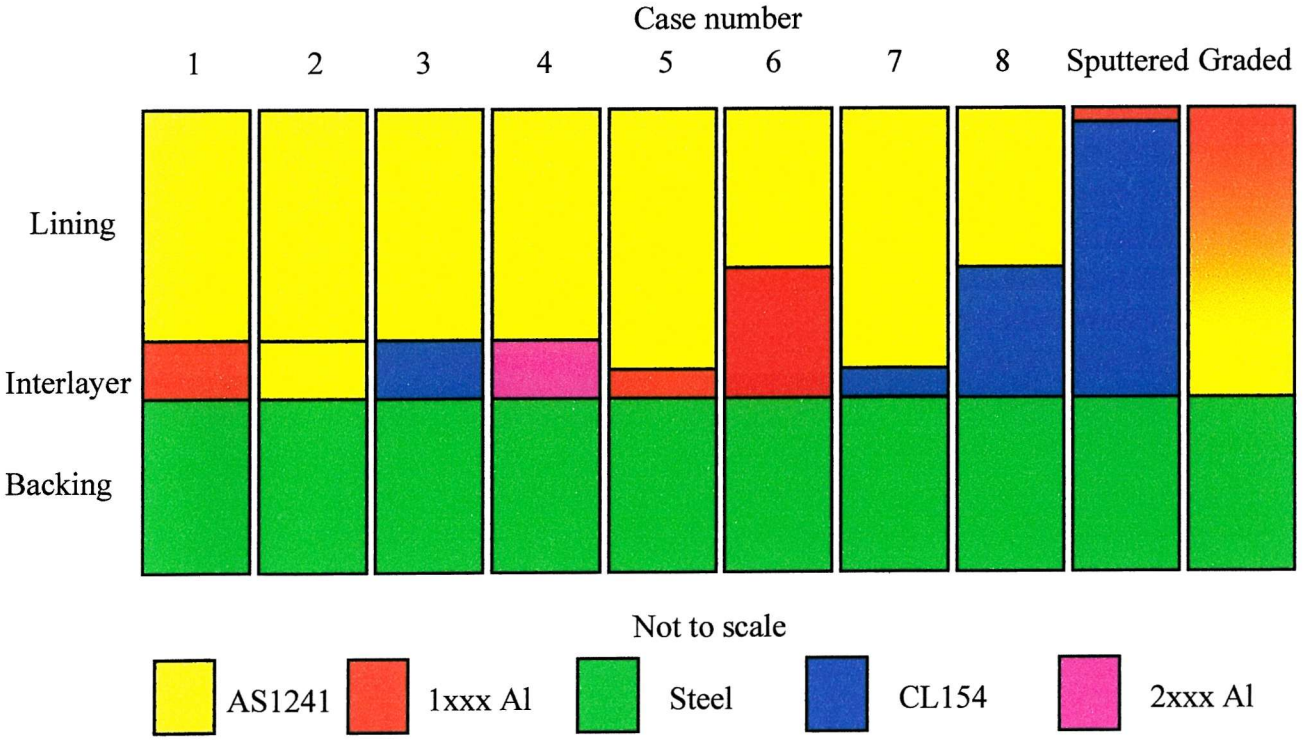

Figure 6.21: Schematics of materials layers, in parametric studies and conceptual bearings

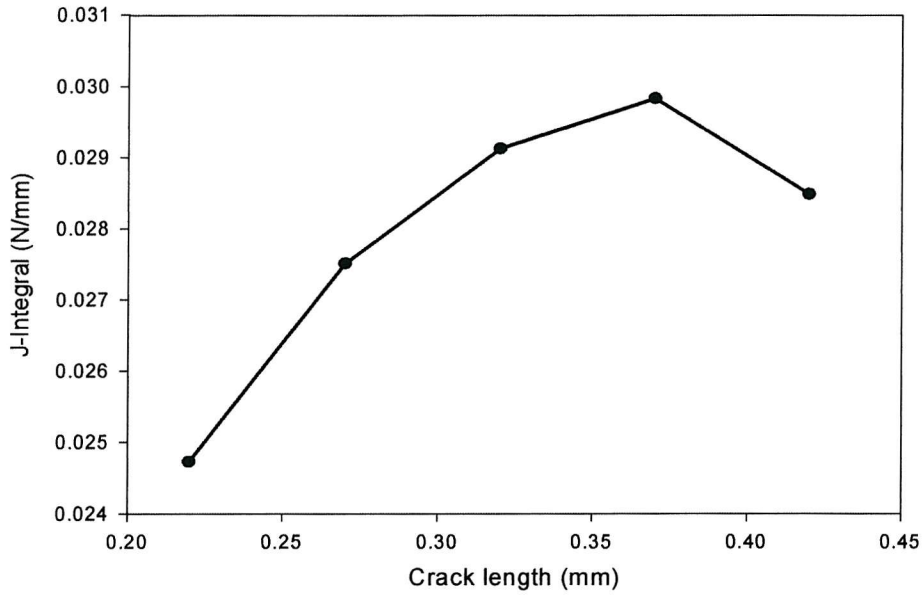

Figure 6.22: Crack tip driving force variation in bearing material with standard thickness CL154 interlayer

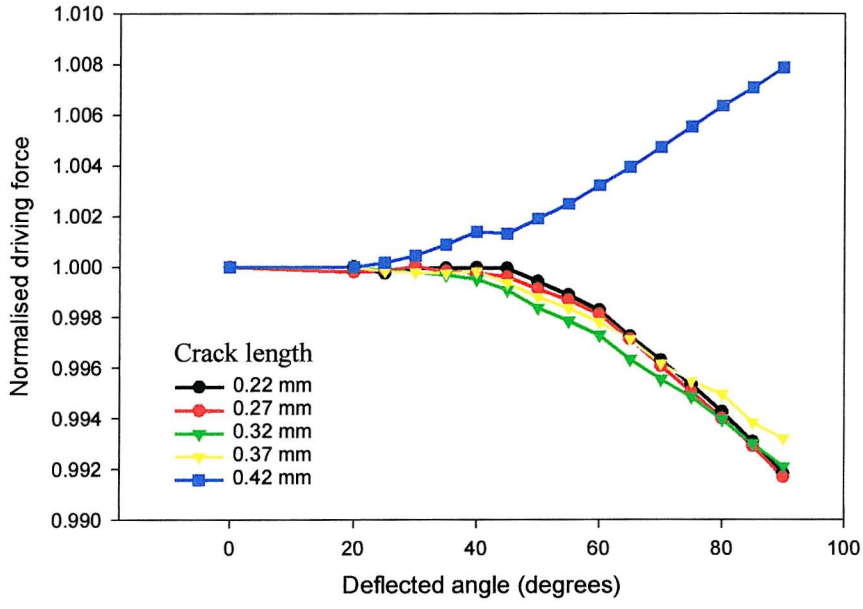

Figure 6.23: Crack tip directional propensity variation in bearing material with standard thickness CL154 interlayer

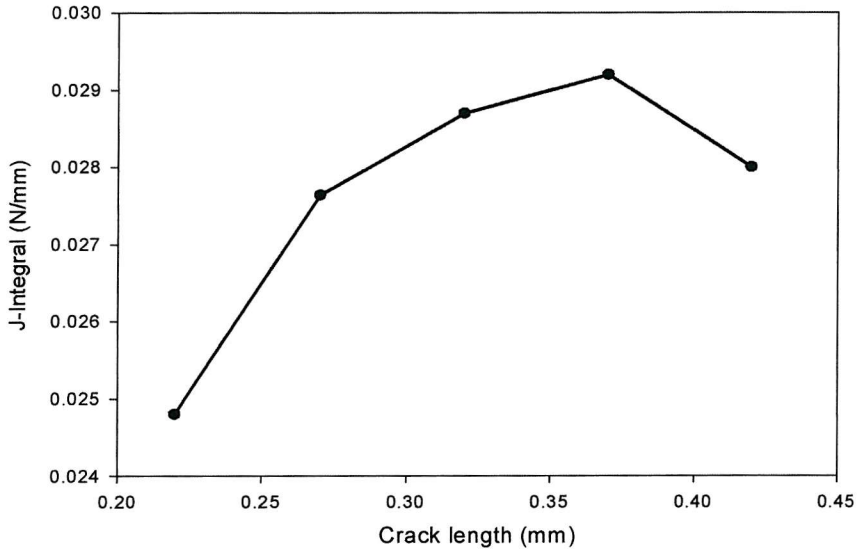

Figure 6.24: Crack tip driving force variation in bearing material with standard thickness 2xxx Al interlayer

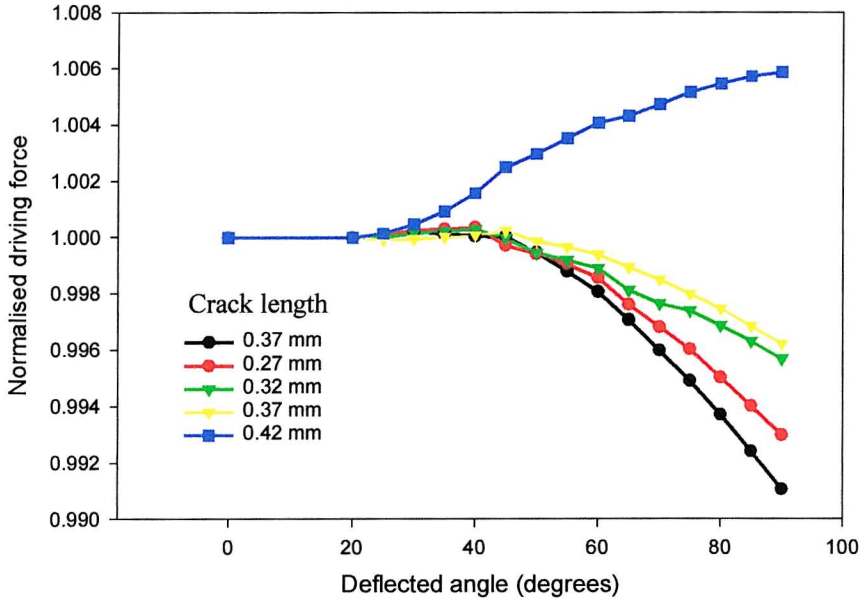

Figure 6.25: Crack tip directional propensity variation in bearing material with standard thickness 2xxx Al interlayer

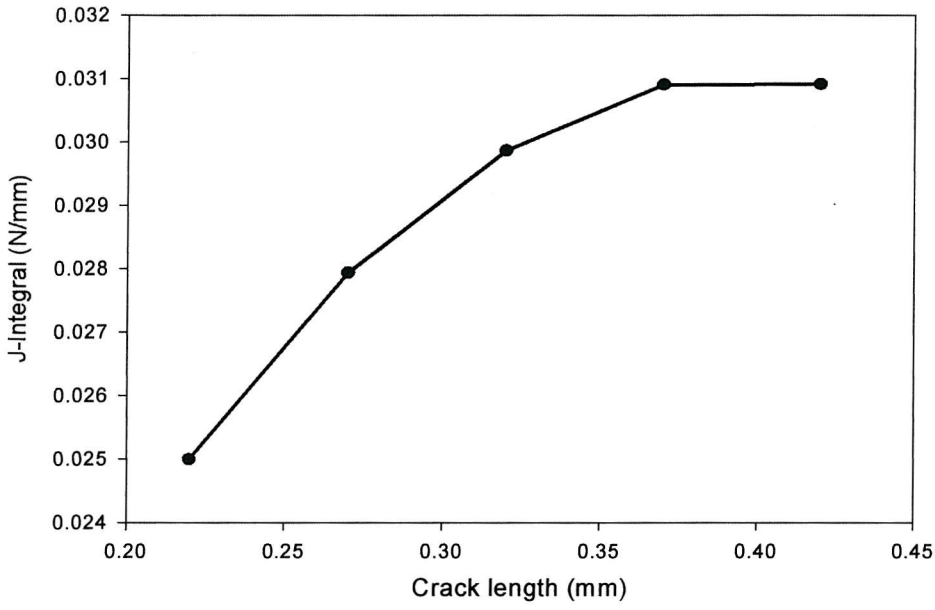

Figure 6.26: Crack tip driving force variation in bearing material with reduced thickness 1xxx Al interlayer

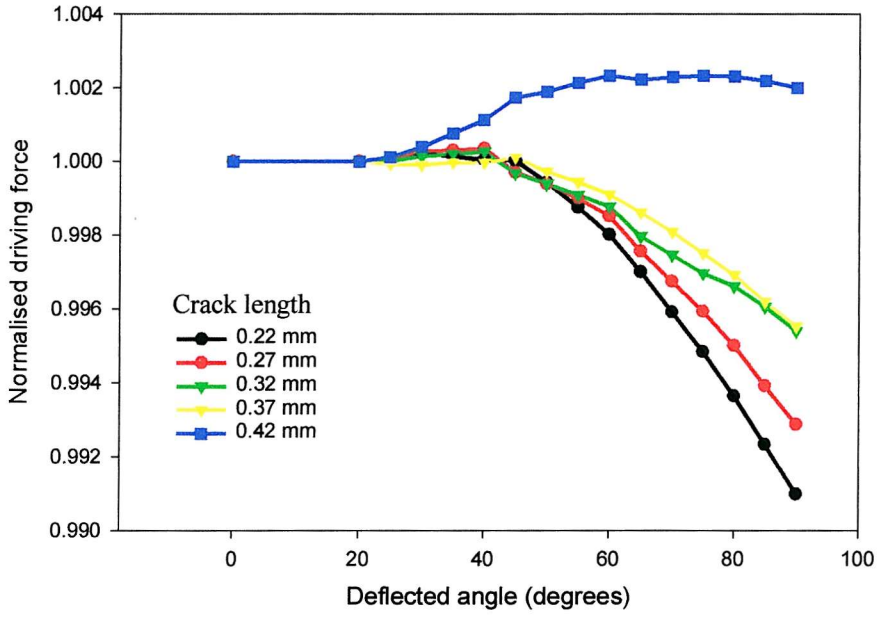

Figure 6.27: Crack tip directional propensity in bearing material with reduced thickness 1xxx Al interlayer

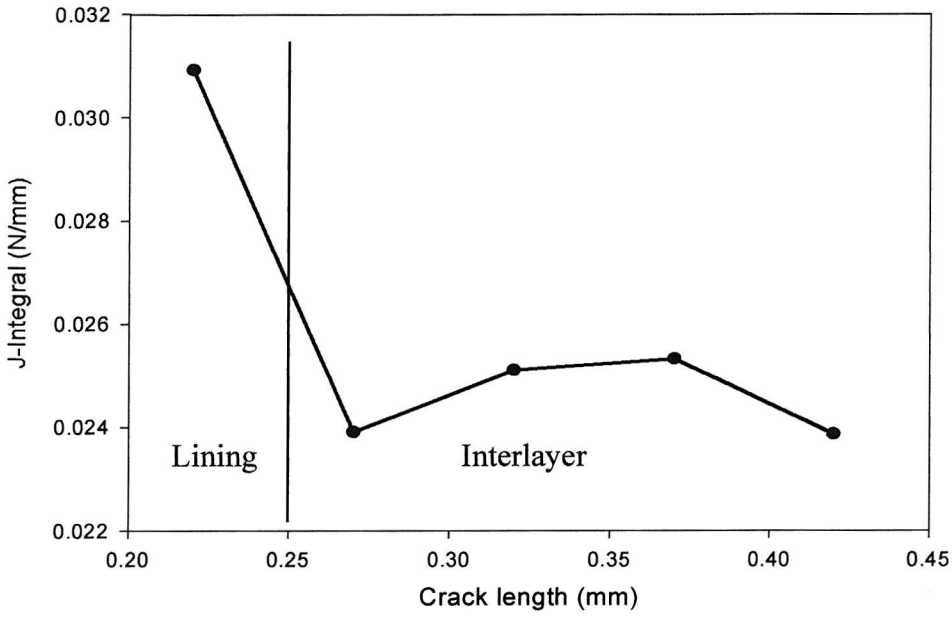

Figure 6.28: Crack tip driving force variation in bearing material with increased thickness 1xxx Al interlayer

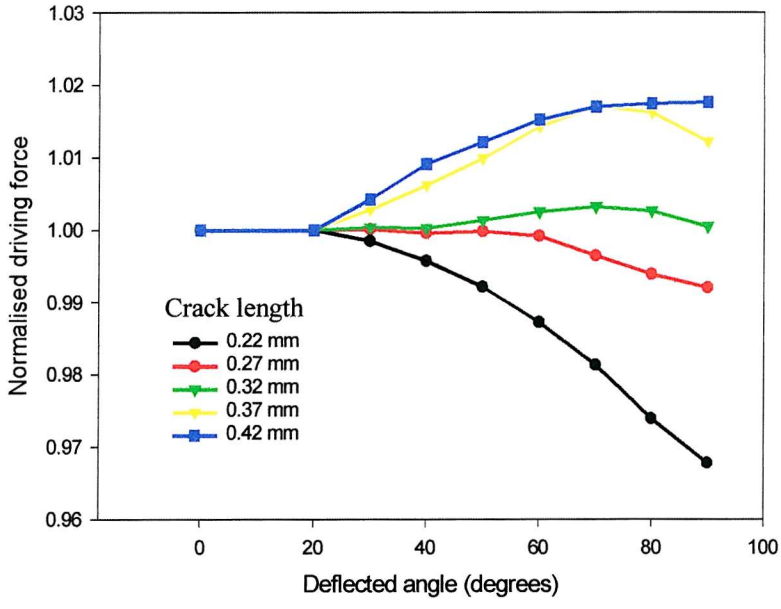

Figure 6.29: Crack tip directional propensity in bearing material with increased thickness 1xxx Al interlayer

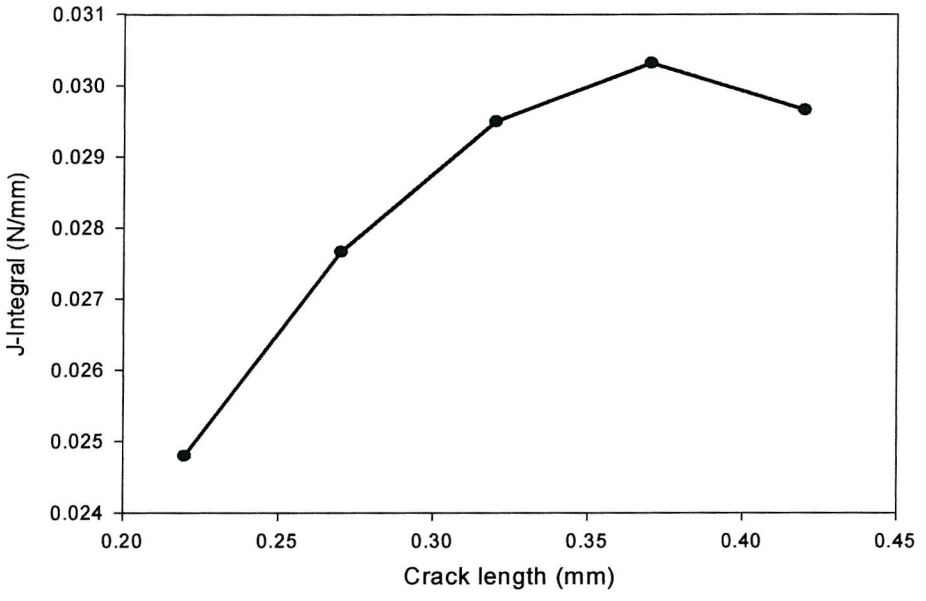

Figure 6.30: Crack tip driving force in bearing material with reduced thickness CL154 interlayer

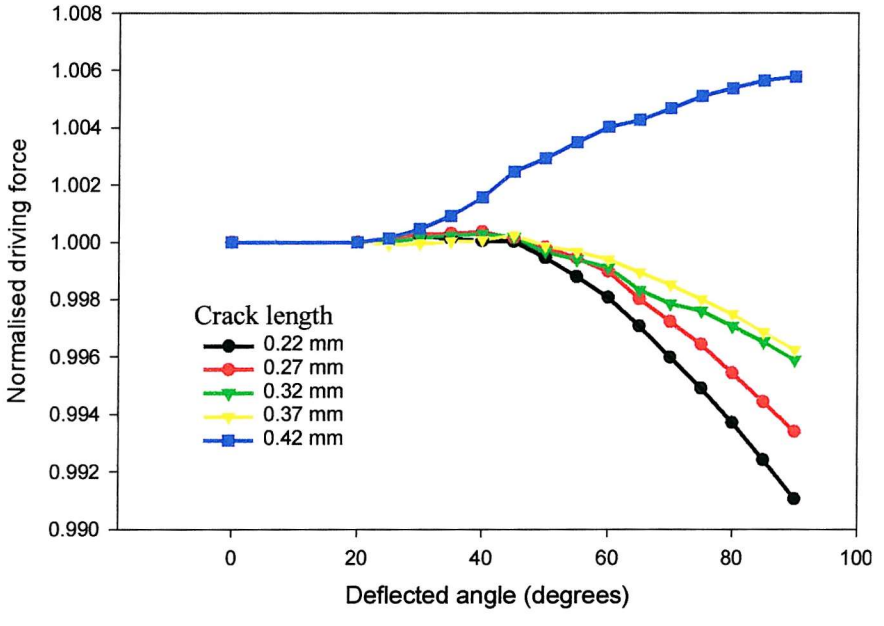

Figure 6.31: Crack tip directional propensity in bearing material with reduced thickness Cl154 interlayer

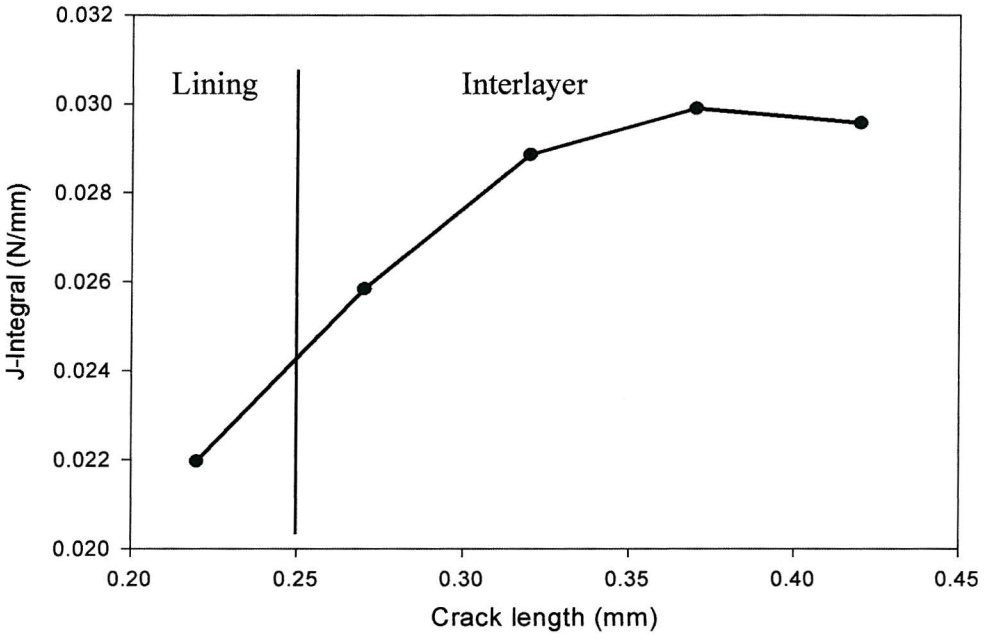

Figure 6.32: Crack tip driving force variation in bearing material with increased thickness CL154 interlayer

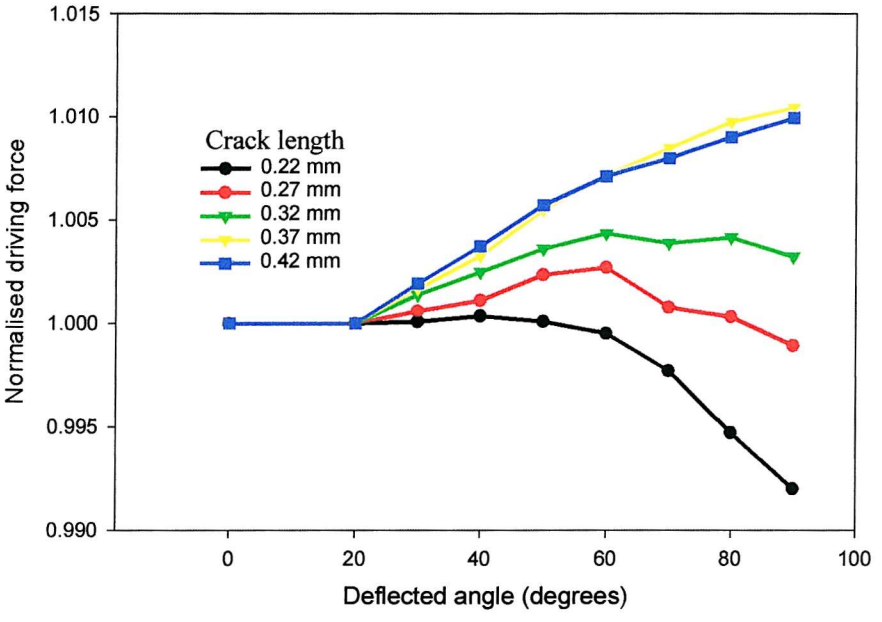

Figure 6.33: Crack tip direction propensity in bearing material with increased thickness CL154 interlayer

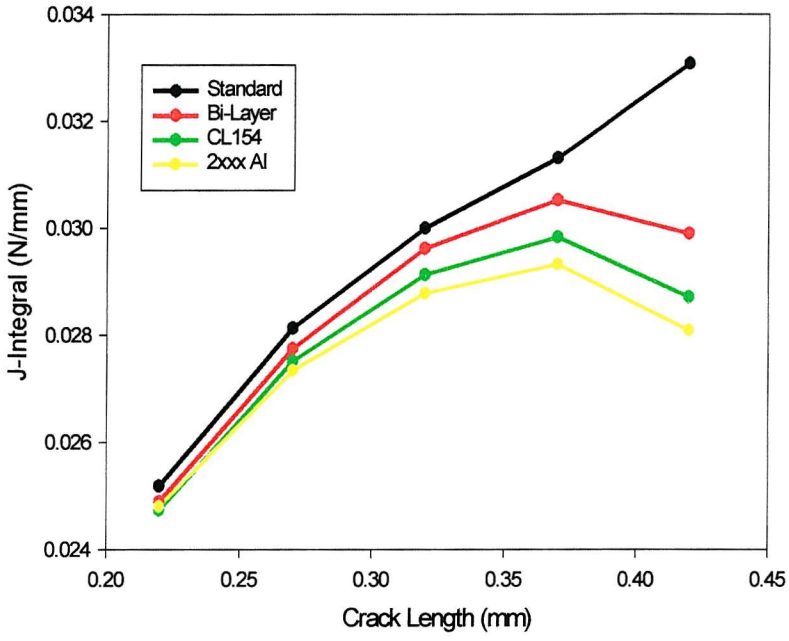

Figure 6.34: Effect of parametrically increasing interlayer yield stress on crack tip driving force

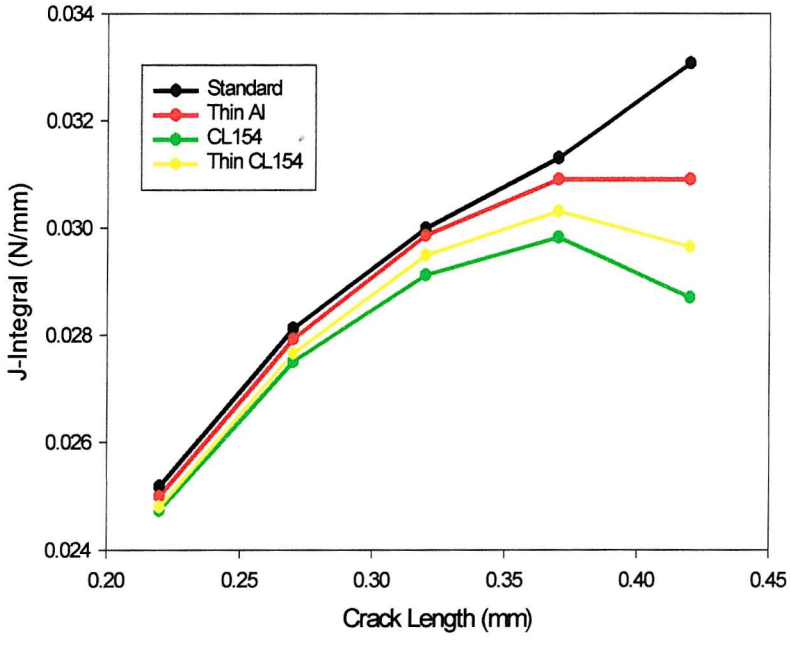

Figure 6.35: Effect reducing interlayer thickness on crack tip driving force

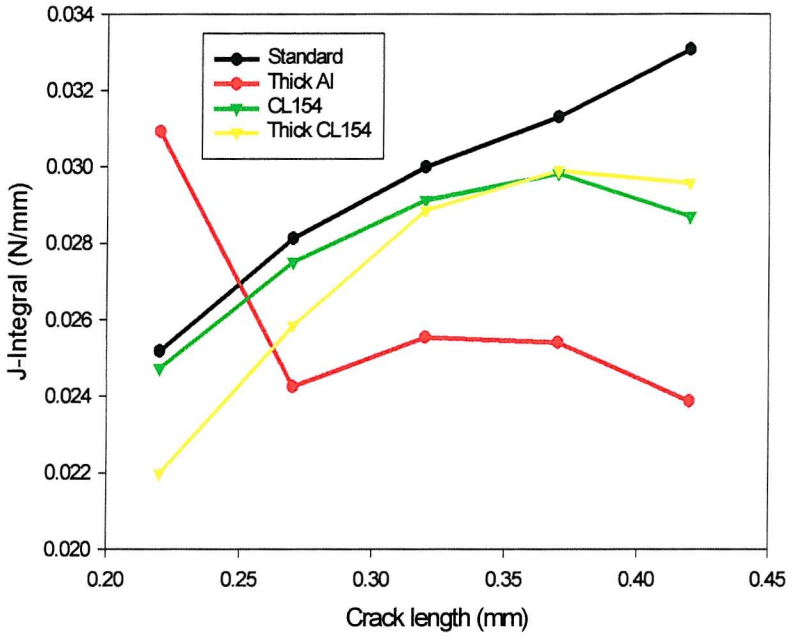

Figure 6.36: Effect of increased interlayer thickness on crack tip driving force

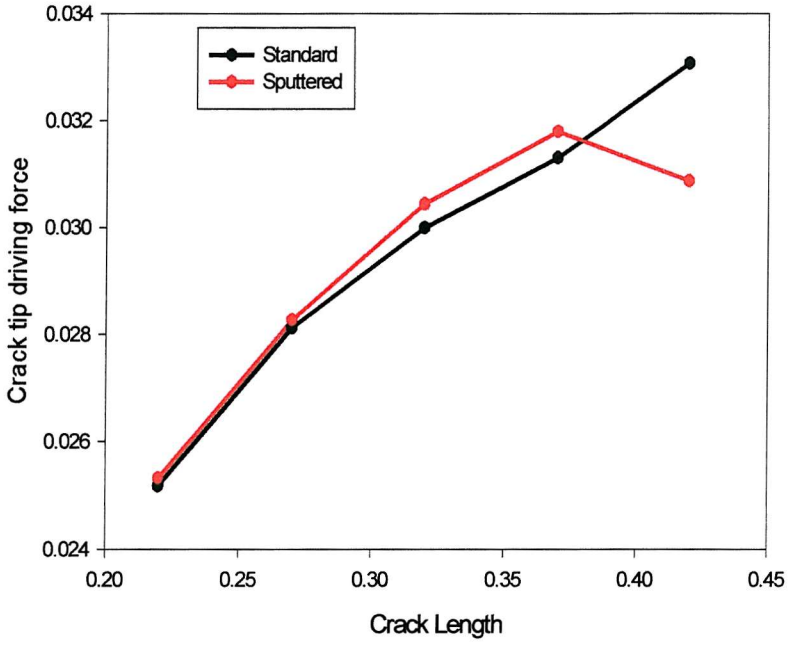

Figure 6.37: Crack tip driving force variation in Sputter coated CL154 bearing material

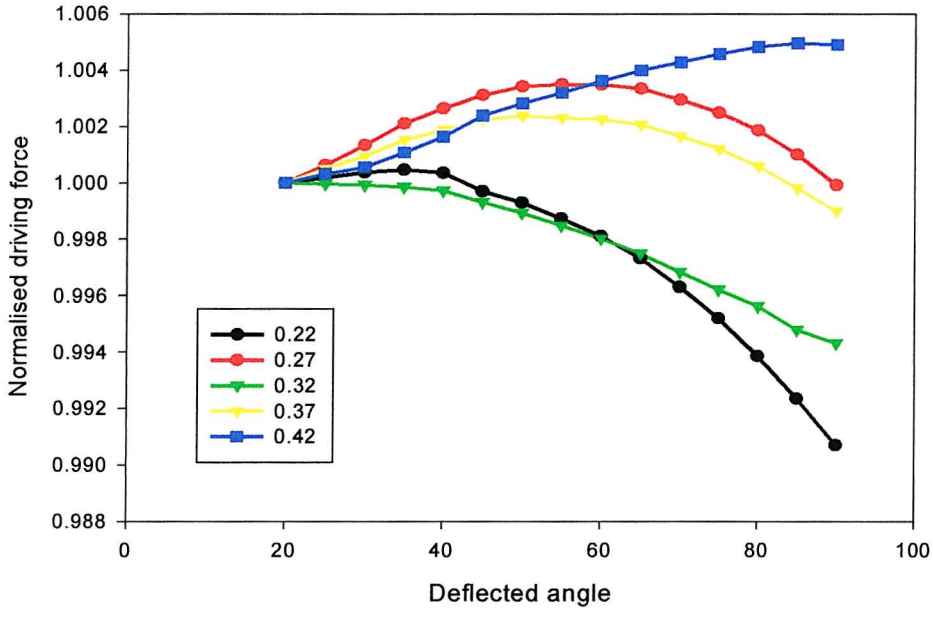

Figure 6.38: Crack tip directional propensity in sputter coated CL154 bearing material

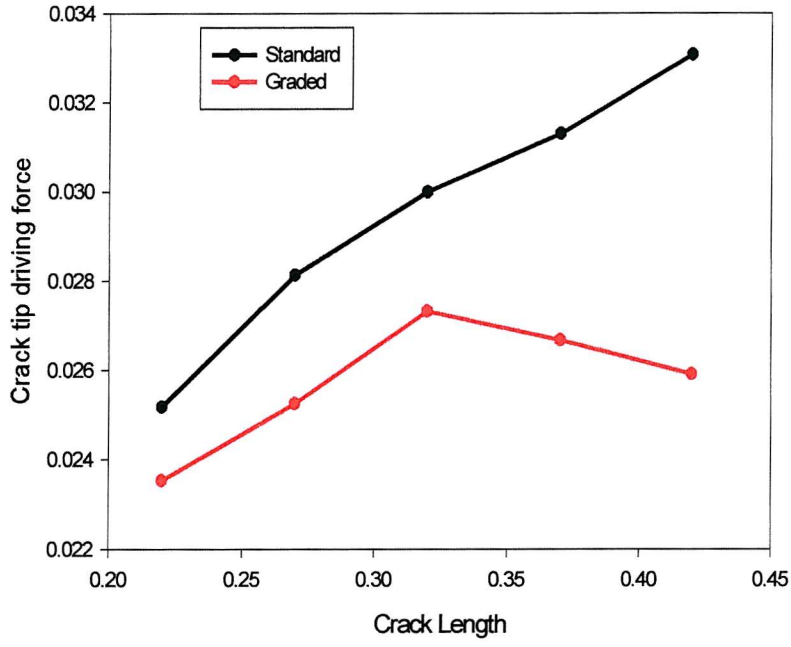

Figure 6.39: Crack tip driving force variation in bearing material with lining of graded material properties

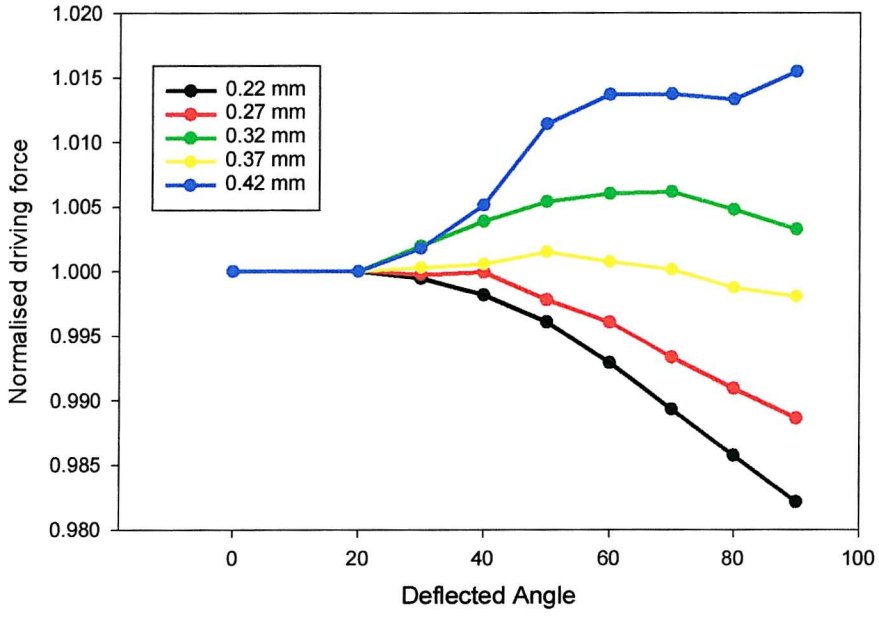

Figure 6.40: Crack tip deflectional propensity in bearing material with lining of graded material properties

7.0 SUMMARY OF KEY RESULTS AND CONCLUSIONS

7.1 Material System

The bearing system studied was known to be a multi-layer structure, comprising lining, interlayer and backing. The AS1241 lining material was found to be a multiphase material, with Si and Sn existing as distinct secondary phase distributions. The Sn was seen to be recticular and appeared to be aligned along the grain boundaries, whilst the Si was spheroidal and often associated with the Sn occasionally being encapsulated within it. In addition evidence of sporadic intermetallic particles was found, which from EDX analysis were found to contain Al, Si and Fe. Comparing the relative peak heights and with reference to a phase diagram, this phase is thought to be $FeSiAl_5$.

Three sample types were used during this project, the finished bearings and the flat strip material contained the full bearing material system, whilst the lining material was also available as a monolithic sheet. Finite body tessellation showed that the lining microstructure within these samples were comparable. Whilst Vickers micro-hardness testing was also used to confirm that the samples had similar mechanical properties and so were in a similar work hardened condition. Traverses of micro-hardness indents through the sample thickness, showed that the interlayer is considerably softer than the AS1241 lining material.

Tensile tests were performed on both monolithic AS1241 and Steel backing material, the resulting stress/strain curves were used in subsequent modelling approaches. The measured tensile yield stress for the steel layer in the finished bearing was found to be considerably higher than that prior to manufacture. This in conjunction with the observed deformed grain structure indicates that this layer undergoes considerable work hardening during the bearing manufacturing process.

7.2 Fatigue Crack Initiation Behaviour

It was shown that as part of a bearing material system, AS1241 can apparently tolerate cyclic stresses in excess of yield without the initiation of fatigue. The

endurance limit to $2*10^7$ cycles was found to be ~80MPa (c.f. yield stress =56.6 MPa, UTS = 172.9MPa). Total strain life fatigue data was found to fit the Coffin-Manson equation with values of the fatigue ductility coefficient and exponent of 4.33 and –0.89 respectively.

Under ambient conditions in three point bend fatigue samples, fatigue cracks were first seen to initiate early in the specimens life ($N/N_f<5\%$) at multiple points on the sample surface in the region of maximum bending stress. These initiations were associated with the interfaces between Si secondary phases and the surrounding matrix. It was seen that the nucleated fatigue crack would propagate around the Si almost decohering it from the matrix before propagating away. Very early growth was seen to occur both parallel to as well as normal to the nominal applied loading, indicating a complex local stress state.

Tessellation approaches were used to show that generally Si phases associated with fatigue crack initiation sites, were larger and more remote from their near neighbours than the background population. Microstructural finite element modelling showed that the matrix becomes highly strained as it is deformed around the hard Si phases due to the compliance mismatch between the two materials. It was shown that for a given background strain level, the magnitude of the strain amplification is dependent on the Si phase size. Hence the large Si phases identified as the principal fatigue crack nucleation sites are also associated with higher values of matrix strain. When microstructural models considering several secondary phases were formulated, it was seen that a reasonable correlation existed between points of high matrix shear strain and fatigue crack initiation sites.

7.3 Crack Propagation and Coalescence Behaviour

Centre crack tension fatigue testing on the monolithic lining material was used to provide a baseline with which to compare the subsequent short crack growth. Examination of the fracture surface produced during this test revealed two distinct regimes of fatigue growth. Near threshold, secondary phases were clearly evident on the fracture surface, the soft Sn appeared to have been propagated through whilst the hard Si retained its spheroidal shape, indicating that the crack tip had preferentially sought out these phases, propagating through the Sn and around the Si. At higher ΔK

levels a much flatter fracture surface was produced, with few secondary phases visible and classical striations were present. Therefore it appears that at low ΔK levels secondary phases are preferentially sought out by the crack tip, whilst at higher ΔK levels the mechanism of fatigue crack growth appears to be less microstructurally sensitive.

In ambient conditions, the short fatigue cracks produced in three point bend tests were seen to propagate along Si/matrix interfaces, through Sn phases and along apparent matrix slip bands. The relative rates of propagation were fastest along slip bands, slower through the soft Sn phases and finally slowest along the Si/matrix interfaces.

Due to the sheer multiplicity of crack initiations, coalescence events were inevitable. These were first observed at a life fraction of ~12%, though they continued to occur throughout the test duration. Micro-cracks were seen to coalesce rapidly to form a large dominant crack, which in turn appeared to produce a field of new micro-cracks ahead of itself. The dominant crack then propagated across the sample by coalescence with these newly formed micro-cracks. It was seen that as a crack approached coalescence, its growth rate increased markedly, finite element modelling showed that this was linked to interactions between the converging crack tip plastic zones, producing a region of enhanced plasticity between the two cracks. It was then shown that this plastic region produced enhanced driving force at the converging crack tips, it is likely that this is linked to the experimentally observed crack acceleration. Cracks converging obliquely were seen to accelerate towards coalescence until an overlap was established, at which point the cracks were seen to decelerate and deflect toward one and other. FE modelling was again used to show that in addition to the enhanced driving force produced as the cracks converge, shielding is produced as an overlap is established. It is likely that this shielding makes continued propagation normal to the nominal loading unfavourable, leading to crack deflection. The extreme case of crack shielding is produced by parallel cracks, it was shown that a small crack may be completely shielded by a dominant crack propagating parallel to it. Such cases were observed experimentally leading to the arrest of the overtaken crack.

The stress intensity factor K was used to compare the behaviour of long and short fatigue cracks, in common with other studies in the literature it was seen that

short cracks appear to propagate at ΔK levels far below the long crack threshold. The large changes in growth rate observed are indicative of the highly microstructurally sensitive growth mechanism of these small cracks.

7.4 Sub-Surface Fatigue Crack Behaviour

Un-coalesced cracks were seen to reduce in growth rate or arrest entirely at a critical length of 0.7-1.2mm. Sectioning studies were used to link this to sub-surface behaviour, where it was seen that a crack initiating at the surface would propagate towards the steel backing layer, however rather than penetrating into the steel layer, the crack was seen to deflect radically at the centre of the interlayer, and then continue propagating normal to its initial direction. The shielding causing form of crack deflection is likely to be beneficial to the component's fatigue life since it measurably reduces crack growth rate.

This behaviour was observed in flat strip samples and in bearings, it has also been observed in Sapphire tested bearings. This similarity in fatigue crack behaviour demonstrates that the accelerated tests carried out in simple well characterised stress states and presented in this thesis, provide a valuable mechanistic insight into bearing fatigue.

Finite element modelling was used to investigate this phenomenon, it was shown that shielding caused by the steel layer is responsible for a drop in crack tip driving force and a consequent propensity for crack deflection when the crack tip penetrates the interlayer. It was also shown that the soft interlayer used in the standard AS1241 bearing apparently causes enhanced crack tip driving force immediately prior to interlayer penetration.

A series of finite element models were formulated to investigate the effect of interlayer properties and thickness in a parametric manner. Generally it was found that interlayers harder than the lining produced a beneficial effect, since shielding became evident at shorter crack lengths, whilst interlayers softer than the lining (including the one used in the tested bearings) exerted a detrimental effect by enhancing crack tip driving force prior to interlayer penetration.

Beneficial effects were also predicted for reduced thickness soft interlayers and increased thickness hard interlayers. The behaviour of a thick hard interlayer has been experimentally investigated by the sponsoring company in the form of a sputter coated bearing (effectively a very thick hard interlayer, with a thin soft lining), which was found to have excellent fatigue performance.

In addition the possibility of graded lining materials was investigated, the fatigue performance of a bearing comprising a steel backing and a lining material whose properties varied from pure aluminium at the surface to AS1241 at the steel interface was predicted to be considerably better than a bearing with a monolithic AS1241 lining. Together with a propensity for early deflection, it was also shown that for much of its length a subsurface crack in this graded material showed little directional propensity indicating a possible highly microstructural growth mechanism, offering the prospect of additional crack retardation mechanisms through the promotion of tortuous crack paths.

7.5 Effect of Environment

Short crack fatigue tests were also performed in vacuum and in oil environments, *In vacuo* fatigue crack propagation appears to be entirely suppressed, no visible fatigue cracks being present, even after more than 25 times ambient lifetime. However decohered Si phases were seen on the specimen surface in post test observations, their presence may indicate that the initiation mechanism is still active. The total lack of visible fatigue crack propagation was attributed to the inert atmosphere at the crack tip promoting more reversible slip and less hydrogen embrittlement effects. In an oil environment the same crack initiation and propagation mechanisms were seen as under ambient conditions, however the fatigue crack growth rate was severely retarded, component lifetimes being extended to 3.5 times that of ambient conditions. This was attributed to a combination of oxide formation and hydrogen embrittlement mechanisms occurring at the crack tip, but at a reduced rate compared to ambient conditions. In addition it is very likely that a viscous fluid induced closure mechanism is active, since the low viscosity oil used, which would easily penetrate the growing fatigue cracks.

7.6 Service Relevance and Further Work

It has been shown that using simple three point bend stress state it is possible to replicate similar fatigue failure modes to those observed in accelerated bearing fatigue rigs. Furthermore under these simple loading conditions it was possible to characterise the fatigue behaviour of the bearing material system in way not possible in an bearing test rig or in service. The fundamental fatigue behaviour of the AS1241 bearing system has been characterised, and the respect roles of both the lining microstructure and the layered construction assessed. This information may be applied in order to refine current bearing designs and further optimise their fatigue performance.

The current study has revealed several areas worthy of further research;

- The Si secondary phases were identified as the principal fatigue crack initiation site in the AS1241 microstructure, it is proposed to compare this behaviour with the fatigue behaviour observed in a Si free bearing system e.g. AS15 or AS16.
- In future work the fatigue testing program should be extended to consider the service environment (oil at elevated temperature).
- To further investigate critical microstructural features for fatigue crack initiation the embedded cell models should be extended to consider cyclic loading.
- It is clear that a failure crack is built up through the successive coalescence of many micro-cracks, a more realistic FEM approach could be applied to further characterise this behaviour by considering crack deflection and cyclic loading.
- Currently the through thickness mesoscopic models may only be used for the prediction of driving force and directional propensity under monotonic loading. It is proposed to extend these models to consider true deflected growth, and it is recommended that a method based on CTOD be adopted to calculate the crack tip driving force under cyclic loading conditions.
- It is important to link the various studies carried out in this and further research programs to the component model developed by the sponsoring company. In this way a global model of bearing performance may be obtained, providing considerable insight into the likely fatigue performance of new bearing designs.
- It is hoped to validate some of the predictions made in the current work by carrying out fatigue tests on the conceptual bearing designs predicted to show potential fatigue performance gains over the standard AS1241 type. These would ideally include; the thick CL154 interlayer variant and the graded lining conceptual bearing.

APPENDIX I – STRESS PREDICTION MODELS

The majority of experimental tests were carried out in such a manner that the stress fields could not be calculated accurately by analytical means, as a result a number of finite element models were developed. This appendix considers both simple analytical approaches, and the development of more advanced FE models. The model development will be discussed in the context of the flat strip test geometry, before the extension to the bearing test geometry is discussed.

Analytical Models

Bending stress levels may be calculated using simple elastic assumptions, for a monolithic bar, the maximum bending stress is given by Eqn I.1

$$\sigma = \frac{(3PS)}{BW^2} \tag{I.1}$$

This is clearly inappropriate in the current case, since the flat strip bearing material cannot be assumed to be a monolithic material. The simple beam theory expression can be extended to consider several layers of material (compound beam theory), by considering an equivalent system, whose layer widths are in the ratio of their Young's modulus. Finding the second moment of area of the equivalent system and then solving the simple beam theory expression given in Eqn I.2, will provide an elastic solution to the maximum surface stress.

$$\sigma = \frac{My}{I} \tag{I.2}$$

Where M is the bending moment, I is second moment of area and y is the distance from the neutral axis. In order to provide solutions more representative of the real system, FE approaches were required.

FE Models

All the models presented here were created and solved using the general purpose FE code ANSYS versions 5.3 to 5.6 inclusive. This code was implemented on a Silicon Graphics Power Challenge compute server.

The first model was simply a finite element equivalent of the compound beam theory solution. The flat strip models took advantage of the symmetric nature of the loading geometry, and the fact that much of the sample was unstressed, as shown in Figure I.1. The model shown in Figure I.2 was created using 8 node quadrilateral elements (plane 82) as shown in Figure I.3, and solved in plane strain, thus simulating the material behaviour along a plane through the centre of the specimen. This first model simply comprised of two layers of material, since the elastic properties of the interlayer and lining are very similar, and hence the interlayer need not be modelled as a discrete layer.

To make this model more representative of the experimental tests, it was necessary to introduce an elasto-plastic material model, rather than the simple elastic one used previously. Since no attempt was made to model cyclic effects, this could simply be done using isotropic deformation plasticity with the properties given in Table I.1. Stress-strain curves were available for AS1241 and for the steel backing layer as a result of the material characterisation tests, and these were implemented in ANSYS as multi linear curves. It was seen that the plastic properties for the interlayer were considerably different than those of the lining, so they could no longer be considered a single material. A material response curve for the interlayer was constructed using yield stress and UTS data given in Table I.1.

Table I.1: Material properties used in finite element modelling

Material	Young's Modulus (GPa)	Poisson's Ratio	Yield Stress (MPa)	Ultimate Tensile Stress (MPa)
AS1241 Lining	69.8	0.33	56.6	187.5
Pure Al Interlayer (when used)	70	0.3	28	76
Mild Steel Backing	207	0.3	420	497

Up to this point all of the models assumed point loading at the nodes, no attempt being made to model the Hertzian contact between the loading roller and the strip. This was addressed by the model shown in Figure I.4, which included a roller and non linear contact elements (shown in Figure I.3), to model the contact between the centre roller and the lower surface of the flat strip. It was found that, at the load levels considered, the size of the contact patch between the steel roller and the steel backing was negligible and did not need to be considered further

Table I.2 gives a summary of the AS1241 top surface stress levels under a given load as predicted by the methods outlined.

Table I.2. Stress levels predicted by all models for a given load

Model	Type	Maximum top surface stress (MPa)
simple beam theory	Analytical	475.00
compound beam theory (no-interlayer)	Analytical	279.11
elastic model (no-interlayer)	F.E.	279.69
plastic model (no-interlayer)	F.E.	106.71
plastic model including interlayer	F.E.	107.17
plastic model including interlayer and contact	F.E.	107.15

Models Used for Stress/Strain Analysis of Material Tests

The model used for calculating the stress and strain levels in flat strip samples was based on the elasto-plastic model including the interlayer, but no contact region. The major difference was an increase in mesh density, the model now using 2450 mapped elements. The model's stress and strain response are shown in Figures I.2 and I.3 respectively, which shown the maximum bending stress and plastic strain on the top surface of the AS1241 under increasing loads.

The model was adapted to the bearing test geometry (Figure I.5), by changing the model geometry and constraint terms to suit the revised sample. The same element density and material models were retained. Figures I.4 and I.5 show this models stress and strain response to loading.

It is clear that the bearing test geometry requires considerably more load to generate a given stress in the lining material, this is unsurprising since these tests are far more constrained. The input files for both these models are given on the subsequent pages.

Final Flat Strip Model Input File

```
/filnam,stest
/title,Flat strip final model
/prep7
*cfopen,stestret,cmd
et,1,82,,,2
mp,ex,1,69.8e3
mp,nuxy,1,0.33
mp,ex,2,207e3
mp,nuxy,2,0.3
mp,ex,3,70e3
mp,nuxy,3,.3
*ulib,asdata1
*use,asda1,1
*ulib,mpcreate1
*use,mpc1,70e3,28,40,78,0.55,3
tb,biso,2,1
tbdata,1,413,3.04e3
load=600
allsel
csys,0
aclear,all
adele,all
ldele,all
kdele,all
lthick=0.44
ithick=0.05
bthick=1.505
span=25
Width=20.09
k
k,,lthick
k,,lthick+Ithick
k,,lthick+Ithick+bthick
k,,,span
k,,lthick,span
k,,lthick+Ithick,span
k,,lthick+Ithick+bthick,span
!h's
l,1,2
l,2,3
l,3,4
l,5,6
l,6,7
l,7,8
!V's
l,1,5
l,2,6
l,3,7
l,4,8
al,1,8,4,7
al,2,9,5,8
al,3,10,6,9
lsel,s,length,,span
lesize,all,,,70,150
lsel,s,line,,1,6,1
lesize,all,0.06
eshape,2
mat,1
amesh,1
mat,3
amesh,2
mat,2
amesh,3
/solu
dl,1,1,symm
dl,2,2,symm
dl,3,3,symm
dk,4,all
fk,5,fx,load/(2*width)
allsel
antype,stat
nlgeom,1
time=1
deltim,(10/load)
autots,off
outres,all,all
solve
finish
/post1
set,last
*get,maxstep,active,,set,sbst
*do,stepno,1,maxstep,1
set,,stepno
*get,timeinc,active,,set,time
loadinc=timeinc*load
ksel,s,kp,,1
nslk,s,1
*get,nodn,node,,num,max
*get,nstressy,node,nodn,s,y
*get,nepply,node,nodn,epel,y
*vwrite,lthick,loadinc,nstressy
,nepply
(F9.3,"     ",F9.3,"     ",F9.3,"
",E15.9)
*enddo
*cfclos
```

Final Bearing Model Input File

```
/FILNAM,curvestrip
/TITLE,final bearing model
/UNITS,SI
/PREP7
*cfopen,CZ1res,cmd
ET,1,82,,,2
MP,EX,1,69.8e3
MP,NUXY,1,.33
mp,ex,2,70e3
Mp,nuxy,2,0.3
MP,EX,3,207e3
MP,NUXY,3,.3
*ulib,asdata1
*use,asda1,1
*ulib,mpcreate1
*use,mpc1,70e3,28,40,78,0.55,2
tb,biso,3,1
tbdata,1,413,3.04e3
load=2250
csys,0
allsel
aclear,all
adele,all
ldele,all
kdele,all
K,,0,0
CIRCLE,1,28.2,,,90,4
CIRCLE,1,26.77,,,90,4
circle,1,26.71,,,90,4
CIRCLE,1,26.423,,,90,4
l,17,12
l,12,7
l,7,2
l,6,11
l,11,16
l,16,21
al,1,2,3,4,20,8,7,6,5,19
al,18,5,6,7,8,21,12,11,10,9
al,17,9,10,11,12,22,16,15,14,13
lsel,s,line,,20,22
lesize,all,0.06
lsel,all
lsel,u,line,,17,22,1
lsel,u,line,,4,16,4
lesize,all,,,8
lsel,s,line,,4,16,4
lesize,all,,,20,0.01
allsell
lsel,s,line,,1,4,1
lccat,all
lsel,s,line,,5,8,1
lccat,all
lsel,s,line,,9,12,1
lccat,all
lsel,s,line,,13,16,1
lccat,all
eshape,2
mat,3
amesh,1
mat,2
amesh,2
mat,1
amesh,3
finish
/solu
lsel,s,line,,17,19,1
nsll,s,1
d,all,uy
dk,2,all
dl,20,1,symm
dl,21,2,symm
dl,22,3,symm
fload=(load*(-1))/(2*28)
fk,6,fy,fload
allsel
antype,stat
nlgeom,1
time,1
deltim,(50/load)
autots,off
outres,all,all
solve
/post1
set,last
*get,maxstep,active,,set,sbst
*do,stepno,1,maxstep,1
set,,stepno
*get,timeinc,active,,set,time
loadinc=timeinc*load
ksel,s,kp,,21
nslk,s,1
*get,nodn,node,,num,max
allsel
*get,nstrx,node,nodn,s,x
*get,neptox,node,nodn,epto,x
*get,nepplx,node,nodn,eppl,x
*vwrite,loadinc,nstrx,neptox,ne
pplx
(F9.3,"    ",E15.9,"    ",E15.9,"
",E15.9)
*enddo
*cfclos
```

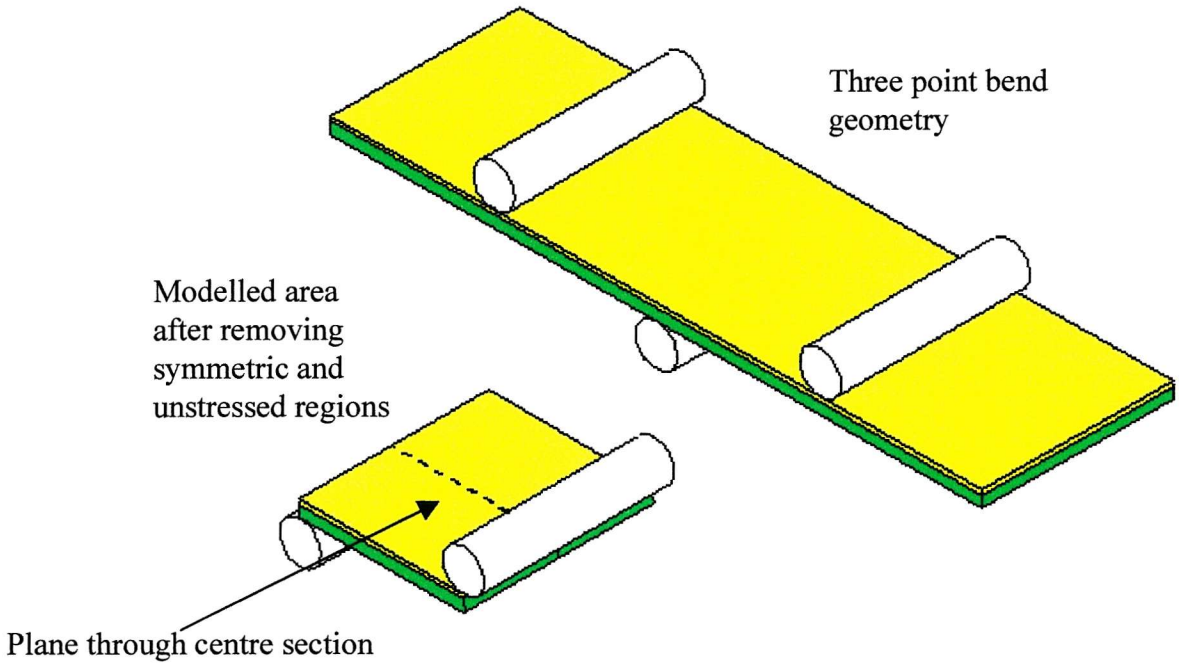

Figure I.1: FE model geometry

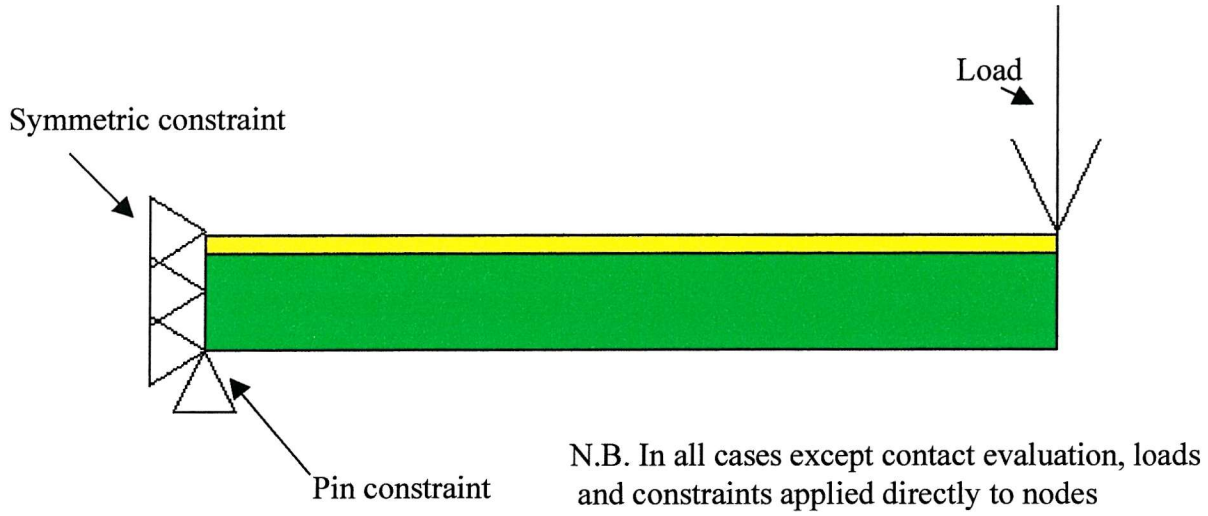

Figure I.2:Model geometry, loading and constraint

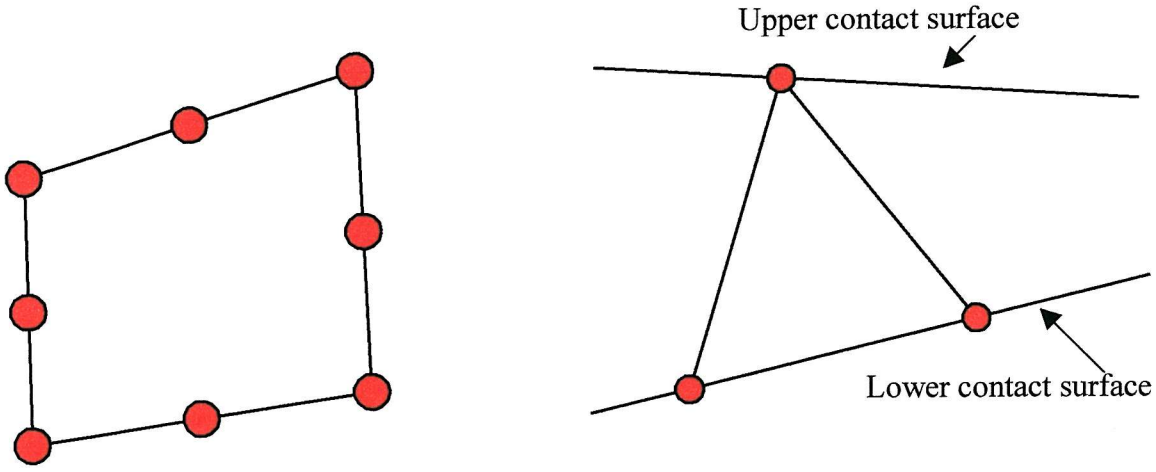

Plane 82, 8 node 2D plane element

Contac 43, 3 node 2D contact element

Figure I.3: Elements used in stress evaluation models

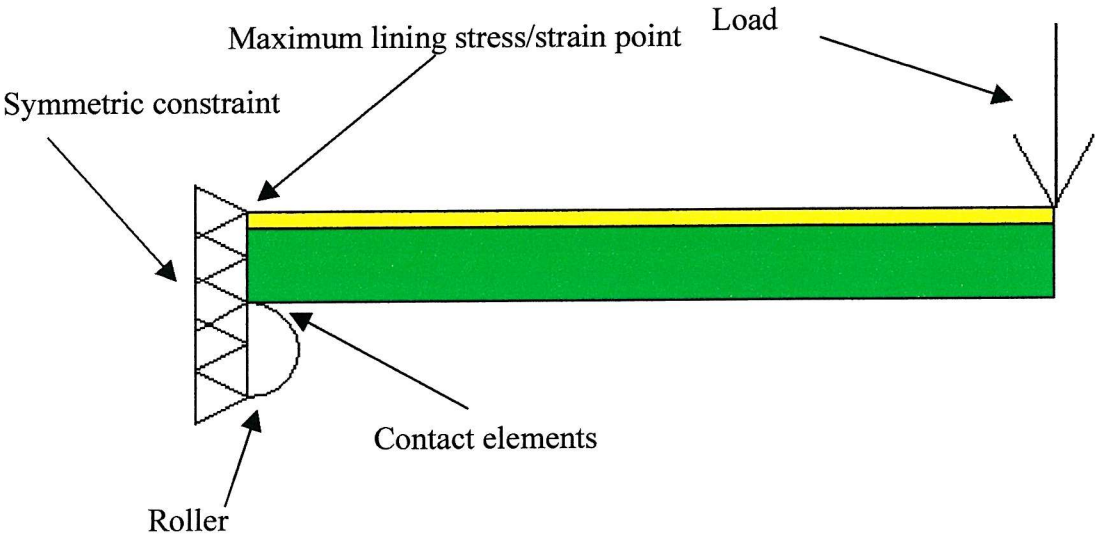

Figure I.4: Schematic of contact model

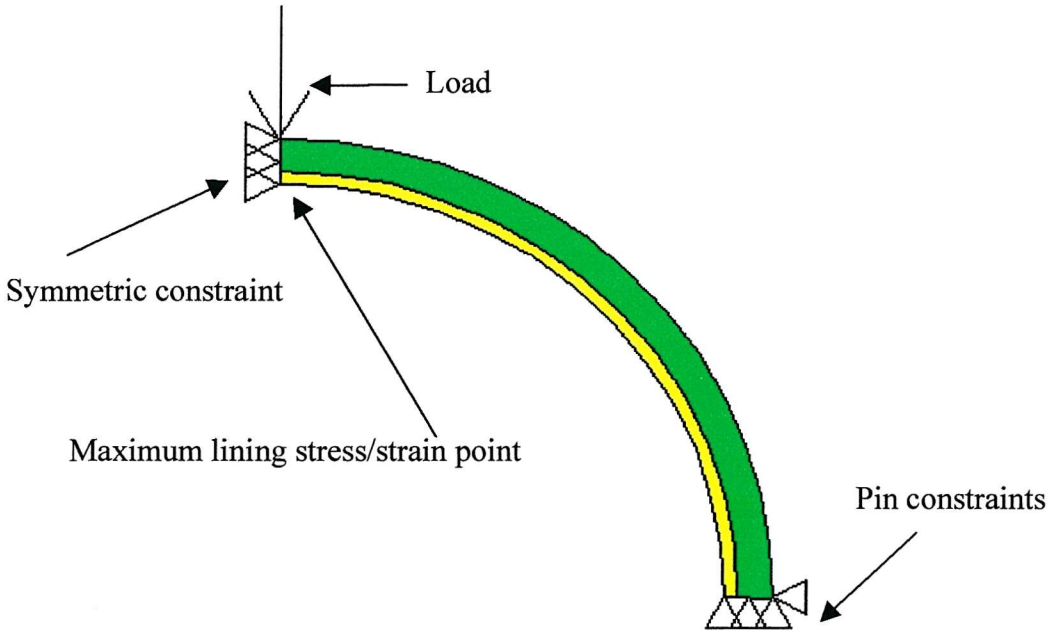

Figure I.5:Schematic of bearing model

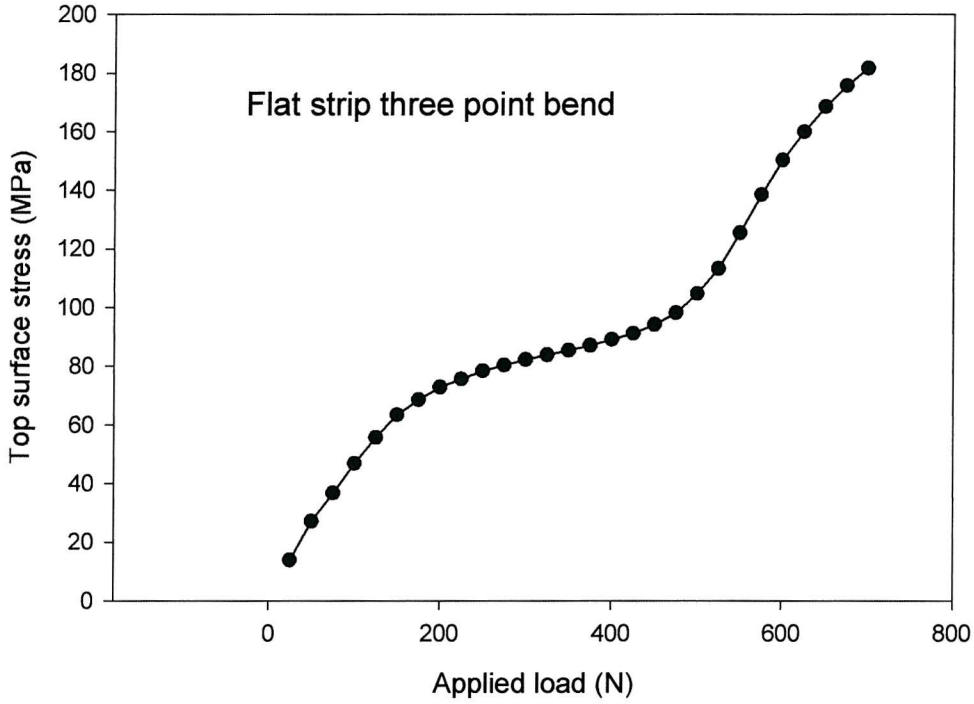

Figure I.6:Variation of maximum stress in flat strip lining material with applied load

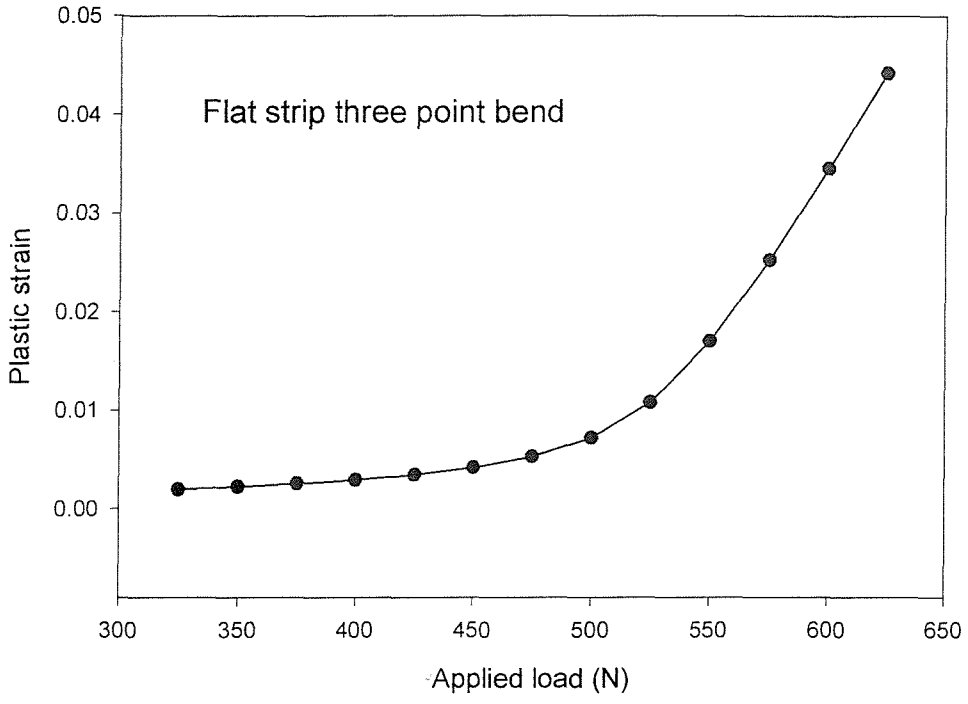

Figure I.7: Variation of maximum plastic strain in flat strip lining material with applied load

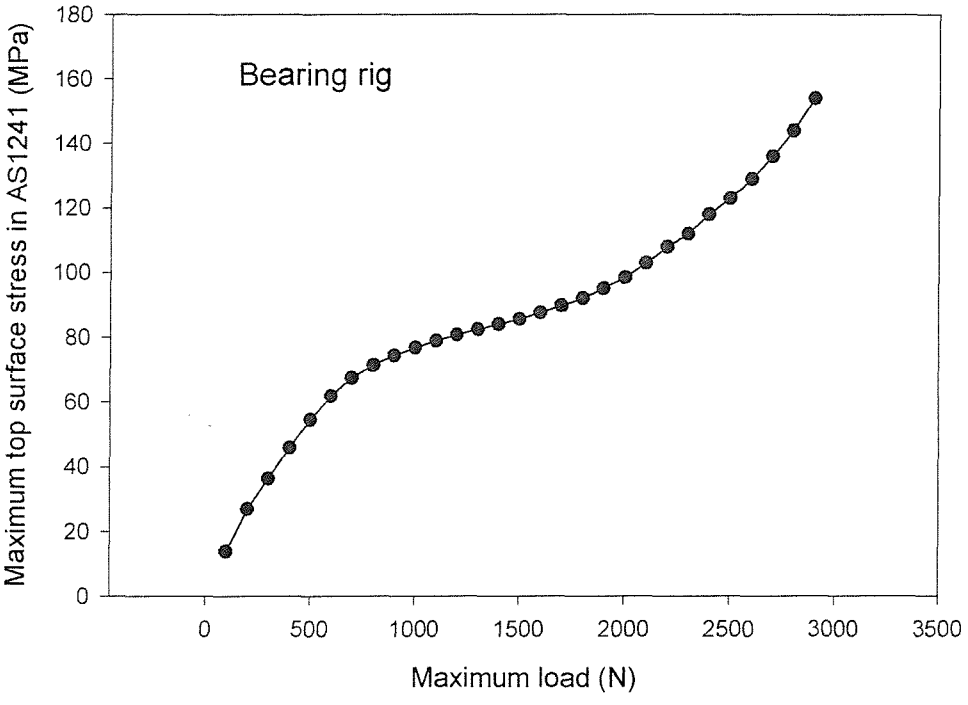

Figure I.8: Variation of maximum stress in bearing lining material with applied load

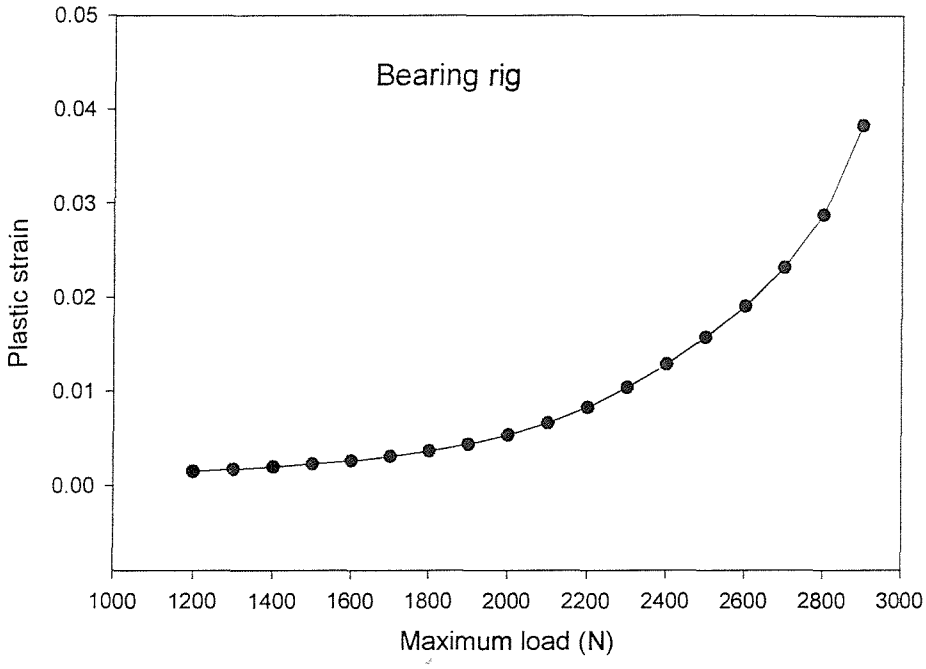

Figure I.9:Variation of maximum plastic strain in bearing lining with applied load

APPENDIX II – MULTI-LINEAR HARDENING CURVES

The majority of finite element models proposed in this thesis require elasto-plastic material models. Experimentally determined stress-strain curves are available for both the steel backing and the AS1241 lining material. However response curves for other materials had to be constructed from yield stress and tangent modulus data alone. Initially these were created as bilinear models, as suggested in the ANSYS5.5 reference guide[1]. However such bi-linear approximations do not represent the true material response particularly well, to increase accuracy a series of multi-linear curves were produced, by removing the sharp gradient change associated with a bi-linear model.

This was achieved by "rounding out" the sharp change in gradient between the elastic and plastic portions of the curve, thereby bringing the material model much closer to the real material response rather than the idealised bilinear case. This rounding is limited to the region between ε_y and ε_2 and consists of a uniform gradient change. The transition region of the curve being built up from the intersection of a series of constructed lines as shown in Figure III.1a. This method is easily implemented in an ANSYS batch file given simple inputs of E, σ_y, σ_2 and elongation to failure, a listing for this macro is given on the following page. Comparison of the bilinear and multi-linear curves are given in Figure II.1b.

Although this macro was not used to simulate AS1241 (a stress/strain curve being available), Figure II.2 shows a comparison between the experimentally determined curve ,the multi linear curve produced from yield stress and tangent modulus data for AS1241 and the simple bi-linear fit. It is clear that the multi-linear model fits the data considerably better than the bi-linear approximation.

A further consequence of this approach is an increase in solution stability since elements do not undergo such a radical change in material behaviour upon exceeding the yield stress.

Macro used for creation of multi-linear hardening curves

```
mpc3
numstep=15
epsint=arg2/arg1
/uis,msgpop,3
*set,ms
*set,cs
*dim,ms,array,numstep+1
*dim,cs,array,numstep+1
intg=arg1
fing=(0.1*arg4)/(0.5*arg5)
ma=intg
mb=fing
ca=0
cb=0.9*arg4-mb*0.5*arg5
xi=(cb-ca)/(ma-mb)
yi=ma*xi+ca
!define steps
xbstep=(0.5*arg5-xi)/numstep
ybstep=(0.9*arg4-yi)/numstep
xastep=(xi-epsint)/numstep
yastep=(yi-arg2)/numstep
ms(1)=ma
cs(1)=ca
*do,line,1,numstep-1,1
ya=arg2+line*yastep
yb=yi+line*ybstep
xa=epsint+line*xastep
xb=xi+line*xbstep
ms(line+1)=(ya-yb)/(xa-xb)
cs(line+1)=ya-ms(line+1)*xa
*enddo
ms(numstep+1)=mb
cs(numstep+1)=cb
tb,miso,arg6,1,numstep+3
tbpt,defi,epsint,arg2
intersections
*do,line,1,numstep,1
xp=(cs(line+1)-cs(line))/(ms(line)-
ms(line+1))
yp=ms(line)*xp+cs(line)
tbpt,defi,xp,yp
*enddo
tbpt,defi,0.5*arg5,.9*arg4
tbpt,defi,arg5,arg4
```

References

[1] ANSYS5.5 Analysis Manual

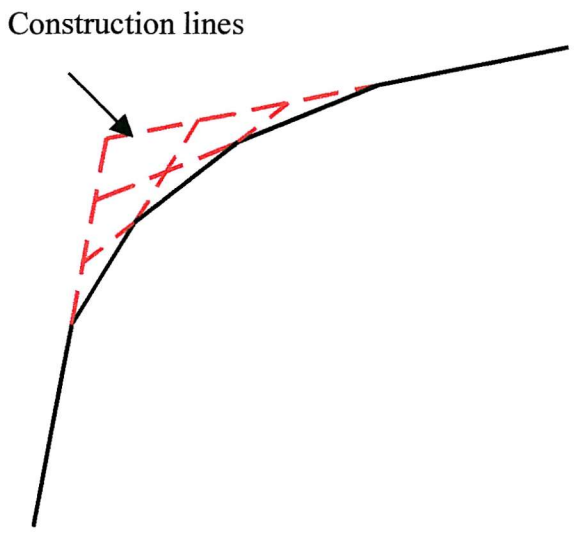

Figure II.1: Construction of material model

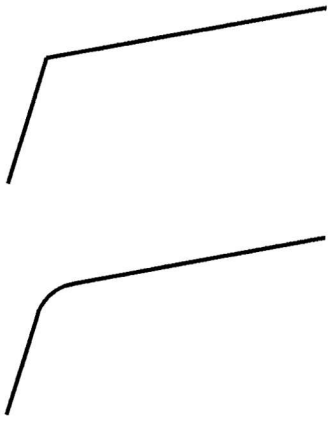

Figure II. 2: Comparison of bi-linear and rounded models

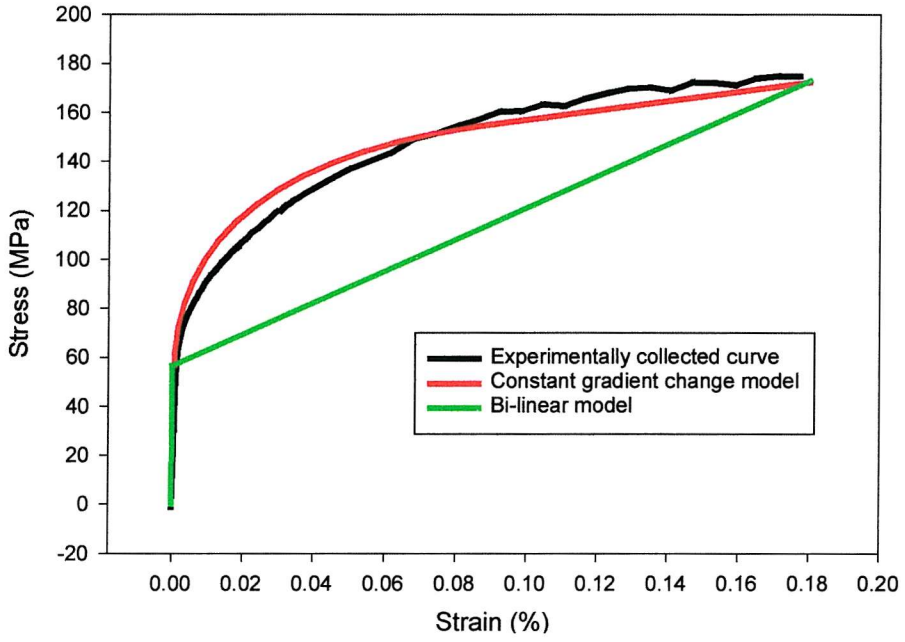

Figure II.3:. Comparison of constant gradient model and experimental stress/strain data for AS1241

APPENDIX III – J-INTEGRAL EVALUATION

In its current form, ANSYS5.5 does not have the ability to calculate the *J*-integral automatically, it was therefore necessary to generate this parameter from other results. This was done using a macro based upon the standard method proposed by Rice[1] rather than the more elaborate domain function method given by Li et al[2].

The macro itself is described initially, whilst a subsequent section is concerned with the process employed to ensure the validity of the approach.

Description of Macro Used for Line Evaluation of *J*-Integral

This macro is based upon one given in a benchmark problem contained in the ANSYS verification manual[3] modified for elasto-plastic conditions. Assuming the crack lies in the *x-y* plane, with *x* parallel to the crack, the 2-D form of the *J*-integral is given in Eqn *III*.1.

$$J = \int_{\Gamma} w dy - \int_{\Gamma} \left(T_x \frac{\partial u_x}{\partial x} + T_y \frac{\partial u_y}{\partial x} \right) ds \qquad (III.1)$$

where,

Γ = any path surrounding the crack tip

w = strain energy density

T_x = traction vector along x axis

T_y = traction vector along y axis

u = displacement vector

s= distance along path Γ

Since the *J*-integral is path-independent, the shape of the contour should not have any bearing on the result, and in the current work a semicircle was provided for use as the *J*-integral contour. In practice the contour was defined by nodes, due to the way the circle was modelled, nodes were present at the octants of the circle. These nodes were used to define the *J*-integral contour, resulting in a semi-octagonal shape. Considering the parameters in Eqn *III*.1, in the first integral, the strain energy density, w, is given by Eqn *III*.2

$$w = \int_0^{\varepsilon_{ij}} \sigma_{ij} d\varepsilon_{ij}$$

(III.2)

It was likely that the contour used in the current work would be at least partially within the crack tip plastic zone, hence the expression for strain energy density may be non-linear, and must therefore be calculated at each solution sub-step and summed to give its correct value, according to Eqn III.3.

$$w \approx \sum \sigma_{ij} \delta\varepsilon_{ij} \equiv \sum \left(\frac{\sigma_{ij}^{q} + \sigma_{ij}^{q-1}}{2} \right) \left(\varepsilon_{ij}^{q} - \varepsilon_{ij}^{q-1} \right)$$

(III.3)

where,

q= solution sub-step number

The second integral is more complex, but only depends on the final values of the traction and displacement vectors $\boldsymbol{T}$ and $\boldsymbol{u}$ respectively. Hence numeric step by step integration is not required. The traction vector components, T_x and T_y may be calculated from common solution parameters according to Eqn III.4.

$$T_x = \sigma_x n_x + \sigma_{xy} n_y$$

$$T_y = \sigma_y n_y + \sigma_{xy} n_x$$

(III.4)

where,

$\boldsymbol{\sigma}$ = Component stress – shown in Figure III.1

$\boldsymbol{n}$ = unit outer normal vector to path Γ (may be mapped directly onto the path from the solution database)

In order to find the derivatives of the displacement vectors $\frac{\partial u_x}{\partial x}$ and $\frac{\partial u_y}{\partial x}$ the path is shifted a small distance (Dx = 1% of total path length) in the positive and negative x directions. In each shifted position, the displacements u_x and u_y are mapped onto the path, the derivatives may then be evaluated according to Eqn III.5.

$$\frac{\partial u_x}{\partial x} \approx \frac{u_x^2 - u_x^1}{Dx}$$

$$\frac{\partial u_y}{\partial x} \approx \frac{u_y^2 - u_y^1}{Dx}$$

(III.5)

Combining these results with the values of the traction vectors found from Eqn III.4, it is possible to evaluate the second integral with respect to *s*, and then in conjunction with the result obtained for the first integral, provide a value of the *J*-Integral. It should be noted that since the contour is semi-octagonal and represents half of a symmetric model, the calculated value should be multiplied by a factor of two to produce the correct value of *J*.

Validation of the *J*-Integral Approach

As an initial step to validate the adopted method of *J*-integral calculation, it was compared with an analytical solution under linear elastic plane strain conditions. An expression for deriving the stress intensity factor, K, in a 3 point single edge notch bend (SENB) specimen, shown in Figure III.2, was obtained[4] and is given in Eqn III.6.

$$K = \frac{6P}{B\sqrt{W}}\left[1.93\left(\frac{a}{W}\right)^{\frac{1}{2}} - 3.07\left(\frac{a}{W}\right)^{\frac{3}{2}} + 14.53\left(\frac{a}{W}\right)^{\frac{5}{2}} - 25.11\left(\frac{a}{W}\right)^{\frac{7}{2}} + 25.8\left(\frac{a}{W}\right)^{\frac{9}{2}}\right] \tag{III.6}$$

The *J* integral is then found from these results using the expression given in Eqn III.7.

$$J = \frac{K^2}{E}\left(1-\nu^2\right) \tag{III.7}$$

A simple elastic finite element model, having the geometry and dimensions as shown in Figure III.2 was created to test the J-integral macro under first elastic and then elasto-plastic conditions. The model was meshed using 8 node quadrilateral elements in plane strain, the mesh was refined at the crack tip and a semi-circular contour provided for evaluation of the J-integral. The model was solved for crack lengths from 0.1mm to 0.425mm, and the predicted values of the *J*-integral were compared with those calculated analytically, the results are shown in Figure I.3. It can be seen that the results compare very well, the average error being ~0.55% and the maximum error less than 2%. It was concluded that the model had demonstrated a sufficient level of accuracy under LEFM conditions to allow its use.

Many authors have used the *J*-integral as a method of evaluating the driving force of fatigue cracks approaching interfaces under elasto-plastic conditions[5,6]. In these situations the near tip behaviour of the crack is cyclically plastic and hence strictly the *J*-integral is invalid. However since no unloading takes place in any of the currently applied modelling strategies, the material behaviour maybe thought of as non-linear elasticity. Thus the *J*-integral should remain valid, providing the contour used for its evaluation remains entirely within a single homogeneous material.

In the interests of simplicity the contour used for *J*-integral evaluation was defined as a semicircle. Due to the shape of the plastic zone evolved at the crack tip the contour will cross the elastic/plastic boundary as shown in Figure III.4, unless the contour is made very small, which may in turn produce undesirable numerical difficulties.

The effect of contour size was evaluated in a series of models using contours of radii 0.005mm to 0.045 mm. It was found that for all cases between 90% and 95% of the contour existed within the region of tangent modulus dominance whilst, along the remainder of the contour lengths the material continued to behave elastically. It was also noted that for very small contours the *J*-Integral was considerably lower than for the larger contours as is shown in Figure III.5. It is believed that this is due to the elements near the crack tip being incapable of providing an accurate solution. It is seen that the values for the *J*-integral converge to an approximately steady value, indicating that under these conditions the *J*-integral is nominally path independent. This demonstrates that although the contour exists both in the elastic and plastic regions the *J*-integral remains valid, since no unloading occurs.

J- Macro Input File

```
*create,jplast2
jpl

!define path
path,jint,5,50,48
ppath,1,arg1
ppath,2,arg2
ppath,3,arg3
ppath,4,arg4
ppath,5,arg5

set,last
*get,maxstep,active,,set,sbst
*do,stepno,1,maxstep,1
*if,stepno,ge,2,then
      set,,stepno-1
      etable,s1sx,s,x
      etable,s1sy,s,y
      etable,s1txy,s,xy
      etable,s1ex,epto,x
      etable,s1ey,epto,y
      etable,s1gxy,epto,xy
*endif

set,,stepno
etable,s2sx,s,x
etable,s2sy,s,y
etable,s2txy,s,xy
etable,s2ex,epto,x
etable,s2ey,epto,y
etable,s2gxy,epto,xy

*if,stepno,ge,2,then
sadd,tsigx,s1sx,s2sx
sadd,tsigy,s1sy,s2sy
sadd,tsigtxy,s1txy,s2txy
smult,msigx,tsigx,,0.5
smult,msigy,tsigy,,0.5
smult,msigtxy,tsigtxy,,0.5
sadd,dex,s2ex,s1ex,1,-1
sadd,dey,s2ey,s1ey,1,-1
sadd,dgxy,s2gxy,s1gxy,1,-1

*else
sadd,msigx,s2sx,,0.5
sadd,msigy,s2sy,,0.5
sadd,msigtxy,s2txy,,0.5
sadd,dex,s2ex
sadd,dey,s2ey
sadd,dgxy,s2gxy

*endif

smult,xbit,msigx,dex
smult,ybit,msigy,dey
smult,txybit,msigtxy,dgxy
sadd,xandy,xbit,ybit
sadd,wstep,xandy,txybit
pdef,clear
pdef,wstep,etab,wstep
pcalc,intg,j,wstep,yg
*get,jastep,path,,last,j

*if,stepno,eq,1,then
      ja=jastep
*else
      ja=ja+jastep
*endif

*enddo

pdef,clear
set,last
pdef,msigx,s,x
pdef,msigy,s,y
pdef,msigtxy,s,xy
*get,dx,path,,last,s
dx=dx/100
pcalc,add,xg,xg,,,,-dx/2
pdef,s1ux1,u,x
pdef,s1uy1,u,y
pcalc,add,xg,xg,,,,dx
pdef,s1ux2,u,x
pdef,s1uy2,u,y
pcalc,add,xg,xg,,,,dx/2
c=1/dx
pcalc,add,dux,s1ux2,s1ux1,c,-c
pcalc,add,duy,s1uy2,s1uy1,c,-c
pvect,norm,nx,ny,nz
pcalc,mult,c1,msigx,nx
pcalc,mult,c2,msigtxy,ny
pcalc,add,tx,c1,c2
pcalc,mult,c1,msigy,ny
pcalc,mult,c2,msigtxy,nx
pcalc,add,ty,c1,c2
pcalc,mult,c1,tx,dux
pcalc,mult,c2,ty,duy
pcalc,add,c3,c1,c2
pcalc,intg,j,c3,s
*get,jb,path,,last,j

jtot= 2*(ja-jb)

*end
```

References

[1] J.R.Rice, A path independent integral and the approximate analysis of strain concentration by notches and cracks, Trans ASME J of Applied mechanics V pp379-386 (1968)

[2] F.Z. Li, F. Shih and A. Needleman, A comparison of methods for calculating energy release rates, Eng Fract Mech V21 No2 pp 405-21 (1985)

[3] ANSYS5.5 Verification Manual

[4] P.P Benham and R.J Crawford, Mechanics of Engineering materials, Wiley, New York (1993)

[5] S. Suresh, Y. Sugimura and E.K. Tschegg, The growth of a fatigue crack approaching a perpendicularly-orientated bimaterial interface, Scripta Met and Mat V27 pp1189-1194 (1992)

[6] Y. Sugimura, P.G. Lim, C.F. Shih and S. Suresh, Fracture normal to a bimaterial interface: effects of plasticity on crack tip shielding and amplification, Acta Met V43 No3 pp1157-69 (1995)

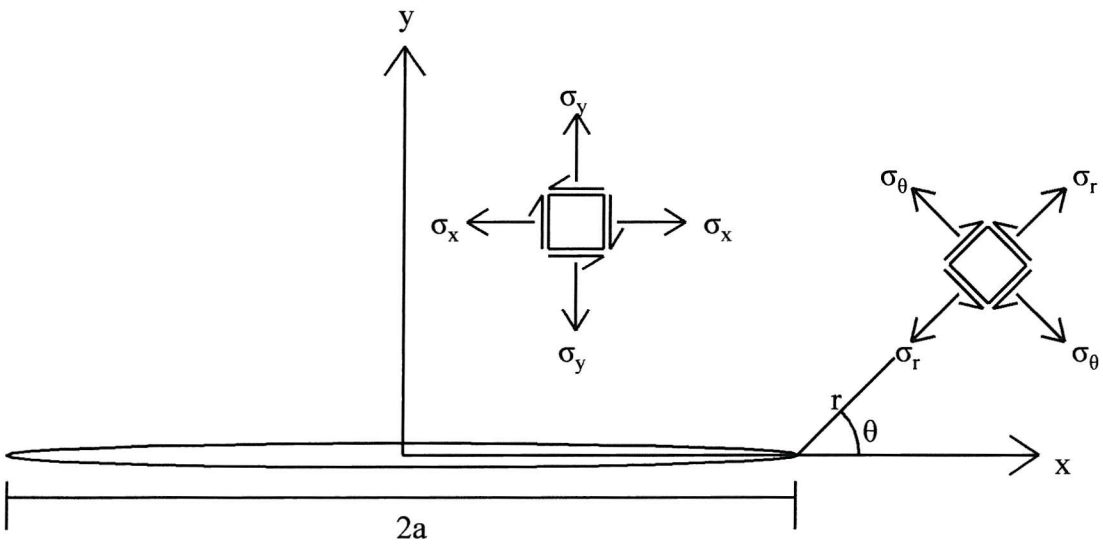

Figure IIII.1: Nomenclature used to describe stresses in an infinite plate containing semi-infinite crack

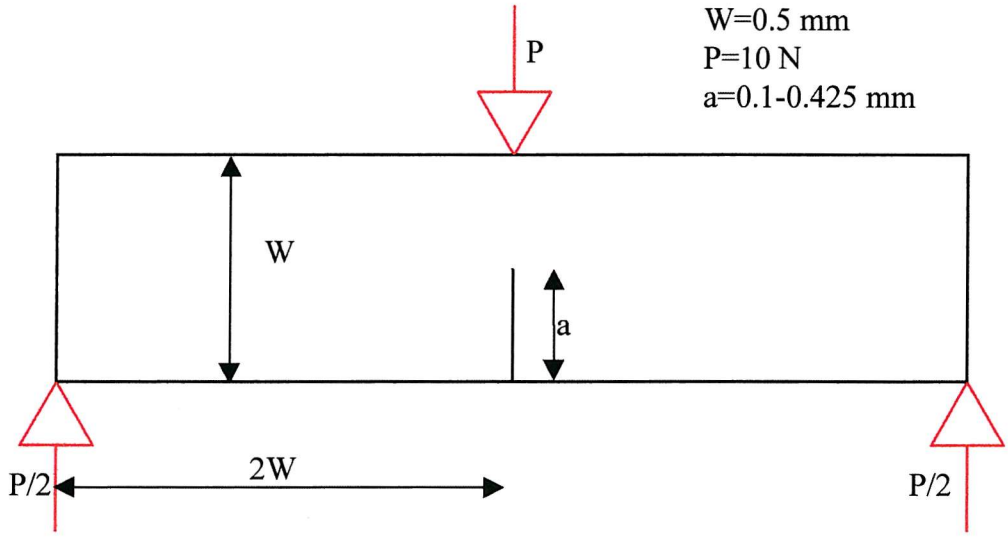

Figure III.2: Schematic of model used for J-integral macro validation

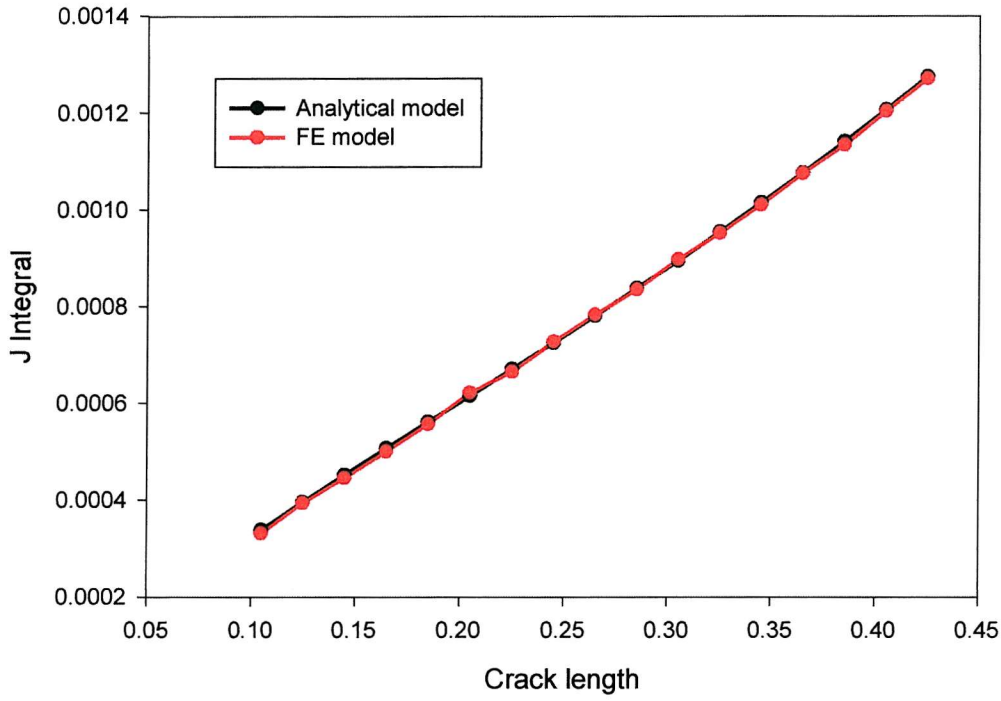

Figure III.3:Comparison of J-Integral calculated by analytical function and finite element model

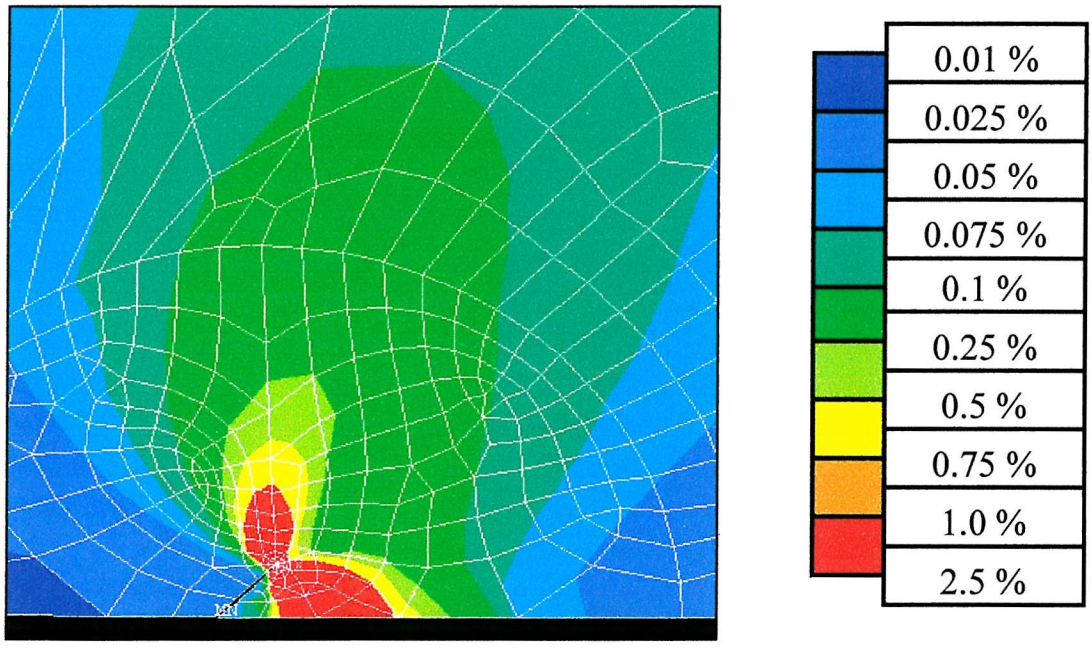

Figure III.4: Near tip plastic strain plot showing contour crossing elastic-plastic boundary

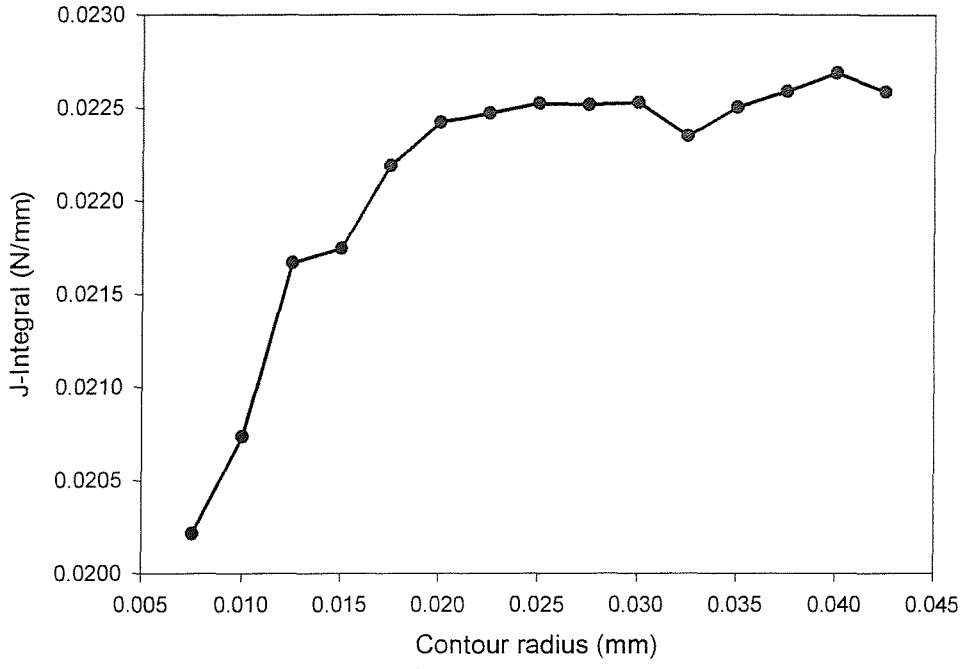

Figure III.5: J-integral variation with contour radius in elasto-plastic model